Technische Universität München

TUM School of Natural Sciences

New insights in gamma-ray astrophysics with modern analysis concepts

Björn Biltzinger

Vollständiger Abdruck der von der TUM School of Natural Sciences zur Erlangung des akademischen Grades eines

Doktors der Naturwissenschaften

genehmigten Dissertation.

Vorsitz:		Prof. Dr. Alejandro Ibarra
Prüfer*innen der Dissertation:	1.	Priv.-Doz. Dr. Jochen Greiner
	2.	Prof. Dr. Lothar Oberauer

Die Dissertation wurde am 23.02.2023 bei der Technische Universität München eingereicht und durch die TUM School of Natural Sciences am 03.04.2023 angenommen.

Abstract

Data analysis in high keV to low MeV gamma-ray astrophysics is challenging, due to the significant cross section of Compton scattering in the interaction of gamma-ray photons with matter. This leads to complications, like measured energy dispersion, that have to be accounted for. Also, no telescope exists today that can focus photons with an energy larger than 80 keV, leading to bad spatial resolution compared to other energy ranges. To mitigate these issues, the data analysis is often based on assumptions and approximations, that can introduce systematic errors or lead to wrong statistical uncertainties, which in turn can lead to wrong physical claims based on the data analysis. I investigated the opportunities that modern data analysis techniques, like forward-folding and Bayesian analysis, offer and applied them to two different gamma-ray instruments: The Gamma-Ray Burst Monitor on Fermi and the Spectrometer on INTEGRAL. For the Gamma-Ray Burst Monitor I developed a physical background model, capable of fitting the observed background variation without the use of empirical polynomials or splines, as has been standard practice until now. I implemented this through the technique of forward-folding the background source photon spectra through the response. This allowed me to reach two achievements: (1) to constrain the cosmic gamma-ray background, which in turn allows to constrain the column density and redshift distribution of Active Galactic Nucleis, and (2) to provide the basis for a new transient search pipeline for the Gamma-Ray Burst Monitor data, capable of detecting transient events previously missed. For the Spectrometer on INTEGRAL I developed a completely new analysis software to analyse Gamma-Ray Bursts. This led to the possibility of fitting physical emission models directly to INTEGRAL data, as well as combined fits with Gamma-Ray Burst Monitor data, for Gamma-Ray Bursts observed by both. With the fit results, I was able to confirm that most Gamma-Ray Burst spectra can be well fitted by optically thin synchrotron emission, unlike previously claimed, and that both fast and slow cooling conditions occur in Gamma-Ray Burst outflows. The detection of slow cooling conditions in Gamma-Ray Burst outflows in combination with the efficient energy dissipation into photons in these objects poses problems for theoretical Gamma-Ray Burst models, that could be overcome with some mechanism that reheats the electrons (e.g. magnetic reconnection). Finally, I derived a new statistical framework to analyse constant point sources with the Spectrometer on INTEGRAL data, deriving statistical sound parameter uncertainties.

Zusammenfassung

Die Datenanalyse in der Gammastrahlen-Astrophysik, in dem Energiebereich zwischen einigen keV und einigen MeV, ist herausfordernd, wegen des signifikanten Wirkungsquerschnittes der Compton-Streuung. Dies führt zu Komplikationen, wie der gemessenen Energiedispersion. Außerdem gibt es bisher kein Teleskop, das Photonen mit einer Energie von mehr als 80 keV fokussieren kann, was zu einer schlechten räumlichen Auflösung im Vergleich zu anderen Energiebereichen führt. Um diese Probleme zu mildern, basiert die Datenanalyse oft auf Annahmen und Näherungen, die systematische Fehler einführen oder zu falschen statistischen Unsicherheiten führen können, was wiederum zu falschen physikalischen Aussagen führen kann. Ich habe die Möglichkeiten untersucht, die moderne Datenanalysetechniken wie die Vorwärtsfaltung und die Bayesische Analyse bieten, und sie auf zwei verschiedene Instrumente angewendet: Gamma-Ray Burst Monitor und Spectrometer on INTEGRAL. Für den Gamma-Ray Burst Monitor habe ich ein physikalisches Hintergrundmodell entwickelt, welches in der Lage ist, die beobachteten Variationen zu erklären, ohne die Verwendung der bisher üblichen empirischen Polynome. Ich habe dies durch die Technik der Vorwärtsfaltung der Photonenspektren der Hintergrundquellen durch die Instrumentantwort umgesetzt. Dadurch konnte ich zwei Ergebnisse erzielen: (1) den kosmischen Gammastrahlenhintergrund einzuschränken, was es wiederum ermöglicht, die Wassserstoff-Säulendichte und die Rotverschiebungsverteilung von Active Galactic Nuclei einzuschränken, und (2) die Grundlage für eine neue Pipeline zur Suche nach transienten Ereignissen in den Gamma-Ray Burst Monitor-Daten zu schaffen, die in der Lage ist zuvor übersehene Ereignisse zu entdecken. Für Spectrometer on INTEGRAL habe ich eine neue Analysesoftware entwickelt, um Gammastrahlausbrüche zu analysieren. Dies ermöglichte den direkten Test physikalischer Emissionsmodelle mit den INTEGRAL-Daten, sowie die kombinierte Anpassung mit Gamma-Ray Burst Monitor-Daten für Gammastrahlenausbrüche. Mit den Resultaten konnte ich bestätigen, dass die meisten Gammastrahlausbruch-Spektren durch optisch dünne Synchrotronemission gut erklärt werden können, anders als zuvor behauptet, und dass sowohl schnelle als auch langsame Abkühlungsbedingungen in Gammastrahlausbrüchen auftreten. Die Entdeckung langsamer Abkühlungsbedingungen in Gammastrahlausbrüchen in Kombination mit der effizienten Energiedissipation in Photonen in diesen Objekten stellt theoretische Gammastrahlausbruch-Modelle vor Probleme, die mit einem Mechanismus überwunden werden könnten der die Elektronen wieder aufheizt (z.B. magnetische Rekonnexion). Schließlich habe ich einen neuen statistischen Ansatz hergeleitet, um konstante Punktquellen mit den Spectrometer on INTEGRAL-Daten zu analysieren und statistisch fundierte Parameterunsicherheiten abzuleiten.

Contents

Acronyms

3ML	Multi-Mission Maximum Likelihood framework
ACD	Anti-Coincidence Detector (LAT)
ACS	Anti-Coincidence Shield (SPI)
AFEE	Analog Front-End Electronics
AGN	Active Galactic Nuclei
ARR	Autonomous Re-point Request
BALROG	BAyesian Location Reconstruction Of GRBs
BAT	Burst Alert Telescope
BATSE	Burst And Transient Source Experiment
BGO	Bismuth Germanate
CGB	Cosmic Gamma-ray Background
CXB	Cosmic X-ray Background
DRM	Detector Response Matrix
ESS	Effective Sample Size
FOV	Field Of View
GRB	Gamma-Ray Burst
GBM	Gamma-Ray Burst Monitor
Geant	Geometry and Tracking
HMC	Hamiltonian Monte Carlo
IBAS	INTEGRAL Burst Alert System
IBIS	Imager on Board the INTEGRAL Satellite
INTEGRAL	International Gamma-Ray Astrophysics Laboratory
IRF	Image Response Function
ISDC	INTEGRAL Science Data Centre
LAT	Large Area Telescope
MCMC	Markov Chain Monte Carlo
MHD	Magnetohydrodynamic
NaI	Sodium Iodide
OSA	Off-line Scientific Analysis
OSV	Fermi GBM Orbital Background Subtraction Tool
PHA	Pulse Height Analysis
PIC	Particle-In-Cells
PMT	Photo Multiplier Tube
PPC	Posterior Predictive Check
PSD	Pulse Shape Discriminator
QQ	Cumulative-Cumulative
RMF	Redistribution Matrix File
SAA	South Atlanic Anomaly
SPI	Spectrometer on INTEGRAL
TTE	Time-Tagged Events

1 Introduction

Analysing astrophysical data in the range between some keV and a few MeV is challenging, due to the nature of the interaction of these photons with matter. At lower energies focusing techniques can be used and the interaction cross section of photons and detector material is dominated by photo absorption (e.g. Hubbell, Gimm, and Overbo 1980), leading to good spatial and spectral resolution. Also, at energies larger than a few MeV the interaction cross section of the photons and the detector material is dominated by pair production (e.g. Hubbell, Gimm, and Overbo 1980), that allows again the accurate determination of the spatial origin and energy of the photons in pair-conservation telescopes (e.g. Atwood et al. 2009).

In the intermediate energy range between some keV to a few MeV, Compton scattering with the detector material has a significant (in part of the energy range even dominant) interaction cross section, leading to issues like partial energy deposition in the detector material. This happens, when the photon only deposits part of its energy in the Compton scatter and leaves the detector afterwards. Also no telescope exist today, that can focus photons with an energy larger than 80 keV and the pair production cross section is zero for $E_{ph} < 2m_{\text{electron}}$ and small for $E_{ph} \gtrapprox 2m_{\text{electron}}$(e.g. Hubbell, Gimm, and Overbo 1980). Therefore, the spatial and spectral resolution of the data in this energy range is much worse compared to other energy ranges, which has to be carefully accounted for.

Due to these issues, the data can not be directly transformed into an image or a spectrum but the data generating detection process has to be accounted for[1]. Often this is mitigated by certain assumptions or approximations. Approaches found in the literature that use strong assumptions in their analysis include:

1. Assume only photo peak interactions (when all the energy of the photon is deposited in the detector) (e.g. Pleintinger et al. 2019)
2. Assume only photo peak interactions in a first step fit and use an approximate correction function in a second step, to account for energy dispersion (e.g. McBreen et al. 2006)
3. Fitting the data with an easy spectral model and projecting the result to a photon flux data points (see Sec. 2.2), which are then fitted with the model of interest (e.g. Ajello et al. 2008). This is also done in neutrino (e.g. IceCube Collaboration et al. 2018) and Cherenkov telescope data analysis (e.g. MAGIC Collaboration et al. 2019).
4. Iterative source removal in images, by removing the brightest sources one by one (Skinner and Connell 2003)

[1] This is also true for the analysis of data at other photon energies, but often much less severe.

5. Maximum entropy maps to image the ^{26}Al emission with the Imaging Compton Telescope (Knodlseder et al. 1999)

All these approaches can introduce strong systematic errors into the result when the assumptions are bad and lead to wrong physical claims. One example for this is shown in Sec. 2.2. To avoid these potential systematic errors and to extract the maximum amount of information from the data, other approaches should be used that include all the processes that affect the data into the modeling (like e.g. Burgess et al. 2017; Burgess et al. 2020; DeLaunay and Tohuvavohu 2022). In this thesis, I present different analysis techniques I developed with this goal and show that it gave new insights into different topics of gamma-ray astrophysics. The structure of the thesis is as follows. In Sec. 2 I introduce the concept of forward folding, that is crucial for all improvements presented in this work. Sec. 3 derives different fitting algorithms and model checking techniques used. A developed physical background model for the Gamma-Ray Burst Monitor (GBM) is shown in Sec. 4, including the physical implications I can conclude with it about the spectrum of the Cosmic Gamma-ray Background (CGB). Sec. 5 shows a newly developed analysis software for Gamma-Ray Bursts (GRBs) detected by the Spectrometer on INTEGRAL (SPI), which is used to test a physical model of the prompt GRB emission. Finally, in Sec. 6 a new statistical framework for the analysis of constant point sources with SPI data is derived.

2 Forward Folding

Forward folding is a key concept for most of the work in this thesis. Therefore, I will introduce the basic concept of forward folding in spectral fitting and show what its benefits are compared to the 'unfolding' of measured data.

2.1 Basic Concept

The basic concept of forward folding is that one starts at the physics that create a phenomenon and forwards propagates this through all steps between the creation of the physical function (e.g. photon spectrum) and the data that can be measured in the end. This can include detector properties and other selection effects, but also physical processes that alter the original signal before it reaches the detector (e.g. absorption). It is fundamentally different to the often used 'unfolding' of the data into a physical data space (e.g. photon spectrum), which is then fitted or over-plotted with a model. The conceptional difference is illustrated in Fig. 2.1 and Fig. 2.2.

The concept of different spaces is crucial for understanding the forward folding analysis: The measured data live in another data space than the model we are interested in and the response is the connection that can transform the model into the data space of the measurements. These data spaces can even have different dimensions. This can be expressed with an first-order Fredholm equation (Craig and Brown 1986):

$$D_{\vec{k}} = \int d\vec{x} F(\vec{x}) \mathcal{R}\left(\vec{x} \rightarrow D_{\vec{k}}\right), \tag{2.1}$$

s where $D_{\vec{k}}$ is the predicted measurement in the measurement bin $\vec{k}$ by a model $F(\vec{x})$ and the response $\mathcal{R}\left(\vec{x} \rightarrow D_{\vec{k}}\right)$ defining the transformation from the model space to the measurement data space. In most cases the measured data space is one-dimensional (e.g. reconstructed energy), but in general it can be n-dimensional. For most realistic cases Eq. 2.1 has to be used in its discrete version, transforming the integral into a sum:

$$D_{\vec{k}} = \sum_i F(\vec{x}_i) \mathcal{R}\left(\vec{x}_i \rightarrow D_{\vec{k}}\right). \tag{2.2}$$

In all cases in this thesis the response is a two-dimensional matrix with the information what the expected spectra in data space is for a given model. But the general concept of a response is not limited to this and can also include other information, like e.g. selection effects in population analysis.

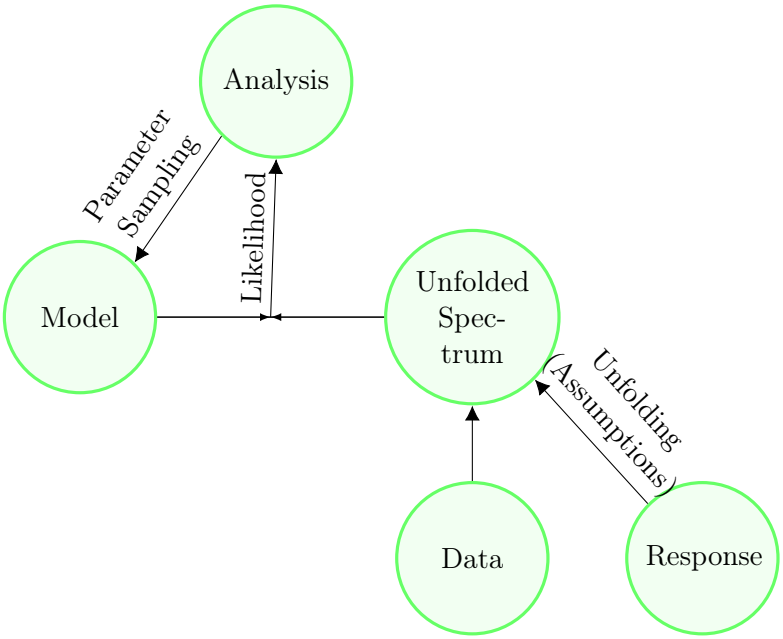

Figure 2.1: Concept sketch of unfolding the data with a response and fitting the model to the unfolded data. This is often done, but most of the times incorporates assumptions, that can lead to biases, because these assumptions are imprinted into the unfolded spectrum. This can lead to wrong claims if the assumptions are not correct. This approach is computationally cheap, because the unfolding is only done once.

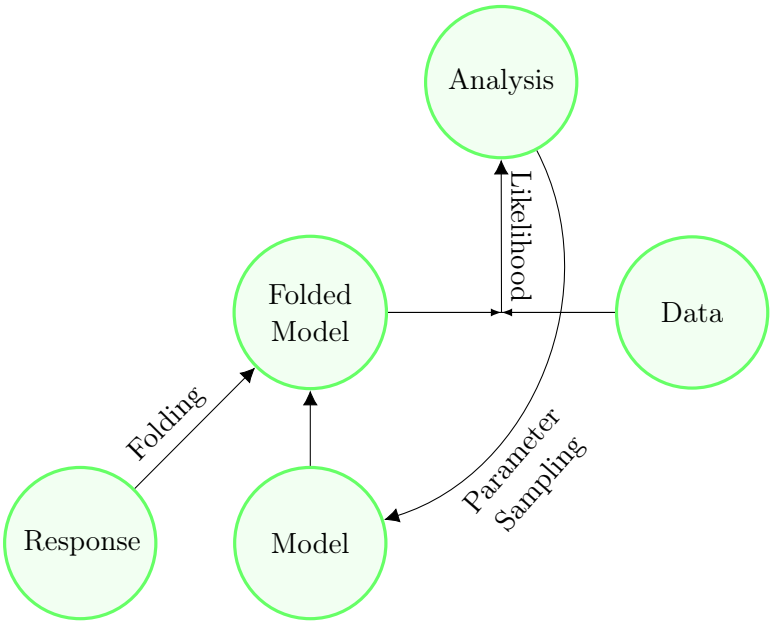

Figure 2.2: Concept sketch of the forward folding approach. The model parameter is sampled and folded with response to generate the model in data space. This has the advantage of relying on no assumptions, but can be computationally expensive.

Unfolding the physical spectrum would need to invert Eq. 2.1 or 2.2 to get $F(\vec{x})$ from $D_{\vec{k}}$. But the response matrix in Eq. 2.2 is in most cases singular and therefore, not invertible, preventing this approach without the use of simplifications that introduce biases in the results. Additionally, due to measurement uncertainties (e.g. Poisson noise), the resulting model spectrum will be unstable to these data fluctuations, as the measured data is not equal to $D_{\vec{k}}$ in that case, but instead is one realisation of $D_{\vec{k}}$ with the measurement uncertainties. This is due to the fact, that model spectra can be arbitrarily different but still result in very similar data after folding with the response Craig and Brown (1986). There exists no general stable solution to unfold first-order Fredholm equations, but many attempts have been made to create tools doing this impossible task. Instead the forward folding method of assuming a physical spectrum and folding it with the response to get a predicted count spectrum and comparing this to the observed data with the appropriate likelihood (see Sec. 3) is the only possible approach in this case.

Summarising, the unfolding approach is computationally much cheaper than the forward folding approach in most cases, but can lead to biases that are hard to identify, as shown in the next section, or unstable solutions. Forward modeling on the other hand is a natural way to include complicated effects into the fit, like e.g. selection effects or detector properties.

2.2 Spectral Fitting

Most of the work I present in this thesis is connected to spectral fitting of X-ray/γ-ray observations. Observing in this energy range is challenging, due to the small cross section of the photons and because it has to be done with satellites, due to the large opacity of the atmosphere at these energies. The technical limitations of the detectors that can be launched into space and the significant Compton scattering cross section in this energy range (e.g. Hubbell, Gimm, and Overbo 1980) lead to sever problems, like energy dispersion. This happens for example if the photon Compton scatters in the detector, depositing some of its energy, but leaves the detector after this without being fully absorbed. Also the transformation of the deposited energy into an electric signal, that is finally measured and sorted into energy channels, has some statistical fluctuations (e.g. Kippen et al. 2007). This leads to the fact that the energy of photons can not be measured precisely and not every photon with the same energy is detected in the same energy bin. Therefore, the energy range that is often assigned to energy data bins has only limited meaning. Neither do all photons detected in this energy bin have an energy in this range, nor are all photons in this energy range detected in this energy bin. For most experiments the assigned energy range to energy bins means that the mean of the photo peak (when all energy of the photon is deposited in the detector) of these photons lies within this energy bin. All physical/technical processes involved in the transformation from the photon energy, E_{ph}, to the energy bin it is detected in, E_{bin}), are summarised by the response matrix $\mathcal{R}(E_{ph} \rightarrow E_{bin})$, for which the model is discretised in reasonable small bins. This response matrix depends on the technical details of the detector and the satellite the detector is mounted on and is usually determined by extensive Geometry and Tracking (Geant) simulation and calibra-

tion measurements before the launch. Therefore, the predicted data by a model can be calculated with the discrete first-order Fredholm equation of the response matrix and the model flux vector:

$$\vec{D}(\vec{\theta}) = \mathcal{R}\vec{F}(\vec{\theta}). \tag{2.3}$$

There have been many ideas how to unfold the model spectrum from the data in this setup, but all of them are either mathematically ill-defined, for any realistic response, or depend on assumptions, that will be wrong in most cases. I will discuss the two most prominent approaches in gamma-ray spectral analysis and their problems in the following.

Photo Peak Unfolding

The easiest approach to unfold the observation into the model space, is by simply assuming that every detected photon is detected with its exact energy. This is done for example for the analysis of constant sources in SPI (see Sec. 5). Under this assumption the response gets diagonal and can be inverted to go from the observed data to data points in the model space. In the case of SPI the energy resolution of the instrument gets part of the model, folding the true model with the energy resolution during the fit to the unfolded spectra (e.g. Pleintinger et al. 2019). But all other effects, like partial energy deposition are ignored in this approach, which is a problem for γ-ray detectors, where for large energies (> 1 MeV), typically $\gtrapprox 50$ % of the detected photons do not deposit all their energy in the detector (Sturner et al. 2003; Kippen et al. 2007).

Unfold with Fit

Unfolding is often done in a second step after fitting the data with an easy model with the forward folding technique. The result of the easy model are converted into an unfolded spectra with units $\frac{photons}{cm^2\,s}$ with the formula

$$\int_{x_1}^{x_2} dx\, F(x) = \frac{\int_{x_1}^{x_2} dx\, M_{best-fit}(x)}{\int_0^\infty dx \int_{x_1}^{x_2} dx'\, \mathcal{R}(x \to x') M_{best-fit}(x)} \int_{x_1}^{x_2} dx\, O(x), \tag{2.4}$$

where $F(x)$ is the unfolded spectrum, $M_{best-fit}(x)$ is the best fit realisation of the model used for the forward folding fit and $O(x)$ the observed spectrum in data (count) space (Arnaud 1996; Freeman, Doe, and Siemiginowska 2001). This effectively weights the observations in every bins with the ratio between expected photon flux and counts in this energy bin from the best fit realisation of the easy model used. This approach has several problems. Firstly it is model dependent, because the unfolded spectrum will change if a different model is used (different $M_{best-fit}(x)$). Secondly it uses the energy bins in the model space and the data space equivalently, which is not correct, therefore, e.g. energy dispersion is not included correctly. Thirdly, the uncertainty in the fit can not be accounted for and only the measurement uncertainties (e.g. Poisson process) are 'corrected' in the same way from the data space to the model space. Finally a fit is only valid under the assumptions that the used model is the correct one. Fitting first with one model and than fitting the output of the first fit with another model is therefore ill-defined. Fig. 2.3

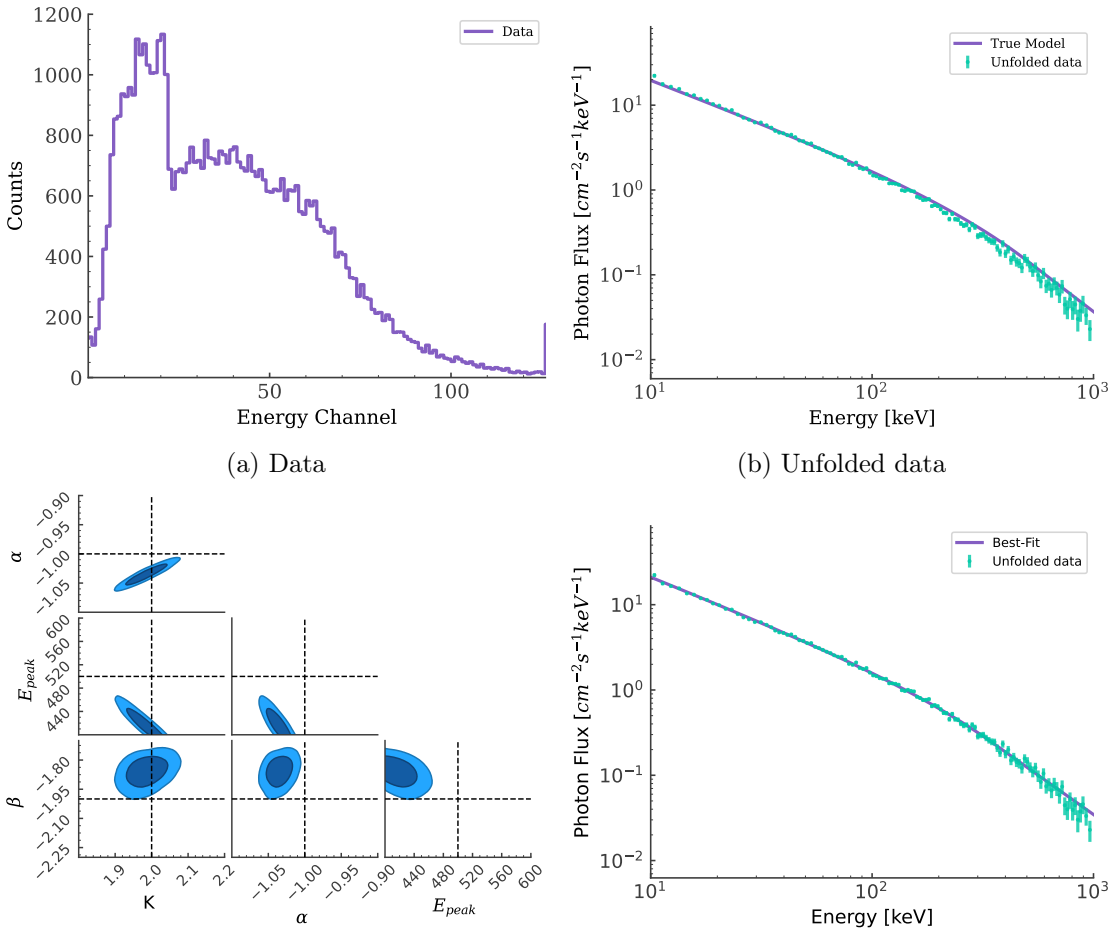

(a) Data

(b) Unfolded data

(c) Corner plot of fit

(d) Fit of unfolded data

Figure 2.3: Unfolding simulated data of a source with a Band function spectrum in one GBM detector (a) with a power law (b) and fitting the unfolded data with a Band function. The fit is not able to recover (c) the simulated values (dashed lines) even though the fit to the unfolded data looks reasonable (d).

shows an example how this approach leads to wrong results in the case of simulated GBM data created by a source with a Band function spectrum (Fig. 2.3a) when unfolded with a simple power law (Fig. 2.3b). The final parameter estimation when fitting the unfolded data again with a Band function is significantly off from the simulated values (Fig. 2.3c) even though the final fit of the unfolded spectrum with a Band function is not an obvious bad fit (Fig. 2.3d). This shows the danger of 'unfolding' data.

The general conclusion is that there is no way to generate a valid unfolded spectrum for any realistic application. It is possible to generate a model spectrum for a given spectral model, by plotting the posterior of the fit in model space. But the assumption for this model spectrum is that the used model is correct. Therefore, it is not valid to generate a model spectrum with one model and fit or over-plot this spectrum with another model, as it breaks the assumption that the first model is the correct one. Unfolded spectra from model fits can be used for a first estimate if the model of interest looks very different, but should never be used for parameter inference.

3 Fitting

Fitting a model to observed data is the process of finding the model configurations that can explain this data adequately and quantify the uncertainties of model parameters or model predictions. In this chapter I will summarise the main concepts, and discuss in detail different fitting approaches. The focus of this chapter is on the Bayesian fitting approaches, as these are the ones used in this thesis.

3.1 Bayes Inference

Bayesian inference is based on Bayes theorem (Bayes and Price 1763)

$$\pi(A|B) = \frac{\pi(B|A)\pi(A)}{\pi(B)}, \tag{3.1}$$

which gives the probability of A given B as a function of the probability of B given A. The notation in data analysis is that A is the predicted data by parameters $\vec{\theta}$ of a model M and B is the observed data D, leading to

$$\pi(\vec{\theta}, M|D) = \frac{\pi(D|\vec{\theta}, M)\pi(\vec{\theta}, M)}{\pi(D, M)}. \tag{3.2}$$

Here $\pi(D|\vec{\theta}, M)$ is the likelihood of the data given the model M with parameters $\vec{\theta}$, $\pi(\vec{\theta}, M)$ is the prior knowledge about the parameters of the model and $\pi(D, M)$ is the marginal likelihood (sometimes also called evidence) of the data given the model M. $\pi(D, M)$ normalises the probability distribution $\pi(\vec{\theta}, M|D)$ and is often used for model comparison via Bayes factors (e.g. Kass and Raftery 1995; Morey, Romeijn, and Rouder 2016)), even though this has been shown by Isi, Farr, and Chatziioannou (2022) that this can lead to wrong results. The final product is $\pi(\vec{\theta}, M|D)$, that is the posterior distribution of the parameters of the model given the observed data. In this framework, the true parameter value is a random variable that we can assign a probability distribution to, given the data, the model and our prior knowledge of the parameter, in a natural way. The fact that the parameters are a random variable and not the data, means that the uncertainty is on the model and not the observed data.

An argument often used against Bayesian inference, is that the use of the prior makes the analysis, and therefore, also the result, subjective, as there is no unique prior to use. In Bayesian analysis the prior is part of the modeling, a poorly chosen prior is equivalent to a poorly chosen model. Using an informative prior has to be well argued for. There are

many applications where an informative prior can be very useful, for example by excluding un-physical parameters from the fit (e.g. negative masses or velocities larger than the speed of light). If we on the other side only have very little prior knowledge of a parameter, we can use weakly-informative priors, such that the likelihood contribution dominates.

For all non-trivial cases the posterior distributions can not be calculated analytically. Therefore, we need numerical procedures to estimate the posterior distributions. In this thesis two different approaches are used, which are both presented in the following subsections.

3.1.1 Nested sampling

Nested sampling is a method which can estimate the marginal likelihood, but can also be used for parameter inference (Skilling 2004). It defines a prior volume χ, which can be expressed as a function of a given likelihood value $\mathcal{L}$:

$$\chi(\mathcal{L}') = \int_{\mathcal{L}(\vec{\theta})>\mathcal{L}'} \pi(\vec{\theta})\mathrm{d}\vec{\theta}. \tag{3.3}$$

Therefore, $\chi(\mathcal{L}')$ is defined as the prior volume with likelihood larger than $\mathcal{L}'$. Recalling the definition of the marginal likelihood

$$\mathcal{Z} = \int \mathcal{L}(\vec{\theta})\pi(\vec{\theta})\mathrm{d}\vec{\theta} \tag{3.4}$$

we can write the marginal likelihood in terms of χ

$$\mathcal{Z} = \int_0^1 \mathcal{L}(\chi)\mathrm{d}\chi, \tag{3.5}$$

because χ can by construction take values between 0 (for $\mathcal{L}' \geq \mathcal{L}_{max}$) and 1 (for $\mathcal{L}' = 0$) (Skilling 2004). This approach projects the N-dimensional integral to a 1-dimensional integral. To approximate the integral one can construct a sorted chain of χ_i values

$$0 < \chi_N < \chi_{N-1} < ... < \chi_0 = 1 \tag{3.6}$$

and use a simple trapezoidal integration rule (Skilling 2006)

$$\mathcal{Z} = \sum_{i=1}^{N} \mathcal{L}(\chi_i)\frac{1}{2}(\chi_{i-1} - \chi_{i+1}). \tag{3.7}$$

In nested sampling the sorted chain of χ_i with associated likelihood values $\mathcal{L}(\chi_i)$ is constructed by drawing an ensemble of 'live-points' from the prior of the parameters and sequentially remove the point with the lowest likelihood with a newly sampled point from the prior with a higher likelihood (see Fig. 3.1). The first removed point has, by construction, an assigned $\chi_0 = 1$, and we can express χ_i as function of χ_{i-1} with

$$\chi_i = t_i\chi_{i-1}, \tag{3.8}$$

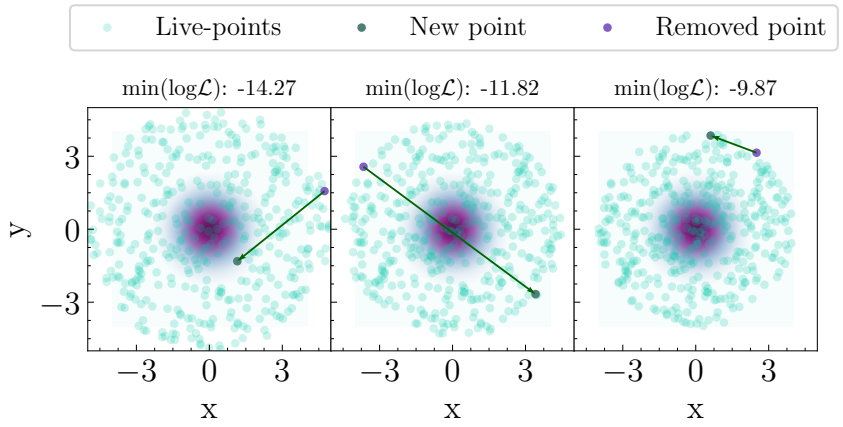

Figure 3.1: Example how the live-points are updated in nested sampling. In this case the mock model has two parameters, the likelihood is a 2D-standard normal distribution and the prior is an uninformative prior between -5 and 5 for both parameters. The three different columns show three different steps in the total sampling, from early (left) to late (right) and the titles show the minimum logarithm of the likelihood of all active live-points.

where t_i follows the distribution (Skilling 2006)

$$\pi(t) = Nt^{N-1}. \tag{3.9}$$

Here N is the number of live-points in the ensemble. This probability distribution is due to the fact, that after drawing a new point with a likelihood higher than the removed point, the ensemble represents a random draw of N points according to the prior in the likelihood range larger than the likelihood of the removed point. This is by construction equivalent to the random drawing of N points in the range of [0, χ_{i-1}], where χ_{i-1} is the prior volume of the previous step. Combining this and Eq. 3.8 gives that t is the maximum of a random draw of N points in the range [0, 1]. Eq. 3.9 is the probability distribution for exactly this scenario. As this is a sequential process of removing the point with the lowest likelihood and adding a point with a higher likelihood over and over again, the prior volume after i steps is given by

$$\chi_i = t_i \chi_{i-1} = \prod_{j=1}^{i} t_j \chi_0 = \prod_{j=1}^{i} t_j, \tag{3.10}$$

because $\chi_0 = 1$ by definition.

With the probability distribution for t in Eq. 3.9, we can estimate the prior volume after many steps to be (Skilling 2006)

$$\chi_i \approx e^{-\frac{i}{N}}. \tag{3.11}$$

This approximates the prior volume at every iteration step and with Eq. 3.7 we can calculate the marginal likelihood if we run this algorithm for sufficient many iterations (see Fig. 3.2).

The posterior distributions can then easily be calculated in a second step, using the estimated prior volumes and likelihood values of the removed points in the sampling. The

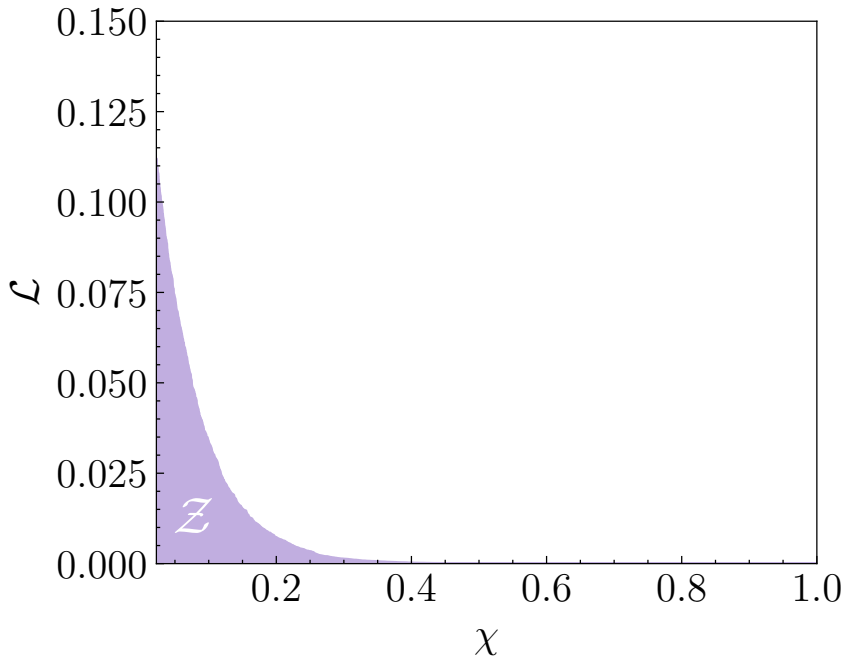

Figure 3.2: Likelihood of the removed points as a function of prior volume from the nested sampling run shown in Fig. 3.1. The marginal likelihood can be approximated as the integral of this function.

removed points x_i are weighted with

$$p(x_i) = \frac{\mathcal{L}_i \frac{\chi_{i-1} - \chi_{i+1}}{2}}{\mathcal{Z}}. \tag{3.12}$$

With the weighted samples we can construct the posterior distribution of the parameters, like shown in Fig. 3.3.

For the efficiency of nested sampling, it is important to sample new points with a high likelihood to be accepted ($\mathcal{L}(p_{new}) > \mathcal{L}(p_{removed})$), without ignoring any of the allowed prior volume in the sampling (Feroz et al. 2019). The simple approach to always sample from the full prior leads to very small acceptance rates in the later states of the fit, especially for high-dimensional problems. Ellipsoidal nested sampling uses the covariance matrix of the current set of live-points, to construct a N-dimensional ellipsoid, that should include most of the prior volume (Mukherjee, Parkinson, and Liddle 2006). Sampling from this ellipsoid, corrected for the prior distribution, is much more efficient than sampling from the whole prior distribution (Mukherjee, Parkinson, and Liddle 2006). But this approach is inefficient if the posterior distribution is multimodal, as the ellipsoid will include all the peaks of the posterior and the volume between the peaks. Multimodal nested sampling solves this problem, by splitting the set of live-points into different sets, if a multimodality is detected. Each of the sets can than nicely capture one of the peaks. This is used in MultiNest (Feroz and Hobson 2008; Feroz, Hobson, and Bridges 2009; Feroz et al. 2019), which is the software used in this thesis.

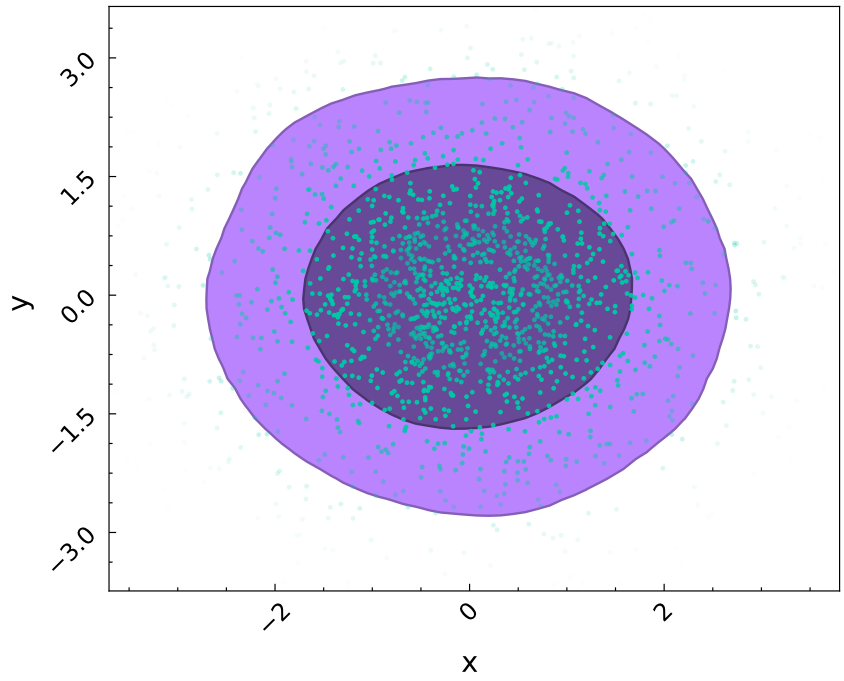

Figure 3.3: Posterior distribution from the nested sampling run shown in Fig. 3.1. The points are the individual samples with the opacity proportional to the sample weight and the filled areas show the one- and two-sigma area.

3.1.2 Hamiltonian Monte Carlo

Hamiltonian Monte Carlo (HMC) is a special case of Markov Chain Monte Carlo (MCMC) that is computationally very effective, especially for high-dimensional problems (many parameters). Therefore, to discuss HMC, we first have to introduce the basic idea of MCMC. The following subsection follows closely Betancourt (2017).

A MCMC is defined by a Markov transition ($\mathcal{T}(x'|x)$), which is a conditional probability distribution, giving the probability to jump to the position x' from the initial position x. Of particular interest are Markov transitions, that preserve the target distribution:

$$\pi(x) = \int_S \mathrm{d}x'\, \pi(x')\mathcal{T}(x|x'). \tag{3.13}$$

If we can construct a $\mathcal{T}$ such that Eq. 3.13 is fulfilled, it will converge towards the 'typical set'. The typical set is defined as the volume of the parameter space with the most probability associated to it ($\pi(x)\mathrm{d}x$). In low dimensions this is typically dominated by the target density $\pi(x)$, which causes the typical set to be close to the maximum of the target distribution. But the higher the dimension of the parameter space gets, the more important the volume part ($\mathrm{d}x$) of the product gets, which causes the volume around the mode of the target distribution to become negligibly small. Therefore, the typical set, counter-intuitively, moves away from the maximum of the target distribution, to the volume of the parameter space that maximises $\pi(x)\mathrm{d}x$ (see Fig. 3.4), which will be important for the derivation of HMC. The idea of MCMC is to construct a $\mathcal{T}$ that fulfils Eq. 3.13 and construct a chain with the algorithm summarised in Fig. 3.5. The points (or samples) in

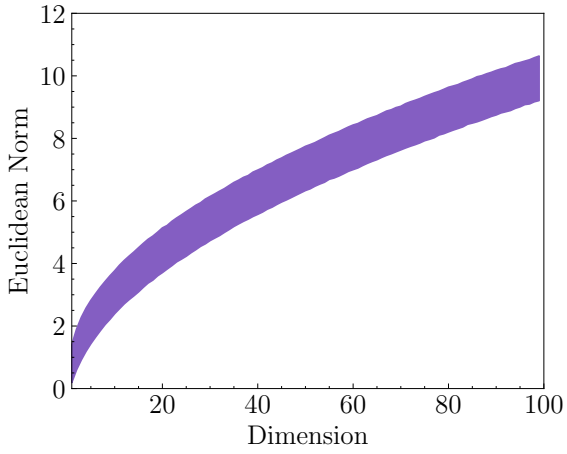

Figure 3.4: Euclidean norm of points sampled from standard normal distributions in different dimensions. The spread of the line shows the $\pm 1\sigma$ of the simulated distribution. As the dimensionality of the model rises the mean of the sampled points, counter-intuitively, moves away from the origin, where the likelihood is largest.

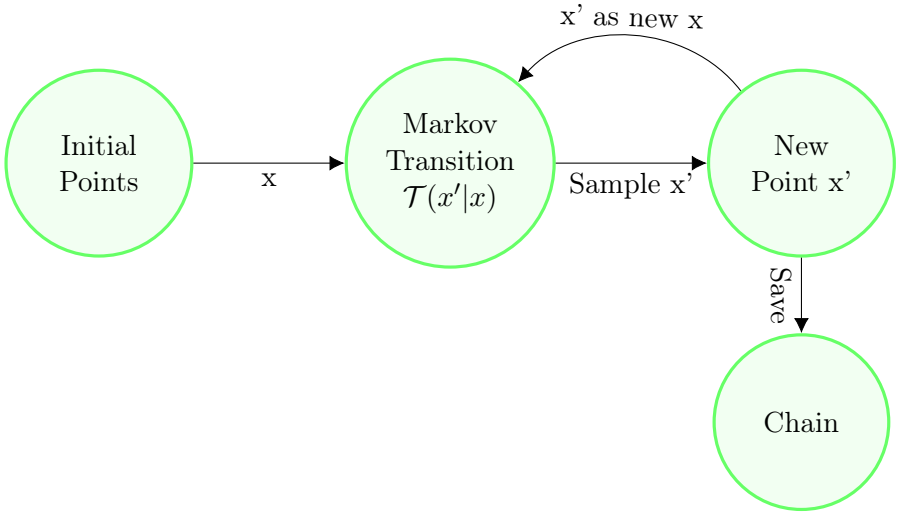

Figure 3.5: Conceptual algorithm to construct a Markov Chain.

a sufficiently long chain can then be used to estimate expectation values for functions of the parameter:

$$\hat{f}_N = \frac{1}{N}\sum_{n=0}^{N} f(x_n), \tag{3.14}$$

where N is the number of samples, and x_n are the individual samples. If we run the MCMC for an infinite time it can be shown that it will converge exactly to the true expectation value (Betancourt 2017):

$$\lim_{N\to\infty} \hat{f}_N = \mathcal{E}_\pi[f]. \tag{3.15}$$

In the ideal case, the Markov chain has three phases:

1. Converge from initial position to typical set
2. Explore the typical set first time
3. Continue to explore the details of the typical set

Typically the first phase is called warm-up and the samples in this phase are not used for the final chain, because they are heavily biased by the initial point of the Markov chain. The second phase improves the estimate of the expectation value drastically, whereas in the third phase the improvements get smaller while the estimator is slowly converging to the true expectation value. The uncertainty of the expectation value estimator with a Markov chain in the third phase can be estimated with a central limit theorem

$$\hat{f}_N \sim \mathcal{N}\left(\mathcal{E}_\pi[f], \sqrt{\frac{Var_\pi[f]}{ESS}}\right), \tag{3.16}$$

with the Effective Sample Size (ESS) (number of uncorrelated samples). This can be calculated from the Markov chains itself (Geyer 1992; Gelman et al. 2014).

This uncertainty estimation is only valid for well behaved problems, with for example not too strong curvature in the typical set. The formal condition that must be satisfied for Eq. 3.16 to be valid is geometric ergodicity (Roberts and Rosenthal 2004), which is for most realistic application impossible to verify. Therefore, empirical diagnostics are used to check whether the idealised Eq. 3.16 is a valid approximation, like the $\hat{R}$ statistic (Gelman et al. 2014). The $\hat{R}$ gives the variation of different Markov Chains, initialised at different position. If its value is not near 1, the geometric ergodicity is most likely not fulfilled and the estimator is meaningless.

The next step is to construct a Markov transition fulfilling Eq. 3.13. The Metropolis-Hastings algorithm is one of the algorithm that can do this (Metropolis et al. 1953; Hastings 1970), which consists of a proposal ($\mathcal{P}(x'|x)$) and a rejection. The concept of this algorithm is shown in Fig. 3.6. In the Metropolis-Hastings algorithm the new point is accepted with a probability of

$$A(x'|x) = \min\left(1, \frac{\mathcal{P}(x'|x)\pi(x')}{\mathcal{P}(x|x')\pi(x)}\right). \tag{3.17}$$

The most common proposal distribution is a normal distribution $\mathcal{P}(x'|x) = \mathcal{N}(x'|x, \Sigma)$, which leads to $A(x'|x) = \min\left(1, \frac{\pi(x')}{\pi(x)}\right)$. This approach naturally has the attributes associated with the typical set: The proposal will sample mostly in the areas with large volume, whereas the acceptance probability avoids walking into areas with small target density. The main problem with this approach is that when the dimensionality of the target distribution increases the fraction of the volume around a given point that is towards the typical set over the total volume around the point decreases. Therefore, the sampling will be very inefficient because either most drawn samples being rejected by Eq. 3.17 or Σ has to be tuned to be very small, but then the chain only moves very slowly and the samples have a strong correlation, reducing the ESS. Either way the Markov chain will explore the typical set very slowly.

HMC uses another approach of a Metropolis-Hastings algorithm. Instead of randomly sampling points in the neighbourhood of the current point in the chain, it uses the information of a vector field aligned with the typical set. This vector field first guides the sampler to converge to the typical set quickly and then to stay in it. To construct a vector field aligned with the typical set, it uses information about the geometry of the typical

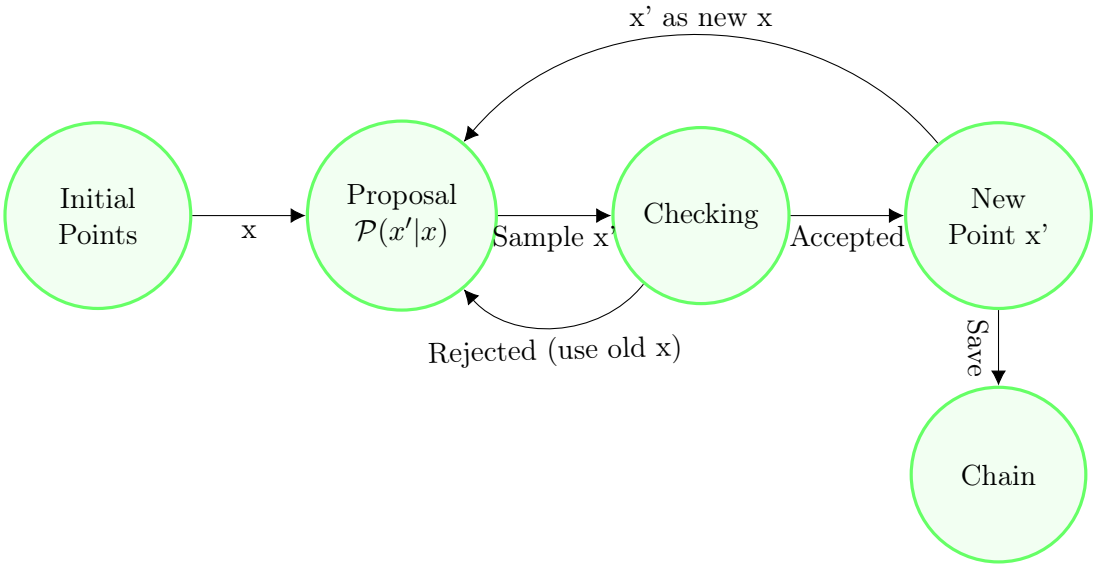

Figure 3.6: Conceptual algorithm to construct a Markov Chain with a Metropolis-Hastings algorithm.

set. The first idea would be to use the gradient of the target distribution, to guide the sampling. But as shown in Fig. 3.4, the typical set in high dimensions is not necessary at the mode of the target distribution, therefore we need something to avoid the sampler to just collapse into the mode but rather stay in the typical set surrounding the maximum of the target distribution. The idea in HMC is to use a simplified analogy to why a satellite can be on a stable orbit in the gradient earth gravity field, if its velocity is exactly correct. This can be achieved by introducing a momentum variable p_n for every position variable x_n:

$$x_n \to (x_n, p_n). \tag{3.18}$$

The conditional probability of x and p is given by

$$\pi(x, p) = \pi(p|x)\pi(x), \tag{3.19}$$

which assures that if the momentum is marginalised out the target distribution is recovered. Constructing the combined probability distribution in the position-momentum space in this way ensures, that the typical set in the position-momentum space projects to the typical set of the target distribution. The system has to have conservative dynamics, which means that the momentum p has to transform opposite to the parameters x under re-parametrisation. Because of this, the probability distributions of q and p also transform oppositely, which means that $\pi(x, p)$ does not depend on the parametrisation and can be expressed it with an invariant Hamilton function H(x, p):

$$\pi(x, p) = e^{-H(x,p)}. \tag{3.20}$$

With this and Eq. 3.19 we can derive Hamilton's equations for this system, which deter-

mines how a 'particle' in this system would evolve in time

$$\begin{aligned} \frac{\mathrm{d}x}{\mathrm{d}t} &= \frac{\partial H}{\partial p} = -\frac{\partial \pi(p|x)}{\partial p} \\ \frac{\mathrm{d}p}{\mathrm{d}t} &= -\frac{\partial H}{\partial x} = \frac{\partial \pi(x|p)}{\partial x} + \frac{\partial \pi(x)}{\partial x}, \end{aligned} \tag{3.21}$$

where $\frac{\partial \pi(x)}{\partial x}$ is the gradient of the log-target density. By construction, this causes the 'particle' to travel in the typical set of $\pi(x, p)$ and therefore also in the typical set of $\pi(x)$. This technique allows efficient sampling of points within the typical set that are far apart from each other (small correlation between different samples). In practice one samples an initial momentum from the distribution $\pi(p|x)$ and integrates Eq. 3.21 over a given time or path length. This gives a new sample, which is the start point for the next integration with a newly sampled momentum. Often a leapfrog integrator is used to integrate Eq. 3.21, if $\pi(p|x)$ is independent of x. Leapfrog integration is a method to numerically approximate the integration of differential systems, for this the total path length of the integration is split into parts with a given step size s and the following algorithm is used:

for step in steps **do**

$p_{step+\frac{1}{2}} \leftarrow p_{step} + \frac{s}{2}\frac{\partial \pi(x)}{\partial x}$

$x_{step+1} \leftarrow p_{step} + s p_{step+\frac{1}{2}}$

$p_{step+1} \leftarrow p_{step+\frac{1}{2}} + \frac{s}{2}\frac{\partial \pi(x)}{\partial x}$

end for.

This algorithm is easy and fast to calculate and has the important property of being exactly reversible, which means that if we integrate for a time t and then go backwards for a time -t, we will always reach exactly the same point we started with. But if the step size is too large this type of integrator can significantly deviate from the true integral. Which in the physical particle analogy would mean that the energy (= H) is not conserved. To avoid this the following Metropolis checking criterion (see general expression in 3.17) is used:

$$\begin{aligned} A(x', p'|x, p) &= \min\left(1, \frac{\pi(x', p')}{\pi(x, p)}\right) \\ &= \min\left(1, e^{H(x,p) - H(x', p')}\right). \end{aligned} \tag{3.22}$$

If the target distribution is well behaved and the step size small enough, the term $H(x, p) - H(x', p')$ is close to zero, and therefore the acceptance rate will be very high. Fig. 3.7 and 3.8 show the path the integrator takes during one integration. In this and all following examples, the momentum probability distribution ($\pi(p|x)$) was set to be a standard normal distribution independent of x.

An important tuning parameter is the step size for the leapfrog steps. If it is too large it will cause the integrator to deviate from the true integration path, which leads to many rejected samples, but if it is too small it will use a lot of unnecessary computational power. Fig. 3.9 shows an example if the step size is chosen well, whereas Fig. 3.10 shows an example with a too large step size, leading to rejected samples.

Also the path length per integration is important, as a too short path length will cause

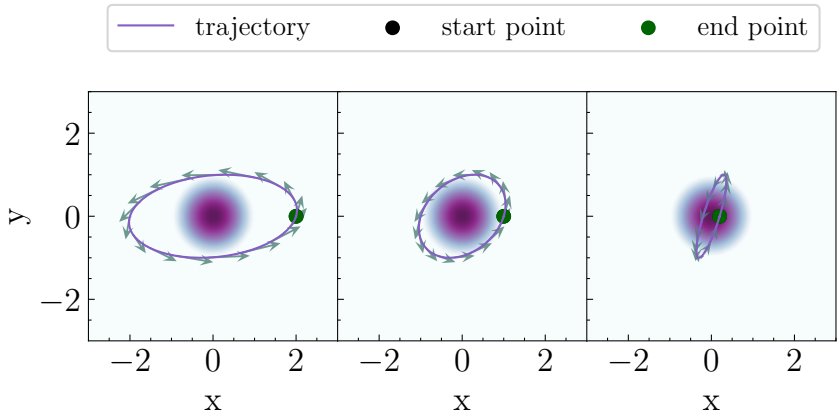

Figure 3.7: Integrator path to sample one new sample point when the target distribution is a two-dimensional standard normal distribution. The three different panels have different starting points of the integration. The path length was set to 2π and the step size to 0.01. In this special case a path length of 2π will always lead to closed circles.

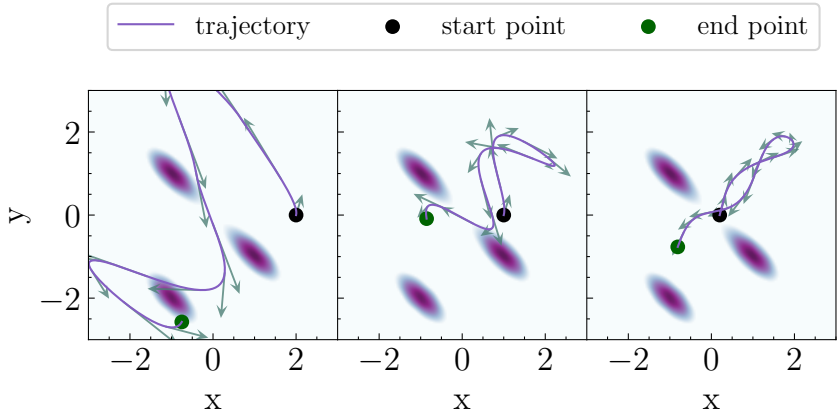

Figure 3.8: Integrator path to sample one new sample point when the target distribution is a superposition of two-dimensional non-standard normal distributions. The three different panels have different starting points of the integration. The path length was set to 2π and the step size to 0.01.

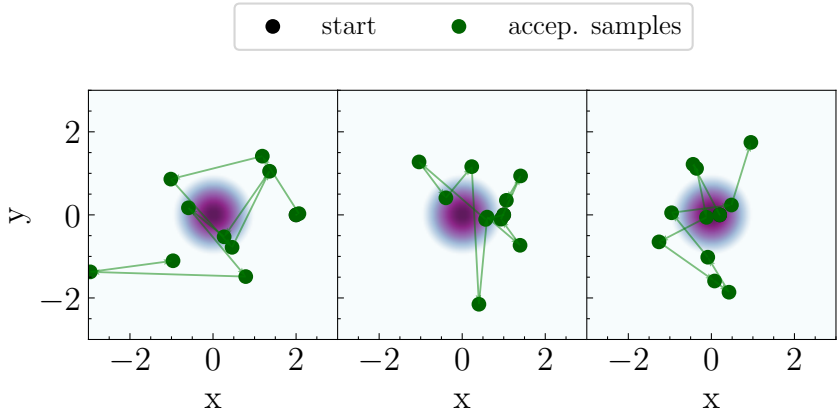

Figure 3.9: This figure shows the first 10 samples constructed with a HMC for three different starting positions. The path length was set to 5 and the step size to 0.1.

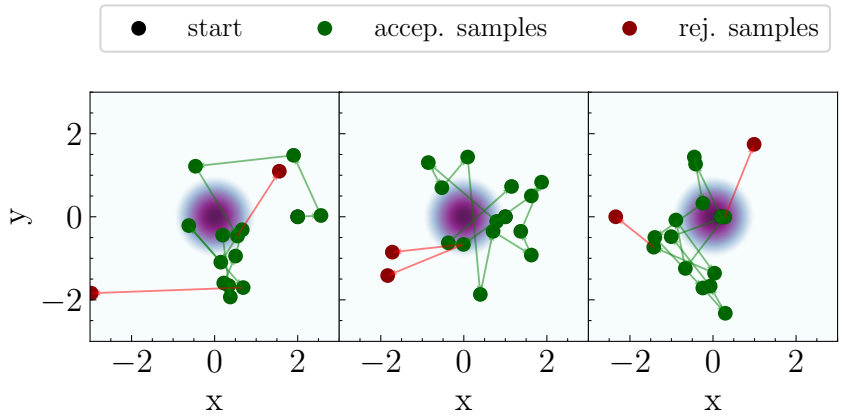

Figure 3.10: This figure shows the first 10 samples constructed with a HMC for three different starting positions. The path length was set to 5 and the step size to 1. This setup leads to some rejected samples, due to the too long step size.

the samples to very slowly explore the typical set, with large correlation of the individual samples, whereas a too long path length will again use unnecessary computational power. Fig 3.11 shows an example of different step size and path lengths for the same problem. Especially showing that a too short path length takes many more samples to explore the typical set.

To analyse the sampler we can have a look at trace plots (see Fig. 3.12). These show that, for this example, even for starting points very far away of the typical set, the sampler converges very quickly towards it.

With the samples from the chain we can construct posterior distributions like shown in Fig. 3.13. It shows that HMC can nicely recover the analytical solution for this easy example if the configuration is good, but it also shows a bias that can be introduced when the integration path length is too short.

In practice the path length and step size have to be adjusted to the problem at hand, to optimise the performance of the HMC. In this thesis the HMC implementation within Stan (Stan 2022) is used. Stan is a framework for statistical modeling. It consists of an auto-differentiable maths library and different fitting/optimisation algorithm. The default sampler is the no-U-turn sampler (Hoffman and Gelman 2014), which is an adaptive variant of HMC, that also includes the tuning of the different setup parameters.

3.1.3 Model checking

Judging if a fit is a good description of the data is a challenging task. Often the used methods like reduced χ^2 incorporate several assumptions that are not fullfilled in any realistic scenario. The reduced χ^2 method is, for example, based on the assumption that all uncertainties involved are normal-distributed. The quality of a fit can be assessed in an general Bayesian framework with Posterior Predictive Checks (PPCs). For PPCs one simulates new data based on the posterior distribution and the data generating process

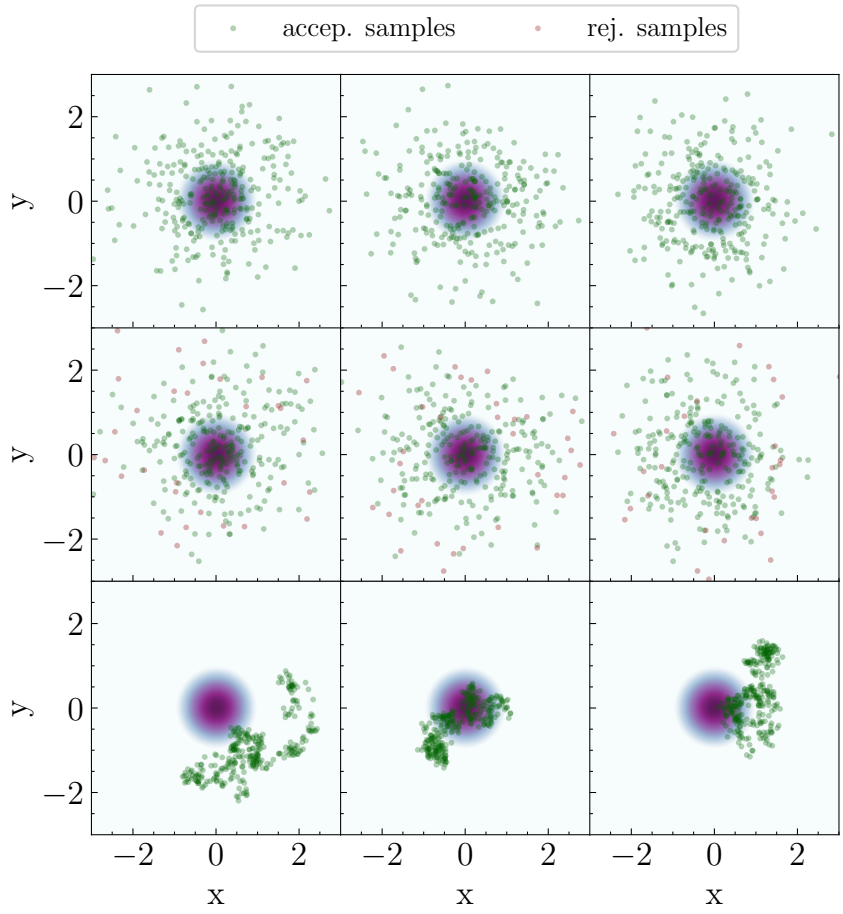

Figure 3.11: This figure shows the first 300 samples constructed with a HMC for three different starting positions and sampler configurations. The top row uses a path length of 5 with a step size of 0.1, leading to a good exploration of the typical set with no rejected samples. The second row uses a path length of 5 with a step size of 1, which leads to some rejected samples. The bottom row uses a path length of 0.1 and a step size of 0.01, leading to a very slow exploration of the typical set which large correlation of the individual samples in the chain.

and compares these to the real data. Mathematically it is defined as

$$\pi(y^{sim}|y^{obs}) = \int \mathrm{d}\theta \pi(y^{sim}|\theta)\pi(\theta|y^{obs}), \tag{3.23}$$

where $\pi(\theta|y^{obs})$ is the posterior distribution of the model parameters given the data and $\pi(y^{sim}|\theta)$ is the probability of simulated data given the model parameters. Eq. 3.23 can be solved numerically by sampling model parameters from the posterior distribution and simulating new data from the model defined by these parameters, constructing the probability distribution for new simulated data given the real data (and the assumed model). In this thesis the PPCs are constructed with this method and 300 samples from the posterior distribution. Usually the PPCs are plotted for a visual check of the fit, by plotting the data and a given credible interval (for example 95%) of the simulated data (see e.g. Fig. 4.12).

An expansion of the PPC plots are Cumulative-Cumulative (QQ) plots, where the same simulated data for the PPC is used, but instead of a comparison of single observational

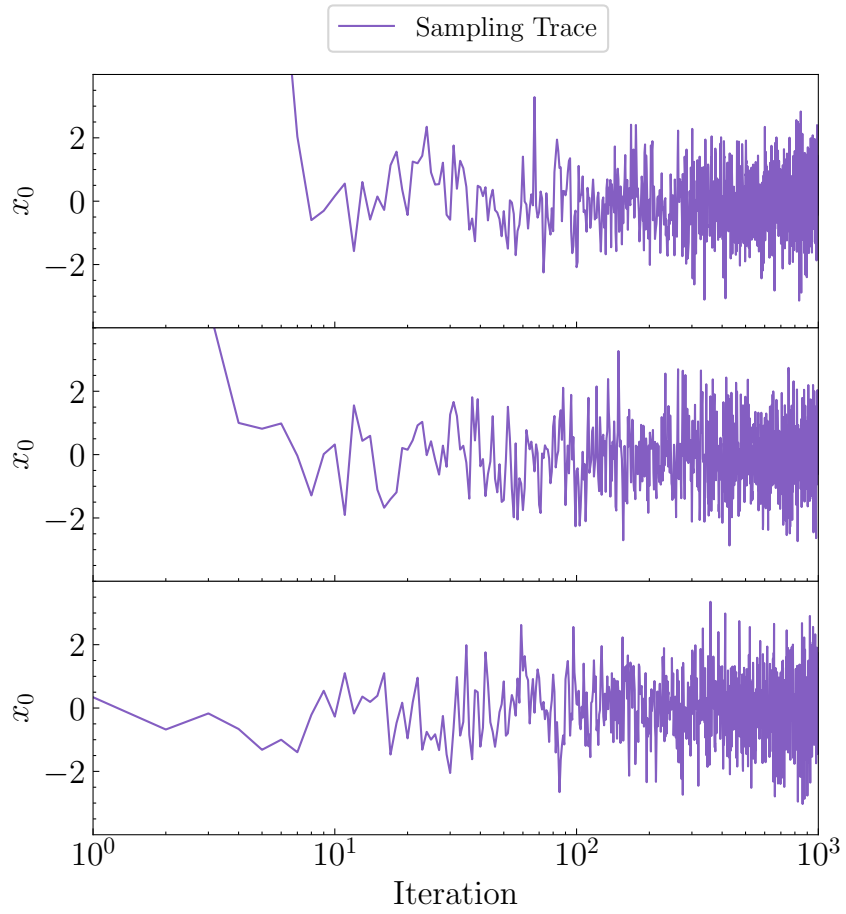

Figure 3.12: Trace plot for a 10 dimensional standard normal distribution as target density and three different starting points. The start of the trace plot shows the warm up phase, where the samples is quickly converging towards the typical set and then explores it in the rest of the sampling. The starting positions are for the top row x_i=50000, for the middle row x_i=500 and for the bottom row x_i=1.

data points to the simulated data points it compares the cumulative observed data to the cumulative simulated data. While PPC plots are strong tools, to identify significant deviations at certain points in the data, QQ plots check for weak long deviations, that show up in the cumulative sum.

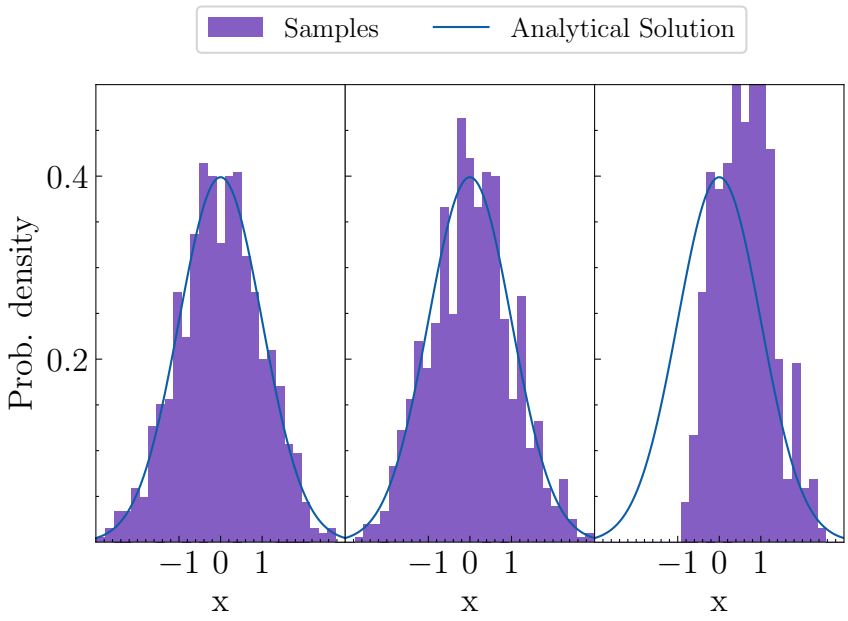

Figure 3.13: Posterior distribution for parameter x. Here the target density is a two dimensional standard normal distribution and the three columns show different sampling setups. The left column is a good setup with a path length of 5 and a step size of 0.1, which can nicely recover the analytical solution. The middle column has a too large step size of 1 that lead to rejected samples, but can still recover the distribution. The right column uses a too short path length of 0.1, which heavily biases the result to the starting position, because the correlation of the samples is very large.

4 Physical Background Model for Fermi/GBM

Parts of Sec. 4.1, 4.2 and 4.3 have been already published with me as main author in Biltzinger et al. (2020). Parts of Sec. 4.4.1 have been already published in Kunzweiler et al. (2022) with me as co-author due to large contributions.

The Gamma-Ray Burst Monitor (GBM) is one of the instruments onboard of the Fermi satellite, which was launched in 2008 (Meegan et al. 2009). GBM is a wide Field Of View (FOV) instrument, observing most of the sky, that is not occluded by the Earth. It consists of 12 Sodium Iodide (NaI) detectors and two Bismuth Germanate (BGO) detectors pointing into different directions (see Fig. 4.1) and covering a total energy range from 8 keV to 40 MeV (Meegan et al. 2009). The pointing of the satellite is designed to cover the northern and the southern sky with the Large Area Telescope (LAT), which is the second instrument on board (Atwood et al. 2009). Due to the too small FOV of the LAT, the satellite is reorienting after every orbit to achieve this desired coverage of both parts of sky. The z-axis of the satellite is therefore pointing with a constant angle (50 degrees for most of the mission) to the north in one orbit and to the south in the next one (Atwood et al. 2009). Additionally there are Autonomous Re-point Requests (ARRs), if GBM detects and localises a Gamma-Ray Burst (GRB) well, to point the LAT quickly towards the GRB. This pointing strategy and the low Earth orbit of Fermi ($\approx$ 550 km) (Abdo et al. 2009b), which leads to an orbital period of $\approx$ 95 minutes, determine the background seen by the individual GBM detectors. This background varies typically on the time scale of minutes and is a superposition of several different background components. This complexity of the background prevented the development of a physical background model for GBM.

Therefore, empirical models have been developed in the past, in particular: (1) Szécsi et al. (2013) fit the background around trigger times of GBM with separate polynomials (up to third order) to different quantities like the angle between the detector and the Earth, forming a geometrical background model. But this approach gives the fit a lot of freedom as it has many free unbound parameters, introduces ambiguity between the different polynomials and does not use physical information of the sources that create the background. It is only suited for GRBs, where excess emission is readily seen by eye. Another work that used the background seen by GBM was done by (2) Ng et al. (2015). In this work they searched for decay lines of sterile neutrinos in the background spectrum of GBM. They used data cuts to get rid of most of the background contamination from e.g.

cosmic rays and the Earth Albedo, but did not try to model all the background sources. (3) Fitzpatrick et al. (2012) used the fact that the detectors of GBM, in most cases, are at the same geographical coordinates and point to the same position in the sky every 30th orbit. This is because after every 15 orbits roughly one day has passed (every integer number of days would work) and therefore the satellite position in geographical coordinates are approximately the same than 15 orbits earlier. Due to the pointing strategy the pointing direction will be not the same after 15 orbits (odd number of orbits), but after 30 orbits. Thus, they assume that the background at time T should be the same as at time T $\pm$ 30 orbits. This is a purely empirical method that for example breaks down, like stated in Fitzpatrick et al. (2012), when there is an ARR or when due to varying solar activity the particle flux changes or the Earth's magnetic field is compressed, which will also be shown in Sec. 4.3.5.

Due to the previous lack of a real background model, the standard approach is to estimate the background for a short time period around GRB triggers with polynomial fits to the data before and after the GRB and assume that the polynomial is also valid in between (Koshut et al. 1996). But this fails when the GRB duration is longer than the background variation (Levan et al. 2014).

I developed a new background model that uses physical forward modeling for all photon background sources plus empirical models for charged particle sources. In the following I first summarise the data formats and response of GBM in Sec. 4.1, the background components that contribute to the total background in Sec. 4.2.1, show that the background model works with some general fits to real data in Sec. 4.3 and show two applications of the model in Sec. 4.4.

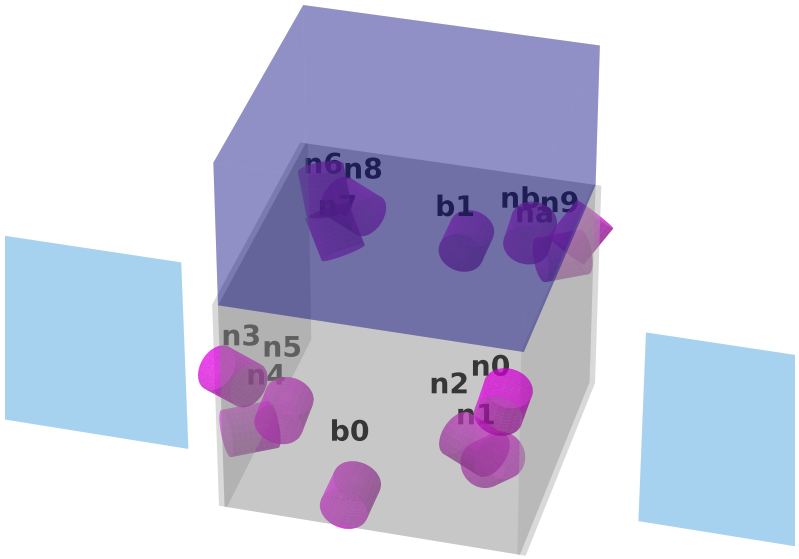

Figure 4.1: Schematic picture of the setup of GBM on board the Fermi satellite. The mounting points and pointing directions for all 14 detectors that are part of GBM are shown. Additionally, the satellite base is indicated in grey, the LAT in dark blue, and the solar panels in light blue. Taken from Biltzinger et al. (2020).

4.1 GBM and its Background

The GBM detectors are scintillation detectors, that respond to the interaction of a high energy photon with the creation of scintillation light. These low energy photons will hit the photo cathode of a Photo Multiplier Tube (PMT), causing the release of a number of photo electrons that gets amplified by the different stages in the PMT. This causes the electronic signal to be strong enough to be measured. The detected photon events are then converted into 128 Pulse Height Analysis (PHA) channels according to the 'height' of the electronic signal at the end of the PMT and are stored as single time tagged events with the corresponding PHA channel number in the Time-Tagged Events (TTE) data files. The height of the electronic signal is proportional to the deposited energy in the crystal, as a higher energy deposition leads to the creation of more scintillation photons and therefore to more released photo electrons at the photo cathode. The recorded data is also binned in 8 second time bins with full spectral resolution of 128 PHA channels in the CSPEC data files and with 256 ms time bins with a reduced spectral resolution of only 8 PHA channels in the CTIME data files. The continuous TTE data is only available since 2010 (Meegan et al. 2009).

The background seen by the individual detectors of GBM is a superposition of several different background sources, whose contributions to the total background are strongly dependent on the energy considered, and the orientation of the detectors with respect to the position of the background sources (more details about the different background sources will be given in Sec. 4.2). Since the off-axis sensitivity of the GBM scintillator crystal is energy-dependent (see Fig. 4.2), the same photon spectrum will result in different count spectra depending on the orientation of the detector with respect to the source position. The dependence on the orientation leads to different background variations for different detectors in the same reconstructed energy range, while the dependence on the energy leads to different background variations for the same detector but different reconstructed energy ranges. The background model needs to be capable to explain these different backgrounds for different detector orientations and PHA channels.

4.1.1 Response

For spectral instruments with large energy dispersion like GBM, modeling the response is crucial for any physical interpretation of the data. The response gives the effective area seen by a photon with a given energy E_{ph} to be detected in one of the detector's PHA channels E_{det}, and therefore connects the physical spectrum of the source with the count rates in the PHA channels. The effects that are incorporated in the response include on the single detector level the geometry of the scintillation crystal, partial energy deposition of the photons in the crystal and absorption of photons by the detector housing and photo-multiplier tubes attached to the crystal. Additionally, on the satellite level, shielding by other components of the satellite and other detectors is taken into account (Kippen et al. 2007).

Each PHA channel has an associated reconstructed energy range, but due to energy

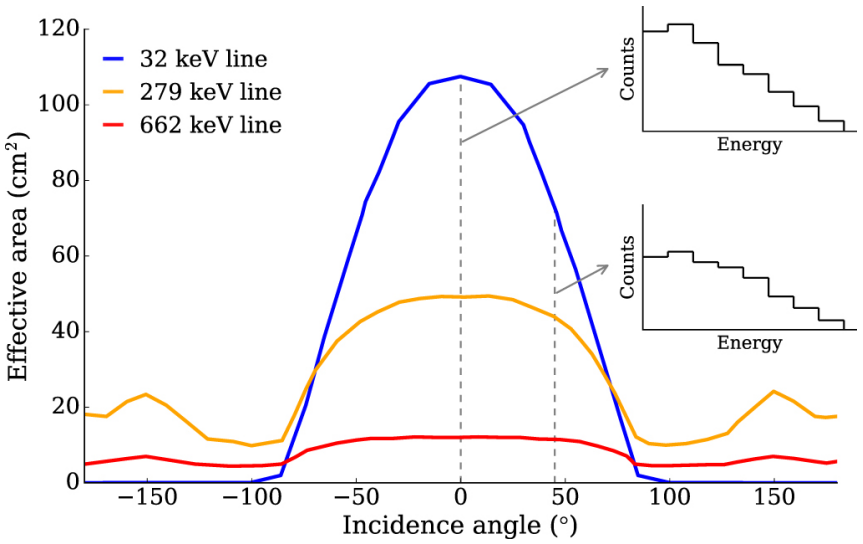

Figure 4.2: Off-axis effective area for different photon energies, leading to different detected count spectra for the same photon spectrum at different incident angles (two small plots). Taken from Berlato, Greiner, and Burgess (2019).

dispersion this does not imply that all photons detected in this PHA channel have a physical energy within the reconstructed energy range associated to this PHA channel (see Sec. 2.2).

The connection of the physical spectrum F [photons cm^{-2} s^{-1}] and the detected count rate spectrum D [counts s^{-1}] (counts in the different PHA channels) via the response $\mathcal{R}$ is given in Eq. 4.1.

$$D(E_{det}) = \int \mathrm{d}E_{ph} \mathcal{R}(E_{ph}, E_{det}, \phi_{source}, \theta_{source}) \cdot F(E_{ph}) \tag{4.1}$$

The quantities ϕ_{source} and θ_{source} define the position of the source in the satellite frame. For GBM θ_{source} is usually defined as the zenith angle and ϕ_{source} the azimuth angle measured from the pointing direction of the b0 detector, with the pointing of the LAT being at $\theta = 90°$.

To determine the Detector Response Matrix (DRM), an on-ground calibration of GBM was performed (Bissaldi et al. 2009). The response can be generated with the Python package gbm_drm_gen[1]. This package interpolates the simulated response for user defined energy bins of the incoming photons, detector PHA channels and positions of the source (Burgess et al. 2017; Berlato, Greiner, and Burgess 2019).

Eq. 4.1 can be used to calculate the expected count rates created by a point sources with a given spectrum and position in the sky as a function of time in the different detectors by:

1. Calculate the position of the point source in the satellite frame for several times with an appropriate time resolution (computation time vs. accuracy of interpolation in step 4).
2. Use the gbm_drm_gen package to get the DRMs for the different positions for each detector

[1] https://github.com/mpe-heg/gbm_drm_gen/

3. Convolve the assumed spectrum with the DRMs to get the expected count rates in the different PHA channels per detector
4. Interpolate between the times for which the point source position was calculated.

For extended sources the procedure has to be adapted, as they cover a range of positions. This can be expressed with (F now has units [photons cm^{-2} s^{-1} sr^{-1}])

$$D(E_{det}) = \int\int \mathrm{d}E_{ph}\mathrm{d}\Omega\mathcal{R}(E_{ph}, E_{det}, \phi_{\mathrm{source}}, \theta_{\mathrm{source}}) \cdot F(E_{ph}) \cdot f(\phi, \theta), \tag{4.2}$$

where $f(\phi, \theta)$ is defined as the occlusion function. For an extended source with a constant flux over its visible surface, that covers a certain region on the sky, this can be written as

$$f(\phi, \theta) = \begin{cases} 1, & \text{if point is covered by source} \\ 0, & \text{else.} \end{cases} \tag{4.3}$$

In general this can also be used to calculate the expected count rates from more complex extended source with a non-constant flux over its surface. The surface integral in Eq. 4.2 can not be solved analytically, because there exists no analytical form of the response $\mathcal{R}$. But we can approximate Eq. 4.2 as a function of time with the following procedure:

1. Build a grid with N_{grid} equally distributed points on a unit sphere around the detector in the satellite frame.
2. For each of these points, calculate the DRM with the `gbm_drm_gen` package.
3. Calculate the region covered by the source in the satellite frame for several times with appropriate time resolution (balancing computation time with accuracy of the interpolation in step 6)
4. Weight the responses of the grid points according to the occlusion function and multiply the result by the solid angle that every point covers ($\frac{4\pi}{N_{\mathrm{grid}}} sr$) to get an effective response.
5. Convolve the assumed spectrum through the effective response to get the expected count rates in the different PHA channels.
6. Interpolate between the times for which the count rate was calculated.

4.2 Background Components

In the following I will describe the different background components split into two groups: Photon background components and charged particle background components. The photon background components can be physically modeled and folded with the response to get the expected count rates, whereas the charged particle background sources, due to the lack of a charged particle response, can only be treated empirically.

4.2.1 Photon Background Components

Point Source

We know of the existence of many sources, with small spatial extension, in the gamma-ray sky. Bright examples for these sources are the Crab nebula, that consists of a supernova remnant with a pulsar (Pacini 1968) and Scorpius X-1, that is a binary star system with a neutron star that accumulates matter from its companion star (Crampton et al. 1976). Due to the spatially slowly varying response these source can be approximated as perfect point sources to GBM. For most these point sources the influence is more significant in the lower energy channels up to 100 keV as they are thermal, with a spectrum rapidly falling with increasing energy. The noteworthy exception is the Crab nebula that emits synchrotron radiation reaching very high energies (Hester 2008). Fig. 4.3 shows the expected count rate as a function of time for one detector and day for the Crab spectrum as given in Madsen et al. (2017):

$$\frac{\mathrm{d}N}{\mathrm{d}E} = 9.7 \cdot E^{-2.1} [\text{photons cm}^{-2}\ \text{s}^{-1}]. \tag{4.4}$$

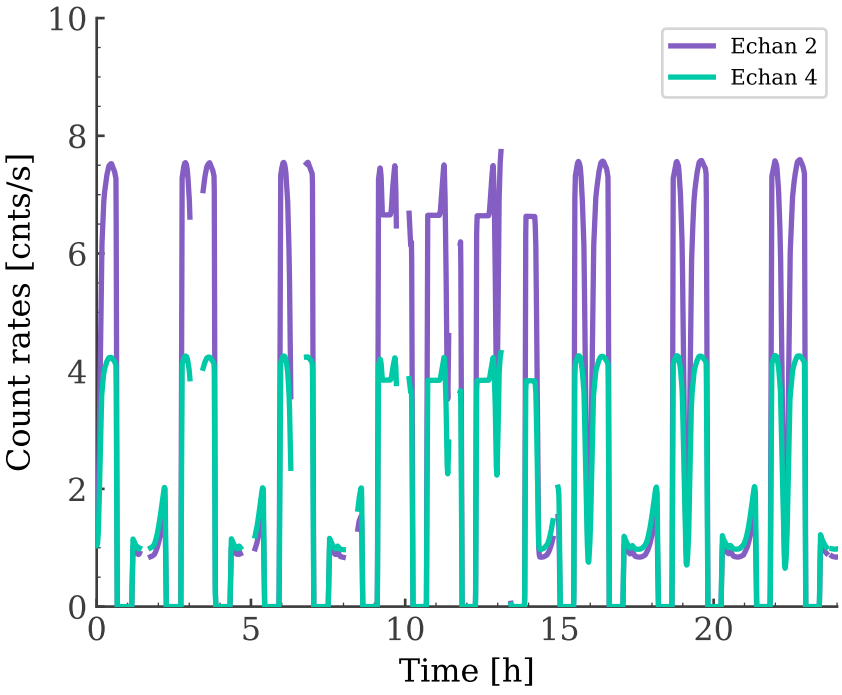

Figure 4.3: Expected temporal variation of the count rate in one detector (n7) by the Crab, for an assumed spectrum like given in Madsen et al. (2017), at the 15th January 2015 for detector n7 and the two CTIME energy channels 2 (reconstructed energy range ≈ 25-50 keV) and 4 (reconstructed energy range ≈ 100-300 keV). The variations are caused by the orbital variations in the orientation of the spacecraft, the asymmetry in the peaks is due to the rocking motion of the satellite and the gaps in the curves are due to the shutoff of the detectors during the South Atlanic Anomaly (SAA) transits.

Sun

The Sun can be treated as a special point-like source, which also emits X-rays in the low keV range. The spectrum was investigated in Hannah et al. (2007), where 2σ upper limits are given for the photon flux of the quiet Sun from 3 keV to 200 keV. Even if these upper limits would be the actual spectrum of the Sun, the influence of the Sun would be very small and only slightly visible in the lowest detector channels of GBM.

An exception are the eruptions of the Sun, when it violently releases a large amount of particles and photons with higher energies. While the particles of these so-called solar flares are deflected by the geomagnetic field, the photons reach GBM and are clearly visible in the data (Ackermann et al. 2012). Information about the flares can be obtained from the yearly flare files which are produced by the National Center for Environmental Information. As we are not interested in this component and it would be a challenging source to include in the background model, times with a solar flare are excluded from the fits.

Therefore, the Sun is not included in any of the following fits.

Cosmic Gamma-ray Background

The Cosmic Gamma-ray Background (CGB) is the extension of the well studied Cosmic X-ray Background (CXB) to higher energies (Ajello et al. 2008). It is an isotropic radiation of gamma-rays, that is the dominant background component in the lower energy channels of GBM. Due to its isotropic spectral distribution, and no correlation with the galactic plane, we know that it must be either produced in our close surrounding ($\ll$ galaxy scale) or on an extra-galactic scale. The most prominent explanation in the literature for the CGB up to several hundred keV is that this radiation is produced by a large population of Active Galactic Nucleis (AGNs), which are not spatially resolved (Hasinger 2004). This claim is mostly backed by the isotropic distribution of AGN and the association of nearly all the CXB flux at 2 keV to known AGNs hosting accreting super-massive black holes (Giacconi et al. 2002; Alexander et al. 2003; Hasinger 2004). However, at energies above 6 keV only about 50% of the CXB flux can be resolved into known AGNs (Worsley et al. 2005). A possible explanation for the unresolved CXB (CGB) flux is a populations of yet undetected highly obscured AGNs with hydrogen column densities of the order $10^{24} cm^{-2}$ (Compton thick) and a space density peak at redshift ≈ 1 (Worsley et al. 2005). Other works included the possibilities of several different populations of AGNs with different hydrogen column densities (Treister, Urry, and Virani 2009; Ananna et al. 2020). One example for this kind of population analysis is given in Fig. 4.4.

The emission from individual AGNs is caused by two main emission mechanisms: (1) The accretion disk surrounding the black hole emitting in the optical and UV bands and (2) a hot corona above the accretion disk emitting in the X-rays and gamma-rays. The Corona is believed to be a cloud of hot plasma close to the accretion disk and thus, the optical and UV photons from the accretion disk can Compton scatter at the hot electrons in this region, increasing the energy of the photons. The radiation of the Corona is typically modeled by a power law with index $\Gamma \approx 1.4 - 2.1$ and an exponential cutoff at high energies

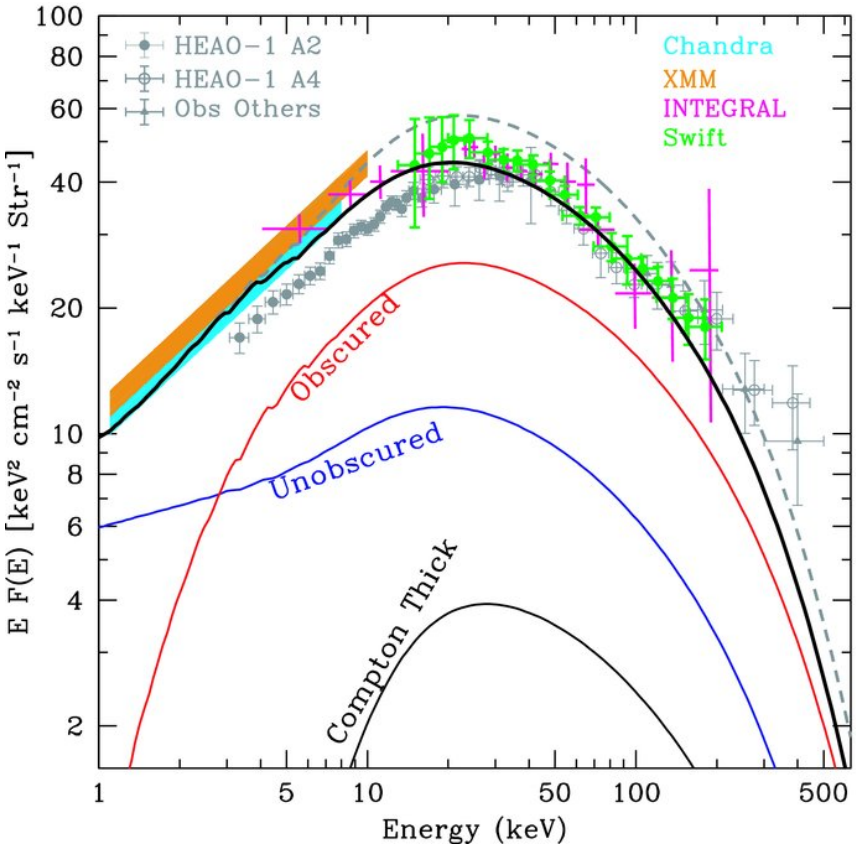

Figure 4.4: Contribution from the different AGN obscuration classes to the total CGB, together with different measurements (Gruber et al. 1999; Hickox and Markevitch 2006; Luca and Molendi 2004; Churazov et al. 2007; Ajello et al. 2008). The fraction of the individual classes determine the curvature of the CGB spectrum. Figure taken from Treister, Urry, and Virani (2009).

(Nandra and Pounds 1994; Ueda et al. 2014; Ricci et al. 2017; Ananna et al. 2020).

$$F(E) = CE^{-\Gamma} exp\left(-\frac{E}{E_{\text{cutoff}}}\right). \tag{4.5}$$

This initial spectrum can get reprocessed by different processes, like the reflection of the accretion disk (Magdziarz and Zdziarski 1995), galactic absorption (Wilms, Allen, and McCray 2000) and absorption by the gas and dust torus surrounding the AGN (Ricci et al. 2017).

In the GBM energy range, a population of these non-detected highly obscured AGNs could create the observed CGB. Due to different redshifts of the AGNs, fine features wash out in the summed spectrum, leaving a smooth effective spectrum. This spectrum is typically modeled by a smoothly broken power law.

Ajello et al. (2008) fitted the CGB spectrum with the Burst Alert Telescope (BAT) data when the Earth was moving through the FOV, and therefore partially blocking the CGB and combined their results with previous measurements (Kinzer et al. 1997; Watanabe et al. 1997; Gruber et al. 1999; Cappelluti et al. 2017) to derive the best fitting spectral shape in the energy range 2 keV - 2 MeV to be

$$\frac{\mathrm{d}N}{\mathrm{d}E} = \frac{0.101}{\left(\frac{E}{30.0keV}\right)^{1.32} + \left(\frac{E}{30.0keV}\right)^{2.88}} [\text{photons cm}^{-2}\ \text{s}^{-1}\ \text{sr}^{-1}]. \tag{4.6}$$

This spectrum leads, together with the temporally changing effective response of the extended source CGB, to the temporal variation in the induced count rates like shown in Fig. 4.5 for one detector and two CTIME energy channels. Note, that the contribution by the CGB to the GBM background is much larger than by the Crab, which is the brightest steady point source in the gamma-ray sky.

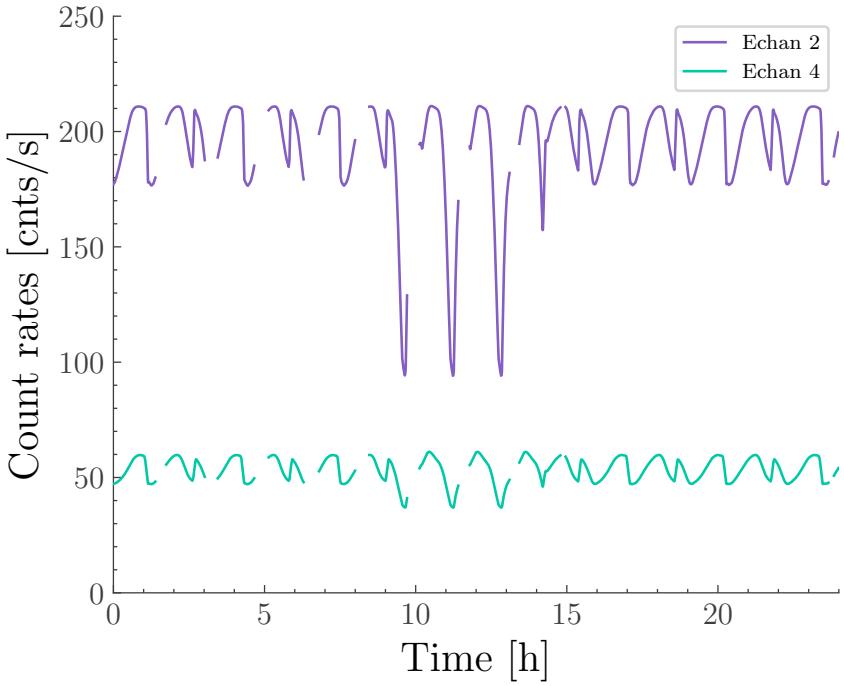

Figure 4.5: Expected temporal variation by the CGB, for an assumed spectrum like given in Ajello et al. (2008), at the 15th January 2015 for detector n7 and the two CTIME energy channels 2 and 4. The strong change in the predicted count rates around hour 10 is due to an ARR, caused by a GRB trigger. The variations are caused by the orbital variations in the orientation of the spacecraft, the asymmetry in the peaks is due to the rocking motion of the satellite and the gaps in the curves are due to the shutoff of the detectors during the SAA transits.

Earth Albedo

The Earth is known to be a source of gamma-rays in the GBM energy range (Thompson, Simpson, and Özel 1981; Ajello et al. 2008). These gamma-rays are produced by cosmic rays colliding with molecules in the Earth's atmosphere leading to π_0-decays and bremsstrahlung (Petry 2005; Abdo et al. 2009a). The spectrum of the produced gamma-rays that are emitted back into space is called 'Earth Albedo' and is shown in Fig. 4.6 in comparison to the CGB spectrum, with the spectral shapes determined in Ajello et al. (2008). For small energies (< 100 keV) the CGB flux per steradian is higher but for larger energy the Earth Albedo is brighter.

It is assumed in the background model, that the Earth Albedo is isotropic over the

whole surface of the Earth, even though the secondary particles produced in the collision of a cosmic ray with an atmospheric molecule tend to fly in the same direction as the primary cosmic ray because of momentum conservation. As cosmic rays mostly consist of protons, they get deflected eastwards upon impinging Earth's magnetic field, therefore the cosmic ray flux from the west as seen by the satellite is larger. It has been shown by Petry (2005) that the East-West asymmetry in the Earth Albedo peaks at a photon energy in the GeV range but is small at lower energies in the MeV range. Abdo et al. (2009a) showed that the effect is also very small for very high energies ($\approx$ TeV) and nearly the whole photon flux with these energies originates from a small ring around the Earth (as seen by the satellite). This 'ring effect' weakens towards lower gamma-ray energies. It is therefore justified to assume that the East-West and the ring effect, that are well observed at higher energies, are not significant in the keV to low MeV energy region and to assume that the Earth Albedo at these energies is isotropic over the whole Earth surface seen by the satellite.

The variation of the background from the Earth Albedo in the individual detectors (see Fig. 4.7) is caused by the different positions of the Earth in the satellite coordinate system for different times and the therefore changing effective response (see Sec. 4.1.1). In Ajello et al. (2008) the spectrum of the Earth Albedo spectrum is modeled successfully with a smoothly connected double power law, to fit the data obtained with BAT when the Earth was passing through its FOV:

$$\frac{\mathrm{d}N}{\mathrm{d}E} = \frac{0.0148}{\left(\frac{E}{33.7keV}\right)^{-5} + \left(\frac{E}{33.7keV}\right)^{1.72}} [\text{photons cm}^{-2}\ \text{s}^{-1}\ \text{sr}^{-1}]. \tag{4.7}$$

Coincidentally, the break in the CGB and Earth Albedo spectrum are nearly at the same energy.

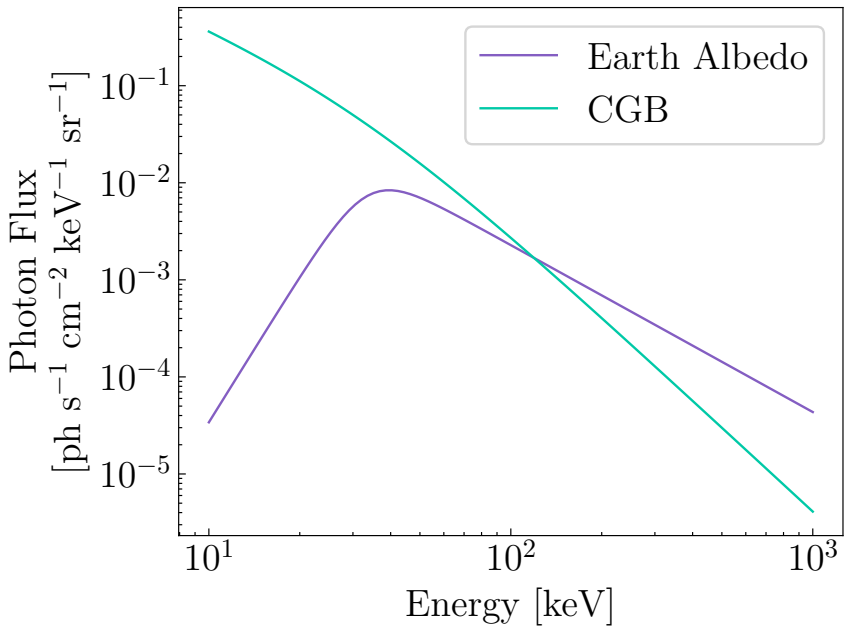

Figure 4.6: Earth and CGB spectrum for values given in Ajello et al. (2008).

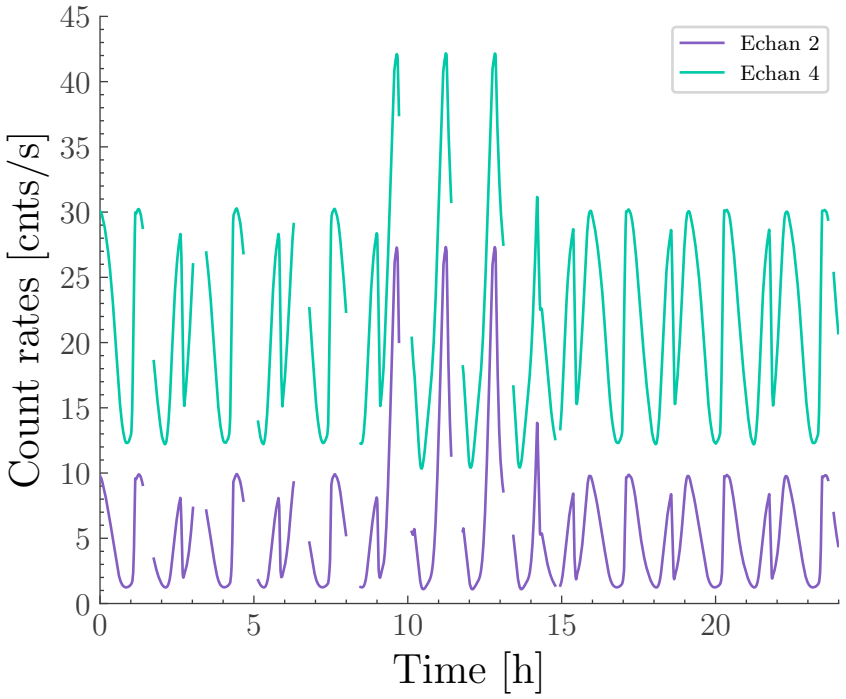

Figure 4.7: Expected temporal variation by the Earth Albedo, for an assumed spectrum like given in Ajello et al. (2008), at the 15th January 2015 for detector n7 and the two CTIME energy channels 2 and 4. The variations are caused by the orbital variations in the orientation of the spacecraft, the asymmetry in the peaks is due to the rocking motion of the satellite and the gaps in the curves are due to the shutoff of the detectors during the SAA transits.

Galactic Centre

The Galactic Centre consists of many spatially resolved and unresolved sources that summed together produce a significant flux in the gamma-ray range (Stefanini 2021). As GBM is not able to spatially resolve any of these sources this contribution can be modeled as a extended source with varying surface brightness.

The spectrum of the Galactic Centre in the keV to MeV range was previously studied with the Spectrometer on INTEGRAL (SPI) detector. Bouchet et al. (2008) found that the spectrum is a superposition of resolved point sources, diffuse emission from unresolved sources, diffuse continuum and annihilation radiation (see Fig. 4.8).

Resolved point sources

In the energy range 25-100 keV the flux of known resolved point sources dominates the Galactic Centre flux. But for GBM all these sources will be unresolved, leading to an effective spectrum by summing the spectra of the individual sources. With the data from Bouchet et al. (2011) this results in

$$F_{\text{resolved}}(E) = 4 \cdot 10^{-4} \left(\frac{E}{100 \text{ keV}} \right)^{-2.9} \tag{4.8}$$

Unresolved point sources

In the energy range below 50 keV there is an additional subdominant contribution that can be modeled with an exponential cutoff

$$F_{unresolved}(E) = 0.1 \cdot exp\left(-\frac{E}{8\ \mathrm{keV}}\right). \tag{4.9}$$

Its origin is still unclear, but one possible origin are accreting white dwarfs (Krivonos et al. 2007).

Diffuse Emission

There exists also a true diffuse emission, where the main contribution is due to inverse Compton scattering of the interstellar light (Bouchet et al. 2008). This component can be modeled as a power law with a flat index of -1.45, which causes it to dominate at energies $> 300keV$.

$$F_{\mathrm{diffuse}}(E) = 1.1 \cdot 10^{-4}\left(\frac{E}{100\mathrm{keV}}\right)^{-1.45} \tag{4.10}$$

Annihilation radiation

Additionally, it is known that there is a population of positrons in the Galactic Centre (Siegert et al. 2016). These positrons annihilate with electrons producing a characteristic line at 511 keV and a continuum below that energy. The continuum arises when the spin of the positron and electron are parallel, prohibiting a single decay into two photons. In this case, the positronium has to decay into an uneven number of photons (but at least three), forming a continuum energy spectrum of the emitted photons. As the contribution of the positron component is subdominant (Bouchet et al. 2008), it is dropped in the analysis in this thesis.

The spatial distribution of the Galactic Centre is modeled with a two dimensional Lorentzian, as motivated in (Türler et al. 2010):

$$L(l,b) = N\frac{\sigma_l^2}{(l-l_0)^2+\sigma_l^2}\frac{\sigma_b^2}{(b-b_0)^2+\sigma_b^2}, \tag{4.11}$$

with l and b being the longitude and latitude in galactic coordinates and N a normalisation constant that assures that $\int\int \mathrm{d}\Omega L(l,b) = 1$. The parameters $l_0 = 0°$, $b_0 = -0.15°$, $\sigma_l = 10.5°$ and $\sigma_b = 0.6°$ are taken from (Türler et al. 2010). In the future, these parameters could also be fitted with the GBM data.

The spatial form from Eq. 4.11 defines the occlusion function (see 4.1.1) and the spectral components listed above are summed for the total spectral model. During the fit a total normalisation factor is fitted to the energy spectrum. Therefore, this assumes that the spectral shape is correct and that all the components follow the same spatial distribution given by Eq. 4.11. Fig. 4.9 shows the expected temporal variation of the count rates produced by the Galactic Centre.

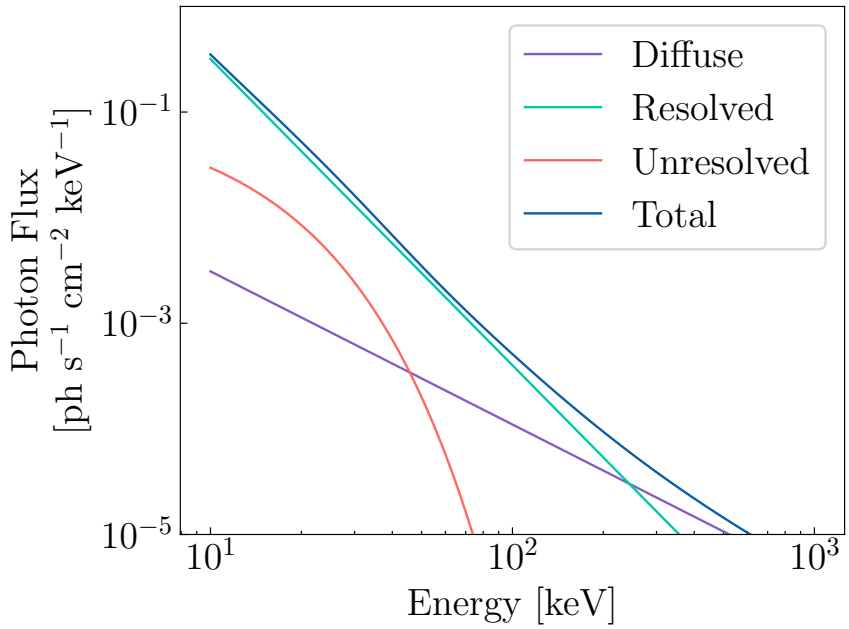

Figure 4.8: Spectrum of the Galactic Centre with the components described in Sec. 4.2.1.

4.2.2 Charged Particle Background Components

South Atlantic Anomaly

There are two volumes in the Earth's magnetic field which have the right properties to permanently trap large densities of charged particles (mostly protons and electrons) in radiation belts. These two regions are called inner and outer Van-Allen Belts and both lie, outside of the South Atlanic Anomaly (SAA), well above Fermi's orbit, which has an altitude of about 550 km, with the inner Van Allen belt being located between 1000 and 6000km (Allen and Frank 1959; Silva and Rocco 2017; Ganushkina et al. 2011).

The SAA is a region located over the South Atlantic, where the Earth's magnetic field is significantly weaker (Schaefer et al. 2016). This originates from an offset of the centre of the dipole, which approximates Earth's magnetic field, from the centre of the Earth and causes the inner Van Allen belt to bend towards the Earth at the position of the SAA (Mozzoni, Mandea, and Cain 2007) and reaching an altitude as low as 100 km that therefore intersects Fermi's orbit at 550 km (Pesce-Rollins 2009). In order to protect the detectors from damage caused by the high flux of charged particles, the detectors are routinely shut down when the satellite crosses the SAA. Nevertheless, the satellite and detector material undergo nuclear excitation by collision with the charged particles and subsequently photons are produced by the de-excitation of the activated material which are measured when the detectors are turned on again. As the high count rates after the SAA originate from nuclear de-excitation, its influence should decay exponentially over time and should have the functional form

$$R_{\mathrm{SAA}}(t) = R_{\mathrm{SAA}}(t_0) exp(-(t - t_0)\tau_{\mathrm{decay}}) \tag{4.12}$$

Because of the different elements in the satellite's and the detector's material, there should

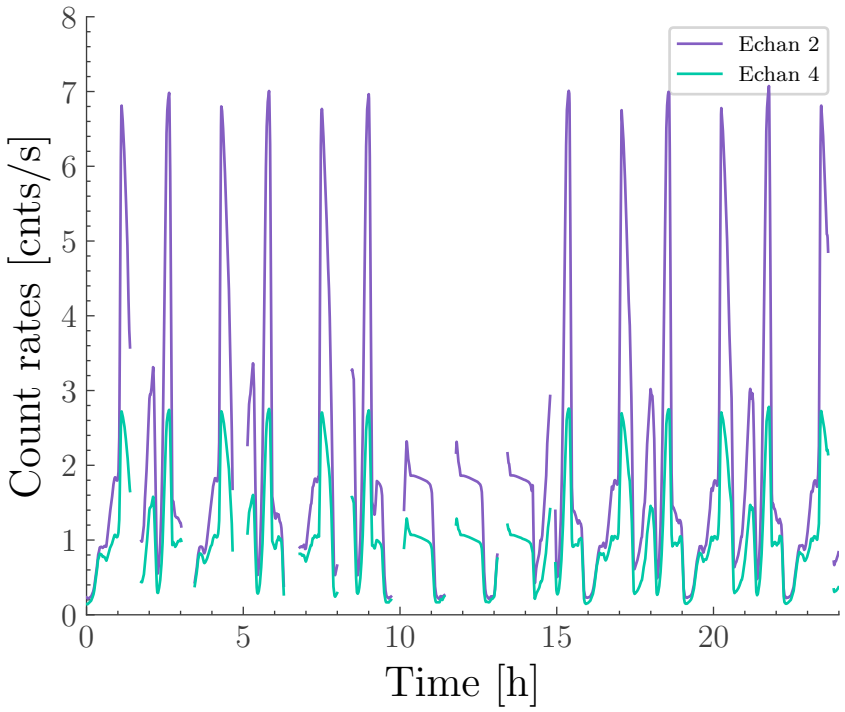

Figure 4.9: Expected temporal variation by the Galactic Centre, for an assumed spectrum like given in Bouchet et al. (2008), at the 15th January 2015 for detector n7 and the two CTIME energy channels 2 and 4. The variations are caused by the orbital variations in the orientation of the spacecraft, the asymmetry in the peaks is due to the rocking motion of the satellite and the gaps in the curves are due to the shutoff of the detectors during the SAA transits.

be a superposition of several exponential decays after each SAA exit. In order to keep the computational effort manageable, two decay functions after each exit are included to allow for a fast and a slow decay. The fast decaying part usually decays in $\approx$ minutes, and is thus gone before the next SAA passage. But the slowly decaying part can take several hours to decay completely, which causes accumulation of background signal by consecutive SAA passages. This activation decays slowly during the long time of the day with no SAA passage.

Fig. 4.10 shows the expected variation by the SAA transits. The presented procedure for the SAA influence depends on the boundaries, which are used by the Fermi team, being correct. If the boundaries of the SAA are wrong it can happen, that the detectors are for example turned off a bit too late, which leads to a rise in the count rates before the official SAA entrance. As the SAA shape and dimension changes due to solar activity, and is also slowly moving over the years, the Fermi team is adapting the SAA boundaries as needed, so that such outliers should be very small in number. To be on the safe side one could always ignore some time (few hundreds of seconds) before and after the nominal SAA transition.

Cosmic Rays

Cosmic rays that hit the satellite can either leave a direct signal in the detectors, that is converted into a certain PHA channel, or excite atoms in the satellite material that upon

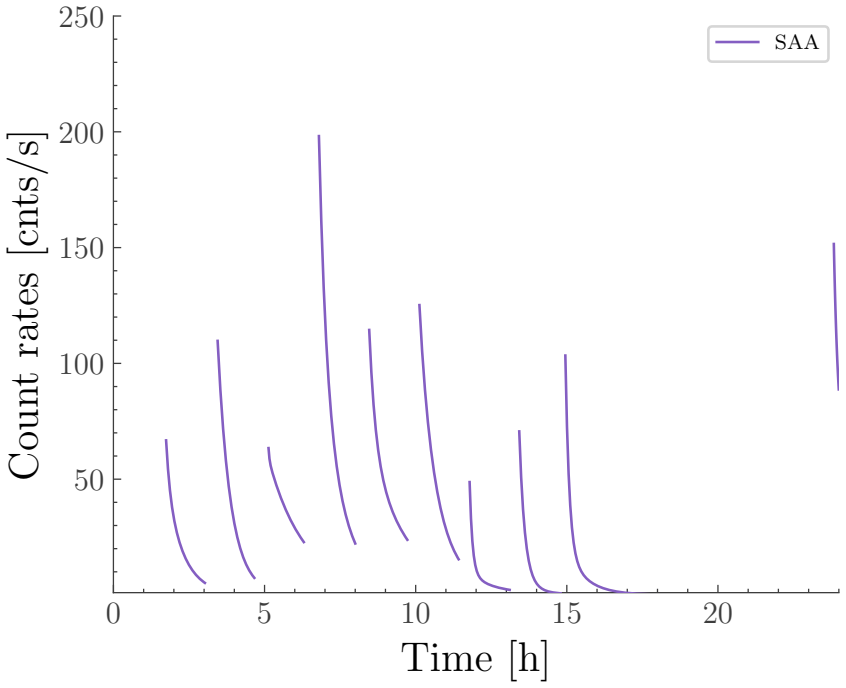

Figure 4.10: Example temporal variation induced by the SAA passages at the 15th January 2015 for detector n7.

de-excitation produce photons (as shown for SPI in Diehl et al. (2018)), which can be measured by GBM's detectors. Due to Fermi's low-Earth orbit and the small inclination, the detectors are well protected by the Earth magnetic field against cosmic rays. Only the cosmic rays with very high energies (> GeV for protons) can reach the satellite (Pesce-Rollins 2009). This shielding of cosmic rays varies during the orbital motion with the different magnetic field strength of the Earth in different orbital positions and therefore the amount and the spectrum of cosmic rays hitting the satellite is time dependent. Here, I will first introduce two empirical approaches to model the count rates due to cosmic rays, based on different observed quantities and finally a more flexible approach with a very general analytic function that I developed later.

McIlwain L-Parameter:

The McIlwain L-parameter (McIlwain 1966) can be used as quantifier to model this shielding effect against cosmic rays by the Earth's magnetic field as has been shown for example for protons and electrons measured by the LAT in Pesce-Rollins (2009). The McIlwain L-parameter is connected to the magnetic cutoff rigidity R_C as given in Eq. 4.13. The parameters K and α change with time and have to be determined for the corresponding time (Shea, Smart, and Gentile 1987).

$$R_C = KL^{-\alpha} \tag{4.13}$$

If one extends the magnetic field line at a position to the magnetic equator, then the L-parameter at that position gives the distance of the magnetic field line at the magnetic equator to the Earth center in units of Earth radii. The correct functional dependence

of the background rate caused by cosmic rays on the L-parameter is not known. All that is known a priori is that a higher L-parameter means a weaker protection by the Earth magnetic field and thus, should lead to a higher background caused by cosmic rays. But a linear relationship between the background rate difference and the L-parameter difference seems to describe the detected background rates quite well for the GBM detectors and the L-parameter range on the Fermi orbit ($\approx 1 - 1.7 r_{\mathrm{Earth}}$ outside of the SAA as shown in Pesce-Rollins (2009)).

$$R_{CR}(L_1) - R_{CR}(L_2) \propto L_1 - L_2 \tag{4.14}$$

For cosmic rays it is assumed that Eq. 4.14 describes the difference in the count rates for different L-parameter values. To get the McIlwain L-parameter values for the different times the weekly spacecraft file[2] is used. Parameter values are provided with a time resolution of 30s. Between these time steps a linear interpolation is used. The total rate by cosmic rays is then defined by

$$R_{CR}(t) = R_{CR}(L_{min}) + C_{CR} \cdot (L(t) - L_{min}), \tag{4.15}$$

where L_{min} is the minimal L-parameter of the data. Therefore, the background model component has two parameters: Firstly, a constant $R_{CR}(L_{min})$, which is the same for all time bins, and secondly, a normalisation C_{CR}, which is multiplied by the difference of the L-parameter of the time bin and the minimal L-Parameter in the data.

The influence of the cosmic rays in this approach depends only on the position of the satellite and is direction independent. This seems to be true to first order, but in the high-energy channels, where the cosmic ray contribution is dominant, a directional differences of a few tens of percent can be observed. This could be explained by the East-West asymmetry of the cosmic ray flux due to the Earth magnetic field (see Sec. 4.2.1).

BGO approximation:

Because the influence of cosmic rays on GBMs background is rising with energy, it dominates in the high-energy channels of the BGO detectors. This can be used as an alternative to model the cosmic ray contribution. To obtain the functional form, the BGO data in the energy range of 8.6 MeV to 16.6 MeV is binned to 100s bins and a spline of 3rd degree with a smoothing prior is fitted. It is then assumed that the variation in the amount of background rates caused by cosmic rays in the lower energies is linearly correlated with the functional proxy obtained from the BGO data; therefore, we only fit for the normalisation C_{BGO} that is multiplied with the fitted spline S_{BGO}.

$$R_{CR}(t) = C_{\mathrm{BGO}} \cdot S_{\mathrm{BGO}}(t). \tag{4.16}$$

The model obtained by the BGO approximation can fit the cosmic ray contribution noticeably better than the model that uses the McIlwain L-parameter (see Fig. 4.11). But one has to keep in mind that the BGO data is not free of other background sources as for example the spectrum of the Earth Albedo extends to the MeV range. This shortfall

[2] heasarc.gsfc.nasa.gov/FTP/fermi/data/lat/weekly/spacecraft/

could be overcome by the use of the Anti-Coincidence Detector (LAT) (ACD) to model the cosmic ray background in GBM. The ACD is primarily used to detected charged particles in 89 tiles around the LAT, in order to exclude the charged particle induced background in the LAT data. Because the count rates of the ACD are also stored, one could use the different tiles to reconstruct the particle flux variation for different sites of the satellite individually. Unfortunately, the data of the ACD is not publicly available.

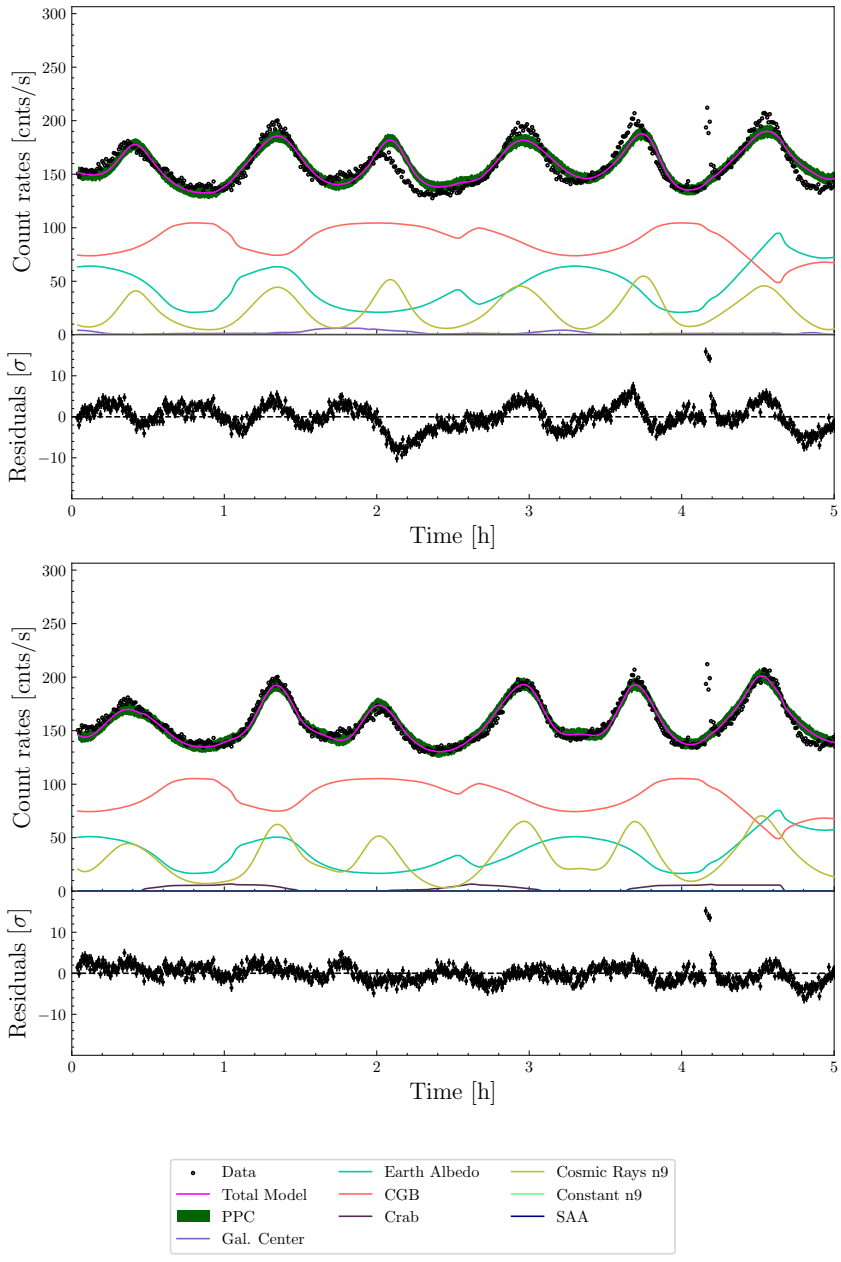

Figure 4.11: Background fits for 5 hours of the 25th of September 2013. The upper plot shows the result with the McIlwain L-parameter approximation and the lower plot with the BGO approximation. With the BGO approximation the fit gets noticeably better. The strong deviation from the background fit at $\approx$ 4 o'clock is caused by the ultra-long GRB 130925A, that will be discussed in more details in Sec. 4.3.1.

Analytic function:

The McIlwain L-Parameter and BGO approximation approaches are based on different observed quantities (McIlwain L-parameter or BGO count rate) including strong assumptions on the connection of these quantities and the cosmic ray induced count rates in the NaI detectors. Here I derive an approach that uses only very weak assumptions but is also computational much more expensive. Instead of basing the temporal variations on these observed quantities I decided to fit it with a general analytic function. The analytic function I choose is based on random Fourier features, which is for example used to approximate the kernel matrix in Gaussian processes (Milton et al. 2019).

In the case of the cosmic ray induced variation, we know that it is changing slowly and quasi-periodically (orbital period of ≈ 95 minutes). Therefore, it is a valid assumption that only a few Fourier features (frequencies) will dominate the whole function. This lead to the construction of the following analytical function, where the exponential assures positive rates:

$$R_{CR,\mathrm{echan}}(t) = C_{\mathrm{echan}} \sum_{n=0}^{N} \exp\left(\sin(\omega_n t)\beta_{n,1} + \cos(\omega_n t)\beta_{n,2}\right), \tag{4.17}$$

where C_{echan}, ω_n, $\beta_{n,1}$ and $\beta_{n,2}$ are free parameters in the fit.

This approach gives the fit a lot of freedom and to prevent it from just perfectly (over) fitting all the data we have to constrain it. This can be done by one or both of the following assumptions: Firstly, we could assume that all NaI on the same side of the Fermi satellite have the same induced count rates by cosmic rays, as they all face in similar directions and secondly, we could also assume that the temporal shape of the induced count rates by cosmic rays is the same in all energy channels.

Either assumption constrains the temporal shapes as it must explain the data in several detectors and/or energy channels at the same time with the addition of the other sources and thus, this approach is only possible when fitting several detectors from the same site and/or energy channels at the same time.

4.3 Proof of Concept

In Biltzinger et al. (2020) I showed that the background model can fit the data of several detectors and energy channels simultaneously for a number of cases. This is summarised in the following. All the fits in this section use the BGO approximation for the cosmic ray component and fix the spectral shape of different photon sources to the values found in the literature (as described above).

4.3.1 Ultra-Long GRB 130925A

Since the background model is fit over a full day, the fit parameters have no room to allow variations between individual satellite orbits, i.e. to accommodate spatially (e.g. transient sources) or temporally (e.g. disturbances in the magnetic field) varying sources. This makes the background fit very stiff, and thus, allows us to readily identify variable sources. This

is demonstrated for September 25, 2013, when multiple emission periods were detected over several thousand seconds from the ultra-long GRB 130925A (Evans et al. 2014). In Fig. 4.12 the data for detector n9 and two CTIME energy channels ranges are displayed, as well as the fitted model. The two GBM triggers are marked as vertical lines. The additional strong deviation at around 5000 seconds after the first GBM trigger is also seen by Konus-Wind (Evans et al. 2014) with the same temporal profile, proving that it is real and not an artefact of the background model fits.

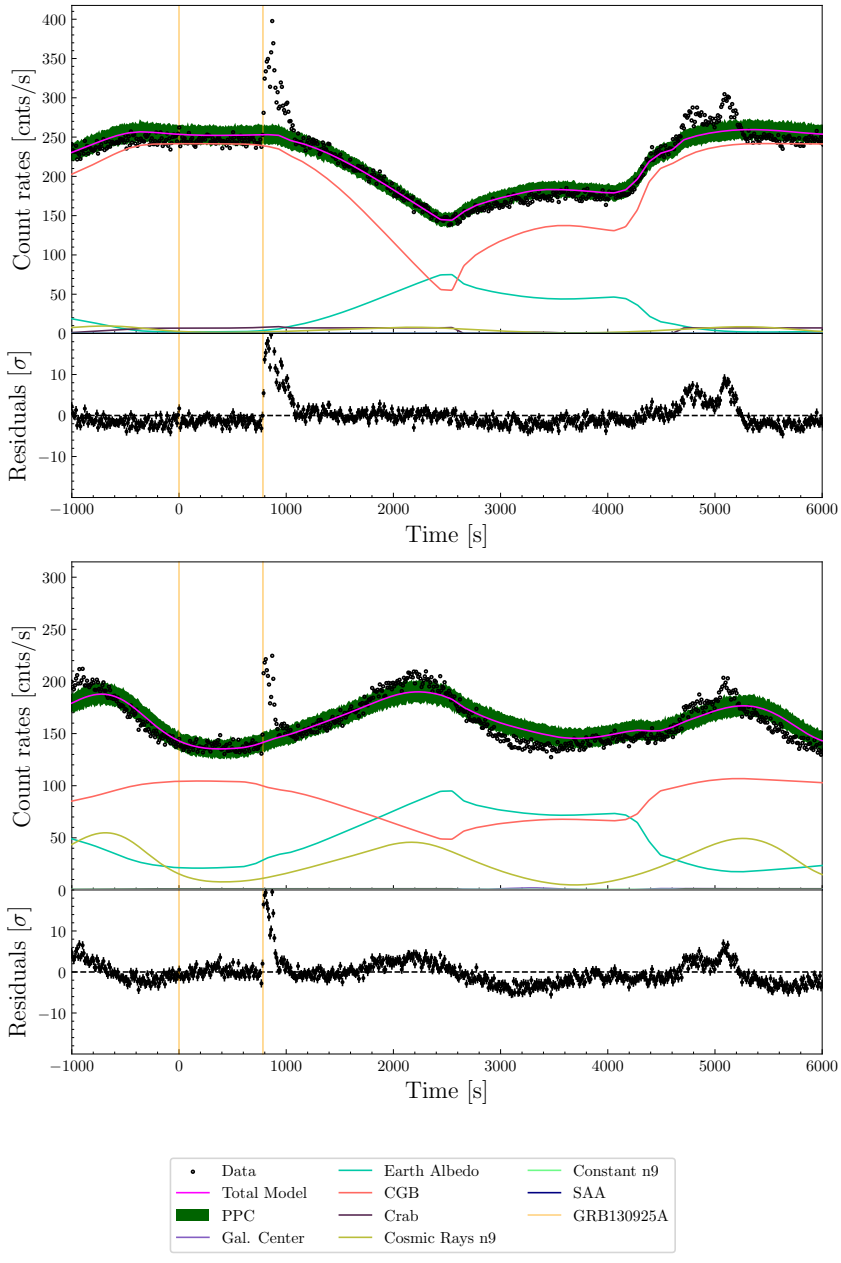

Figure 4.12: Data and background fit for the time around the ultra-long GRB130925 for detector n9 and CTIME energy channel 2 (upper) and 4 (lower). The GRB is nicely visible as deviation from the background fit, that can explain the variation of the rest of the data well, as shown by the residuals and Posterior Predictive Checks (PPCs).

4.3.2 Ultra-Long GRB 091024

On the 24th October 2009, the ultra-long GRB 091024 (Gruber et al. 2011) was detected by Fermi-GBM (Bissaldi and Connaughton 2009), BAT (Sakamoto, Barthelmy, and W. 2009) and Konus-Wind (Golenetskii et al. 2009). It consisted of multiple emission peaks with a total duration of about 1000 seconds. The last emission peak had a duration of about 230 seconds, which makes it an ideal test case, to evaluate if this long, multiple emission period could effect the background model fit.

Fig. 4.13 shows the background fits for two different detectors and two different reconstructed energy ranges around the trigger time of GRB 091024. It is clearly visible in the residuals and with the PPCs (see Sec. 3.1.3), that the model can explain most of the observed data very well. Also the multiple emission peaks of GRB 091024 are clearly visible as deviations from the background fit, demonstrating again the usefulness of a physically motivated background model to identify long-duration emission, and the possibility to use the fitted background model as background estimation during the active time of the transient source.

4.3.3 GRB 110920A

GRB 110920A was a bright, single-pulse GRB that occurred only about 100 seconds after a SAA exit of GBM. This causes the background to have a significant component from the exponential decay of the activated material. Nevertheless, the background model can fit the background around GRB 110920A very well (see Fig. 4.14) and the GRB is clearly visible as deviation from the background fits even without excluding the active time of the GRB from the fit. Therefore, this normal long GRB could have been found with the background model without prior knowledge of the time of the GRB event.

Using the physical background model as background estimation during the active time of the GRB is well defined, even when the GRB is shortly after an SAA transit, whereas the classical approach of fitting polynomials can lead to ambiguous answers depending on the exact background time selections.

4.3.4 V404 Cygni Flaring

In June 2015 V404 Cygni went into outburst, producing multiple flares which GBM triggered on (Jenke et al. 2016). The 21st of June was a very active day, on which GBM triggered 10 times. Fig. 4.15 displays the light curves of GBM for two detector-energy channel pairs for part of the day. The time of all GBM triggers are marked with blue vertical lines. One can clearly see from the PPCs and the residuals that there were several more long and weak emission periods on this day, that did not trigger GBM (vertical blue lines in Fig. 4.15). V404 Cygni was so active on that day that it disturbed the background fit a bit, as the background fit is slightly too high for the non-active times of V404 Cygni. But still the several emission periods are well visible in the plots even though the active times of V404 Cygni are not excluded from the fit. This is due to the use of physically derived background sources and not arbitrary polynomials and therefore very strongly restrict

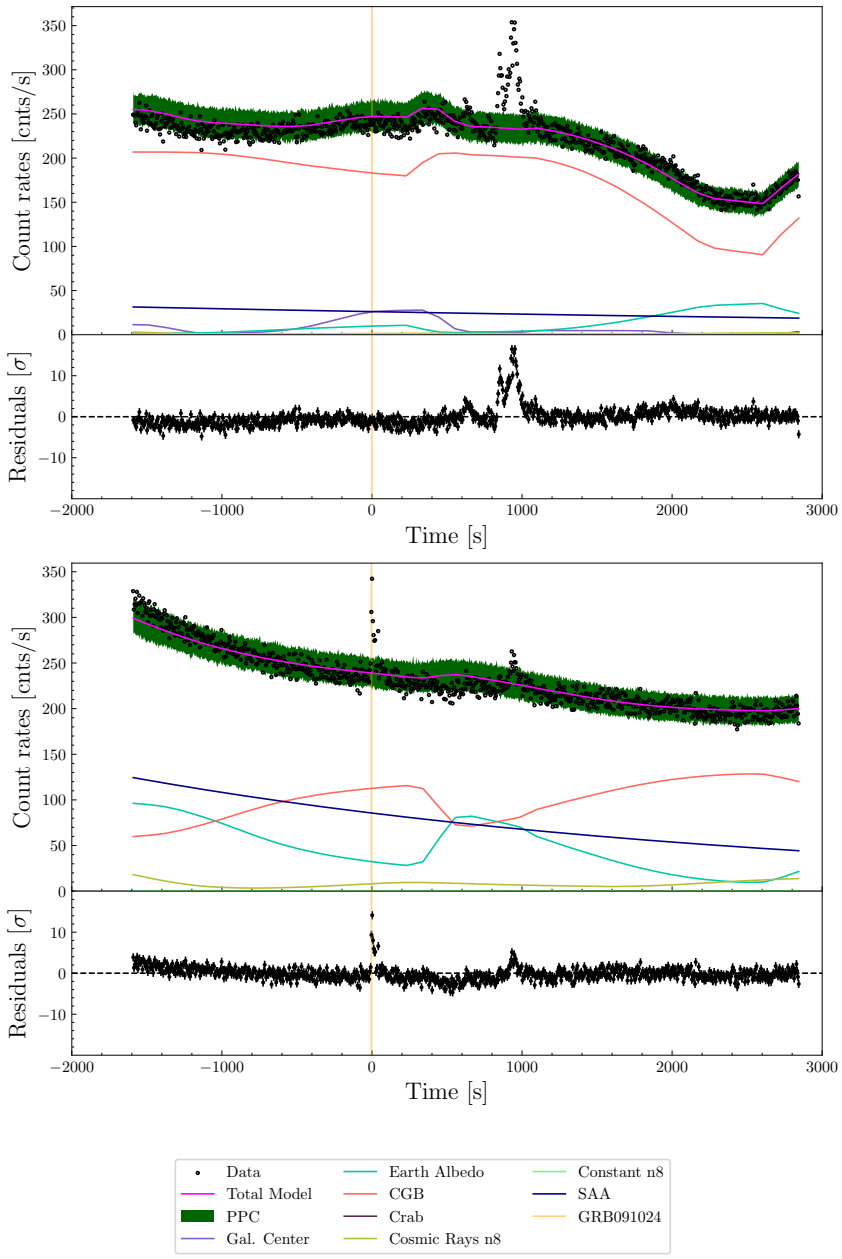

Figure 4.13: Data and background fit for the time around the ultra-long GRB091024 for detector n0 (n8) and CTIME energy channel 2 (4) in the upper (lower) plot. The GRB is nicely visible as deviation from the background fit, that can explain the rest of the data well, as shown by the residuals and PPCs.

what kind of shapes can be fitted by the background model. This makes the presented background model a promising tool to search for long source emissions in the data of GBM in the future, even in the extreme conditions of a flaring bright source. If one wants to use the fitted background model as an accurate background estimation during the active times of the source, one should of course redo the analysis and exclude the times when the source was active from the fit, to get rid of this disturbance.

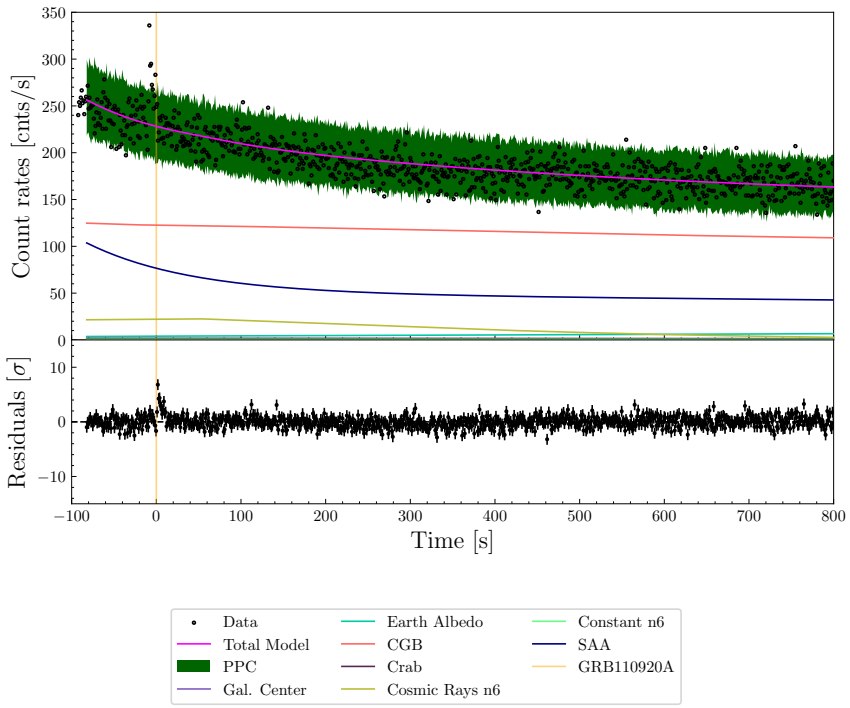

Figure 4.14: Data and background fit for the time around the long GRB 110920A for detector n6 and CTIME energy channel 3. The GRB is nicely visible as deviation from the background fit, that can explain the rest of the data well, as shown by the residuals and PPCs.

4.3.5 Comparison to Fermi GBM Background Subtraction Tool

The advantage of the presented background model with respect to the Fermi GBM Orbital Background Subtraction Tool (OSV), which is based on the (Fitzpatrick et al. 2012) method, is demonstrated for September 25, 2013 (Fig. 4.16). One can see that the physical background model fit is capable of explaining the background variations, whereas the OSV fails, mainly due to an ARR after the second GBM trigger. But also during days without ARR, the OSV method has its limitations, as it depends on having no deviation of any kind (besides ARR also transients etc) also 30 orbits before and after the day in question. The following summaries the advantages of the presented physical model over the OSV:

- Not affected by ARR or other deviations from the normal pointing mode
- Not affected if the satellite was in an SAA 30 orbits before or after the time of interest
- Not affected by GRBs or any transient sources occurring 30 orbits before or after the time of interest
- More robust method that does, for example, not need the radiation environment or magnetic field to be stable for at least 3 days (due to the +/- 30 orbits that are used in the OSV)
- Treats the data in a statistically correct way which allows to derive proper errors on the background counts
- Allows to study and understand the different components of the background (also interesting for future missions)

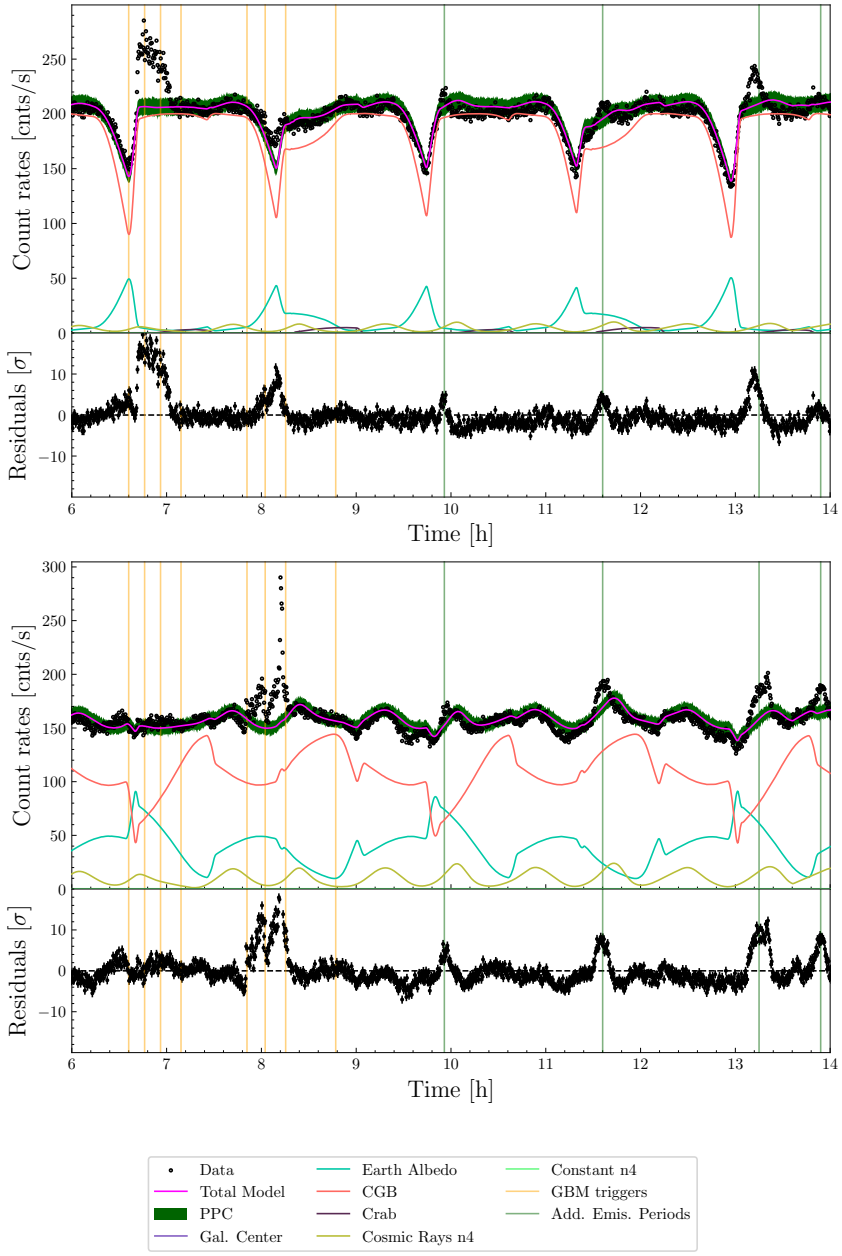

Figure 4.15: Data and background fit for parts of the 21st of June 2015, when V404 Cygni was in a strong outburst state, for detector n0 (n4) and CTIME energy channel 2 (3) in the upper (lower) plot. The active time of V404 Cygni is nicely visible as deviation from the background fit, that can explain the rest of the data well, as shown by the residuals and PPCs, with the yellow vertical lines indicating the GBM triggers and the green vertical lines indicating additional emission periods. Only the part of the day with no SAA transit was used in this case such that the SAA exit has not to be included in the fit.

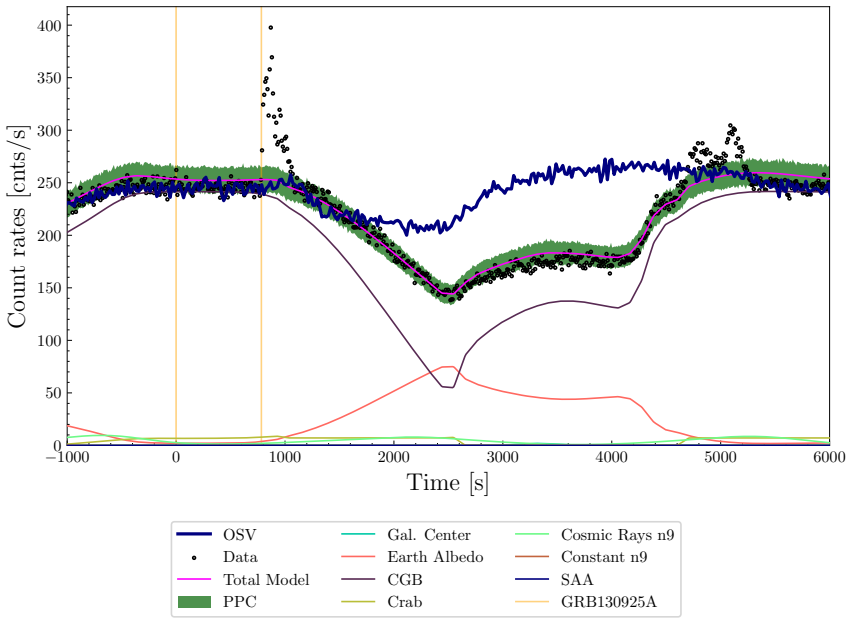

Figure 4.16: Data and background fit for the time around the ultra-long GRB130925 for detector n9 and CTIME energy channel 2 (reconstructed energy range ≈ 25-50 keV). Both the background estimation by the OSV and the physical background model are shown. For a ≈ 3000 second time interval the OSV is not able to usefully estimate the background, due to an ARR, that causes the pointing to be different than 30 orbits before and/or after. The physical background model does not dependent on these assumptions and can explain the background in the whole time span well.

4.4 Applications

4.4.1 Transient Pipeline

The developed physical background model was successfully used in Kunzweiler et al. (2022) to build a pipeline to search for transients of different kind in the GBM data that were previously missed. Due to the ability of the model to fit the background of a whole day we were able to find sources much weaker and of longer duration than the normally detected GRB triggers.

For this pipeline the data of all detectors and CTIME energy channels 0-5 of one day is fitted with the derived background model.

To identify possible transients in the next step, the background subtracted light curves are examined with a change point algorithm, that detects significant variations in the light curve, that fit to the expected variations of a physical transient photon source. This is achieved with an adapted Pruned Exact Linear Time (PELT) algorithm, which was introduced by Jackson et al. (2005), to identify optional partitions in a data series. The PELT algorithm is very efficient in one dimension, but gets computationally intractable in higher dimensions (Scargle 1998; Jackson et al. 2005; Fryzlewicz 2014). But in this use-case there are 12 detectors and 6 energy channels used, leading to an effective 72-dimensional data space. To overcome the dimensionality problem, the 72-dimensional data space is reduced to two dimensions by only using the length and the angle of the data vector

spanned in the original 72-dimensional data space (Grundy, Killick, and Mihaylov 2020). This approach is common in change point detections (Horváth and Hušková 2012; Zhang et al. 2010; Enikeeva and Harchaoui 2019). The length and angle measurements have nice physical properties: While a significant increase of the length of the vector indicates a general stronger deviation of the data from the model, a significant increase in the angle indicates a change in the relative fluxes of the individual light curves. Therefore, for a transient event we expect a change in both quantities as the data should deviate stronger from the background model fits and the induced rates in the detectors and energy channels is different, leading to a change in the relative fluxes. A particle event on the other side would for example change the length but not the angle that strongly as it induces count rates in all detectors.

Consecutive detected change points are then grouped and the significance of the data over the background is calculated, taking into account the uncertainties in the background model fit. The significance can be calculated with (Vianello 2018)

$$S = \sqrt{2}\left(nlog\left(\frac{n}{B^{MLE}}\right) + \frac{\left(b - B^{MLE}\right)^2}{2\sigma_B^2} - n\right)^{0.5}, \tag{4.18}$$

where n are the detected counts, B^{MLE} is the maximum likelihood estimation of the background counts and σ_B the uncertainty on the background counts. Intervals with significance than less than 5 σ are dropped and consecutive intervals with significance than larger than 5 σ are combined.

The final test if a real transient source is detected is to localise it with BAyesian Location Reconstruction Of GRBs (BALROG) (Burgess et al. 2017) by fitting the spectrum and location simultaneously. Only if the signal is produced by a real photon source this will lead to constrained localisations, because in every other case the signal can not be explained by a photon spectrum folded with the response.

To test the abilities of the developed transient pipeline many simulations of point source transient sources on top of simulated background were conducted. These simulations were analysed with the pipeline without knowledge where the simulated source is and when it is active. The tests show that sources brighter than two Crab can be detected efficiently for durations longer than 1000 seconds (see Fig. 4.17).

The pipeline was used to analyse all days in the two time periods 2020/06/16 – 2020/07/14 and 2020/10/24 – 2020/11/17. It detected more than 300 transients in that time, from which an outburst of Vela X-1 is the most notable. It was detected on the 17th of June 2020 in three different time intervals (Kunzweiler et al. 2022):

1. 19:48:35 UTC with a duration of 665.6 s and a significance of 12.9 σ
2. 20:04:53 UTC with a duration of 1593.6 s and a significance of 33.4 σ
3. 20:21:42 UTC with a duration of 153.6 s and a significance of 5.3 σ.

All of these emission periods were automatically localised to the same location and a manual localisation of all emission periods together yielded a final position of RA=$(237.5^{+2.2}_{-3.5})^\circ$ and Decl.=$(-42.1^{+2.4}_{-2.3})^\circ$. At the same time Vela X-1 was observed in a bright state by

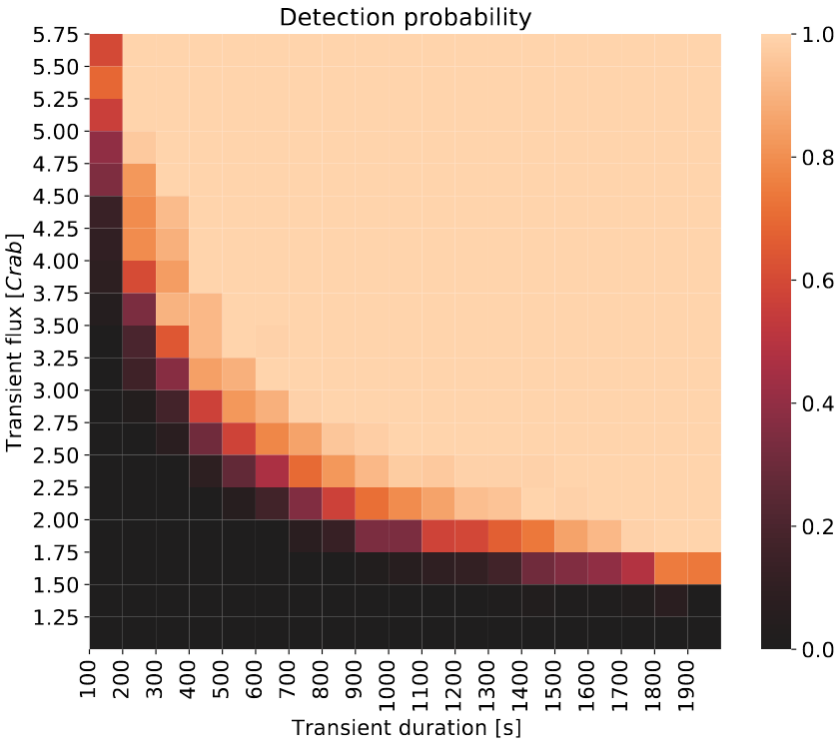

Figure 4.17: Detection probability of point sources with a Crab like spectrum for different fluxes and durations. Taken from Kunzweiler et al. (2022).

BAT, confirming the detection of this source with GBM. Especially interesting is that the detected rates oscillate with a period of ≈ 142 seconds (see Fig. 4.18). This matches nicely to Vela X-1, which is a pulsing high-mass X-ray binary with a neutron star and a supergiant star (Bildsten et al. 1997). The known spin period of the neutron star of 283.53 seconds (Kreykenbohm et al. 2008) fits perfectly with the determined period of 142 seconds measured with the GBM data (emission by south and north pole of neutron star).

The presented analysis in this subsection is based mostly on the work of my colleague Felix Kunzweiler, that he did for his master thesis. I mostly contributed in the form of the connection of his transient search algorithm and the physical background model and discussion about the project, especially the localisation.

4.4.2 Constrain the Cosmic Gamma-Ray Background

Due to the physical motivation of the background model we can also learn about the individual background components. As shown in Sec. 4.2.1, the CXB/CGB is a major background component and it is a topic of great interest in astrophysics as it can be used to test different AGN spectral and population models (Ananna et al. 2020). As GBM covers the energy > 8 keV I want to analyse the CGB spectrum with the background in GBM in this chapter.

To reduce possible systematic uncertainties the data selection is adjusted for this chapter. First, all times within 12000 seconds from a previous SAA exit are excluded to minimise their effect. This also reduces the fitting parameter significantly. Second, the

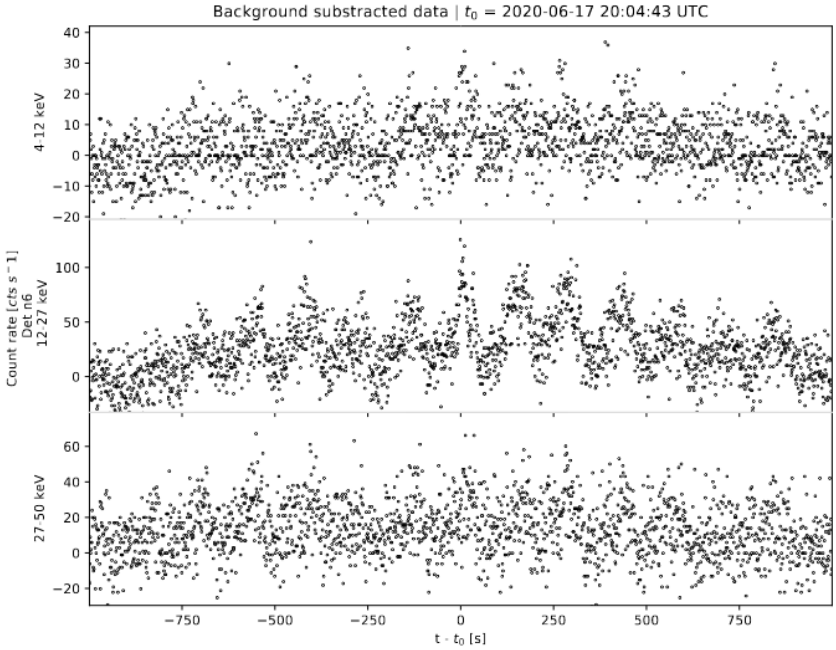

Figure 4.18: Background subtracted light curves for detector n6 and three energy channels. Taken from Kunzweiler et al. (2022).

data of only two consecutive orbits are used, to reduce the possible brightness variations of point sources and the induced systematic error when they are assumed to be constant.

In the fit, the spectral shape of the CGB is modeled with an extension of the smoothly broken power law, namely the Beuermann function (see Eq. 4.19)(Beuermann et al. 1999), that has an additional parameter n to allow the curvature of the break to be independent of the the low- and high energy slopes. All parameters are free during the fit.

$$\frac{\mathrm{d}N}{\mathrm{d}E} = C\left(\left(\frac{E}{E_{\mathrm{norm}}}\right)^{n\alpha} + \left(\frac{E}{E_{\mathrm{norm}}}\right)^{n\beta}\right)^{-\frac{1}{n}} \tag{4.19}$$

The spectrum of the Earth Albedo is fixed to the values in Ajello et al. (2008), due to an degeneracy of the CGB and Earth Albedo component. Following the approach in Sec. 4.1.1 for extended sources, the combined count rates produced by Earth Albedo and the CGB is

$$\begin{aligned} R_{\mathrm{CGB+Earth}}(t) = \frac{4\pi}{N}\Big(\sum_{i=1}^{N} f_{NE}(t,p_i)\mathcal{R}(p_i)F_{\mathrm{CGB}} + \\ \sum_{i=1}^{N} f_E(t,p_i)\mathcal{R}(p_i)F_{\mathrm{Earth}}\Big), \end{aligned} \tag{4.20}$$

where f_E is the occlusion function for the grid points occluded by the Earth (see Eq. 4.3) and f_{NE} for the grid points not occluded by the Earth (and therefore covered by the CGB).

By definition of the occlusion function it holds for all times that

$$\sum_{i=0}^{N} \mathcal{R}(p_i) = \sum_{i=0}^{N} f_E(t, p_i)\mathcal{R}(p_i) + \sum_{i=0}^{N} f_{NE}(t, p_i)\mathcal{R}(p_i). \tag{4.21}$$

Substituting Eq. 4.21 into Eq. 4.20 gives

$$\begin{aligned} R_{\mathrm{CGB+Earth}}(t) = \frac{4\pi}{N}\Big(& \sum_{i=1}^{N} f_{NE}(t, p_i)\mathcal{R}(p_i) F_{\mathrm{CGB}} + \\ & \Big(\sum_{i=1}^{N} \mathcal{R}(p_i) - \sum_{i=0}^{N} f_{NE}(t, p_i)\mathcal{R}(p_i)\Big) F_{\mathrm{Earth}}\Big), \end{aligned} \tag{4.22}$$

that can be rearranged into

$$\begin{aligned} R_{\mathrm{CGB+Earth}}(t) = \frac{4\pi}{N}\Big(& \sum_{i=1}^{N} f_{NE}(t, p_i)\mathcal{R}(p_i)\Big(F_{\mathrm{CGB}} - F_{\mathrm{Earth}}\Big) + \\ & \sum_{i=1}^{N} \mathcal{R}(p_i) F_{\mathrm{Earth}}\Big). \end{aligned} \tag{4.23}$$

Eq. 4.23 shows that the time variation only depends on the difference of the CGB and Earth Albedo spectrum and not on the individual spectra. The second term in Eq. 4.23 is constant in time. This could be used to break the degeneracy of possible Earth Albedo and CGB spectra, but unfortunately there are other constant sources in the background model (see Sec. 4.2.2). Therefore, I have to fix one of the two (Earth spectrum) and the resulting CGB is only meaningful in respect to the fixed Earth Albedo spectrum.

Other photon background sources included in the fit are all point sources with a flux larger than 0.5 Crab in the BAT transient monitor (Krimm et al. 2013) for the analysed day and the Galactic Center with the fixed spectral shape shown in Sec. 4.2.1.

For the cosmic ray component the general analytic function Eq. 4.17 is used, because this function is the most flexible. Relying on the linear correlation of the cosmic ray component and the McIlwain L-parameter or BGO count rates can most likely not perfectly capture the true temporal variation. To constrain Eq. 4.17 the temporal variation of the cosmic ray rates is assumed to be the same in all energy channels (see Sec. 4.2.2).

To fit this complicated model, that includes the folding of the spectrum defined by the current parameter values with the response in every fit step, a Stan implementation of this model was developed. Stan is very well suited for complicated models with many parameters (Carpenter et al. 2017).

To check if the model is able to disentangle the CGB from the other components, without internal systematic uncertainties, I simulated the background with a real geometry setup of one day with the following sources: CGB, Earth Albedo, Galactic Centre, Crab and cosmic rays. For the cosmic ray contribution the BGO approximation is used as truth in the simulation. The simulated data for 10000 seconds of two detectors and 12 energy channels covering a range from 10 keV to 600 keV reconstructed energy have been fitted simultaneously, with the fitting setup described above. The resulting spectrum of

the CGB is shown in Fig. 4.19 together with the simulated spectrum. While the fit can nicely reconstruct the spectrum at small energies it fails at higher energies. Fig. 4.20 shows that the cosmic ray component was not able to fully reproduce the simulated variation, which most likely causes the problems. Therefore, some flux was wrongly redistributed from the cosmic ray component to the CGB. This shows how sensible the results are to small systematic errors at high energies, as the influence of the CGB is only minor in this energy range. From this I conclude that the fits are not reliable at high energies, before more details in the modeling of the cosmic rays have been included in the future. Fig. 4.20 suggests for example, that the approach with the general analytic function Eq. 4.17 can not reproduce varying periodicities. Therefore, the function should be tuned in an upcoming work, to fit this case better.

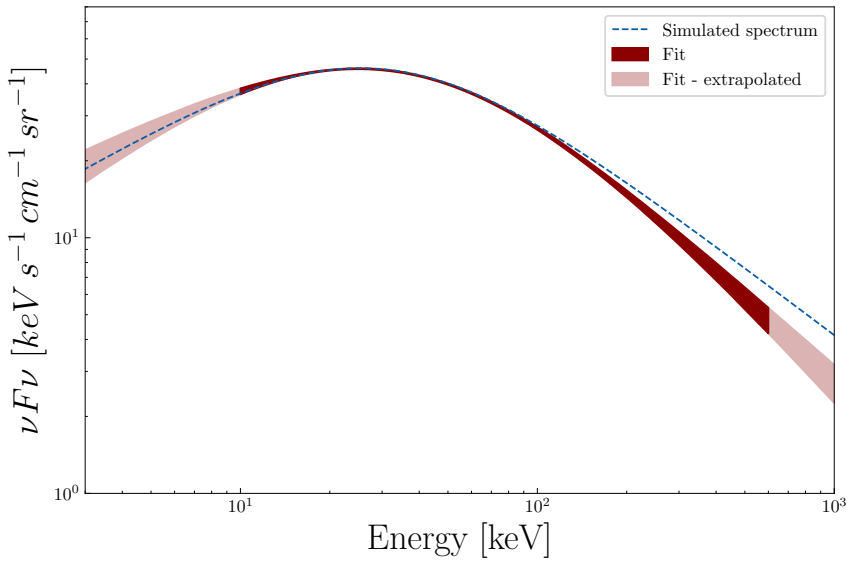

Figure 4.19: Posterior of the CGB spectrum for a simulated background. The cosmic ray induced background was simulated with the BGO approximation and fitted with Eq. 4.17. It shows that the fit was not able to re-produce the simulated CGB spectrum.

But up to ≈ 100 keV the CGB is dominant and small problems with the cosmic ray component are not that important. To test this, I repeated the fit, but only with five energy bins between ≈ 10 keV and 100 keV reconstructed energy. This time the fit is able to reproduce the whole spectrum (Fig. 4.21) and also the PPC plots show no significant deviation of the model from the data (Fig. 4.22 and 4.23).

Following the results from the simulations, I fitted real data only in the energy ranges up to 100 keV reconstructed energy. For this I tested different days for a low number of bright point sources, again to reduce the possible sources of systematic uncertainties. I choose the 24th of April 2020, for which 10000 seconds temporally far away from the SAA passages were used with the data from three detectors (n3, n4, n5) and five energy bins between ≈ 20 keV and 100 keV reconstructed energy. The result for the CGB spectrum is shown in Fig. 4.24 in comparison to other measurements. The PPCs (Fig. 4.25 and 4.26) show that the fit is a good description of the data, with only small deviations. Therefore, it is reasonable to assume that no major background component is missing in the background

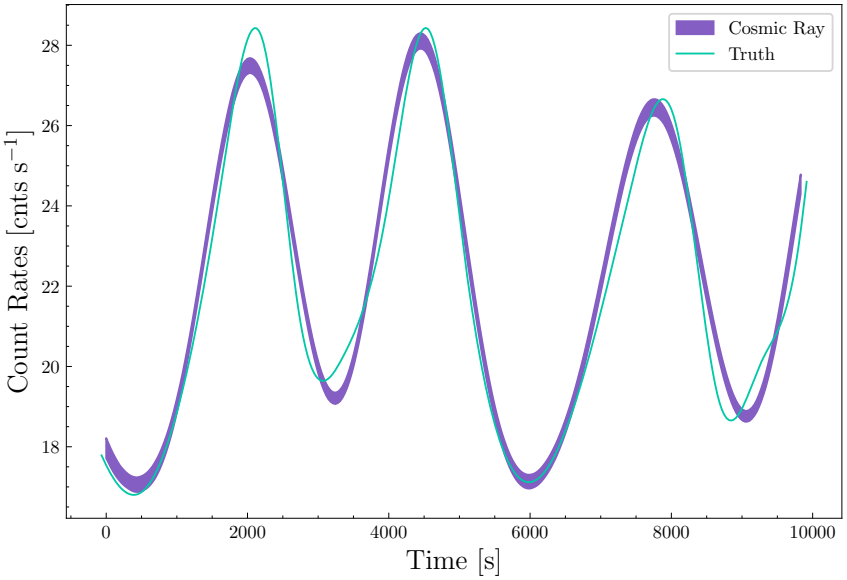

Figure 4.20: Posterior of the temporal variation of the cosmic ray component for a simulated background. The cosmic ray induced background was simulated with the BGO approximation and fitted with Eq. 4.17. It shows that the fit is not able to re-produce the simulated variation, introducing systematic errors on the other reconstructed sources.

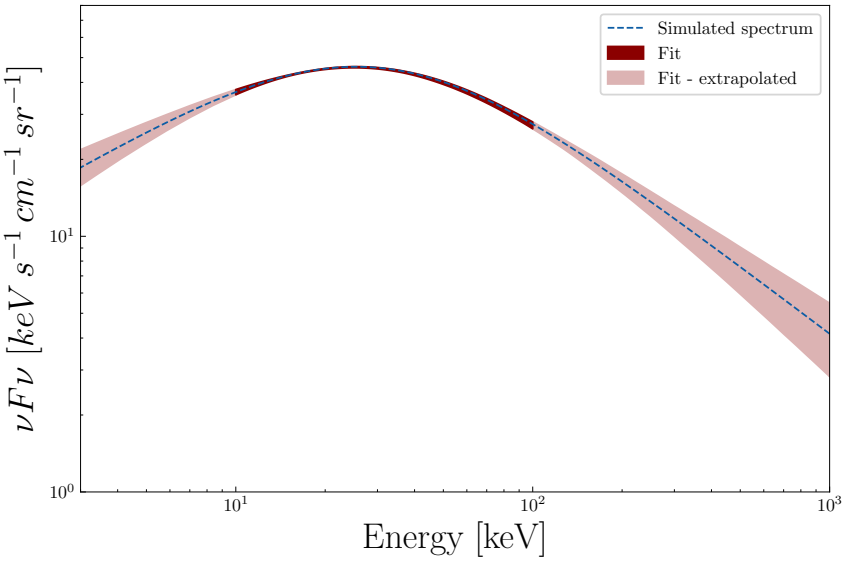

Figure 4.21: Posterior of the CGB spectrum for a simulated background.. The cosmic ray induced background was simulated with the BGO approximation and fitted with Eq. 4.17. In this case the fit was able to reproduce the simulated spectrum.

model.

To test the dependency of this result on the assumed Earth Albedo spectrum I did the fits with two more different Earth Albedo spectra: (1) with the normalisation of the Earth Albedo reduced by 20% and (2) with a different spectral shape (see Fig. 4.27), mimicking the Earth Albedo spectrum given in Churazov et al. (2007). The resulting CGB spectra are compared in Fig. 4.28, showing that the results change. But in the low energy region ($<$ 30 keV) the result is independent of the assumed Earth Albedo spectrum. This is due

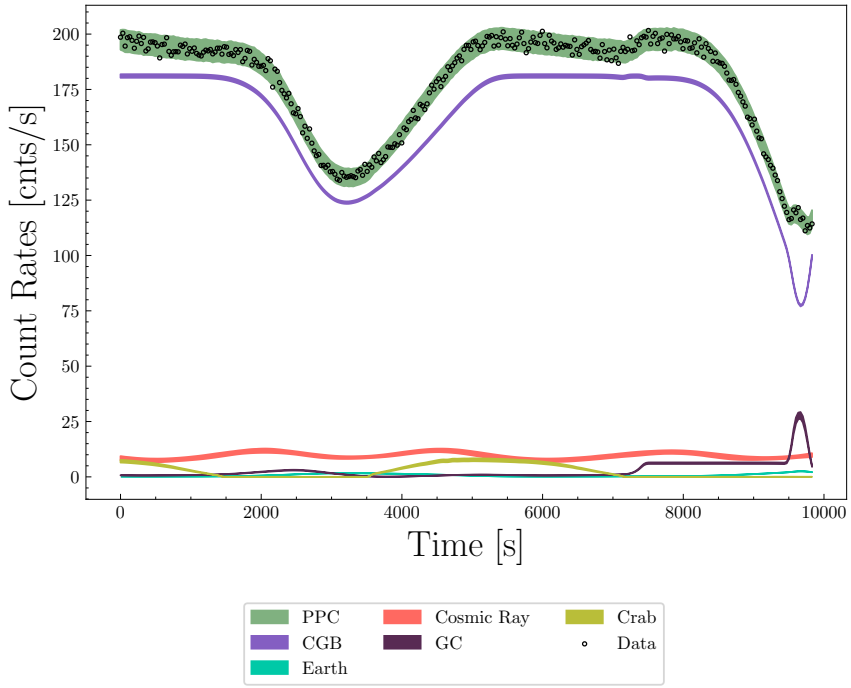

Figure 4.22: PPC plot for one of the simulated used detectors in a lower energy channel (Reconstructed energy ≈ 10-20 keV). The data is well represented by the PPCs, indicating a good fit.

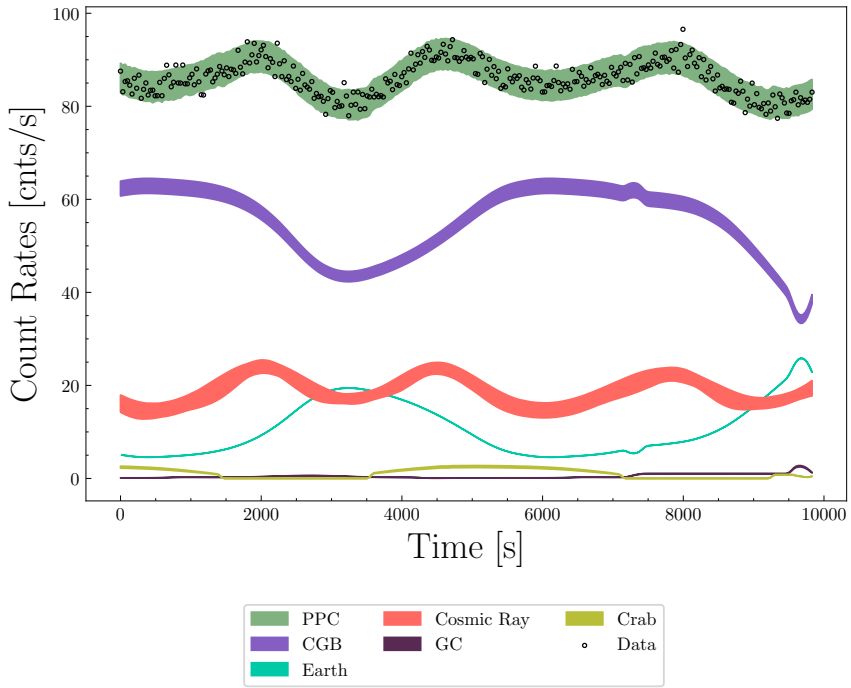

Figure 4.23: PPC plot for one of the simulated used detectors in a higher energy channel (Reconstructed energy ≈ 70-100 keV). The data is well represented by the PPCs, indicating a good fit.

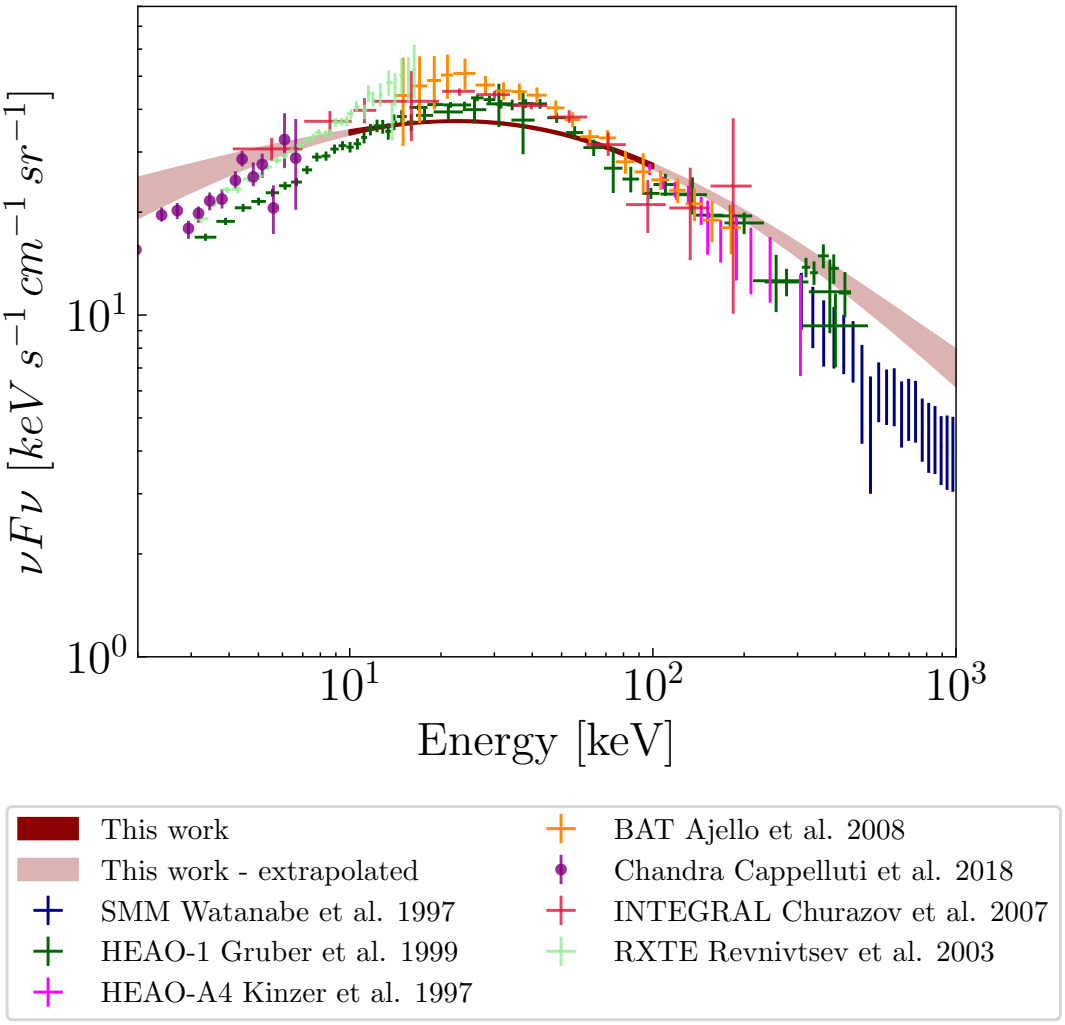

Figure 4.24: Posterior of the CGB spectrum from the fit of the background model. Other measurements of the CGB spectrum are shown with the different error bars. (Kinzer et al. 1997; Watanabe et al. 1997; Gruber et al. 1999; Revnivtsev et al. 2003; Churazov et al. 2007; Ajello et al. 2008; Cappelluti et al. 2017)

to the fact that the CGB is much brighter in this energy range and the degeneracy problem in Eq. 4.23 disappears when $F_{\mathrm{CGB}} \gg F_{\mathrm{Earth}}$.

The resulting CGB spectrum shows a significantly lower flux than measured by Ajello et al. (2008) in the energy range of highest energy flux ($\approx$ 30 keV) but fits well to the result of Gruber et al. (1999). This significantly smaller flux, as well as the smaller peak energy (see Fig. 4.29), compared to Ajello et al. (2008), is independent of the assumed Earth Albedo spectrum, which has influences on the results derived for AGN population models, like in Ananna et al. (2020). The smaller peak energy leads to a different AGN population, as either a smaller ratio of Compton thick to Compton thin AGNs, a higher typical reflection or a different redshift distribution (Compton thick AGNs shifted to higher redshift) is needed to explain the smaller peak energy (see Fig. 4.4).

Assuming the Earth Albedo spectrum from Ajello et al. (2008) also results in a broader peak (see Fig. 4.29), but this result does change strongly when changing the assumed Earth Albedo spectrum. The following conclusions are therefore based on the assumption

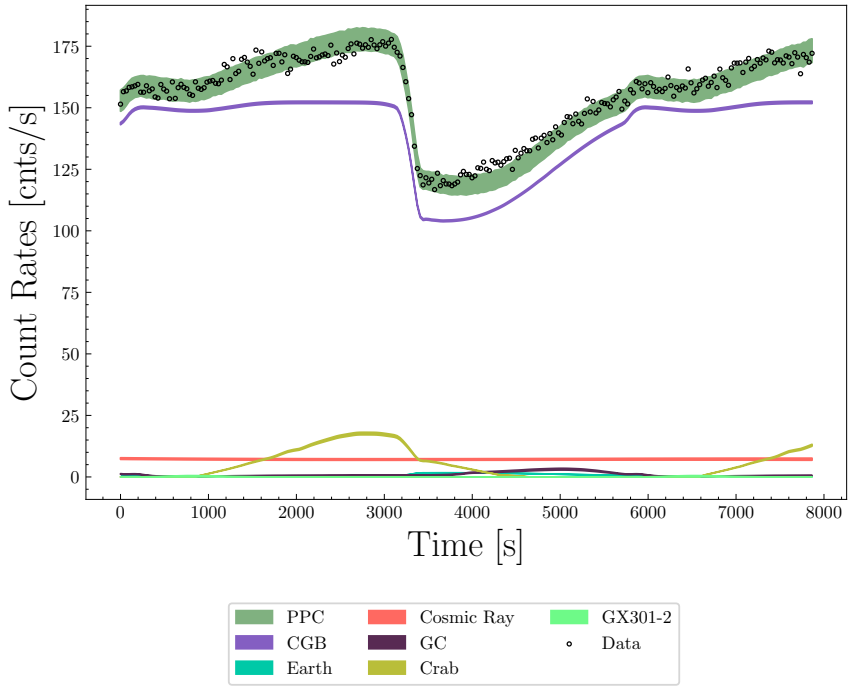

Figure 4.25: PPC plot for detector n3 in a lower energy channel (Reconstructed energy ≈ 10-20 keV). The data is well represented by the PPCs, indicating a good fit.

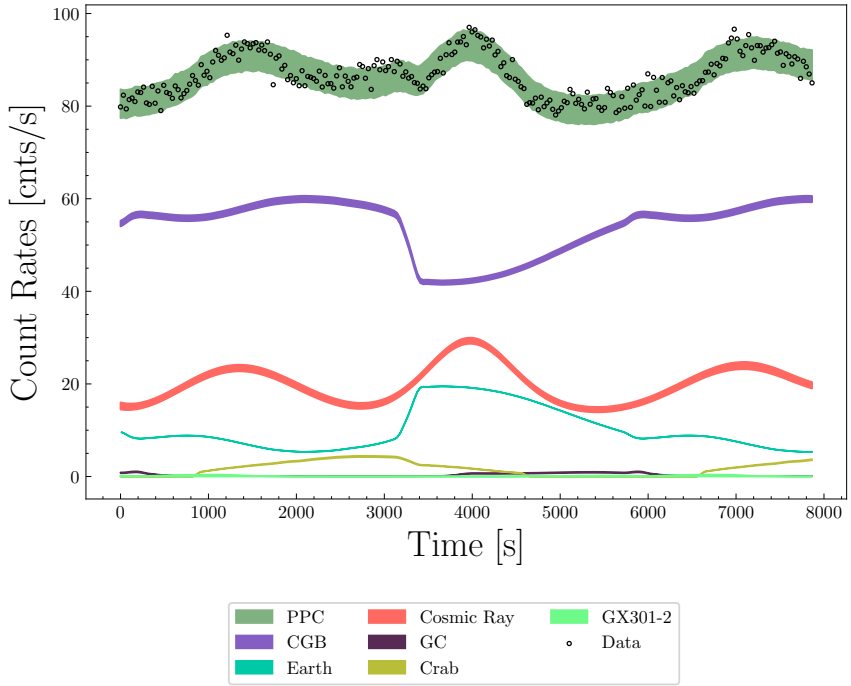

Figure 4.26: PPC plot for detector n3 in a higher energy channel (Reconstructed energy ≈ 70-100 keV). The data is well represented by the PPCs, indicating a good fit.

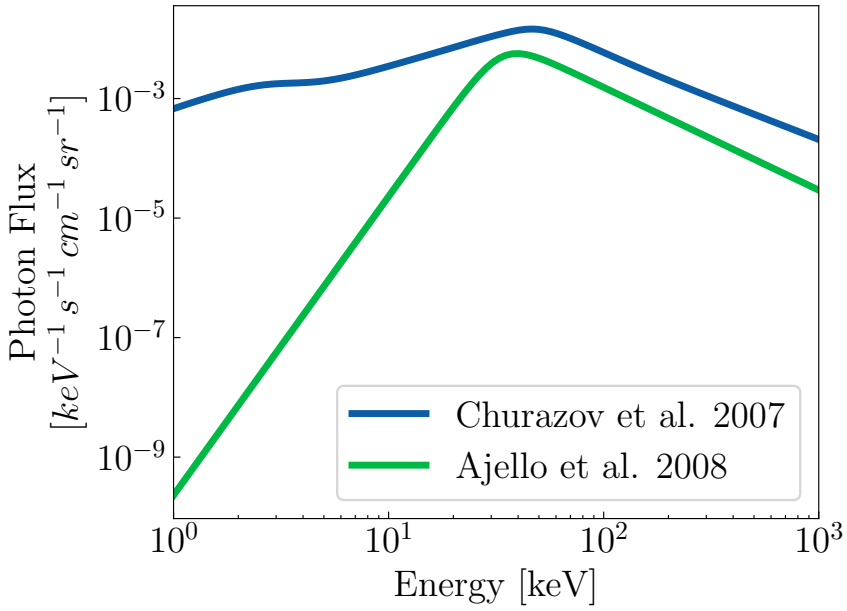

Figure 4.27: Previously determined Earth Albedo spectrum as given in Ajello et al. (2008) and Churazov et al. (2007).

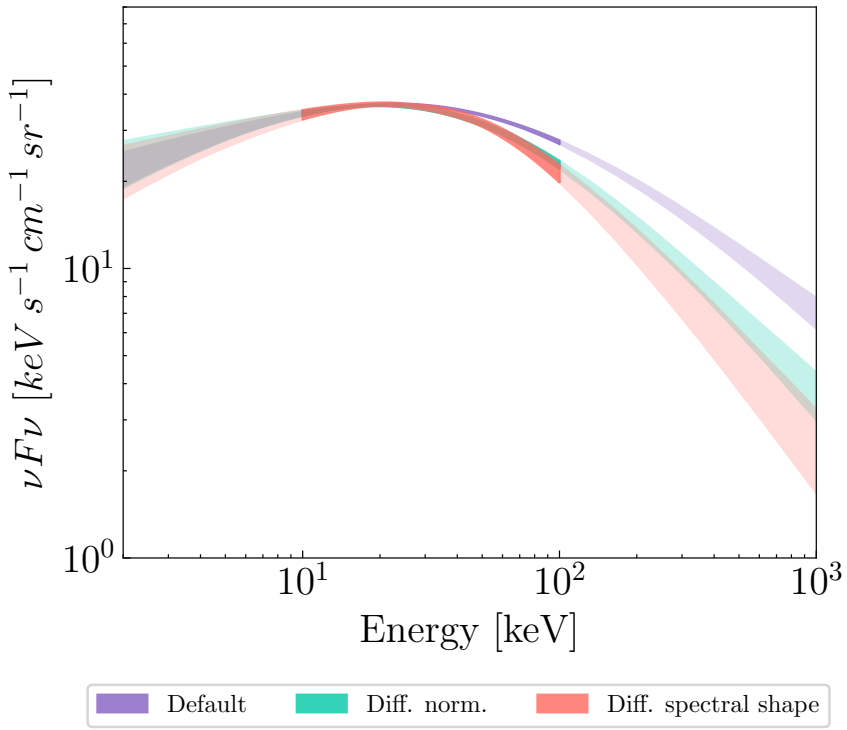

Figure 4.28: Posterior of the CGB spectrum from the fit of the background model with different assumed Earth Albedo spectra. The purple curve shows the result when assuming the default best fit solution from Ajello et al. (2008), green if the Earth Albedo spectrum normalisation is reduced by 20 % and red when the spectral shape is changed to match the results of Churazov et al. (2007).

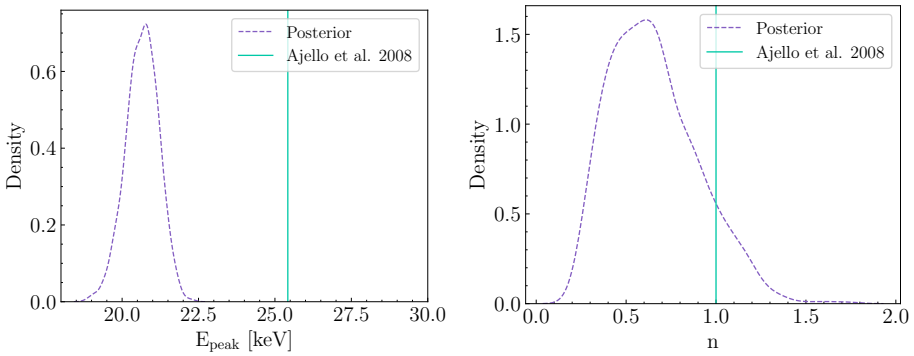

(a) (b)

Figure 4.29: Posterior distribution of the peak energy (a) and the curvature parameter n (b) (see Eq. 4.19) compared to the best fit value in Ajello et al. (2008). For n a smaller value means that the transition between the two asymptotic power laws is slower and in Ajello et al. (2008) a simple smoothly broken power law is used, that is a special case of the Beuermann function with $n = 1$.

that the Earth Albedo spectrum from Ajello et al. (2008) is the truth, but more work has to be done in the future to break this degeneracy, before the derived CGB spectral peak shape can be used to confidently constrain AGN population models. The peak shape of the CGB is determined by different AGN population parameter distributions, like the redshift, the cutoff energy and the reflection parameter. This combined with the column density distribution (e.g. fraction of Compton thick AGNs) defines the curvature of the peak in the resulting CGB spectrum (Ueda et al. 2014). Fig. 4.30 shows that the spectral peak shape, in the energy range used in the fits, fits well to the predictions by Ueda et al. (2014), if the fraction of Compton thick AGNs with $logN_H > 24$ is significantly smaller. This hints to the possibility that the fraction of highly obscured Compton thick AGNs was overestimated in previous works.

The next steps for this analysis in the future should be the development of a physical CGB spectral model, based on single AGN spectral models and AGN population parameters. This could then be used in this background model instead of the empirical Beuermann function, to maximise the information we can extract from the data for this specific topic.

4.4.3 New Instruments

The software I developed can be used as a general simulation and fitting tool for new missions. It is public and written in a general way, that allows other instrument teams to adjust it to their detector specifications and orbit. Currently the BurstCube team (Perkins et al. 2020) is working on using the model to simulate a realistic background for their specific case.

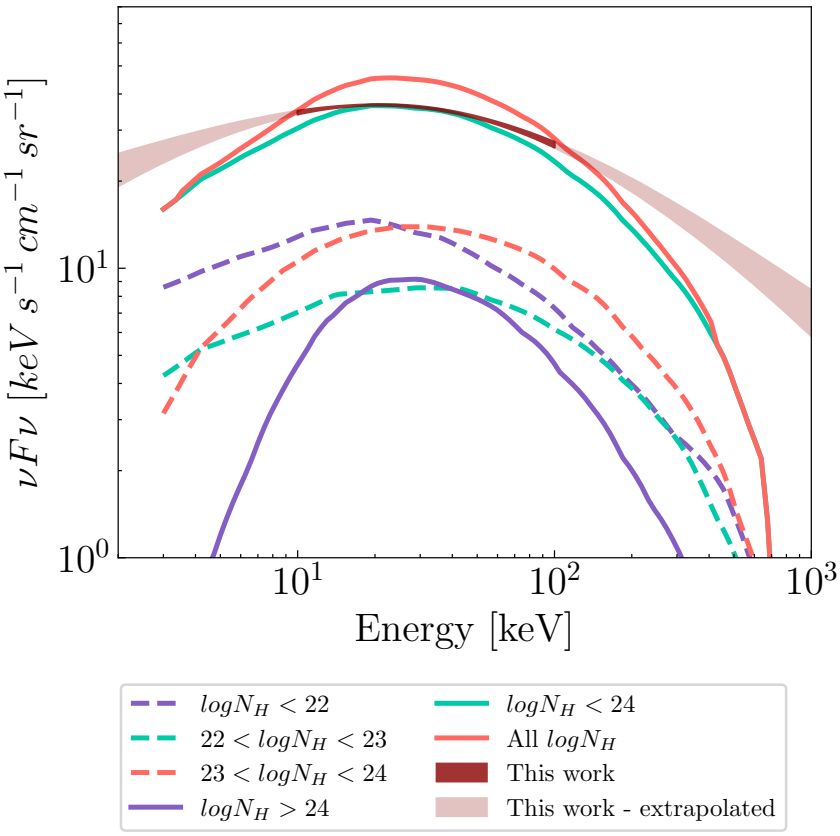

Figure 4.30: Posterior of the CGB spectrum from the fit of the background model compared to the prediction of the contribution by the different obscuration classes of AGNs given in Ueda et al. (2014). It is interesting that the sum of all components below $logN_H = 24$, results in a spectrum with a similar peak structure then determined with the background model fits, hinting to the possibility that the fraction of highly obscured Compton thick AGNs was overestimated in previous works. Data for the predicted contribution of the different obscuration classes of AGNs taken from Fig. 13 in Ueda et al. (2014).

4.5 Software design

The developed background model software is an open-source pure python package, that uses object oriented programming to efficiently structure the different tasks. These different tasks include data reduction, response generation, modeling, likelihood calculations and plotting. Fig. 4.31 shows a schematic overview of the package and Fig. 4.32 - 4.35 show the class diagrams for the different components of the software. The full package is publicly available at `https://github.com/BjoernBiltzinger/GBM-background-model`.

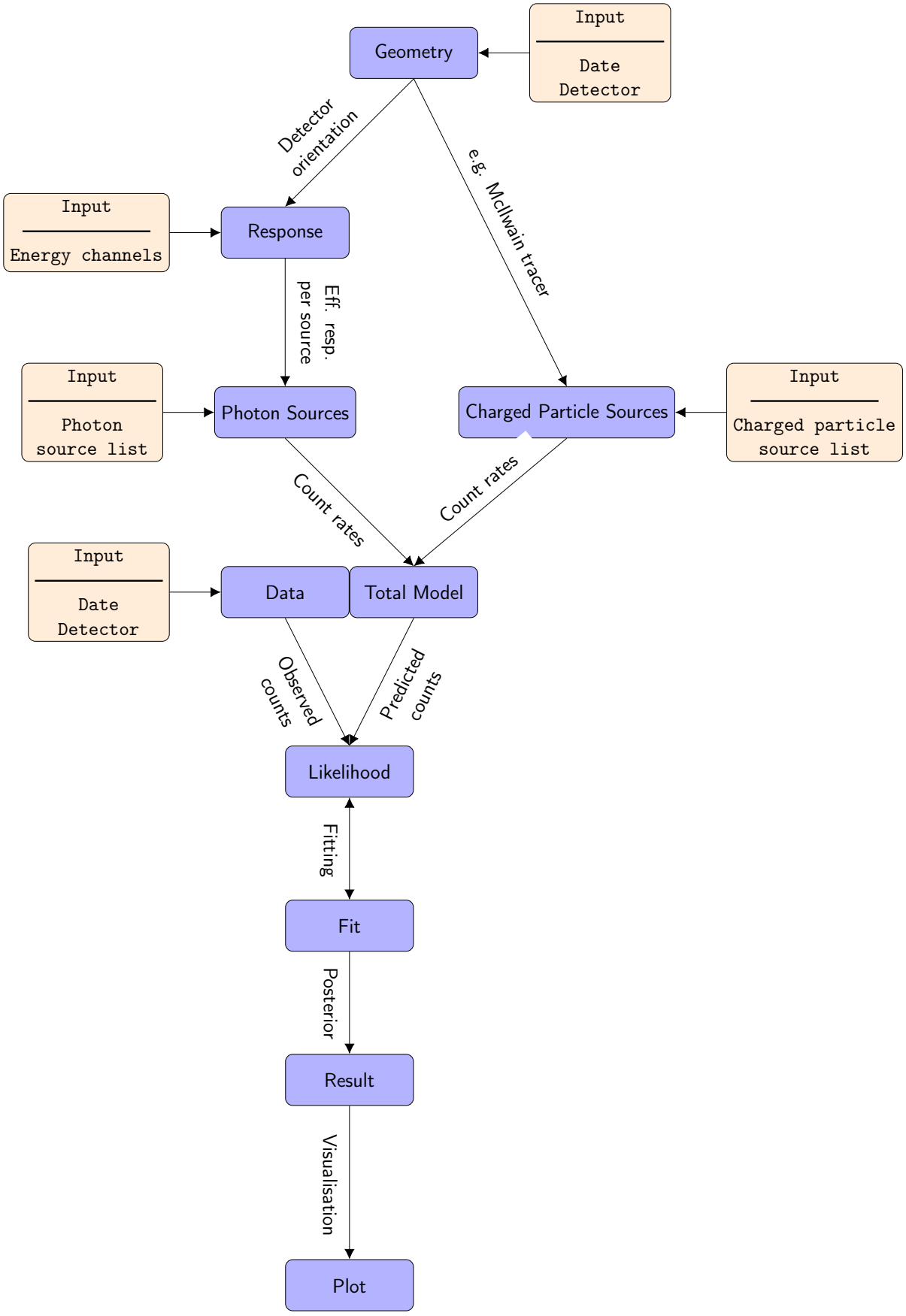

Figure 4.31: Schematic overview of the developed background model package.

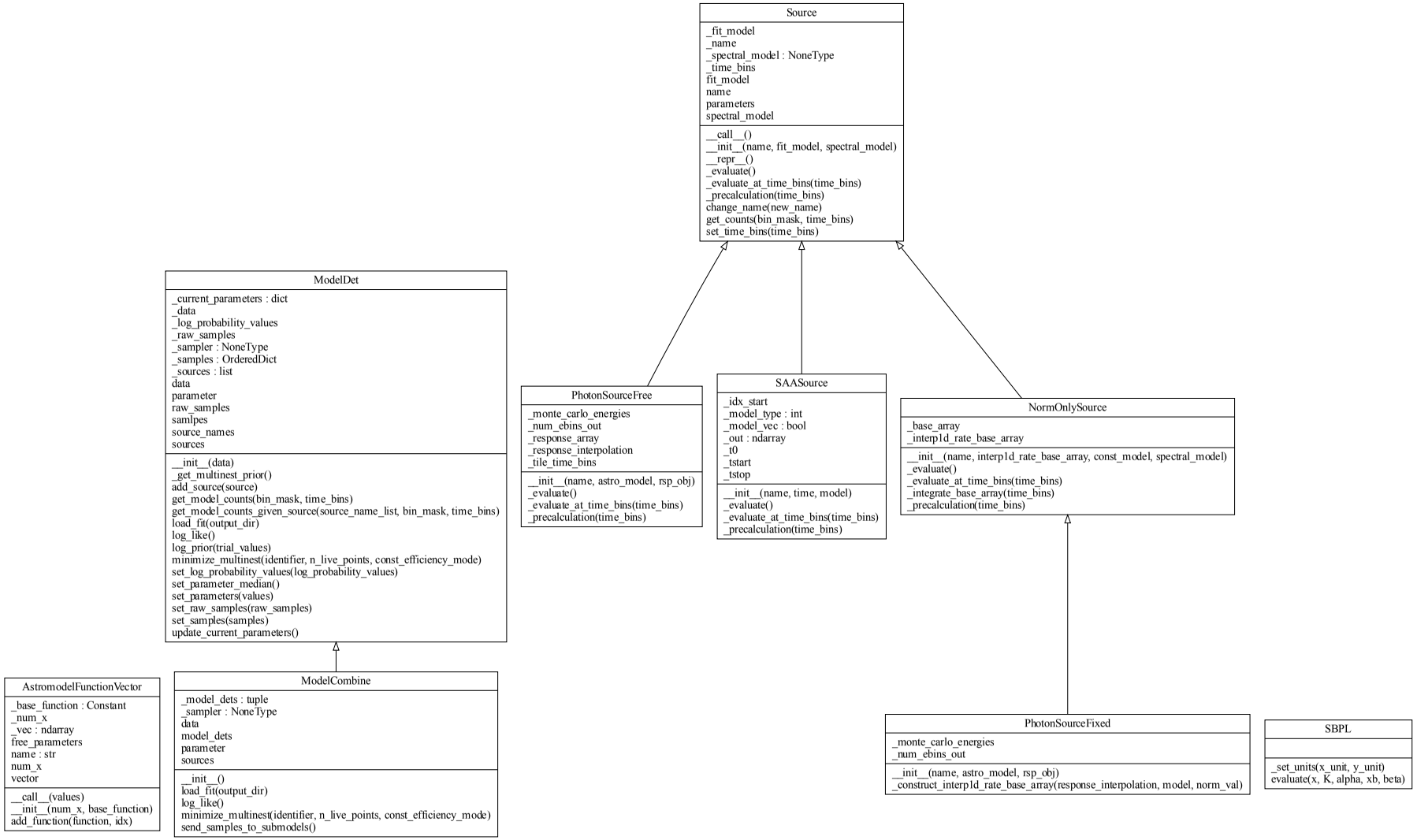

Figure 4.32: Class diagram of the modeling sub-module of the developed background modeling software.

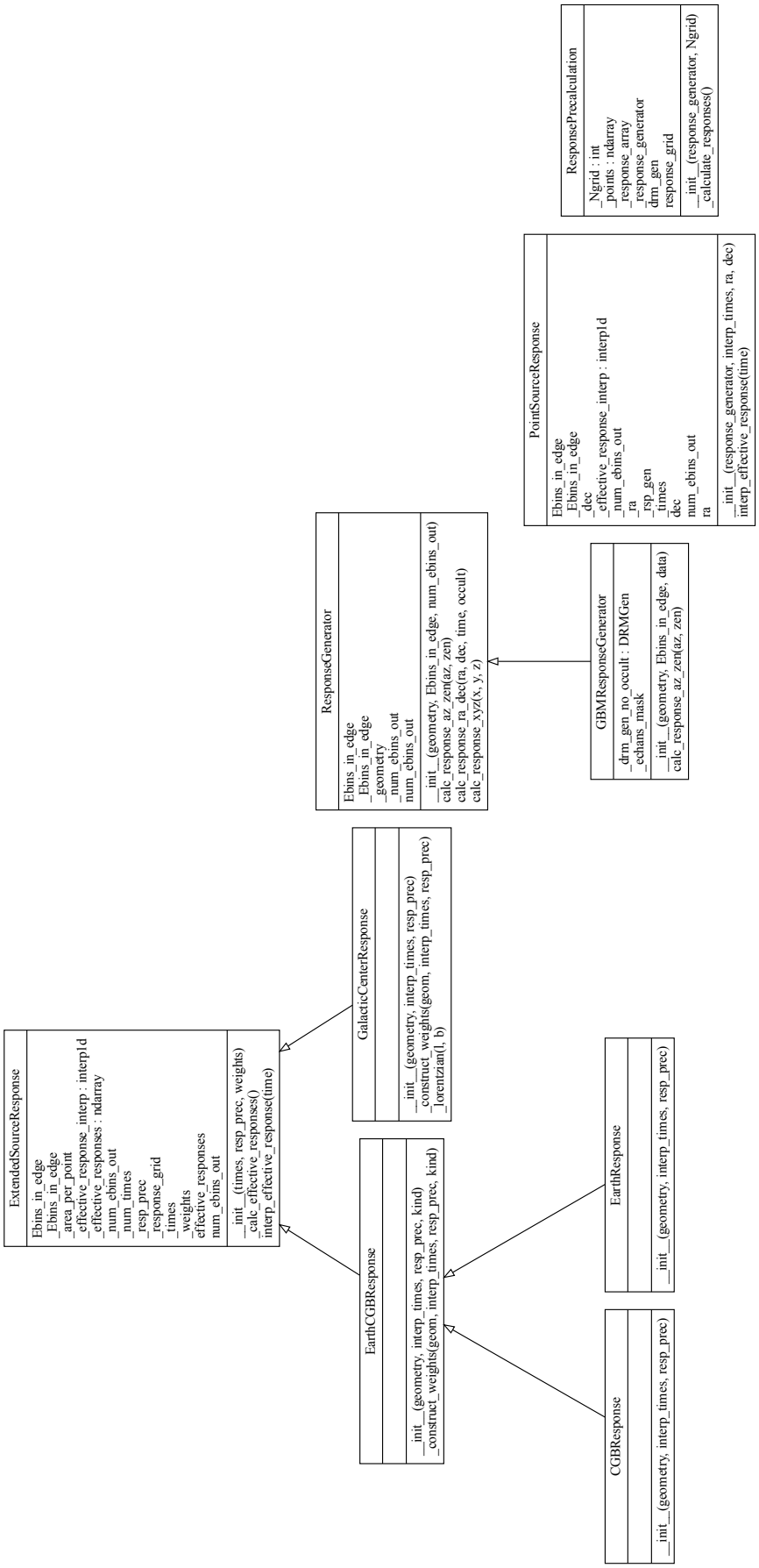

Figure 4.33: Class diagram of the response generation sub-module of the developed background modeling software.

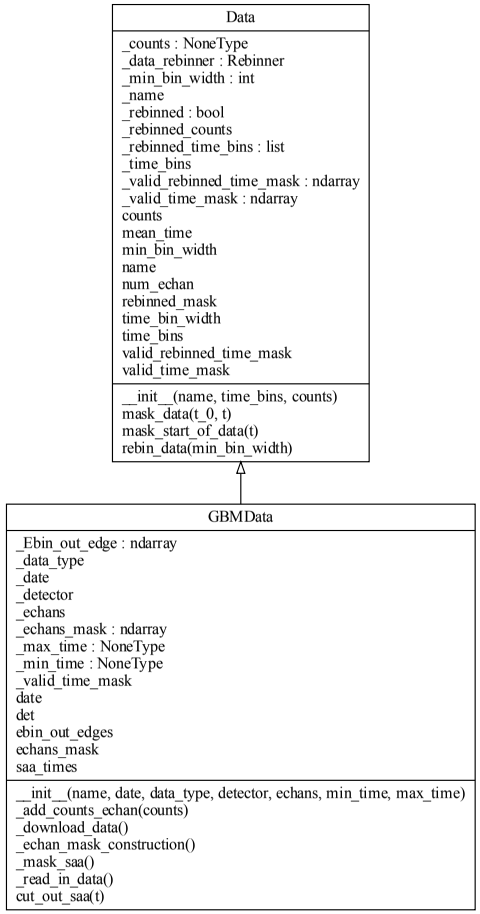

Figure 4.34: Class diagram of the data reduction sub-module of the developed background modeling software.

Figure 4.35: Class diagram of the utilities sub-module of the developed background modeling software.

5 New GRB Analysis technique for INTEGRAL/SPI

Parts of Sec. 5.2 have been already published with me as main author in Biltzinger et al. (2022). Also parts of Sec. 5.3.1 are submitted for publication with me as main author in Biltzinger, Burgess, and Greiner (submitted).

The International Gamma-Ray Astrophysics Laboratory (INTEGRAL) has been launched in 2002 and observes the photon sky with four instruments:

- The Optical Monitoring Camera observing optical light with a V filter (Mas-Hesse et al. 2003).
- The Joint European X-Ray Monitor observing in the energy range 5 - 35 keV (Lund et al. 2003).
- The Imager on Board the INTEGRAL Satellite (IBIS) (Mereghetti et al. 2003c) consisting of two layers: The INTEGRAL Soft Gamma-Ray Imager and the Pixellated Imaging CsI Telescope. It covers an energy range of 15 keV - 1 MeV (175 keV - 10 MeV) for the INTEGRAL Soft Gamma-Ray Imager (Pixellated Imaging CsI Telescope) (Goldwurm et al. 2003).
- The Spectrometer on INTEGRAL (SPI) covering an energy range between 20 keV and 8 MeV (Vedrenne et al. 2003).

SPI is a coded mask instrument that consists of 19 individual semiconductor detectors made of germanium (Ge) and a tungsten mask 1.7 meter above the detector plane. The semiconductor detectors give rise to the excellent energy resolution of 2.5 keV at 1.3 MeV (Vedrenne et al. 2003), which is much better than for example for the Gamma-Ray Burst Monitor (GBM), which has an energy resolution of ≈ 10 % (Meegan et al. 2009). Around the detectors and the tube connecting the detector layer and the mask, Bismuth Germanate (BGO) detectors are mounted, forming the Anti-Coincidence Shield (SPI) (ACS), that reduces the measured background events from cosmic-ray interactions in the Ge detectors. The geometry setup leads to a fully coded Field Of View (FOV) of $\approx 16°$ and a partially coded FOV of $\approx 31°$.

The good energy resolution makes SPI an ideal instrument to measure line features in the gamma-ray energy range, like tracers of stellar nucleosynthesis (e.g. ^{26}Al) (Pleintinger et al. 2019). But its high energy coverage and good energy resolution can also help to better constrain continuum spectra in this energy range. Therefore, SPI is also a valuable Gamma-Ray Burst (GRB) detector and could help determining the true emission processes

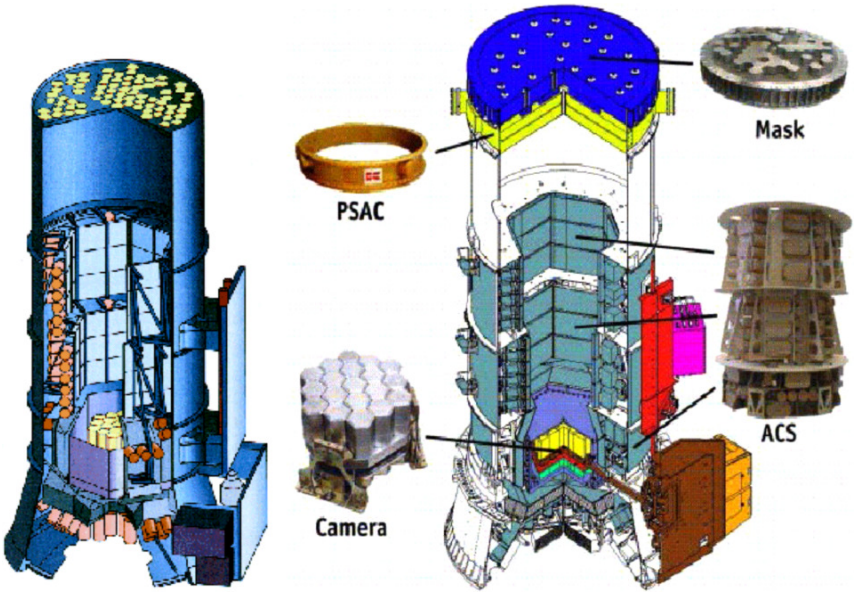

Figure 5.1: Sketch of SPI showing the individual components like the germanium detectors, the mask and the anticoincidence shield. Taken from Diehl et al. (2018).

in GRBs, which is still under debate, with several different physical models competing (see next Sec. 5.1 for a summary).

Due to a lack of physical models that can be fitted directly to data often empirical functions, like the Band function (Band et al. 1993), are used and the parameters of the empirical function fits are used to infer about the underlying physics of the emission. But, in recent years, it has been shown that this approach can be misleading and that it is preferable to fit physical models directly to the data (Burgess 2014; Oganesyan et al. 2019; Burgess et al. 2020). A prominent example of this is the so-called 'line of death' for synchrotron emission (Crider et al. 1996; Preece et al. 1998), which states that synchrotron radiation cannot be the universal emission if fits with a Band function give a low-energy power law slope larger than -2/3. Burgess et al. (2020) showed that this conclusion is flawed and that one can fit GRB spectra well with a physical synchrotron model even though the same spectra violate the line of death if fitted with a Band function. Another proposed proxy for physical emission processes in GRBs is the spectral curvature of empirical model fits to GRB data (Yu et al. 2015; Axelsson and Borgonovo 2015). This too has been shown to be an inaccurate indicator of the emission process (Burgess 2019). Therefore, physical models need to be used directly to deciphering the emission processes occurring in the relativistic outflows of GRBs. In addition the detector properties of instruments like GBM make it difficult to distinguish between different physical models that predict only slightly different curvatures, because of large energy dispersion and coarse energy resolution. These effects imply that several different models can be a good explanation of the data. Here SPI could help, as it should be able to distinguish between different models better due to the much better energy resolution (even though it still suffers from energy dispersion). To fit physical models directly to the SPI data and extract the maximum amount of information from the data in a robust statistical framework I developed a new analysis package for GRBs detected by SPI called `PySPI`, which will be explained and compared to the official

analysis tool Off-line Scientific Analysis (OSA) (Courvoisier et al. 2003) in detail in Sec. 5.2. In Sec. 5.3 I will describe the applications for which I used `PySPI`.

5.1 Gamma-Ray Bursts

GRBs have been first detected in the sixties by the Vela satellites (Klebesadel, Strong, and Olson 1973). They are short but bright transient gamma-ray outbursts with cosmic origin, with typically a highly variable light curve with several peaks and no general structure. One of the first possible explanations were galactic neutron stars, mainly fulled by the claim of detected cyclotron lines in GRB spectra (Murakami et al. 1988). But in the nineties the launch of the Burst And Transient Source Experiment (BATSE) revealed that the spatial distribution of GRBs is isotropic, leading to the conclusion that GRBs must be extra-galactic events (Meegan et al. 1992). This changed the assumed properties of GRBs fundamentally, as they have to be internally much brighter to explain the high observed flux, when they are at extra galactic distances. Today, GRBs have been detected up to extreme distances of up to redshifts ≈ 10 (Salvaterra 2015), which could make GRBs an ideal tool to test cosmology, like it is done with supernova Ia. But GRBs are detected to much higher redshifts than supernova Ia (≈ 2) (Riess et al. 2018), which would allow to constrain cosmology in the early universe. Unfortunately, GRBs can not be standardised at the moment, making it impossible to use them directly for cosmology. Some attempts have been made to standardise GRBs with empirical multi dimensional correlations, e.g. in Dainotti, Sarracino, and Capozziello (2022). But up to now it has not been convincingly shown that this approach works and the contribution of GRBs in a combined analysis with supernova Ia in Dainotti, Sarracino, and Capozziello (2022) shows a negligible influence by the added GRBs. The first step to really standardising GRBs would be to fundamentally understand the emission mechanism, but even today, more than 50 years after the discovery of GRBs, we still do not know what the emission mechanism of GRBs is. But we have observed many interesting features of GRBs in the last 50 years. Besides their extra-galactic origin, and the extreme luminosity following from that fact, we know that the energy spectrum can not be explained by a simple black body, but the spectrum can often be approximated with a Band function (Band et al. 1993), which is a smoothly broken power law and the νF_ν spectrum typically peaks in the keV to MeV region. Also the discovery of afterglows in the nineties (Mészáros and Rees 1997; Vietri 1997) changed our picture of GRBs crucially, as it allowed for the measurements of the redshift and therefore the energetics of GRBs. Table 5.1 summarises different physical implications by the different observational facts.

In the following I will summarise the main theory aspects of GRBs: the progenitors, prompt emission mechanism and afterglow production.

5.1.1 Relativistic Outflow of GRBs

There are at least two arguments that the outflow of GRBs must be ultra-relativistic. One is the compactness problem (Ruderman 1975) and the other the Cavallo-Rees limit

Observation(s) or previous physical implication(s)	**Physical Implication**
Spatially isotropic distribution	Extra-galactic origin
High Flux Extra galactic origin	Extremely luminous
Extremely bright	Compact objects as central engine
Non repeating	Cataclysmic event
Rare	Exotic event
Extremely bright Short time	Energy transform into radiation very efficiently
Variability of light curve	Several emission periods or areas
Not black body spectrum Band function good approximation	Particle acceleration
Extremely bright Not black body spectrum (optically thin) Fast variation of light curve	ultra-relativistic

Table 5.1: Physical implications by the different observational facts.

(Cavallo and Rees 1978).

The compactness problem states, that the expected source size s should be

$$s < c \cdot \delta t. \tag{5.1}$$

The typical time variability δt is on the order of 10 ms for GRBs, which leads to a very small $s < 3000km$. Together with the observed flux, F, and knowing that these sources are at cosmological distances, d, the opacity by pair production can be estimated to be (Piran 2005)

$$\tau = f_p \frac{\sigma_T F d^2}{s^2 m_e c^2} = f_p 10^{13} \left(\frac{F}{10^{-7}\frac{ergs}{cm^2}}\right) \left(\frac{d}{3000Mpc}\right)^2 \left(\frac{\delta t}{10ms}\right)^{-2}. \tag{5.2}$$

Therefore, the source would be optically thick, leading to a thermal black body spectrum. But the spectra of GRBs are known to be non-thermal.

If the outflow is relativistic this problem is avoided, because (1) the photons at the source had a much lower energy of $\frac{E_{obs}}{\Gamma}$, causing the pair production to be less efficient (f_p gets reduced by a factor of $\Gamma^{-2\alpha}$, with α being the high-energy slope of the photon spectrum) and (2) the relativistic effects allows the radius to be Γ^2 times larger, leading to a opacity of

$$\tau = \frac{f_p 10^{13}}{\Gamma^{4+2\alpha}} \left(\frac{F}{10^{-7}\frac{ergs}{cm^2}}\right) \left(\frac{d}{3000Mpc}\right)^2 \left(\frac{\delta t}{10ms}\right)^{-2}, \tag{5.3}$$

which gives an optically thin regime if $\gamma > 100$.

The Cavallo-Rees limit limits the luminosity variation with time that can be generated to be (Cavallo and Rees 1978; Vietri 2008)

$$\frac{\Delta L}{\Delta t} \lessapprox q\frac{2\pi m_p c^4}{3\sigma_T} = 2q10^{42} erg\, s^{-2}. \tag{5.4}$$

This follows from the argument that a source of radius R that contains a density of n baryons and electrons releases an energy of (Vietri 2008)

$$E = q\frac{4\pi}{3}R^3 n m_p c^2, \tag{5.5}$$

where q is the energy extraction coefficient, giving the energy emitted by an electron normalised by the rest energy of a proton and for any non-relativistic case $q \ll 1$. The time photons need to leave the source can be approximated with

$$\Delta t \gtrapprox \frac{R}{c}(1+\tau), \tag{5.6}$$

where τ is the optical depth. Combining Eq. 5.5, 5.6 and using $E = \Delta L \Delta t$ gives

$$\frac{\Delta t}{\Delta L} \gtrapprox \frac{3\sigma_T(1+\tau)^2}{8\pi m_p c^4 q\tau}. \tag{5.7}$$

Inverting this equation and setting $\tau = 1$ (global minimum) gives Eq. 5.4, which is strongly violated by the observed $\frac{\Delta L}{\Delta t} \gtrapprox 10^{51} erg\, s^{-2}$. This simple calculation shows that GRBs can not be Newtonian sources.

Both these arguments need a distance measurement, that is only available since the discovery of afterglows (Mészáros and Rees 1997; Vietri 1997) (see Sec. 5.1.4). Before this the theoretical models had to be derived without this observational constrain or assume it to be true.

5.1.2 Inner Engine

The duration distribution of detected GRBs can be divided into two groups: Short ($\lessapprox$ 2s) and long ($\gtrapprox$ 2s) GRBs (Kouveliotou et al. 1993). While the time durations of the two groups do overlap and no hard cut can be made, it is concluded that there must be at least two different progenitor types to explain the observed duration distribution of GRBs (Kouveliotou et al. 1993).

Long GRBs ($\gtrapprox$ 2s) have been associated with star forming regions in the late nineties (Paczyński 1998a; Paczyński 1998b) and later have been detected in combination with hydrogen poor supernova Ic (Hjorth et al. 2003; Stanek et al. 2003; Cano 2013). This led to the conclusion that the core collapse of fast spinning, massive stars at the end of their lifetime causes long GRBs (Hjorth et al. 2003; Stanek et al. 2003; Levan et al. 2016). It is general consensus that due to the core collapse either a black hole (e.g. Paczynski 1991) or a millisecond magnetar (e.g. Wheeler et al. 2000) is formed. This concept is supported by the observation of the supernovas, that indicate a high mass of the progenitor star and

a compact remnant (e.g. Mazzali et al. 2003).

If a black hole is created, it could either form directly or after some time from the fall back from a supernova that was not energetic enough to eject everything (MacFadyen, Woosley, and Heger 2001). In these scenarios also an accretion disk can form. It was shown by Popham, Woosley, and Fryer (1999) that for an accretion rate of 0.1 $M_{\odot}s^{-1}$ the neutrino creation in this process is strong enough to energise the fireball (see next section) of GRBs (see also Meszaros and Rees 1993; Meszaros, Laguna, and Rees 1993; Rees and Meszaros 1994) by annihilation of these neutrinos via

$$\nu + \bar{\nu} \rightarrow e^{-} + e^{+}. \tag{5.8}$$

Instead of a black hole a highly magnetised rapidly rotating neutron star (Magnetar) could be formed, especially if the progenitor star is already rapidly rotating (Metzger et al. 2011). The spin-down of this magnetar could power the jet by the emission of magnetic dipole radiation, releasing a magnetically dominated relativistic wind (Metzger et al. 2011).

Short GRBs ($\lessapprox$ 2s) are generally believed (Eichler et al. 1989) to be produced by the merger of compact objects (two neutron stars or neutron star with black hole). This has been confirmed in one case, namely GRB170817A, that has been detected by LIGO and VIRGO (Abbott et al. 2017) as gravitational waves from a neutron star merger and by GBM (Goldstein et al. 2017) and the ACS (Savchenko et al. 2017) as short GRB.

Most theoretical models assume that the central engine in this case is again a black hole with an accretion disk, but there are also several papers, motivated by explaining the long lasting x-ray emission of some short GRBs, suggesting that again a magnetar could form as the central engine of short GRBs (e.g. Metzger, Quataert, and Thompson 2008; Bucciantini et al. 2012).

Even though there are only a few remaining possible progenitors of GRBs it has not been possible to self-consistently simulate the whole process from the progenitor to the fully developed jet and GRB emission, yet. Most GRB simulations start either with a launched jet or in recent years with the existence of the central engine (e.g. Bromberg and Tchekhovskoy 2015). Therefore, this part of GRB physics stays a large uncertainty.

5.1.3 Prompt Emission

The prompt emission of GRBs is characterised by the short but very bright emission that is observed first. Its time variability is very high and the light curves are complex. The luminosity during this phase is the largest electromagnetic luminosity that we know in the universe. As we know from observations that the spectrum is non-thermal, there must be one or several processes apart of a classical photosphere. Some options for these high energy non-thermal spectra are: synchrotron, synchrotron self-Compton or dissipative photosphere. All of them are based on generating a population of accelerated non-thermal particles that emit photons, e.g. radiate synchrotron emission in a local or global magnetic field. Therefore, the first theoretical question is how these population of accelerated particles are produced in the GRB outflow. We also know that these processes must hap-

pen several times with different strengths at different times in the outflow, to produce the complex multi-peaked light curves observed. Two general models are the most discussed in the context of GRBs, on which I will focus in the following: the Fireball model and the Poynting flux dominated model.

Fireball

In the classical Fireball model (Cavallo and Rees 1978; Shemi and Piran 1990; Meszaros and Rees 1993; Piran, Shemi, and Narayan 1993; Meszaros, Laguna, and Rees 1993) it is assumed that the energy release of the GRB happens in a small radius of a few km. The derivation of the properties of a simple fireball in the following follows closely the derivation in Vietri (2008).

The fraction of energy to baryonic mass release

$$\eta = \frac{E}{Mc^2}, \tag{5.9}$$

often called dimensionless entropy in the literature (Bégué and Burgess 2016), is much larger than one in case of GRBs. This leads directly to relativistic velocities of the outflow $\gamma \gg 1$. The arguments why it must be relativistic is given in Sec. 5.1.1.

The energy per particle, if there are no photons, can be estimated with

$$E_{\text{particle}} = \eta m_p c^2 >> 1\text{GeV}. \tag{5.10}$$

This energy makes the electrons in this region ultra-relativistic and causes pair production from the interaction of these electrons with protons. The pairs then produce photons via reactions like

$$e^+ + e^- \rightarrow \gamma + \gamma. \tag{5.11}$$

Given an estimated energy release of 10^{51} erg in a radius r_0 of 10 km this leads to an thermalised population of photons with an energy of $\approx$ 1 MeV. Photons with this high energy will create electron-positron pairs and the density of these pairs depends on the temperature and if $kT \lessapprox m_e c^2$ can be expressed with(Shemi and Piran 1990):

$$n_{\text{pair}} = 4.4 \cdot 10^{30} \left(\frac{kT}{m_e c^2}\right)^{1.5} e^{-\frac{m_e c^2}{kT}} cm^{-3}. \tag{5.12}$$

With this we can estimate the opacity due to inverse Compton scattering to be

$$\tau \approx n_{\text{pair}} \sigma_T r_0 \approx 10^{12}. \tag{5.13}$$

This shows that the plasma is optically thick and that the photons and electrons are strongly coupled, which makes the whole process adiabatic, as the majority of photons can not escape the region.

The strong coupling of photons and electrons as well as of electrons and protons via Coulomb interaction, causes the population of the different particles to thermalise to a

common temperature T. The energy density of the photons is

$$e_{ph} \propto T^4, \tag{5.14}$$

whereas, the kinetic energy density of the pairs is

$$e_{\mathrm{pair}} = n_{\mathrm{pair}} kT. \tag{5.15}$$

With Eq. 5.12 we can see that $e_{ph} \gg e_{\mathrm{pair}}$. Therefore, the plasma energy density is dominated by the photons, that can not escape from the plasma due to the huge optical depth. Because the whole process is adiabatic, this leads to an equation of state close to a perfect photon gas with the pressure $p = \frac{e_{ph}}{3}$. Assuming a spherical symmetric explosion for simplicity here, we can characterise the behaviour of the expansion. By using the determined pressure of the plasma with the equations of relativistic hydrodynamics we can calculate the following expressions (Piran, Shemi, and Narayan 1993; Kobayashi, Piran, and Sari 1999):

$$r^2(nm_p + \frac{4e}{3})\gamma^2 = \mathrm{const} \tag{5.16}$$

$$r^2 e_{ph}^{0.75}\gamma = \mathrm{const} \tag{5.17}$$

$$r^2 n\gamma = \mathrm{const} \tag{5.18}$$

Which leads for $e >> nm_p$, which is the case at early times since $\eta >> 1$:

$$\gamma \propto r \tag{5.19}$$

$$n \propto r^{-3} \tag{5.20}$$

$$e_{ph} \propto r^{-4} \tag{5.21}$$

This shows that the outflow is accelerated during the expansion in a classical Fireball.

During this expansion the energy density decreases with r^{-4} and the baryon density only with r^{-3} such that the assumption $e >> nm_p$ is not valid anymore after some time. It will eventually reach the phase when the energy in baryons exceeds the energy density $nm_p >> e$, which leads to

$$\gamma = \mathrm{const} \tag{5.22}$$

$$n \propto r^{-2} \tag{5.23}$$

$$e_{ph} \propto r^{-\frac{8}{3}}. \tag{5.24}$$

Therefore, after the accelerating expansion period of the Fireball there will be a stable expansion phase with a constant γ. When this happens, the Fireball consists of different pulse of energy with a frozen radial profile, propagating with very high Lorentz factors (Kobayashi, Piran, and Sari 1999).

This can not happen later than when the whole energy release has been converted to

kinetic energy, which happens when $\gamma Mc^2 = E$ giving, with Eq. 5.9, an upper limit for the maximum radius of the acceleration phase of

$$r_{max} = \eta r_0. \tag{5.25}$$

But it can happen sooner, when the photons decouple from the plasma because $\tau \lessapprox 1$ at some point. The exact moment when this happens depends on the composition of the outflow.

When the electron population is dominated by pair production the opacity will drop significantly when the temperature reaches $kT \approx 15keV$, because the pairs will disappear at this temperature. Using Eq. 5.21 gives that $T_{pair} = T_0 \frac{r_0}{r_{pair}}$ leading to $r_{pair} = r_0 \frac{T_0}{T_{pair}}$. Therefore, the maximal Lorentz factor is given by

$$\gamma_{pair} \approx 2400\gamma_0 \left(\frac{E}{10^{51}erg}\right)^{0.25} \left(\frac{10^6 cm}{r_0}\right)^{0.75}. \tag{5.26}$$

When on the other side many electrons are associated to baryons, they will not disappear when the temperature drops below 15 keV, but the density will decrease with $\propto r^{-3}$. The opacity for a radially outwards propagating photons is then given by

$$\tau = n_0 \left(\frac{r_0}{r}\right)^3 \sigma_T r = \frac{3M}{4\pi m_p r_0^3} \left(\frac{r_0}{r}\right)^3 \sigma_T r. \tag{5.27}$$

And the radius for which $\tau = 1$ is given by (using Eq. 5.9)

$$r_{thin} = \left(\frac{3E\sigma_T}{4\pi m_p c^2 \eta}\right)^{0.5}. \tag{5.28}$$

The behaviour of the Fireball is defined by η, because η defines the order or the different radii discussed above. For this we define these two quantities of η:

$$\eta_{pair} = \frac{3E\sigma_T}{4\pi m_p c^2 \gamma_{pair}^2} \tag{5.29}$$

$$\eta_{thin} = \left(\frac{3E\sigma_T}{4\pi m_p c^2 r_0^2}\right)^{\frac{1}{3}} \tag{5.30}$$

If $\eta > \eta_{pair}$ the plasma gets optically thin before all energy is converted into kinetic energy ($r_{thin} < r_{max}$), therefore a part of the initial energy will get radiated as black body radiation in the moment of photon decoupling. As we do not observe thermal spectra this can not be the case in most GRB outflows. r_{thin} must be at least close to r_{max}, to not emit too much energy as thermal spectrum. If $\eta > \eta_{pair}$ the contribution from the electrons associated to baryons stops before the contribution by pairs does ($r_{thin} < r_{pair}$). Therefore, in this case the Fireball would keep accelerating to r_{pair}. The maximal possible Lorentz factor can be reached when $r_{thin} = r_{max}$ giving $\gamma = \eta_{thin}$ (Vietri 2008).

These simple analytical calculations show that a Fireball with $\eta \gg 1$ will lead to an expanding shell with relativistic speed. If the central engine is emitting the energy not just at one time but the energy injection varies with time, like to be expected for an accreting

black hole for example, this will lead to different shells propagating with different Lorentz factors. These shells will collide and create (internal) shocks, which accelerate electrons to very high energies and create high energy synchrotron radiation. Daigne and Mochkovitch (1998) have shown that a mechanism like this, with many different shell collisions in a GRB outflow, can produce light curves and energy spectra with similar properties like observed. The shells will merge and the Lorentz factor and internal energy of the new shell is defined by energy and momentum conservation (Kobayashi and Sari 2001):

$$\gamma \approx \sqrt{\frac{m1\gamma_1 + m_2\gamma_2}{\frac{m1}{\gamma_1} + \frac{m2}{\gamma_2}}} \tag{5.31}$$

$$E_{int} = m_1(\gamma_1 - \gamma_2) + m_2(\gamma_2 - \gamma_1) \tag{5.32}$$

The internal energy will be in the form of two relativistic shocks: A forward and a reverse shock (Kobayashi and Sari 2001). Shocks form if a large amount of energy is released in a small volume and the Hugoniot shock jump conditions for relativistic shocks in non-relativistic un-shocked plasma, read (Blandford and McKee 1976; Piran 2005)

$$n_2 = 4\Gamma^2 n_1 \tag{5.33}$$

$$e_2 = 4\Gamma^2 n_1 m_p c^2 \tag{5.34}$$

$$\Gamma^2_{\rm shock} = 2\Gamma^2, \tag{5.35}$$

with $n_{1,2}$ ($e_{1,2}$) the number (energy) density in front and behind of the shock, Γ ($\Gamma_{\rm shock}$) the Lorentz factor of the shocked plasma (shock) measured from in the reference frame of the un-shocked gas (Blandford and McKee 1976). Therefore the pressure of the shocked plasma is of the order $\frac{e_2}{3} \approx \Gamma^2 n_1 m_p c^2$. Also the magnetic field is amplified by

$$B_{||,2} = \Gamma B_{||,1}. \tag{5.36}$$

Using the fractions ϵ_e and ϵ_B, that summarise the (unknown) fraction of the energy density in electrons and in the magnetic field gives

$$e_e = \epsilon_e e_2 = 4\epsilon_e \Gamma^2 n_1 m_p c^2 \tag{5.37}$$

$$e_B = \frac{B^2}{8\pi} = \epsilon_B e_2 = 4\epsilon_B \Gamma^2 n_1 m_p c^2. \tag{5.38}$$

$$\tag{5.39}$$

e_e is the energy that will be used for the acceleration of electrons to relativistic velocities due to the shell collision. The main mechanism that accelerates the electrons is diffusive shock acceleration (Baring 1997; Piran 2005) that occurs when the electrons get bounced between the two sides of the shock. This process will be dominated by first-order Fermi acceleration, unless when the shock speed is low and close to the Alfven speed $v_A = \frac{B}{4\pi\rho}$ and second-order Fermi gets important (Baring 1997).

The average energy gain per shock crossing cycle and the probability to escape from the acceleration cycle after each cycle gives a power-law spectrum, with an index p, for the population of accelerated electrons:

$$N_e(E)dE \propto E^{-p}dE. \tag{5.40}$$

These electrons cool in the local magnetic field from the shell collision or a global magnetic field of the GRB outflow by synchrotron radiation. This can explain the observed non-thermal spectrum.

To calculate the synchrotron radiation spectrum it is assumed that a power-law electron distribution has formed with a minimal Lorentz factor

$$N_e(\gamma) \propto \begin{cases} \gamma^{-p}, & \text{if } \gamma > \gamma_{min} \\ 0, & \text{else} \end{cases} \tag{5.41}$$

The synchrotron spectrum of an electron with Lorentz factor γ can be approximated with a power law $F_\nu \propto \nu^{\frac{1}{3}}$ up to the energy flux peak $\nu_{\rm peak}(\gamma)$ and an exponential decay for larger ν (Piran 2005). The typical observed photon frequency (synchrotron frequency) is given by

$$\nu_{\rm peak}(\gamma) = \frac{q_e B}{2\pi m_e c}\gamma^2\Gamma, \tag{5.42}$$

where the factor of Γ is due to the blue-shift of the photons as the emitting shell is moving towards us. For electrons that cool rapidly (on a time scale smaller than the hydrodynamic time scale) the time integrated spectrum has to be accounted for, resulting in an $F_\nu \propto \nu^{-\frac{1}{2}}$ spectrum in the range $\nu_{\rm peak}(\gamma_{cool}) < \nu < \nu_{\rm peak}(\gamma)$, where γ_{cool} defines the minimal energy an electron needs to cool on the hydrodynamic time scale (Rybicki and Lightman 1985). The resulting power spectrum can be calculated with

$$F_\nu = \int_{\gamma_{min}}^{\infty} N_e(\gamma)P_\nu(\gamma)\mathrm{d}\gamma, \tag{5.43}$$

where $P_\nu(\gamma)$ is the power emitted by electrons with Lorentz factor γ with the frequency ν. For small frequencies with $\nu < \nu_{\rm peak}(min(\gamma_{min}, \gamma_{cool}))$ the spectrum is always a super position of the different tails with $F_\nu \propto \nu^{\frac{1}{3}}$. Very high energetic photons (large γ) on the other hand will decay rapidly and deposit basically all their energy at $\nu_{\rm peak}(\gamma)$. As the electron energy spectra is a powerlaw with index $-p$ and the synchrotron frequency is $\propto \gamma^2$, the energy flux spectrum by these high energy electrons is given by $F_\nu \propto \gamma^{-p} \propto \nu^{-\frac{p}{2}}$. In the intermediate range between the low and the high energy end, the spectrum can have different shapes depending on the physical properties of the outflow. To characterise this the cooling frequency $\nu_{\rm cool}$ is used. $\nu_{\rm cool}$ gives the minimal frequency such that the electrons with this synchrotron frequency (energy of these electrons denoted by γ_{cool}) cool on the hydrodynamic time scale (and therefore rapidly). If $\gamma_{\rm cool} < \gamma_{min}$ all accelerated electrons cool rapidly. In this case, the frequency range $\nu_{\rm peak}(\gamma_{cool}) < \nu < \nu_{\rm peak}(\gamma_{min})$ is populated by the time integrated radiation of all electrons with $\propto \nu^{-\frac{1}{2}}$. This is called fast cooling and is summarised in Eq. 5.44.

$$F_\nu \propto \begin{cases} \nu^{\frac{1}{3}}, & \nu < \nu(\gamma_{cool}) \\ \nu^{-\frac{1}{2}}, & \nu(\gamma_{cool}) < \nu < \nu(\gamma_{min}) \\ \nu^{-\frac{p}{2}}, & \nu(\gamma_{min}) < \nu, \end{cases} \tag{5.44}$$

Slow cooling is defined as the other case with $\gamma_{\rm cool} > \gamma_{min}$. In this case, not all electrons will cool rapidly (only $\gamma > \gamma_{cool}$), alternating the resulting spectrum. The $\propto \nu^{\frac{1}{3}}$ part of the spectrum extends up to $\nu_{\rm peak}(\gamma_{min})$, while in the frequency range $\nu_{\rm peak}(\gamma_{min}) < \nu < \nu_{\rm peak}(\gamma_{cool})$ the spectrum can be calculated with Eq. 5.43. Using the simplification that all the power will be emitted at the characteristic peak energy ($P_\nu(\gamma) \propto \gamma^2 \delta(\nu - \nu_{\rm peak}(\gamma))$) and that $N_e(\gamma) \propto \gamma^{-p}$ results in $F_\nu \propto \nu^{-\frac{p-1}{2}}$ (Rybicki and Lightman 1985):

$$F_\nu \propto \begin{cases} \nu^{\frac{1}{3}}, & \nu < \nu(\gamma_{min}) \\ \nu^{-\frac{p-1}{2}}, & \nu(\gamma_{min}) < \nu < \nu(\gamma_{cool}) \\ \nu^{-\frac{p}{2}}, & \nu(\gamma_{cool}) < \nu, \end{cases} \tag{5.45}$$

These derivations include several simplifications, like an isotropic pitch angle distribution of the electrons and approximated single electron synchrotron emission spectra. The here derived spectra (see Fig. 5.2) are therefore only approximations of the true spectra.

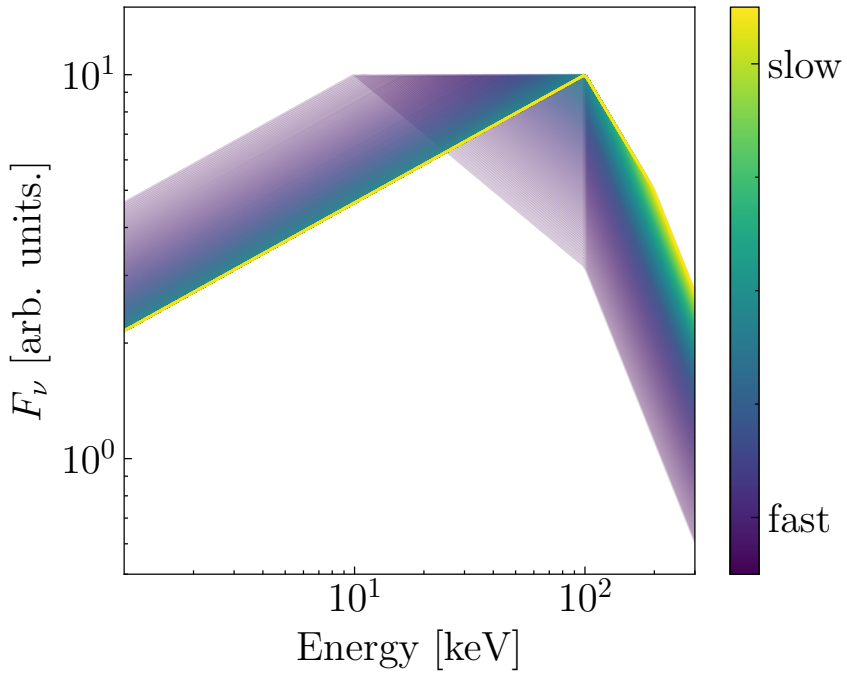

Figure 5.2: Simplified example synchrotron spectrum for different ratios of γ_{cool} and γ_{min} as described in Eq. 5.44 and 5.45. For observations the much stronger second break in the fast cooling regime is especially important.

The position of the shell collisions can vary and can either happen well below, close to or well above the photosphere ($\tau = 1$). The position will change the observed spectrum strongly. If the shell collision is well above the photosphere the produced synchrotron radiation will escape freely and we will observe a perfect synchrotron spectrum. When

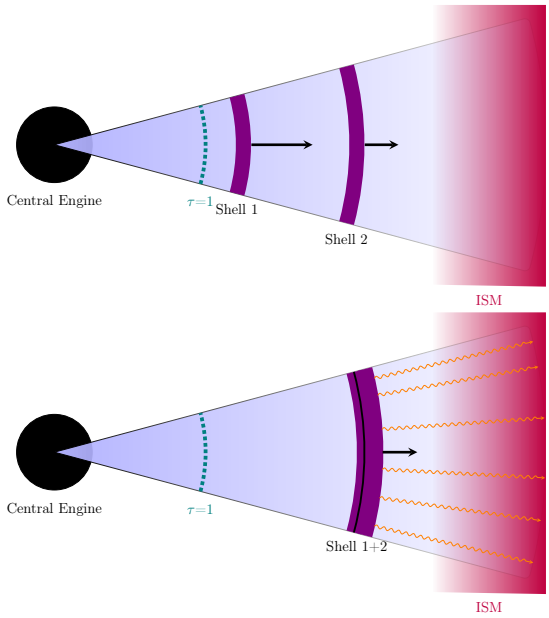

Figure 5.3: Sketch of two shells propagating with different speed (upper sketch) and colliding (lower sketch) in the optical thin regime of the outflow. Most of the produced radiation in the collision can freely escape to infinity (observer), producing a spectra depending on the physical quantities in the shell collision (e.g. synchrotron).

the collision takes place well below the photosphere the radiation can not escape and the photon spectrum will thermalise again before escaping at the photosphere. Therefore, the spectrum will be thermal in this case. A mixture of these two cases will occur if the collision is close to the photosphere, as part of the emitted synchrotron spectrum will thermalise but the optical depth is not large enough to create a perfect black body spectrum. Sketches for the setup of these cases are given in Fig. 5.3, 5.4 and 5.5.

Poynting flux dominated

Simulations by Bromberg and Tchekhovskoy (2015) have shown that a Poynting flux dominated jet (Vietri and Stella 1998; Lee, Wijers, and Brown 2000; Drenkhahn and Spruit 2002) can be launched self-consistently from the rotation of a strongly magnetised compact object. In this model the dissipation of the magnetic field energy into heating the plasma is due to magnetic reconnection. It results in an efficient production of synchrotron emission, that could explain the observed prompt emission. Great improvements in Magnetohydrodynamic (MHD) and Particle-In-Cells (PIC) simulations of these kind of models in the last few years have increased their plausibility significantly.

The magnetisation of the jet is defined by

$$\sigma = \frac{L_{\text{poynting}}}{L_{\text{kinetic}}}. \tag{5.46}$$

For a Poynting flux dominated jet we have $\sigma \gg 1$. From analytical, idealised, MHD it can be shown that, like in the Fireball model, the outflow will first accelerate and then reach a freely expanding phase with constant Lorentz factor (Drenkhahn 2002). The photosphere

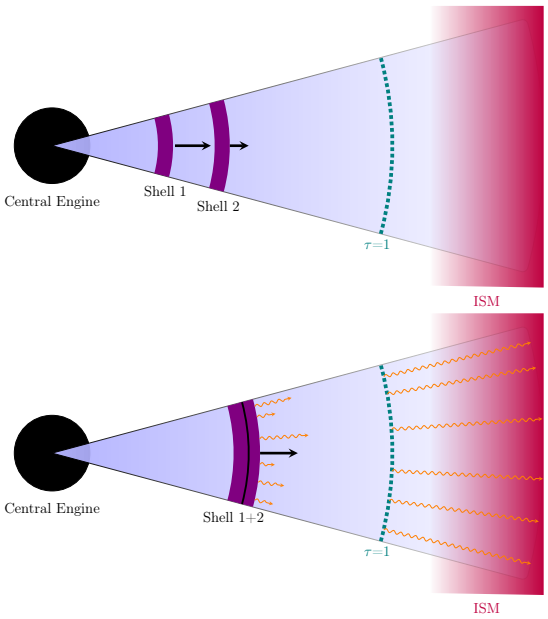

Figure 5.4: Sketch of two shells propagating with different speed (upper sketch) and colliding (lower sketch) deep in the optical thick regime of the outflow. Most of the produced radiation in the collision does not escape and gets thermalised before reaching the photosphere (τ=1). The resulting spectrum will be a black body spectrum.

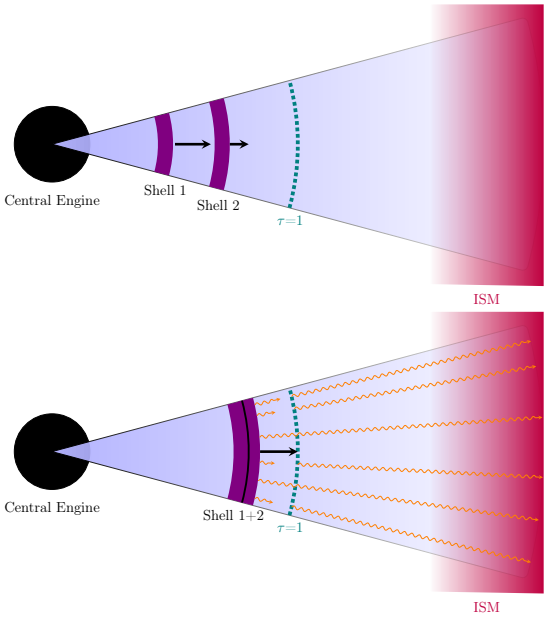

Figure 5.5: Sketch of two shells propagating with different speed (upper sketch) and colliding (lower sketch) in the optical thick regime but close to the photosphere of the outflow. Some of produced radiation in the collision can escape with no or only very few scatterings but the rest gets thermalised before reaching the photosphere (τ=1). The resulting spectrum will be a modified black body spectrum.

radius is of the order (Drenkhahn and Spruit 2002)

$$r_{ph} \approx 10^{11} cm \left(\frac{L}{10^{50}}\right)^{\frac{3}{5}} \left(\frac{\sigma_0}{100}\right)^{-\frac{3}{2}}, \tag{5.47}$$

where σ_0 is the initial magnetisation. The energy dissipation that can power the prompt emission has to be above the photosphere. It can be calculated that for a initial magnetisation $\sigma_0 \gtrapprox 100$ at least some part of the magnetic energy will be dissipated above the photosphere and could therefore explain the observed prompt emission (Drenkhahn 2002).

The magnetic energy is dissipated by magnetic reconnection in reconnection layers (Giannios and Spruit 2005). During this process the released energy is used to accelerate electrons to relativistic energies with a power law distribution (Comisso and Sironi 2019). These electrons will cool rapidly in the strong magnetic field. As the cooling time is very short compared to the reconnection time, it is not a valid assumption that the power law of accelerated electrons is created ones and just cools after its creation (like it is often done in Fireball models), but that the electron distribution is an equilibrium between the cooling and the heating by reconnection (Giannios and Spruit 2005). Also PIC simulations by Comisso and Sironi (2019) imply that the pitch angle distribution of electron velocity and magnetic field line directions are not isotropic and that the anisotropicity depends on the energy of the electrons. This would effect the radiated synchrotron spectrum and is currently ignored in the analysis of GRB spectra.

5.1.4 Afterglow

When the ejected matter swept up enough interstellar material (see Fig. 5.6), the expansion can not continue with a constant Lorentz factor but slows down creating an external shock. This dissipates some of the outflow's energy into high energy electrons that then emit synchrotron radiation (Mészáros and Rees 1997; Vietri 1997; Sari, Piran, and Narayan 1998).

The significant de-acceleration will start when enough matter has been swept up, which is the case at (Sari 1997; Chiang and Dermer 1999; Bégué and Burgess 2016)

$$r_d = 5.4 \left(1 - \frac{k}{3}\right)^{\frac{1}{3}} E_{0,54}^{\frac{1}{3}} n_{0,2}^{-\frac{1}{3}} \Gamma_{0,2}^{-\frac{2}{3}}, \tag{5.48}$$

where $E_{0,54}$ is the energy of the GRB in units of $10^{54} erg$, $n_{0,2}$ the circum-stellar medium density in units of $10^2 cm^{-3}$, $\Gamma_{0,2}$ the Lorentz factor after the acceleration phase in units of 10^2 and k defines the radial density profile of the circum-stellar medium

$$n(r) = n_0 r^{-k}. \tag{5.49}$$

Therefore, k=2 for a stellar wind and k=0 for a constant circum-stellar medium. The Lorentz factor of the outflow will then decrease for $r > r_d$ with

$$\Gamma(r) = \Gamma_0 r^{-g}. \tag{5.50}$$

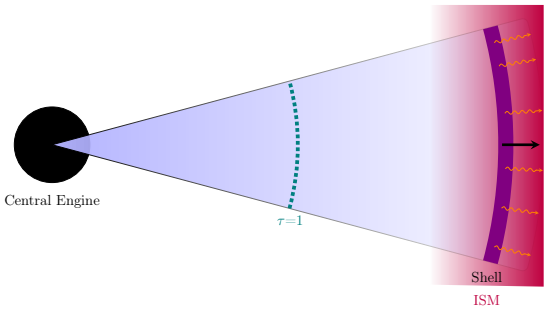

Figure 5.6: Sketch of an external shock produced form the interaction of the outflow and the ISM. This happens well above the photosphere (τ=1), therefore the radiation can escape freely. This continuous movement of the shell through the ISM produces the slowly decaying afterglow.

The value of g is determined by the properties of the circum-stellar medium and expansion regime. Part of the released energy will be dissipated in the shock and accelerate high energy electrons, creating synchrotron emission in a second step (Bégué and Burgess 2016).

This leads to a long lasting emission, with decreasing luminosity and peak energy over time, which can be observed in X-rays or longer wavelength.

External shocks have also been proposed as model for the prompt emission, but these models have problems explaining the fast variations in most GRB light curves (e.g. Kobayashi, Piran, and Sari 1997). Nevertheless, they could still be a viable model for long single-pulsed GRBs, like shown in Burgess et al. (2016). External shocks can dominate the prompt emission if η (see Eq. 5.9) is in an intermediate range, such that the photosphere is not reached during the accelerating phase, when much energy of the outflow plasma is still in the form of thermal photons, but η is large enough to create the early onset of the radiation (Bégué and Burgess 2016).

The afterglow in the optical is especially interesting, as it enables the determination of the distance of the GRBs. Absorption of the optical radiation in the close surrounding of the GRB imprints characteristic absorption features in the spectrum, that get red-shifted due to the large distance. By modeling the absorption in the optical spectrum the redshift can be recovered, giving the distance for an assumed cosmological model. This is also important for the prompt emission, as it constrains the energetics (Kulkarni et al. 1999; Greiner et al. 2009).

5.2 New Analysis technique for INTEGRAL/SPI

All instruments, especially gamma-ray instruments, suffer from energy dispersion and finite energy resolution. The information about this is encoded in the response matrix, which gives the probability that a photon with a certain energy and starting position on the sky will be detected in one of the electronic channels of the detector. These response matrices are usually not invertible, and therefore we have to forward folded (see Sec. 2) the photon spectrum through the response matrix into the data space of the detected counts and compare them, using the correct likelihood. This is a general statement that also applies

to SPI. In the following subsection, I will first cover some general concepts for SPI and then the standard analysis method within the standard analysis tool OSA and the newly developed `PySPI`. The main difference is that the method in `PySPI` is a full forward-folding method, fulfilling the statement above, which results in maximising the information we can get from the data in the analysis.

5.2.1 Response

As described in Sec. 2.2, the response connects the photon spectrum to an expected detected count spectrum for a given source position. The response encapsulates all the information about the probability of a photon with a certain energy and incoming direction to be detected in a certain electronic channel of the detector. This includes, for example, information about partial energy deposition of the photon in a crystal and the process that transforms the deposited energy into the electronic signal that is measured. For SPI, the response is split into two components, namely the Image Response Functions (IRFs) and the Redistribution Matrix Files (RMFs). The IRFs contain information about the total effective area over which a photon can interact with the detector and the RMFs contain information about the probability in which electronic channel the photon will be measured. For SPI, both these components were derived with extensive Geometry and Tracking (Geant) simulations (Sturner et al. 2003). The SPI IRF files give the total effective area for three different interaction types: (1) photo peak events (all energy deposited in the Ge crystal); (2) non-photo-peak events that first interact in the Ge crystal, and (3) non-photo-peak events that first interact in passive material. These effective areas were calculated for 51 photon energies and on a 0.5 degree grid out to 23.5 degrees from the on-axis direction. For each of the three interaction types, there is one RMF to define the shape of the redistributed spectra, assuming that this shape does not depend on the detector or the incident angles of the photons. The procedure used to construct the response includes several simplifications to keep the computational costs and storage space at manageable levels (Sturner et al. 2003). Re-simulating the response without these simplifications could improve the scientific output of SPI, but would be computationally very expensive, even today.

To test how much improvement is possible I simulated the response with the software Geant4_SPI (Chauvin 2021) that does not use many of the simplifications in Sturner et al. (2003). It is a full Geant simulation, simulating the deposited energy in the different SPI detectors. It does not include a simulation of the electronics, that transform the deposited energy into energy channels, which is important, especially for the energy resolution. I simulated the response for one position (position of GRB120711A) for 590 photon energies and with high statistics (total of 10^{12} photons), to generate a very fine response. This took $\approx$ 2 million CPU hours. A comparison of the newly simulated response to the official response simulations for three photon energies and one SPI detector is shown in Fig. 5.7. The new simulations recover the same features, but with much better resolution. Also the photo peak response for the new response simulation agree with the official response files (see Fig. 5.8). An application of this newly simulated response in combination with `PySPI`

is given in Sec. 5.3.5.

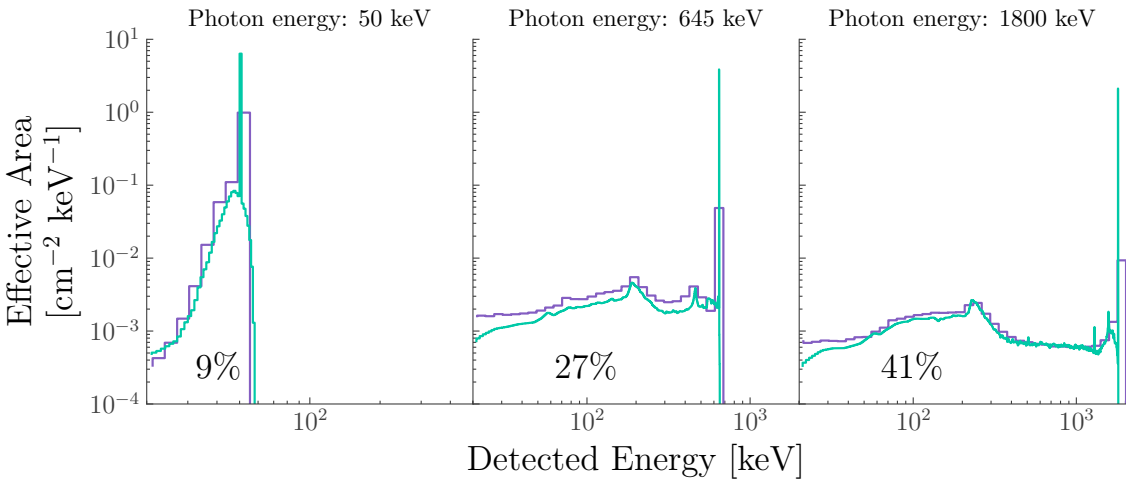

Figure 5.7: Response for three different photon energies (50, 645 and 1800 keV) coming from the position of GRB120711A. The newly simulated response has the same features as the official responses, but can resolve the features like photo peak and Compton edges better. The number in each plot gives the probability for the different photon energies, to only deposit part of its energy in the crystal (non-photopeak events).

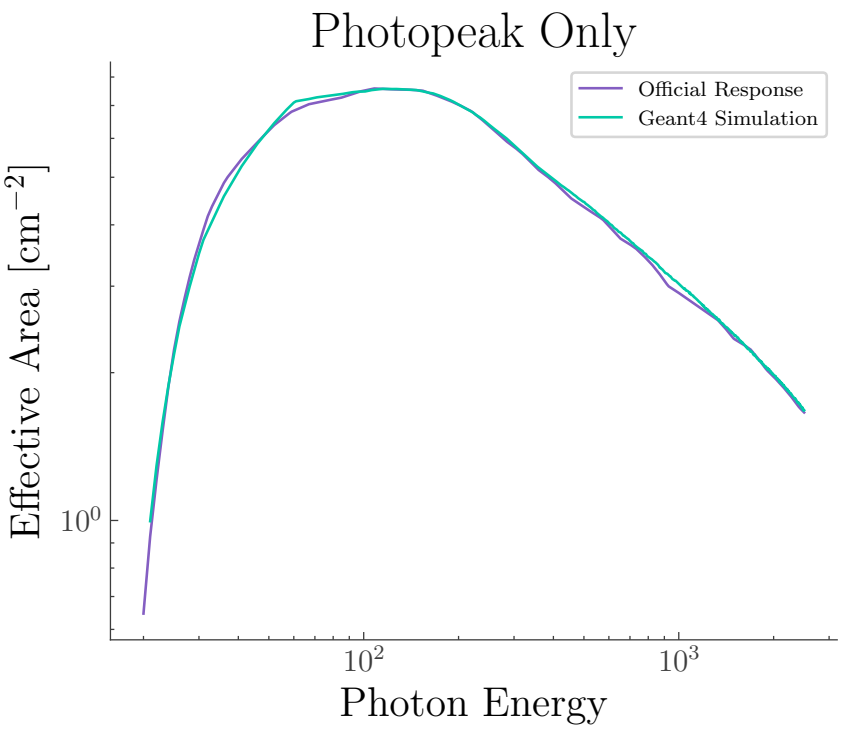

Figure 5.8: Comparison of the total photo peak effective area of the newly simulated response and the official response, showing that the two match perfectly.

It is important to realise that even though the energy resolution of SPI is very good there is a huge energy dispersion, leading to $\gtrapprox s40$ % of the photons with energy > 1 MeV not being detected in the photo peak. With other words, SPI is very good at measuring the deposited energy in the germanium crystals but often not all the energy of the photons

is deposited in the crystal, especially for photons with large energies.

Re-simulating the whole response with modern computer clusters would improve the scientific output of the SPI mission significantly, but would need a lot of work, to optimise the Geant code and getting the many CPU hours needed, as well as including a simulation of the electronics.

5.2.2 Electronic noise

According to Roques and Jourdain (2019), there are spurious events in the SPI data, which are photons with small energy (< 100 keV) that get detected at a higher energy due to saturation of the Analog Front-End Electronics (AFEE) by previous high-energy deposition. It is also known that these spurious events do not show up in events that also have a detection in the Pulse Shape Discriminator (PSD) electronics.

The PSD trigger has been originally planed to reduce the instrumental background, because the detected electronic pulse of gamma-ray interactions in the crystal is different to β-decays due to cosmic ray bombardment, as the latter should deposit the energy in a much smaller volume than the gamma-ray interaction (Vedrenne et al. 2003). Unfortunately, the first in-flight performances showed that the signals of the instrumental background and the sources are too similar and the PSD is not able to efficiently discriminate between the two. Therefore, the PSD is not used for its original purpose (Roques et al. 2003).

The PSD electronics have a low-energy threshold of $\approx$450 keV and a high-energy threshold of $\approx$2700 keV (the exact values have been changed a few times during the mission (Roques and Jourdain 2019)). Therefore, only events that deposit more than this low-energy threshold in the germanium crystal can trigger this electronic chain, which eliminates the < 100 keV events that are detected at the wrong energies by the AFEE.

In Fig. 5.9, the feature at 1.5 MeV is nicely visible in the non-PSD events but is missing in the PSD events.

Even though this problem is most significant in the area around 1.5 MeV, it is also important at lower energies down to 400 keV. The electronic noise is not stable and depends on the signal strength (Roques and Jourdain 2019), and therefore it can not be included in the response and has to be treated differently.

5.2.3 `PySPI`

To fit SPI GRB data, I developed a new Python package `PySPI` (Biltzinger, Burgess, and Siegert 2022). In the following, I summarise the main points of GRB analysis within `PySPI`.

Background

GRBs are transient sources with a typical duration of up to a few tens of seconds. Therefore, we can use the time intervals during a single pointed observation (science window), when the transient source is not active, as an independent temporal off-source observation (see Fig. 5.10). This approach is similar to what is done with other instruments that use spatially off-source observations to make source independent background measurements.

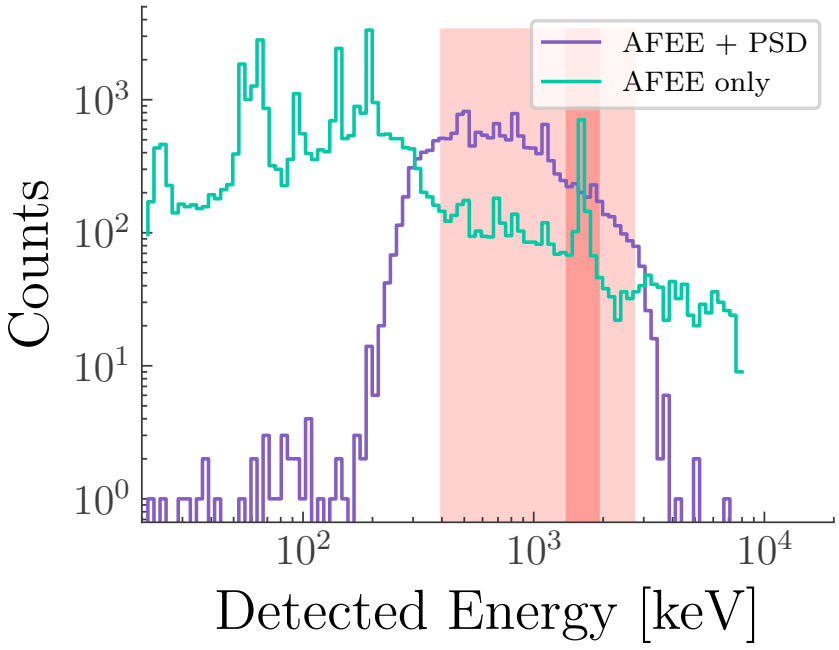

Figure 5.9: Integrated data for 1000 seconds of SPI exposure for detector 0. Around 1500 keV (dark green area) there is a un-physical peaked feature in the events with only a detection in the AFEE (electronic noise), which is not visible in the events with detection in AFEE and PSD electronics. The light red area gives the energy region in which only events with also a PSD detection should be used according to Roques and Jourdain (2019).

The probability distribution for the background model rates per energy channel is the Poisson distribution:

$$\mathcal{L}(B_i, t_b|b_i) = \frac{(t_b b_i)^{Bi}}{B_i!} e^{-t_b b_i}, \tag{5.51}$$

where b_i are the background rates per energy channel, B_i are the detected counts in the off-source observation, and t_b is the exposure of the off-source observation.

Likelihood

With the defined background distribution, we can construct a combined likelihood of source and background observation, given by Eq. 5.52, that connects the source and background model with the Poisson process data of the background and active time interval via the response. Here, θ summaries all the parameters of the source model, D_i are the measured counts in the selected active time interval of the transient source, $m_i(\theta)$ are the predicted count rates from the model evaluated at the parameters θ, and t_d is the exposure of the selected active time interval.

$$\mathcal{L}(D_i, B_i, t_b, t_d|\theta, b_i) = \frac{(t_d(m_i(\theta) + b_i))^{D_i}}{D_i!} e^{-t_b(m_i(\theta)+b_i)} \cdot \frac{(t_b b_i)^{B_i}}{B_i!} e^{-t_b b_i} \tag{5.52}$$

If there was a spectral model for the background, we would fit the background and the source model at the same time with the likelihood given in Eq. 5.52, but we do not have such a model for the SPI background. The background in SPI is dominated by the interaction

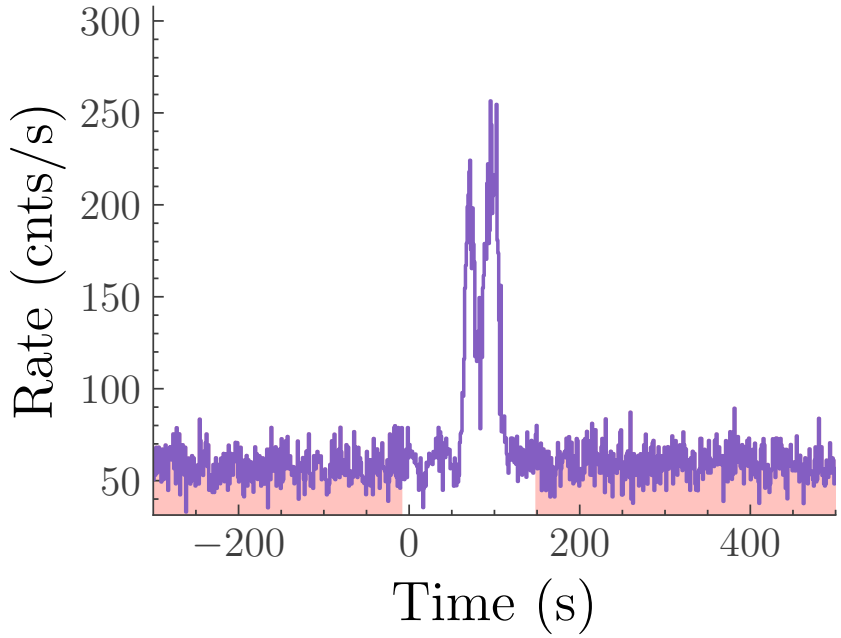

Figure 5.10: Light curve for SPI detector 0 for GRB 120711A. The transient source is clearly visible as well as the constant background for the time when the transient is not active. The time interval used for the independent background observation is marked with the green shaded area.

of cosmic rays in the satellite material, which produces nuclear de-excitation line emission for example (Siegert et al. 2019). For this reason, the background consists of several hundred different nuclear lines, which makes an accurate spectral model for the background impossible at present. However, we can marginalise over the parameters b_i using only the simple fact that they cannot be negative, which leaves us with Eq. 5.53.

$$\mathcal{L}_{\mathrm{marg}}(D_i, B_i, t_b, t_d|\theta) = \int_0^\infty \frac{(t_d(m_i(\theta)+b_i))^{D_i}}{D_i!} e^{-t_b(m_i(\theta)+b_i)} \cdot \frac{(t_b b_i)^{B_i}}{B_i!} e^{-t_b b_i} \tag{5.53}$$

The marginalisation is equivalent to integrating out the background rate parameter assuming a uniform prior from zero to ∞. It takes all the possible values of b_i into account and sums the likelihood for the different background contributions. Because solving this integral is computationally expensive and numerically challenging, we use a profile likelihood as an auxiliary but still statistically sound figure of merit. For the profile likelihood, we use the fact that the derivative of the likelihood at its maximum is zero ($\frac{\partial \mathcal{L}}{\partial b_i}(b_{i,max}) = 0$). This defines the background rates $b_{i,max}$ that maximise the likelihood for a given model $m_i(\theta)$ and observed quantities. $b_{i,max}$ can be expressed analytically as function of the model parameters θ:

$$b_{i,max}(\theta) = \frac{1}{2(t_b+t_d)}\Big(B_i + D_i - m_i(\theta)(t_b+t_d) + \tag{5.54}$$

$$\sqrt{(B_i + D_i + m_i(\theta)(t_d+t_d))^2 - 4m_i(\theta)D_i(t_d-t_b)}\Big) \tag{5.55}$$

These values are then substituted into the likelihood Eq. 5.52 to eliminate the b_i dependency. This gives the exact solution for the maximum of the likelihood; for likelihood values close to the maximum, the assumption is that most of the likelihood in the integrand in Eq. 5.53 is in a small area around $b_{i,max}$. This profile likelihood method has been used in many spectral analysis works (e.g. Loredo and Wasserman 1995; Burgess 2019) and is also available in XSPEC as 'cstat' and 'pgstat' (Arnaud 1996).

Response

In `PySPI` the official response files, as described in Sec. 5.2.1, are interpolated to the defined energy bins and source positions, and one response matrix incorporating all the information about the effective area and energy redistribution is constructed. This also takes the transparency of the mask into account, which is not negligible, especially at high photon energies, but often ignored (e.g. Bošnjak et al. 2014).

Electronic noise

In `PySPI`, the energy range in which only the PSD events should be used to avoid including spurious events (see Sec. 5.2.2) can be selected. To account for the larger dead time of the PSD electronics, an effective area correction can be either fixed to 85%, as suggested by Roques and Jourdain (2019), or treated as a free parameter of the model.

General procedure

Every Ge detector is treated as an independent detector unit. The workflow during a fit step is a forward folding method: (1) sample model parameters, (2) calculate the model flux and responses individually for all detectors for the given source position, (3) fold the model with responses to get the predicted model counts in all detectors, (4) calculate the log-likelihood for all detectors, and (5) sum these log-likelihoods to get the total log-likelihood of the SPI data for the given model parameters. The BAyesian Location Reconstruction Of GRBs (BALROG) algorithm for localising GRBs with GBM employs the same method (Burgess et al. 2017), which shows that forward folding makes it possible to localise photon sources with a non-imaging instrument. It is important to realise that the instruments SPI and GBM are fundamentally very similar; they both consist of individual detectors that have different responses for a given source position. In GBM, this is due to the different pointing directions of the detectors, and in SPI it is due to the varying obscuration by the mask. Even though SPI is defined as a coded-mask instrument, it does not require special treatment. The information that the mask encodes into the data is automatically included by using the different responses for the detectors and a forward folding method. A similar approach was used by DeLaunay and Tohuvavohu (2022) that introduces a new forward folding method to detect and localise faint GRBs with the coded-mask instrument Burst Alert Telescope (BAT).

Software interface

`PySPI` constructs a plug-in for the Multi-Mission Maximum Likelihood framework (3ML) (Vianello et al. 2017). This allows one to fit SPI data together with data from other instruments, such as GBM. `PySPI` is open source software, and is publicly available on GitHub[1], including documentation with examples.

INTEGRAL OSA software

As I introduced a new analysis software, I compared it to the existing analysis software OSA to check whether or not the results are in agreement. In this chapter I briefly summarise the standard analysis tools for GRB analysis, which are part of the OSA software (Courvoisier et al. 2003). Analysing GRB data from SPI with the OSA tools is a multi-step process.

The first steps involve selecting the science window containing the GRB, the time intervals for active time and background time, and the energy bins for the analysis. One can either find the location of the GRB with the SPI Iterative Removal of Sources (SPIROS), which is an iterative source-removal algorithm for SPI data (Skinner and Connell 2003), or set it manually if it is already known. The next steps encompass the spectral fitting, which is done in another two-step procedure.

The first step in the spectral fitting with OSA is to use only the photo-peak response of the detectors. These responses depend on the source position, as this defines for example the absorption by the mask. With these responses and the measured data in the individual SPI detectors, taking into account the different background rates, a photon flux is fitted individually per energy channel. These pseudo photon fluxes are not the final result, as at this point, energy dispersion and detector energy resolution have not yet been accounted for. The pseudo photon flux data points are fitted with a spectral photon flux model and a correction response. The correction response, that is available through OSA, depends on the energy bins that are used and should account for energy dispersion. In this step, the energy channels are fitted simultaneously, as it is impossible to incorporate energy dispersion in a way that fits every energy channel individually. This fitting can be done in different spectral fitting software, such as XSPEC or 3ML and the likelihood used in this fit is a Gaussian likelihood, which is the main problem of this approach. The Poisson likelihood appropriate for the observed data is converted into a Gaussian likelihood of the source only with a backwards folding technique, resulting in all the problems covered in Sec. 2.

I compared the output of `PySPI` and OSA for the time-integrated bright GRB120711A and `PySPI` is able to constrain the parameters of the model significantly better while being consistent with the result of GBM for the same GRB (see Fig. 5.11).

5.2.4 Comparison to previous INTEGRAL/SPI analysis

Most of previous SPI analysis of GRBs used the standard OSA approach described in Sec. 5.2.3, with the two-step method, whereby first only the photo peak response is used

[1] `https://github.com/BjoernBiltzinger/pyspi`

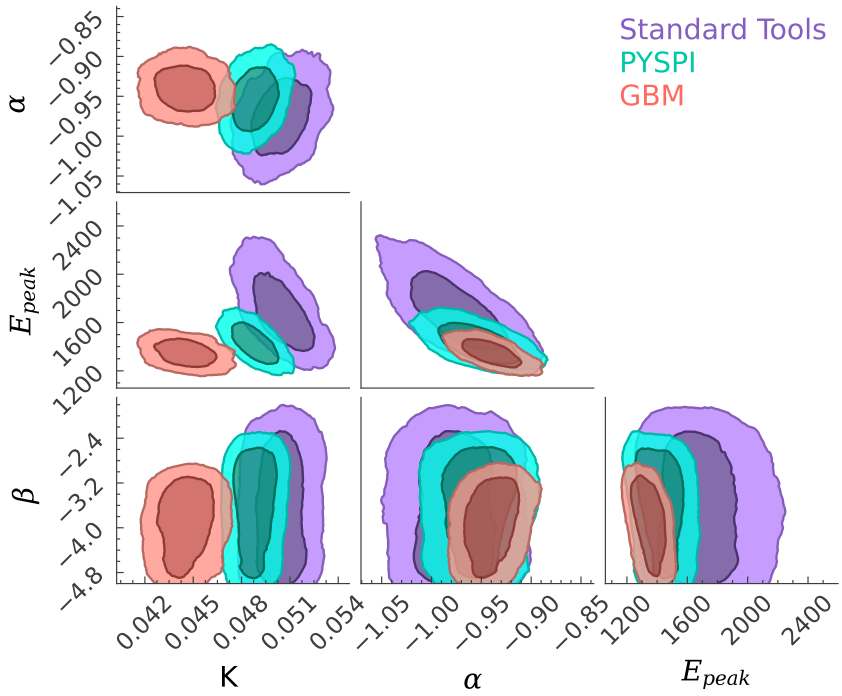

Figure 5.11: Corner plot for the fit of a Band function model to the time integrated data of GRB120711A with the standard tool OSA and `PySPI` for the SPI data and the standard analysis within 3ML for the GBM data. `PySPI` can constrain the parameters significantly better compared to OSA and is consistent with the results from the GBM data. Only the normalisation is off by $\approx 10\%$ which is well within the typical calibration offsets of gamma-ray detectors. The contours give the one and two sigma parameter space.

to incorporate the background and the mask pattern on the detectors, and then an energy redistribution correction response is applied. This was used to fit empirical GRB models to SPI data (Malaguti et al. 2003; Mereghetti et al. 2003b; Mereghetti et al. 2003a; Kienlin et al. 2003b; Kienlin et al. 2003a; Beckmann et al. 2004; Moran et al. 2005; Filliatre et al. 2005; Filliatre et al. 2006; McBreen et al. 2006; Grebenev and Chelovekov 2007; McGlynn et al. 2008; Foley et al. 2008; McGlynn et al. 2009; Martin-Carrillo et al. 2014).

The noteworthy exception is Bošnjak et al. (2014), that performed a joint analysis of SPI and IBIS data of GRBs and created a spectral catalogue of INTEGRAL GRBs. Bošnjak et al. (2014) constructed a response for every SPI detector and forward folded the photon model directly into the data space of every detector, which is similar to the approach in `PySPI`. Compared to their paper, there are two main differences in `PySPI`, namely response generation and treatment of the electronic noise.

For the response generation, Bošnjak et al. (2014) state that they calculate a response function taking into account the exposed fraction of each detector for the GRB position and that the net spectrum is zero for a completely shadowed detector. Thus, they used an idealistic mask with zero transparency at all energies. In `PySPI` on the other hand we use the official response simulations that also include some transparency, especially at high energies. The second point is that the electronic noise is ignored completely in Bošnjak et al. (2014). Roques and Jourdain (2019) showed that the effect of the electronic noise gets stronger for bright sources, and therefore it is important to account for this effect in

the case of GRBs.

5.3 Application

I used `PySPI` for several different applications, that I will discuss in the following.

5.3.1 Time-Resolved spectral catalog of SPI GRBs

There is no complete catalog of SPI-detected GRBs, with the last catalog covering SPI data being published by Bošnjak et al. (2014), covering GRBs up to February 2012. The authors performed combined fits of SPI and IBIS (Mereghetti et al. 2003c)) data for all GRBs in the FOV of IBIS and detected with INTEGRAL Burst Alert System (IBAS). Therefore, an up-to-date catalog is important to test models against the unique SPI data and evaluate the GRB detection properties of SPI. Here I first checked for missed GRBs in the SPI data and then analysed all detected SPI GRBs and created a time-resolved spectral catalog. This allows me to constrain physical models, and compare the detection properties of SPI to GBM, which observes GRBs in a similar energy range.

Data selection

The initial data selection consisted of all 140 GRBs listed in the IBAS catalog with IBIS positions between the launch of INTEGRAL and the end of 2021. During the detection times of 13 listed GRBs, SPI was not operational and for one GRB (GRB 140206A) the background in the pointing covering the GRB time was not stable (see Fig. 5.12). Due to its high orbit and stable pointings the background should be constant within a pointing. If this is not the case, it is most likely due to a technical problem or a flaring source in the FOV. In either case, the background treatment (see Sec. 5.2.3) is not valid. The remaining 126 GRBs light curves were analysed with the Bayesian blocks method (Scargle et al. 2013) with p0 = 0.05, to determine the optimal time bins with approximately constant signal. This is important, as a strongly changing signal is indicative of a change in the physical conditions during the time bin, which would result in systematic uncertainties when the spectrum is fitted with only one spectral model, instead of a superposition of different spectral models (Burgess 2014). In order to constrain the models, I only used time bins with a significance larger than five over the background. I also limited the time bins to be not longer than 40 seconds. The significance was calculated according to Li and Ma (1983) for a Poisson distributed signal with Poisson distributed background measurements. Out of the 126 GRBs, 74 contained at least one time bin above this threshold.

Search for missed GRBs in SPI data

To check for missed GRBs in the SPI data I first checked all GRBs detected by GBM and/or BAT onboard of the Swift satellite (Barthelmy et al. 2005), whether they produced a significant signal in SPI while not being listed in the IBAS catalog table. For every GRB, I took the position given in the GRB catalog of the experiment that detected the GRB and

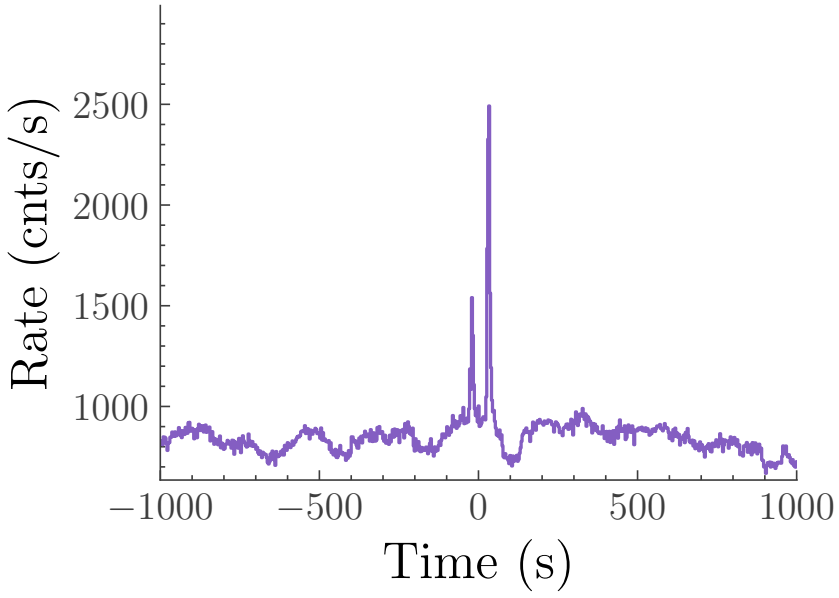

Figure 5.12: Light curve for 2000 seconds centred on the detection time of GRB 140226A. The unstable background is clearly visible, which prohibits the analysis of this GRB with background treatment in `PySPI`. The background variation seen in this case is not physical and points toward a problem with the instrument for this pointing.

calculated the angle between the optical axis of SPI and the GRB position at the trigger time of the GRB. If the angle was less than 20 degrees plus the position uncertainty (only in case of GBM bursts; for Swift the position uncertainty is negligible compared to the 20 degree search radius), I calculated the significance of the signal in all SPI detectors combined during the T90 time interval. All GRBs that resulted in a significance of more than 5 in the SPI data were checked manually and I found two, which were not listed in the IBAS catalog. One is GRB 190411A, which is a long GRB with a T90 duration of about 20 seconds (Kienlin et al. 2020) with a clear significant signal ($> 10\sigma$) in SPI (see Fig. 5.13). The other one is GRB 080413, which is a long GRB in the Swift/BAT catalog with a T90 duration of about 50 seconds (Lien et al. 2016) with a weak, but significant signal ($> 5\sigma$) in the SPI data (see Fig. 5.15). With `PySPI` I was able to localise both GRBs with the SPI data, by fitting the spectrum and the location at the same time, which is a newly developed localisation method for SPI first presented in Biltzinger et al. (2022). The result is displayed in Fig. 5.14 and 5.16, which shows that the localisation determined with `PySPI` and the SPI data is well constrained and in agreement to the localisations of the other instruments. Due to its brightness, I added GRB 190411A to the spectral analysis following in the next sections.

In addition, to make sure no GRB in the SPI data was missed, I performed a search for significant data excess in the SPI data during all detected GRBs since the launch of INTEGRAL. The trigger times are taken from `http://www.ssl.berkeley.edu/ipn3/masterli.txt` and the significance of the SPI light curve for the corresponding science window in a 5, 20 and 50 second interval centred on the trigger times was calculated. If any of the intervals gave a significance larger than five I checked the light curves manually,

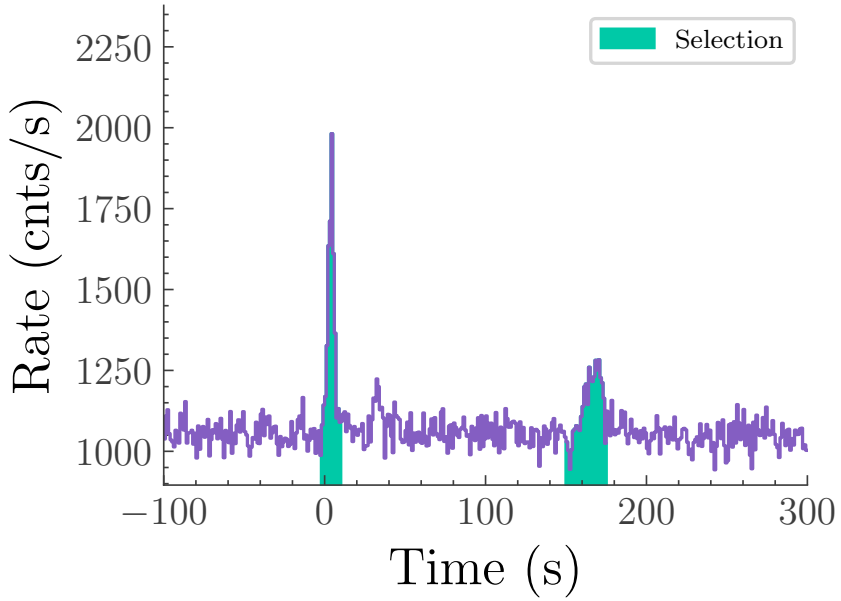

Figure 5.13: Light curve of GRB190411A with the data of all SPI detectors summed. The filled area marks the active time of the GRB.

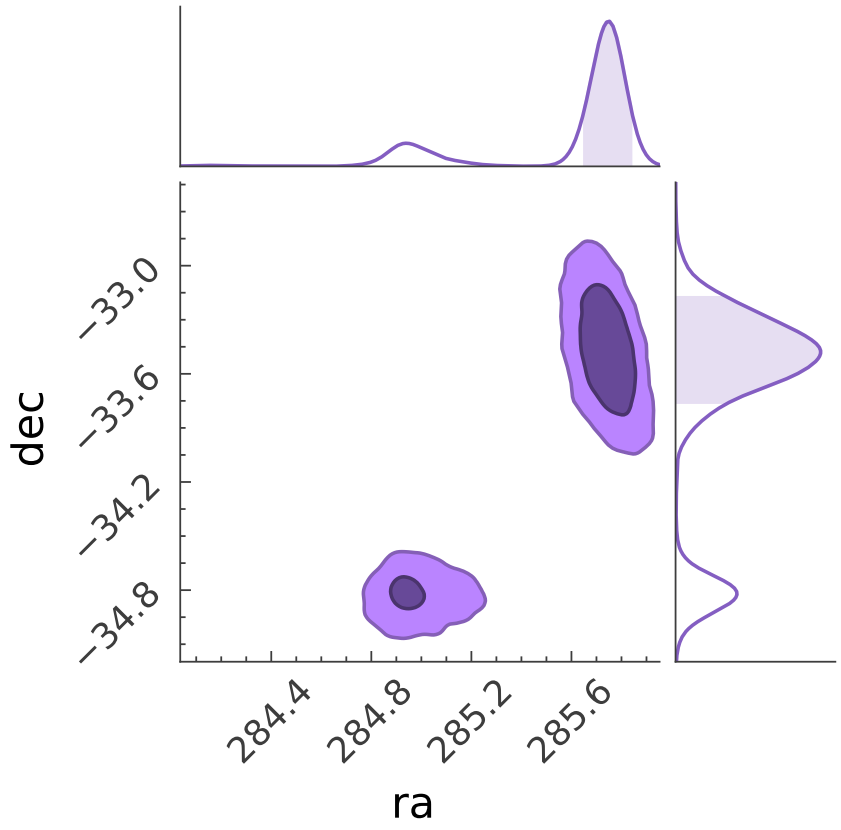

Figure 5.14: Localisation of GRB190411A with SPI data. The contours give the one and two sigma parameter space, which is in agreements with the GBM position (RA=285.9 deg, Decl.=−36.3 deg with an uncertainty of 2.8 deg (Kienlin et al. 2020)). The multi-modality could either be due to the mask pattern or an interpolation artefact due to the 0.5 degree resolution of the response simulation. I checked that the multi-modality is not due to the two peaks in the lightcurves being from different sources with positions on the sky, as the localisation for the single peak exposures give the same results.

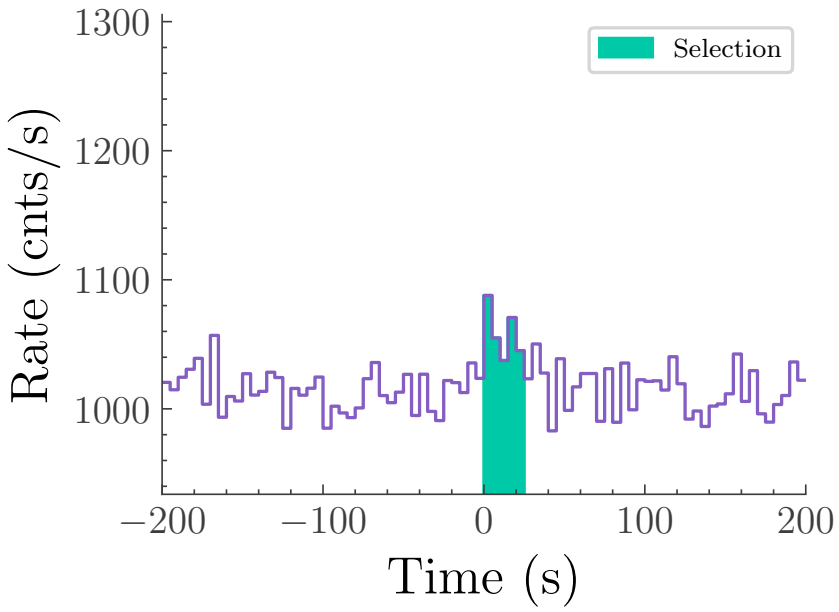

Figure 5.15: Light curve of GRB080413 with the data of all SPI detectors summed. The filled area marks the active time of the GRB.

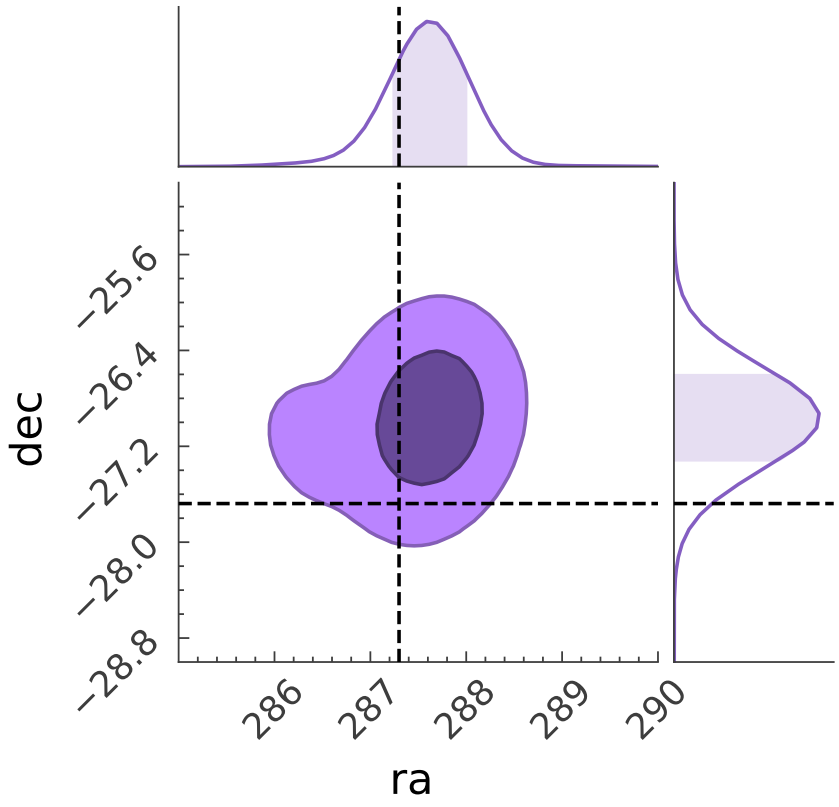

Figure 5.16: Localisation of GRB080413 with SPI data. The contours give the one and two sigma parameter space and the dashed lines indicate the Swift BAT localisation.

to filter observations with non-stable background rates or other obvious problems. For 39 GRBs (see Tab. 4), that are not listed in the IBAS catalog, a clear signal is visible in the SPI data. Especially interesting is that also the famous GRB 190114C, detected by MAGIC in the TeV energy range (MAGIC Collaboration et al. 2019), is visible in the SPI data (see Fig. 5.17). For all these GRBs, there are either previous localisations from other instruments which place the GRB outside of SPI's coded FOV, or the localisation fits fail. Therefore, none of these GRBs is in the coded FOV of SPI and thus, no spectral analysis is possible, because no response through the BGO shield is available.

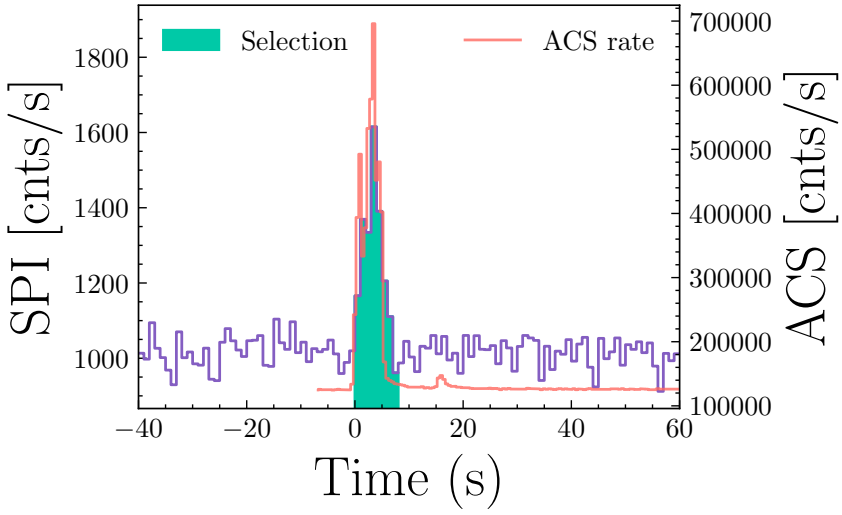

Figure 5.17: Light curve of GRB190114C with the data of all SPI detectors summed, where the filled area marks the active time of the GRB. The red curve shows the light curve of the ACS count rates, showing that the temporal shape is the same.

Data reduction

For all GRBs, the data files were obtained from the INTEGRAL Science Data Centre (ISDC) file transfer protocol server. The data files were read in with `PySPI` to create plugins for 3ML.

The data was split in two energy ranges: (1) Low energy range below the PSD lower energy limit and (2) High energy between the PSD lower and upper energy limit. This is needed to account for the previously discussed electronic noise that affects SPI data (see Sec. 5.2.2). Therefore, all single detector events are used in the lower energy range, but only the events with also a PSD detection in the higher energy range. The exact value of the PSD lower and upper energy limits for all revolutions is taken from Roques and Jourdain (2019). To account for the higher dead time if only the events with PSD detection are used I use a 85% correction factor. The background can be estimated from the time intervals in the same pointing when the GRB is not active and assuming that the background is stable on the time scale of one pointing, i.e. typically 1800 s. Every Ge detector is treated as an independent detector unit, with an individual response for the given source position, and all detectors with a significance larger than 3.5 in the lower (non-PSD) energy range are used.

Catalog

The two most prominent empirical models to fit GRB spectra are the Band function and the cutoff power law (CPL). Therefore, I created the spectral catalog for these two models.

The Band function (Band et al. 1993) was designed to fit most GRBs well at the time of invention. It is a special smoothly connected double power law with fixed curvature. I used the parametrisation with the νF_ν peak energy E_p, the low energy slope α and high energy slope β:

$$F(E) = K \begin{cases} \left(\frac{E}{E_{piv}}\right)^{\alpha} \exp\left(-\frac{(2+\alpha)E}{E_p}\right), & E \leq (\alpha-\beta)\frac{E_p}{(\alpha+2)} \\ \left[\frac{(\alpha-\beta)E_p}{E_{piv}(2+\alpha)}\right]^{\alpha-\beta} \left(\frac{E}{E_{piv}}\right)^{\beta} \exp(\beta-\alpha), & \text{else} \end{cases} \tag{5.56}$$

The cutoff power law has, instead of a second power law, an exponential cutoff at high energies. Again, I used the parametrisation with E_p and the power law slope α:

$$F(E) = K \left(\frac{E}{E_{piv}}\right)^{\alpha} e^{-\frac{E(2+\alpha)}{E_p}} \tag{5.57}$$

For both models the pivot energy E_{piv} is fixed to 100 keV.

All time bins identified in Sec. 5.3.1 were fitted with both models with 3ML and pymultinest (Buchner et al. 2014), which is a python wrapper for MultiNest (see Sec. 3.1.1) (Feroz and Hobson 2008; Feroz, Hobson, and Bridges 2009; Feroz et al. 2019). The number of live points for MultiNest was set to 1000.

Also an effective area correction between 0.7 and 1.3 for all detectors but one is added to the fit. This is needed to archive good fits, as without the effective area correction most fits failed, which indicates some calibration offsets between the individual SPI detectors. This could for example be caused if the mask is misaligned a bit in comparison to the simulations. In this case there would not be an constant offset of the individual detectors, but different offsets depending on the position of the GRB in the FOV of SPI different. This is also what I found in the fits for the SPI catalog as shown in Fig. 5.18. An example of how the fits fail without an effective area correction is given in Fig. 5.19. I defined a fit to be bad if more than 10% of the energy bins of all detectors are outside the 95% credible interval of the Cumulative-Cumulative (QQ)-plots (see Sec. 3.1.3). Out of the 289 time bins fitted, 29 (31) failed for the Band function (cutoff power law). Example Posterior Predictive Check (PPC)- and QQ-plots for a good and a bad fit are given in Fig. 5.19 and the table with all parameters is given in Tab. 1 and 2, which shows that it is often not possible to determine the peak energy and high energy spectral slope.

This is not what was expected, as the good energy resolution of SPI should result in well constrained spectral shapes. After investigating this problem, I conclude that this is due to two problems: low effective area and coarse response. The effective area of the SPI detector, especially above a few hundred keV is small compared to GBM, since the two BGO detectors increase the effective area in the few hundred keV to few MeV energy range substantially (see Fig. 5.20). Also the coarse response interferes with the strength of

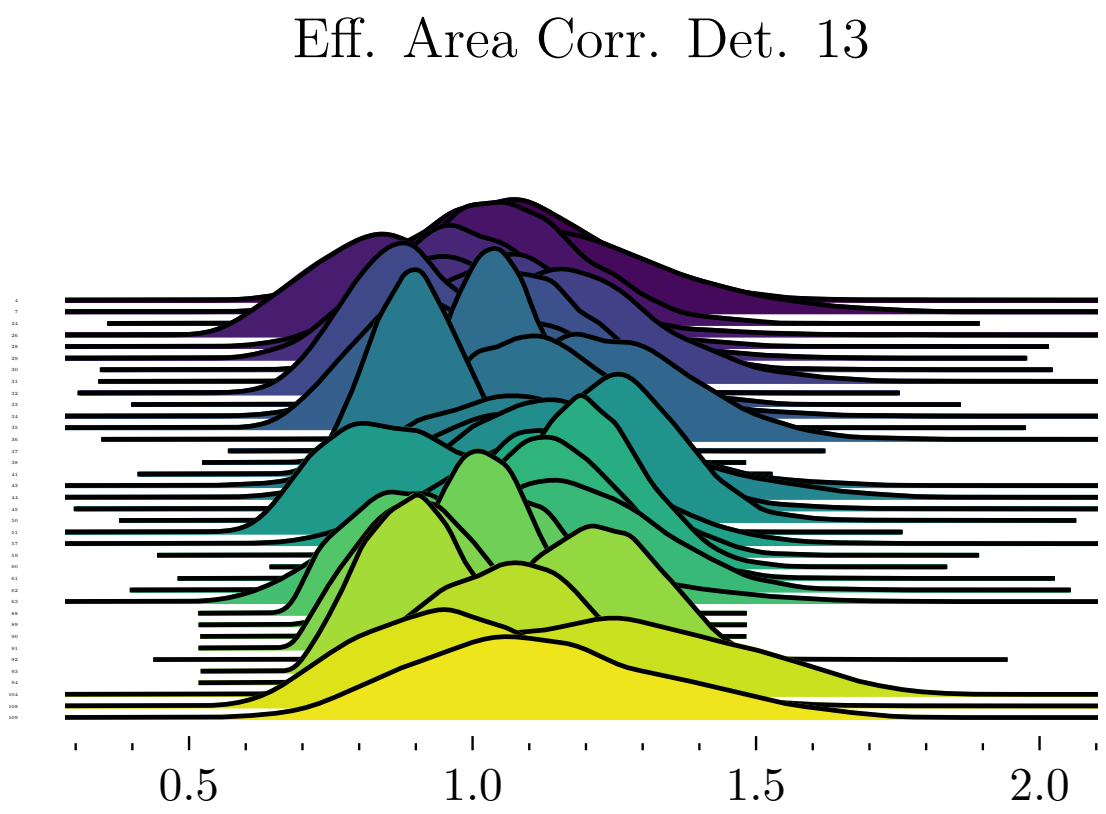

Figure 5.18: Effective area correction of detector 13 with respect to detector 0 for different GRBs. It shows that there is no unique offset.

SPI, namely the good energy resolution. The response was only simulated for 51 photon energies between 20 and 8000 keV with the redistribution matrix also only determined for very broad 50 output energy bins. In Sec. 5.3.5 I will discuss the improvements that would be possible with a high resolution response.

As β is unconstrained for most time bins, I only compare the cutoff power law parameter distributions to the GBM catalog. For this I applied the same filter logic as the GOOD selection in Yu et al. (2016), namely that the relative uncertainty on the parameters is less than 0.4. In Fig. 5.21 I plot α against E_{peak} for the GBM time-resolved spectral catalog (Yu et al. 2016) and our filtered sample. This figure shows that only for a few time bins the fits were able to constrain the parameter well enough to pass the GOOD selection criterion. But the parameter distributions obtained with SPI are similar to the ones found in (Yu et al. 2016) for GBM data. Interesting is that all time bins in this sample with a peak energy above 700 keV are from one GRB, namely GRB 120711A (see Fig. 5.21), which was extremely bright. This shows that SPI is only able to constrain such high peak energies for extremely bright GRBs, due to its lack of effective area compared to GBM. Fig. 5.22 also shows that the α distribution in the SPI sample is similar to the one in the GBM sample.

5.3.2 Joined Fits with Fermi/GBM

`PySPI` is a plugin for 3ML, which is designed for multi-mission data fitting: The spectral

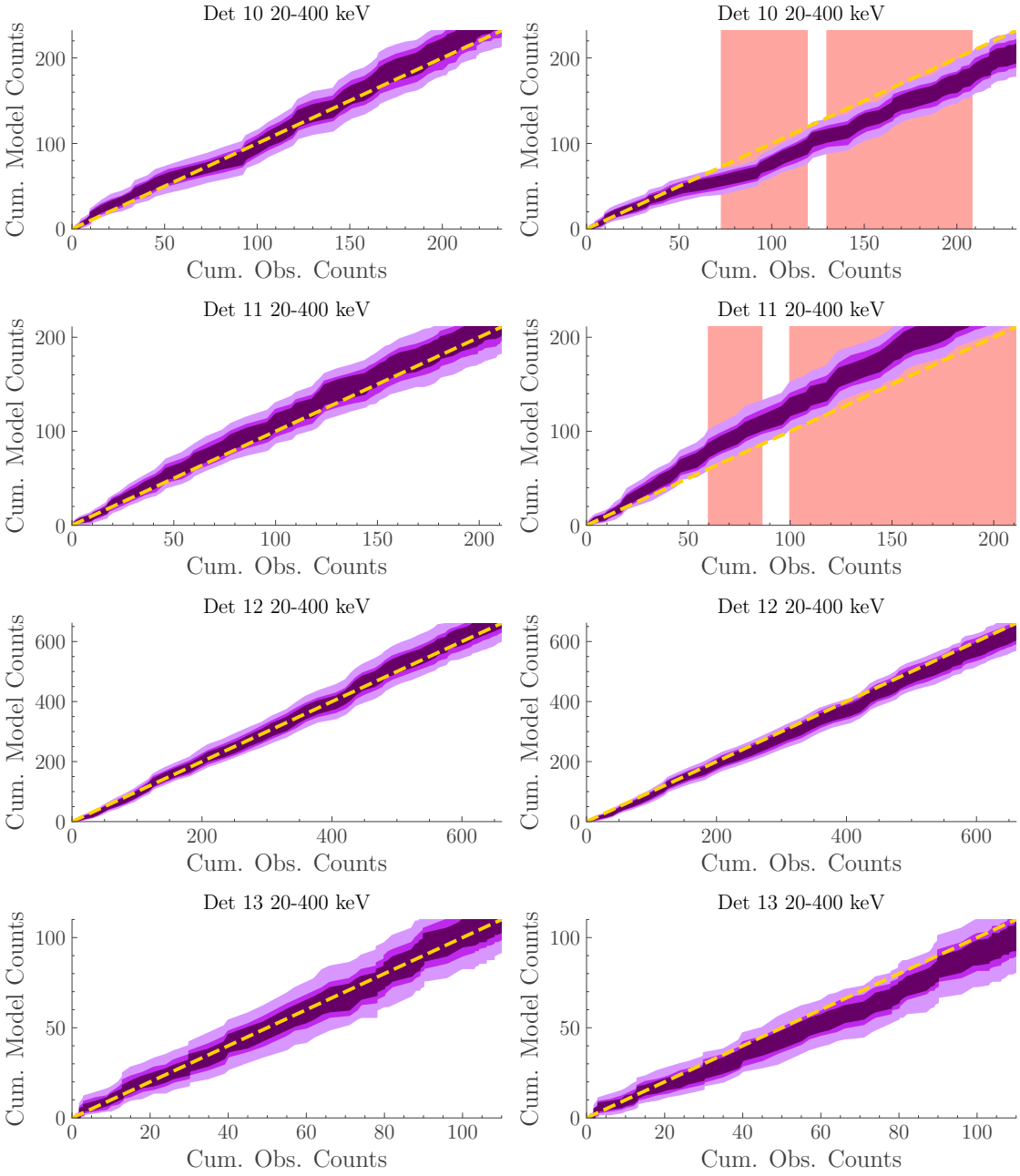

Figure 5.19: QQ-plots for one fit with (left) and without (right) free effective area correction parameter, for four different SPI detectors in the reconstructed energy range 20-400 keV. These plots show the result for the band function fits of the time slice 121.17-122.48s of GRB181201. The red intervals mark strong deviations (> 95 %) of the true data from the simulated data, indicating a bad fit. The contours give the 50 %, 75% and 95% credible intervals.

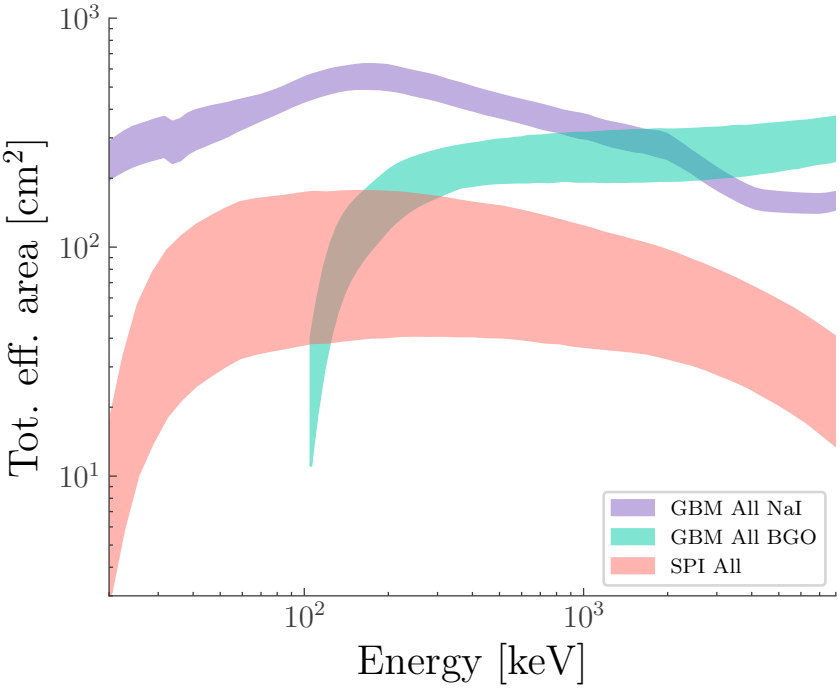

Figure 5.20: Comparison of the total effective area of GBM and SPI over the SPI energy range. The spread of the lines indicates the full distribution of effective areas depending on the position of the source in the FOV. For SPI this is restricted to all possible positions in the fully-coded FOV.

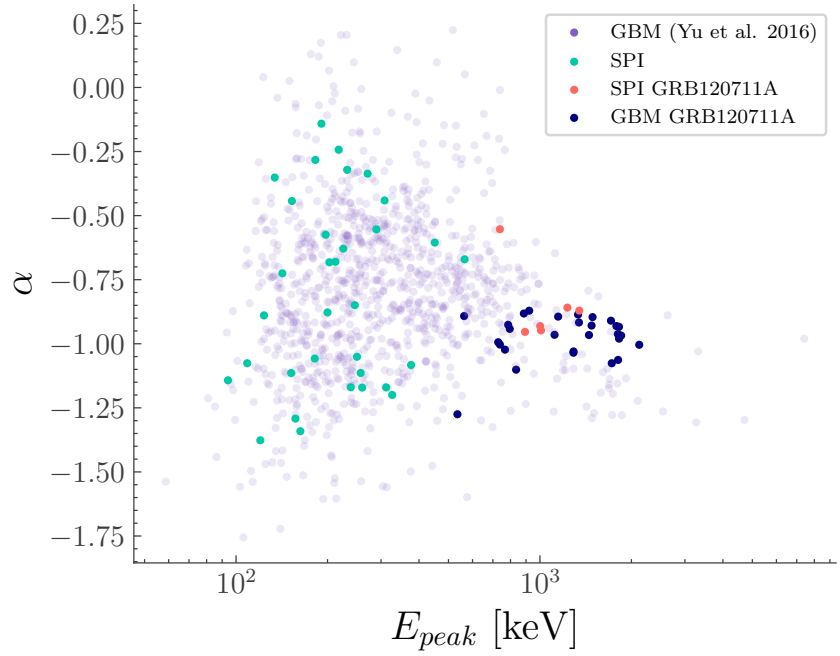

Figure 5.21: Pair plot of best-fit α and E_{peak} values for the cutoff power law fit of the GRBs that are well constrained in our sample and those from the time-resolved GBM catalog (with the GOOD selection criterion fulfilled). For visual purpose I did not include error bars in this plot. The uncertainties on the parameters for the SPI data points are given in Tab. 2 and those for the GBM data points can be found in the time-resolved GBM catalog in Yu et al. (2016).

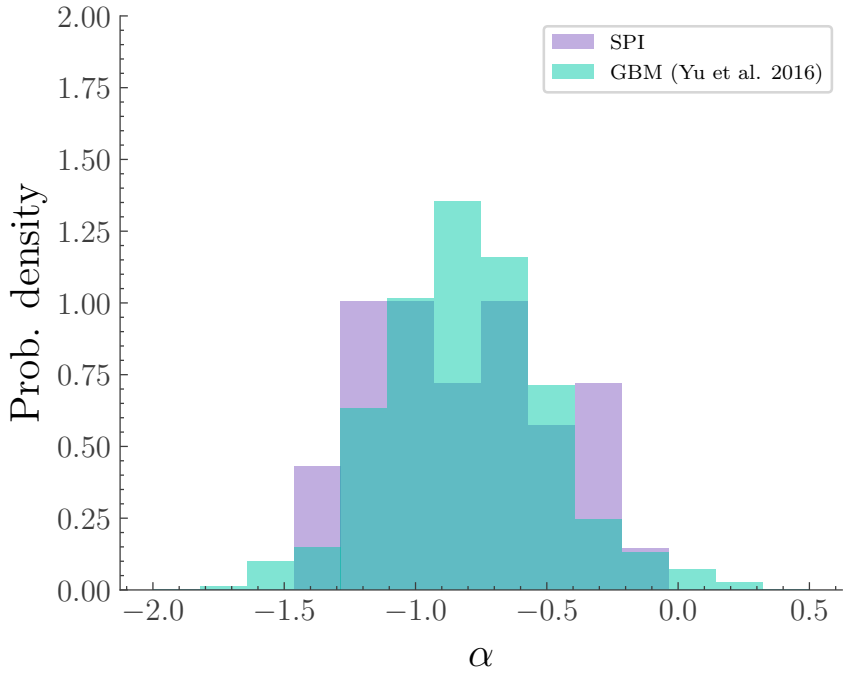

Figure 5.22: Distribution of best-fit α values for the cutoff power law fit of the GRBs that are well constrained in our sample and those from the time-resolved GBM catalog (with the GOOD selection criterion fulfilled).

models are folded with the response of the different instruments and a log-likelihood is calculated per instrument. To fit the data together, we can simply add the log-likelihoods together and use different Bayesian sampler to estimate the posterior distributions of the model parameters given the observed data in the different instruments. In the case of SPI it is especially interesting to fit its data together with the data of GBM, as it covers a similar energy range, but the two instruments have different properties: GBM has larger effective area but much worse energy resolution. This combination results in better constrained parameters, as shown in Fig. 5.23. As `PySPI` is an open-source tool everyone can now easily fit SPI and GBM data together, which has never been possible before.

5.3.3 Fits of physical synchrotron model

Especially the very good energy resolution of SPI could allow to help answering the question of the true emission mechanism of GRBs. In my work I used a physical synchrotron model called `Pynchrotron` (Burgess et al. 2020) to fit the data of SPI. The main motivation for this is to check if such a model can fit the data and to directly learn about the physics in a GRB, instead of using empirical models that can easily lead to wrong claims like the already mentioned synchrotron line-of-death (Burgess et al. 2020).

`Pynchrotron`

The `Pynchrotron` model was previously used to successfully fit many single-pulse GRBs observed with GBM in Burgess et al. (2020), which also includes a detailed description of the model. Here, I summarise the main points.

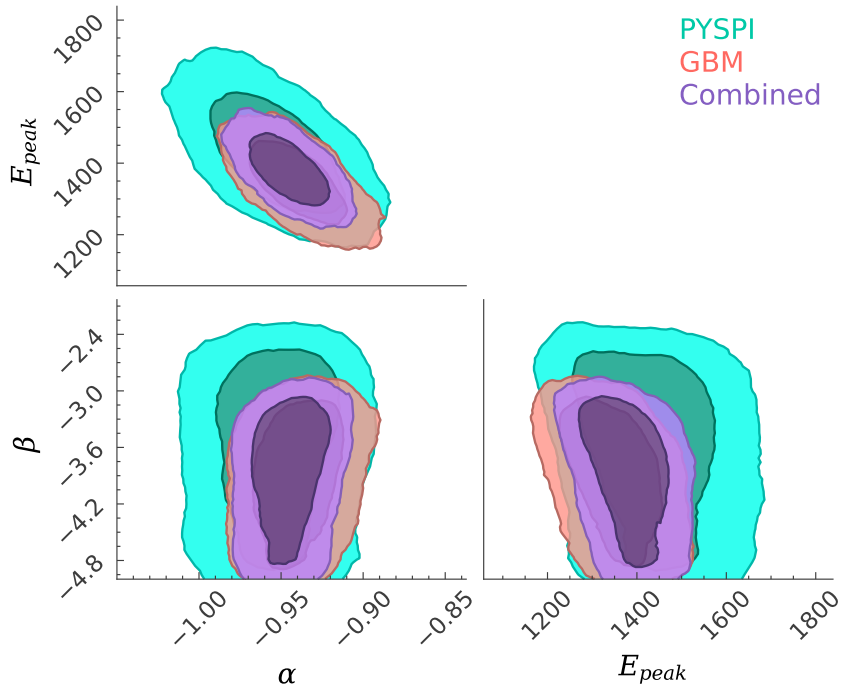

Figure 5.23: Corner plot for the fit of a Band function model to the time integrated data of GRB120711A with `PySPI` for the SPI data and the standard analysis within 3ML for the GBM data, as well as a combined fit. The results from SPI and GBM agree within their uncertainty region and the combined fit provides better constraints on the parameter than the individual ones. The contours give the one and two sigma parameter space.

The core of the model is the assumption of some generic acceleration mechanism that constantly accelerates electrons into a power-law spectrum

$$N(\gamma) \propto \gamma^{-p} \tag{5.58}$$

between γ_{min} and γ_{max}. These electrons are cooled via the emission of synchrotron photons in a magnetic field. So the electron spectrum at a given time is a superposition of the newly injected electrons at that time and the already to some part cooled electron distributions of earlier injections. But the model does not include reheating of the cooled electrons.

The resulting photon spectrum is the sum of the photon spectra at every time-step in the cooling process and is defined by five quantities: (1) the magnetic field strength (B), (2) the slope of the injected electron spectrum (p), (3) the lower boundary of the injected electron spectrum (γ_{min}), (4) the upper boundary of the injected electron spectrum (γ_{max}), and (5) the characteristic Lorentz factor of electrons that cool efficiently on a time scale smaller than the hydrodynamic time scale (γ_{cool}). There exists a strong degeneracy between B and γ_{min}, as their combination sets the peak of the photon spectrum. Therefore, $\gamma_{min} = 10^5$ is fixed and only B is fitted. With this parametrisation the resulting γ_{cool} and γ_{max} are only meaningful with respect to the fixed γ_{min}.

The model does not include any geometry aspects and the acceleration of the electrons could be caused by e.g. optically thin internal shock collisions in the Fireball model or by magnetic reconnection in a Poynting flux dominated outflow. If it is able to fit the

data well, then it shows that there is no need for a thermal component, like for example a dissipative photosphere model.

Catalog

I used the same data as in Sec. 5.3.1, but limit the analysis to time bins with a significance $> 15\sigma$. Only 14 out of 158 fits are determined as bad fits, which shows that the simple physical synchrotron model can explain the prompt emission of GRBs well. Fig. 5.24 and 5.25 show the corner plots and PPC plots for one of the fits. I also report the values for the electron power law slope p and $\chi = log(\frac{\gamma_{cool}}{\gamma_{min}})$ for these fits in Tab. 3. Here χ defines the synchrotron regime with $\chi < 0$ being fast and $\chi > 0$ slow cooling. For most fits the parameters are not well constrained, which is again mostly due to the small effective area, especially at high energies (see Fig. 5.20). However, for some bright GRBs the synchrotron cooling regime could be determined, and both, clearly fast and clearly slow cooling time bins, exist (see Fig. 5.26). Identifying the cooling regime of an emission period is important to understand the underlying physics. The emission periods with slow cooling electron spectra challenge relativistic shock models, as these models depend on a maximum amount of energy conversion into photons via synchrotron emission from the accelerated electrons (Burgess et al. 2020) to overcome their inefficiency of converting internal energy into accelerated electrons (Sari, Narayan, and Piran 1996). This co-existence of slow and fast cooling regimes result is in agreement with the findings of Burgess et al. (2020) based on GBM data.

For the eight brightest GRBs I show χ as a function of time in Fig. 5.27. Due to the large uncertainties, a clear trend can not be determined, but individual time bins with clear fast and slow cooling exist.

Additionally I analysed GRB120711A with a combined fit of SPI and GBM data. For these fits I shifted the light curves of GBM by -0.37 seconds to account for the light travel time for the given GRB and satellite positions. The result is shown in Fig. 5.28 and for some time bins the parameters are constrained better. Unfortunately, all other bright SPI GRBs were not seen by GBM, preventing combined fits on a larger sample.

5.3.4 GRB emission process

As shown, synchrotron emission can fit the data of most bright SPI detected GRBs well, supporting the same findings for GBM detected GRBs in Burgess et al. (2020). Therefore, the claimed synchrotron 'line of death' (Crider et al. 1996; Preece et al. 1998), excluding synchrotron as sole emission model for most GRBs, is not correct. The synchrotron 'line of death' seen in many GRBs is an artefact, caused by the fitting with empirical functions and applying the constrained parameters to a physical model, instead of directly forward folding the physical model to the data. This is a prime example of the problems and false claims that can happen, when using non forward folding techniques of the model actually tested. For GRB theories it follows that synchrotron is still a valid possible emission mechanism and for most GRBs no other components, like a photosphere (e.g. Pe'er, Mészáros, and Rees 2006) or sub-photosphere dissipation (e.g. Ryde et al. 2011), need to be included.

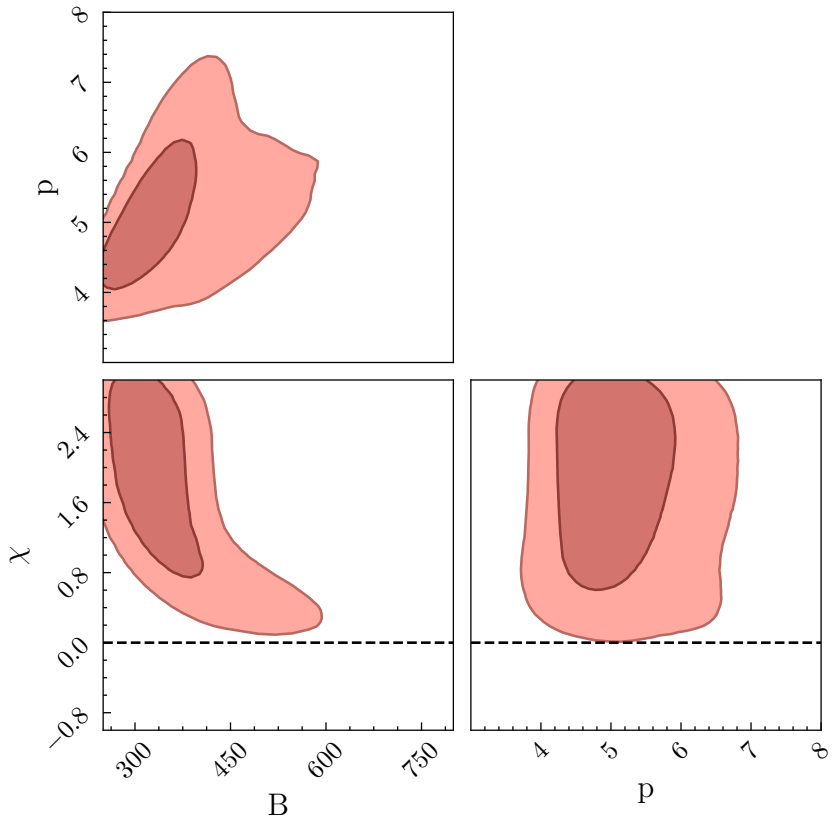

Figure 5.24: Corner plot, showing the posterior for the fit of the physical synchrotron model to one of the time bins. The dashed lines indicates the boundary between fast and slow cooling regime.

Additionally, the existence of slow cooling emission periods (see Fig. 5.27) and the required efficient energy transformation into photons, could be an indicator of the reheating of electrons (Burgess et al. 2020) e.g. due to second-order Fermi acceleration (Beniamini, Duran, and Giannios 2018; Xu, Yang, and Zhang 2018) or magnetic reconnection (Bromberg and Tchekhovskoy 2015). In the case of magnetic reconnection, it has been recently shown by (Comisso and Sironi 2019) with PIC simulations, that the pitch angle distribution of the electrons can be non-isotropic and even energy dependent. This would have implications on the produced photon spectrum, like limb-brightening (Beloborodov et al. 2011), which for example fits the properties seen for GRB 130925A in the optical wave length (Greiner et al. 2014). Therefore, a natural next step in the modeling of synchrotron emission will be to drop the assumption of isotropic pitch angle distributions and instead use the energy dependent pitch angle distributions found in these recent PIC simulations.

5.3.5 Response simulation

As already mentioned in Sec. 5.2.1 I did extensive Geant simulations for one position in the SPI FOV to create a response with a very high resolution. To check if such a high resolution response could improve the data analysis with SPI I simulated a bright GRB with this new response and fit it with the physical synchrotron model. Fig. 5.29 shows the posterior distributions of this fit compared to the ones using the simulated GBM data

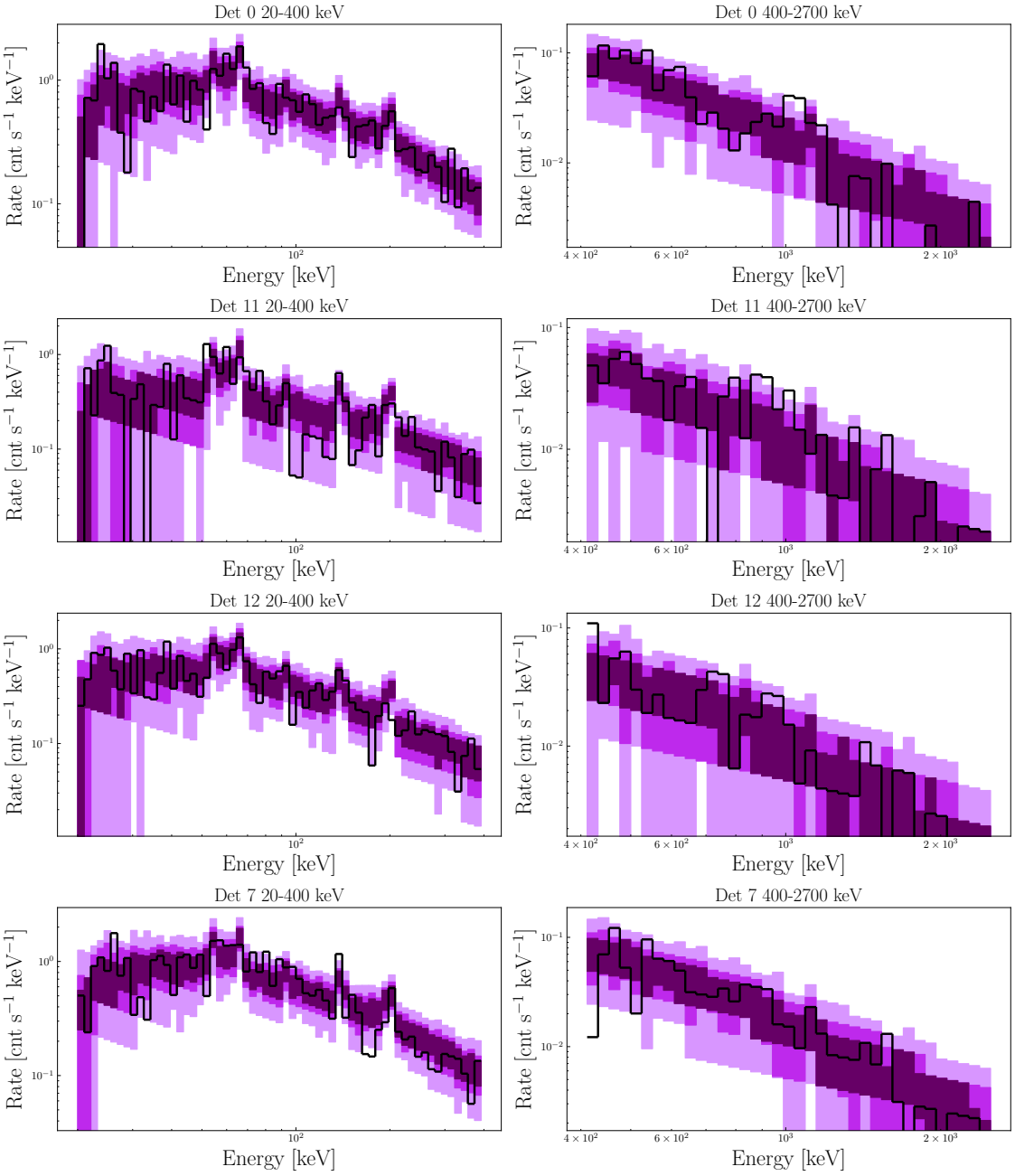

Figure 5.25: PPCs for the fit of the physical synchrotron model to one of the time bins and four of the used detectors. The black line shows the measured data.

of the same GRB. The position and time of the GRB was set to the ones from the real GRB120711A, that was observed by GBM and SPI.

The result shows, that the good energy resolution would allow to constrain the spectral shape better than GBM if the full potential of the energy resolution would be used (and the GRB is bright). Therefore, re-simulating the full response and re-analysing the observed GRBs should be done in the near future.

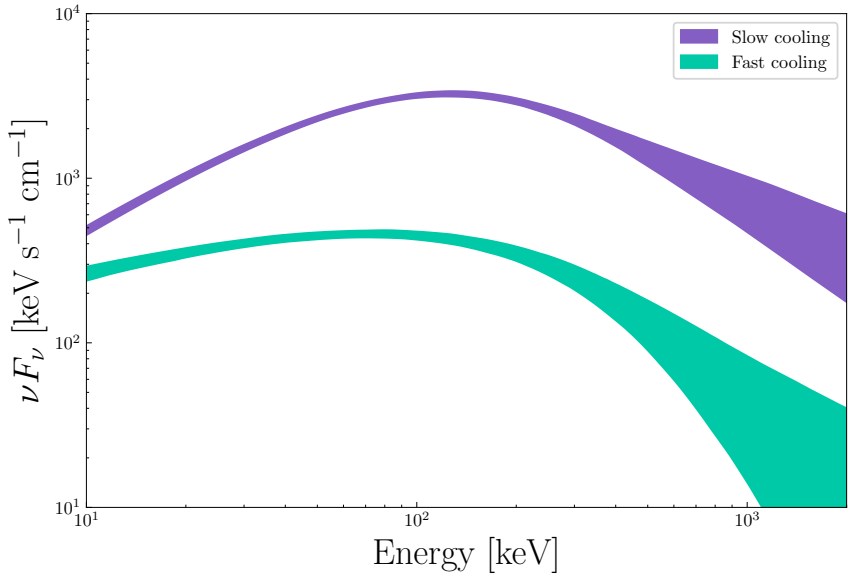

Figure 5.26: Posterior spectra of the physical synchrotron spectrum for two time bins of GRB 181201A. The spectrum in one of the time bins was identified as slow cooling and in the other as fast cooling, caused by a difference in the curvature.

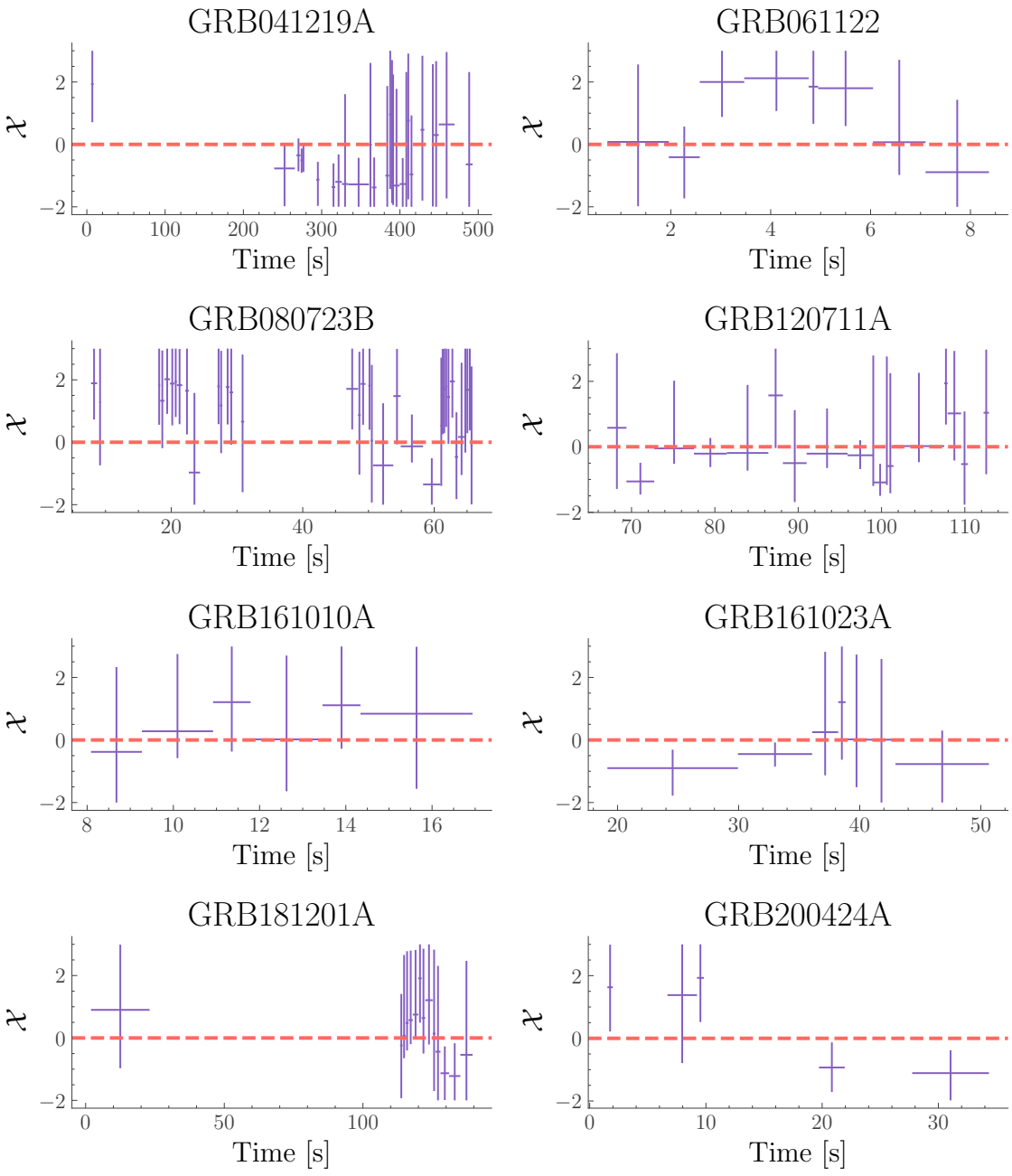

Figure 5.27: Time evolution of χ for the eight brightest GRBs in our sample. Values below (above) the red dashed lines indicates fast (slow) cooling.

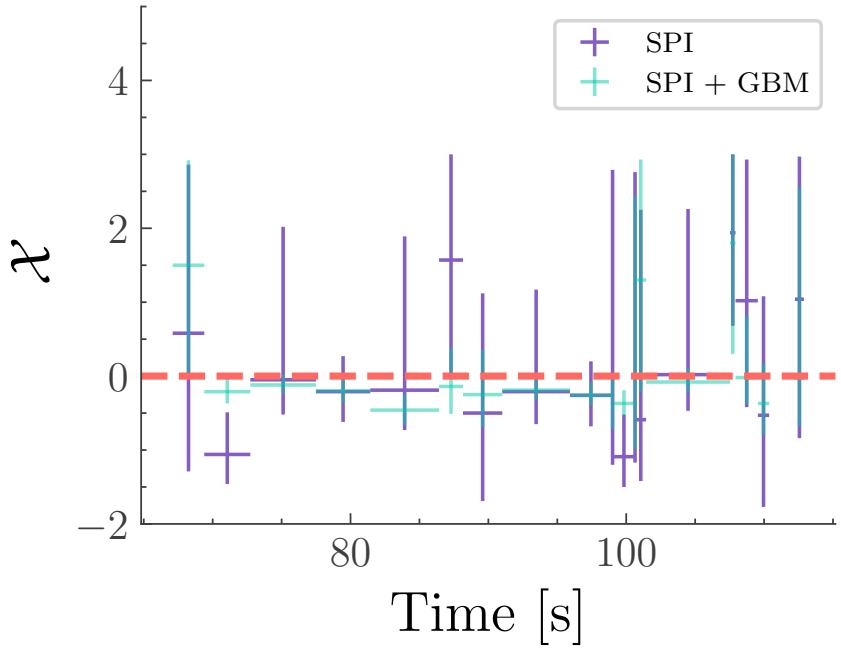

Figure 5.28: Time evolution of χ for GRB120711A for SPI only and SPI+GBM fits. Values below (above) the red dashed lines indicates fast (slow) cooling.

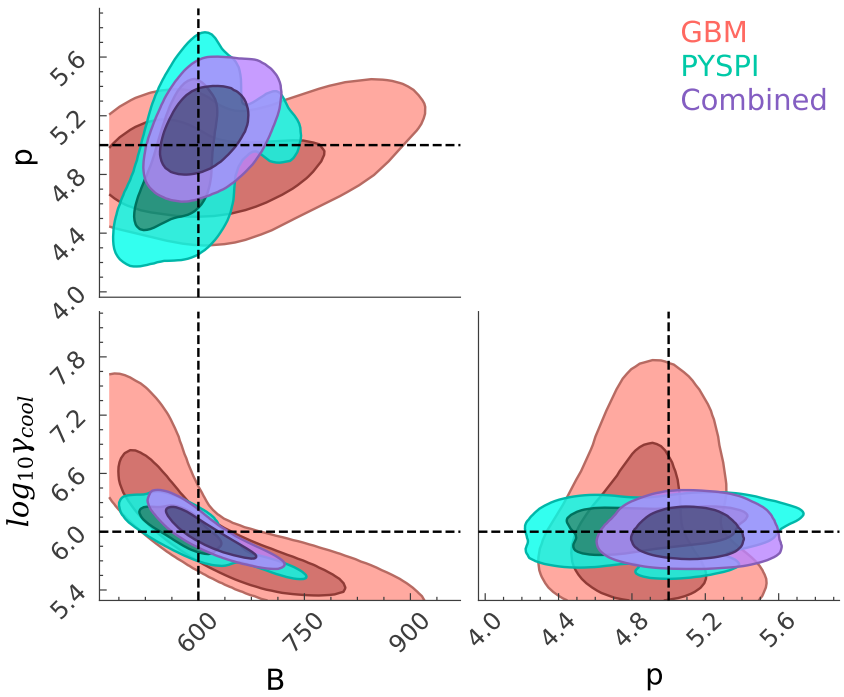

Figure 5.29: Corner plot of the fit of the `Pynchrotron` model to the simulated data of SPI and GBM of a bright GRB at the position and time of GRB120711A. For the SPI data simulation and fit I used the newly simulated high resolution response. The SPI data can constrain the parameters much better than the GBM data. The contours give the one and two sigma parameter space.

5.4 Software design

`PySPI` is an open-source pure python package, that uses object oriented programming to efficiently structure the different tasks needed for SPI data analysis. These different tasks include data reduction, response generation and likelihood calculations. In Fig. 5.30 a schematic overview of the `PySPI` package is shown and Fig. 5.31 - 5.33 show the class diagrams for the different components of the software. The full package is publicly available at `https://github.com/BjoernBiltzinger/pyspi` and has been published in the Journal of Open Source Software (Biltzinger, Burgess, and Siegert 2022).

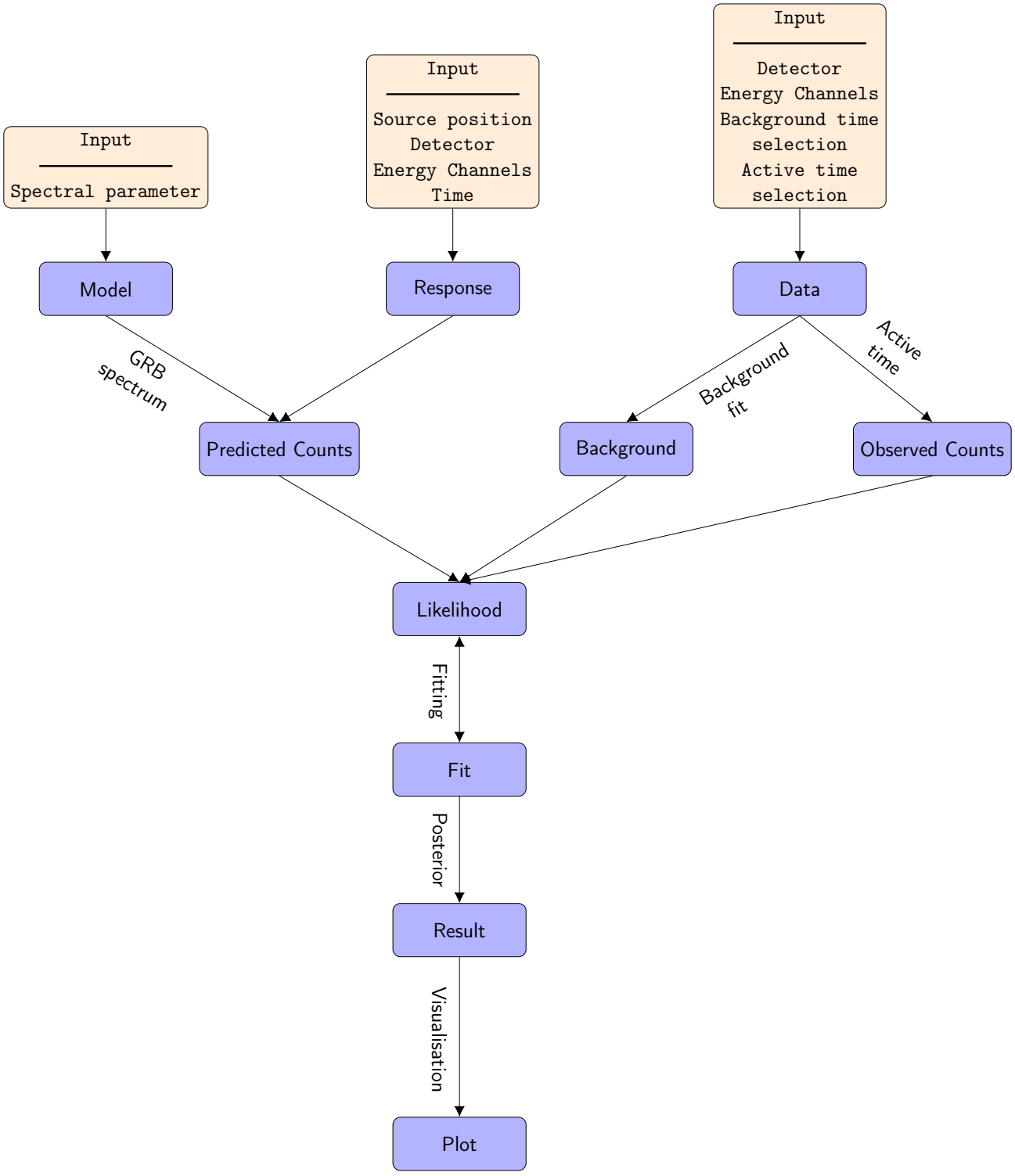

Figure 5.30: Schematic overview of the developed `PySPI` package.

Figure 5.31: Class diagram of the likelihood and background sub-modules of `PySPI`.

Figure 5.32: Class diagram of the response sub-module of PySPI.

Figure 5.33: Class diagram of the utility sub-module of PySPI.

6 New background method for constant point sources in INTEGRAL/SPI

One of the main challenges when analysing Spectrometer on INTEGRAL (SPI) data is the instrumental background. Due to the high orbit (up to 150,000 km from Earth) the International Gamma-Ray Astrophysics Laboratory (INTEGRAL) (Winkler et al. 2003) is not well protected by the Earth magnetic field against cosmic rays. Therefore the constant bombardment of charged particles from the Sun activates the satellite and detector material, resulting in a high intensity of gamma-rays from the de-excitation of these activated nuclei (Diehl et al. 2018). Due to the good energy resolution of SPI and the discrete de-excitation lines from different nuclei, the instrumental background count spectrum is a superposition of many Gaussian-like peaks plus a power law accounting for continuum processes (Diehl et al. 2018). The background intensity is very high, dominating the total detected counts for any non-transient source (Diehl et al. 2018). The best approach to deal with the background would be again a forward model, that folds the charged particle flux hitting the satellite with a response to predict the measured counts from this component. This would constrain the background best and limit for example the difference of possible background variations between different energy channels with physical constrains. Unfortunately, this response it not known and would be very difficult to simulate, as to simulate the propagation of the charged particles through the satellite material and the excitation of atoms on their path, would be very time consuming. Therefore, we are left with sub-optimal empirical methods. The current standard background treatment method uses the fact that due to the pointing pattern and the mask the effect of, even strong, sources get negligible (smear out) for the summed data of many pointings (e.g. all pointings of one orbit) (Siegert et al. 2019). Therefore it is assumed that it is a valid assumption that the summed data reflects the instrumental background. The summed data is fitted with a model containing all known background lines and a broken power law individually for all SPI detectors. Getting the ratio of the fit for the different SPI detectors (often called background pattern), should then give the general instrumental background pattern of the individual detectors, that is also valid for all single pointing observations in that orbit (Siegert et al. 2019). This constrains the background in the fits, as only the background for one of the SPI detectors is fitted freely, while the background in the others follow directly from these ratios. To combine several pointings the background is scaled with a tracer, which can for example be the rates of saturated events, assuming that this traces the flux of incoming cosmic rays. Siegert et al. (2019) has shown that the variation in this tracer

(and therefore the background) between two pointings is on the order $< 1\%$ and that the empirical relations between the tracer and the background variation is only valid if the time between the pointings is not too long (in Siegert et al. (2019) for the case of a Crab nebular analysis a time between a few hours and a few days is suggested for different energy ranges). This method was successfully used in several applications (e.g. Siegert et al. 2015; Pleintinger et al. 2019; Leung and Siegert 2022), but also exhibits some limitations. Firstly, it still adds many fit parameter for the background treatment (at least one per energy channel) and secondly statistical and systematical uncertainties on the background ratios and tracers are not included in the final fit. In the following I will present a new idea for the background treatment for SPI which I developed, that is statistically more robust and does not add any fit parameters for the background.

6.1 Concept

As already mentioned the observed data in SPI is background dominated (except most Gamma-Ray Bursts (GRBs) and bright transient sources) and the background count spectrum is complex, but we can not forward model it with the information we have. The only information we have about the background is that its majority is induced by charged particles from the Sun or cosmic rays. Therefore, it is stable on a long time period ($\approx$ days), unless there is a solar flare, and should be independent of the pointing direction of the satellite (Diehl et al. 2018). Therefore, it is a valid assumption that the background rates in two pointings close to each other in time is the same. On the other hand the physical photon source contributions (e.g. point sources or extended sources) will be different in the two pointings, due to a different response when the satellite is oriented differently with respect to the source position on the sky. The predicted total count rate in the two pointings can be written as

$$\begin{aligned} m_1 &= b + sc(s, \mathcal{R}_1) \\ m_2 &= b + sc(s, \mathcal{R}_2). \end{aligned} \tag{6.1}$$

The background count rate (b) is the same in both pointings, while the source contribution sc is different, because the response $\mathcal{R}$ for the source s changes. Eq. 6.1 reflects all the assumptions used in this approach. The next step is to build a combined likelihood of the two pointings (with detected counts C_1 and C_2), where each one is a Poisson likelihood (Cash 1979):

$$\mathcal{L}(C_1, C_2|b, s) = \mathcal{L}(C_1|b, s)\mathcal{L}(C_2|b, s), \tag{6.2}$$

or the log-likelihood

$$log\mathcal{L}(C_1, C_2|b, s) = log\mathcal{L}(C_1|b, s) + log\mathcal{L}(C_2|b, s). \tag{6.3}$$

Plugging in the Poisson likelihood in Eq. 6.3 and dropping constant non-model dependent terms we get

$$\begin{aligned} log\mathcal{L}(C_1, C_2|b, s) = & C_1 log(t_1(b + sc(s, \mathcal{R}_1))) - t_1(b + sc(s, \mathcal{R}_1)) + \\ & C_2 log(t_2(b + sc(s, \mathcal{R}_2))) - t_2(b + sc(s, \mathcal{R}_2)), \end{aligned} \tag{6.4}$$

where t_1 and t_2 are the exposure times of the two pointings.

The likelihood depends on the source spectra s and the background rates b. As we are not interested in b, but can not forward model it and do not have further information about it we would usually marginalise over b in a Bayesian analysis. This means we would integrate over b, taking all possible values of b into account. Unfortunately there is no analytical solution for the integral in this case and the numerical solutions are slow and unstable. To avoid these problems we can use a profiled likelihood, by maximising the likelihood with respect to b at every fit step and fixing b to this value b_{MLE} for the likelihood evaluation. Therefore we approximate the integrand with a delta function at b_{MLE}. The profiled likelihood approach is often used in astrophysics data analysis (Rolke, López, and Conrad 2005) under the name of 'pgstat' and 'cstat' (Arnaud 1996). It has been shown that this works well as long as there are no data bins with zero counts. The solution for b_{max} can be calculated by differentiating Eq. 6.4 with respect to b, equate it to zero and solve for b:

$$b_{MLE} = 0.5 \left(\frac{C_t}{t_t} - sc_t \sqrt{(\frac{C_t}{t_t} - sc_t)^2 + 4 \left(\frac{C_1 sc(s, \mathcal{R}_2) + C_2 sc(s, \mathcal{R}_1)}{t_t} - sc(s, \mathcal{R}_1) sc(s, \mathcal{R}_2) \right)} \right), \tag{6.5}$$

with $C_t = C_1 + C_2$, $t_t = t_1 + t_2$ and $sc_t = sc(s, \mathcal{R}_1) + sc(s, \mathcal{R}_2)$.

Using this approach will result in the most general solution, obeying only the assumption that the background rate is the same in the two pointings. Including more than two pointings in a simultaneous analysis is also possible by adding the log-likelihoods of many pairs of pointings.

6.2 Simulations

In this section I test if enough information about the source and background are encoded in the data in this approach to constrain the source spectrum. To do this I simulate the count spectrum of a Crab-like source in two different pointings, with two different responses for the source (two degree offset of the pointing positions) and take the count rates from a real SPI data file as background rates. This way I test the method with a realistic background.

From the source plus background count rates in Fig. 6.1 I simulate data by drawing from a Poisson distribution and fit the data with the likelihood given in Eq. 6.4 where I substitute b with b_{MLE} from Eq. 6.5. I use MultiNest (Feroz and Hobson 2008; Feroz, Hobson, and Bridges 2009; Feroz et al. 2019) and do the fits for three different exposures of the pointings: 1800 seconds, 3600 seconds and 18000 seconds. The results are shown in Fig. 6.2, showing that the presented method is able to constrain and reconstruct the

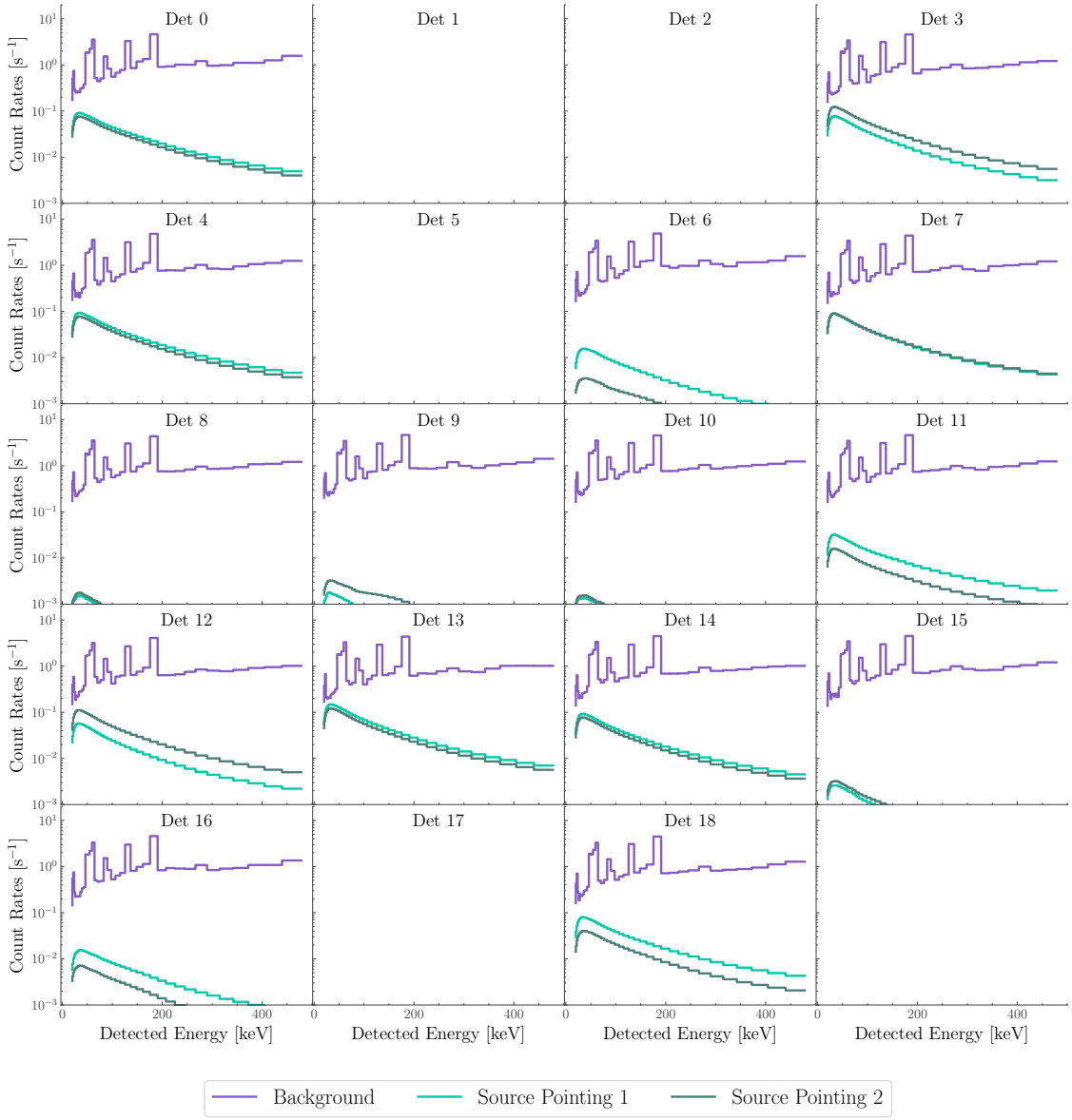

Figure 6.1: Simulation of (Crab-like) source and background count rates for two SPI pointings, with two degree offset in the pointing direction.

simulated values.

6.3 Application

The data of one orbit (1019) with SPI observations was fitted with the presented background treatment. For this all observations with the Crab in the Field Of View (FOV) were grouped in pairs and analysed simultaneously, by adding the log-likelihood, as described in Sec. 6.1. I only include events up to reconstructed energy of 80 keV, to avoid the well-known break in the spectrum of Crab at $\approx$ 100 keV (Jourdain 2009), to keep it as simple as possible for the beginning. As during this orbit there was an additional source close to the Crab in a bright state (1A 0535+262) (Krimm et al. 2013), I also included this source in the fit. The result is displayed in Fig. 6.3, which shows that the spectral parameters

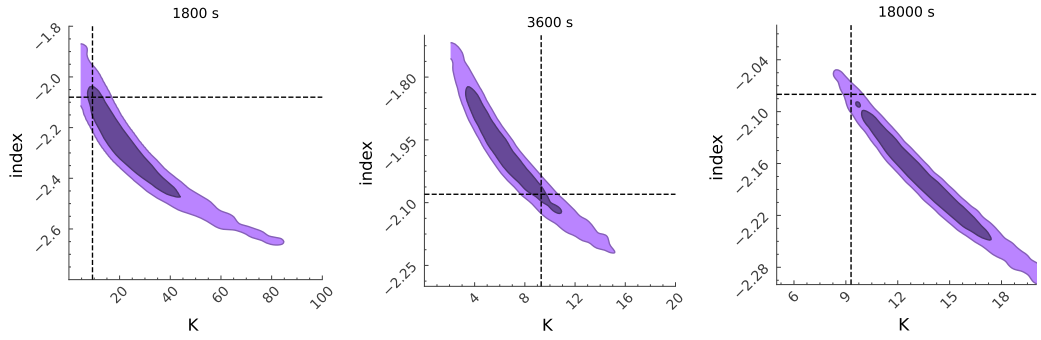

(a) (b) (c)

Figure 6.2: Corner plots for the fits of the simulated data with three different pointing exposure times (short to long). The simulated values are marked with the dashed lines and are consistent with the fit results in all three cases. The shaded areas mark the one- and two-sigma levels.

were constrained to exquisite accuracy (only one orbit of data used). The result for the Crab agree between to the result from the standard analysis software `SpiModFit`, but for the other bright source in this orbit, '1A 0535+262', the results are different (see Tab. 6.1). The discrepancy has to be further investigated in future work (Möller 2023). Part of the problem could be that in the background method in `SpiModFit` the uncertainties on the background pattern are not included in the fit, but the background patterns are assumed to be perfectly known. The new method provides a sophisticated statistical analysis framework, that correctly includes all the uncertainties and does not add any fitting parameters to the fit, unlike the background pattern method.

	SpiModFit	New Method
F_{Crab} @ 40 keV $[\frac{10^{-3}ph}{cm^2 s^1}]$	$4.06^{+0.01}_{-0.01}$	$4.05^{+0.03}_{-0.04}$
α_{Crab}	$-2.23^{+0.01}_{-0.01}$	$-2.20^{+0.02}_{-0.02}$
$F_{\text{1A 0535+262}}$ @ 40 keV $[\frac{10^{-3}ph}{cm^2 s^1}]$	$6.05^{+0.02}_{-0.02}$	$7.26^{+0.02}_{-0.02}$
$\alpha_{\text{1A 0535+262}}$	$\text{-}3.26^{+0.01}_{-0.01}$	$-2.62^{+0.01}_{-0.02}$

Table 6.1: Fit results for the point sources Crab and 1A 0535+262 with the SPI data of orbit 1019. The uncertainties give the one sigma statistical uncertainties.

This only shows one first application with real data. The main part of testing it in more detail and analysing different sources will be done in the upcoming Master thesis of Julius Möller, whom I co-supervise (Möller 2023).

The framework presented here can be expanded in the future in several ways. Firstly one could tie together more than two pointings, as the method can also be derived for groups with more pointings, and only the calculation of b_{MLE} gets more complicated. Secondly the development of a background count spectrum model (with not too many parameters) would improve the analysis, as at the moment the background between two energy channels can jump arbitrarily. This gives the fit a lot of freedom that is not physical. And finally

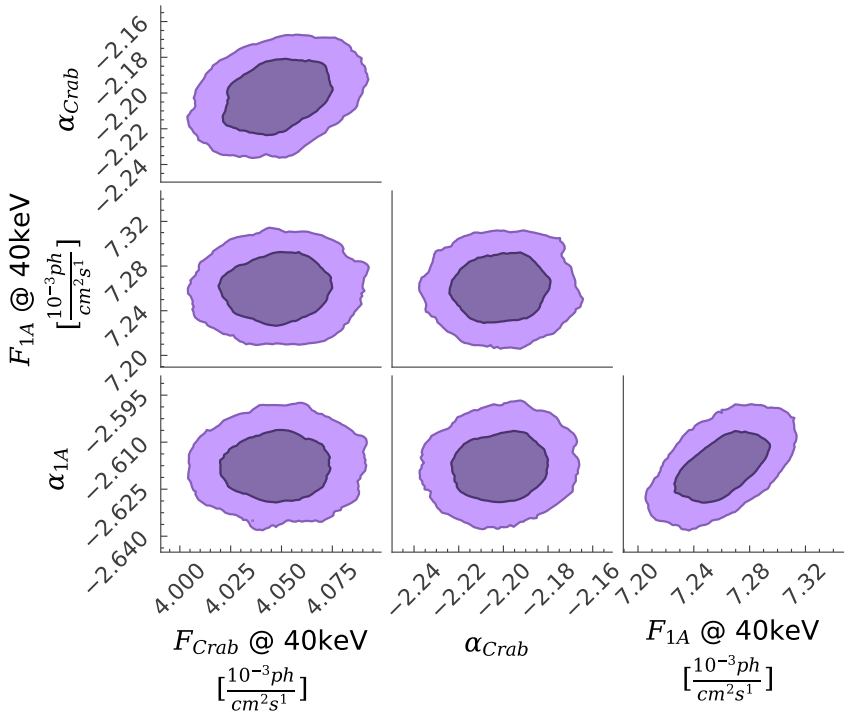

Figure 6.3: Corner plot for the fit of Crab and 1A 0535+262 to the data of orbit 1019. Both sources are well constrained and the derived parameter distributions for the Crab are close to values in the literature.

the development of a stable and fast numerical integration scheme for the marginalisation integral would improve the method further.

7 Conclusion

In this thesis I applied modern data analysis techniques, like forward folding and Bayesian statistics, to different topics in gamma-ray astrophysics, showing its advantages and possible implications on the field.

The developed physical background model for Gamma-Ray Burst Monitor (GBM) allowed, for the first time, to constrain the Cosmic Gamma-ray Background (CGB) spectrum, that is a major component in the background, with GBM. This resulted in a different spectral shape (lower peak energy and broader peak) compared to previous measurements, which has implications on previous Active Galactic Nuclei (AGN) population model test that excluded certain AGN models, due to the inconsistency with the measurements of the CGB. The lower peak energy of the CGB spectrum found here, indicates either a smaller Compton thick to Compton thin ratio of AGNs or a different redshift distribution. Also, the development of a transient search pipeline was possible, that can reliable identify long transient events in the GBM data, that were previously missed, like for example an active state of Vela X-1 at the 17th June of 2020. Finally, the background model gives unambiguous background estimates for GRBs, that could be used in the future instead of the manual, ambiguous, time selections by humans.

The newly developed analysis software `PySPI` for GRBs detected with SPI, allowed for the first time the combined fits of SPI and GBM and the fitting of a physical synchrotron emission model directly to the SPI data by forward folding. Even though it was shown that the effective area of SPI at high energies is too small to constrain most GRB spectra well, I was able to analyse a few bright GRBs in detail. This led to the conclusion, that the simple optical thin synchrotron model can explain the observed data well and no other components, like photosphere or sub-photosphere dissipation are needed. Also the previous observation with data from GBM that both, fast and slow, cooling conditions occur in GRB outflows was confirmed with the data from SPI. This has important consequences on theoretical GRB outflow models, as the combination of slow cooling and an efficient energy dissipation into photons has to be explained. A possible solutions for this problem is the reheating of the electrons, for example by magnetic reconnection.

Finally, the presented new background treatment method for the analysis of constant point sources in SPI could improve this kind of data analysis with SPI and similar instruments significantly. It depends only on the assumption that the background rate is stable over several pointings, which is also part of the assumptions used in the current background treatment, and gives a sophisticated statistical technique that does not add any fitting parameters to the fit. I have shown that it works well with simulated data and

for a first fit of the Crab nebula spectrum (more details will follow in Möller 2023).

I have shown that modern data analysis can increase the information we can extract from data even for instruments that are already operating since many years. The usage of forward folding and Bayesian statistics for the gamma-ray instruments GBM and SPI allowed me to derive new physical insights in different astrophysical topics.

Appendix

Table 1: Parameter constrains for empirical Band model fits. Entries with no parameter values indicate that the fit has failed for this time bin and spectral model. Entries with 'u.l.' and 'l.l.' indicate upper and lower limits and 'unconst.' that the parameter is unconstrained.

Global			**Band**		
GRB-Name	**Ref. Time**	**Active Time [s]**	α	β	E_{peak} **[MeV]**
GRB030227	08:42:02	2.88-8.24	$-1.91^{+0.17}_{-0.09}$	$-3.49^{+1.49}_{-1.39}$	unconst.
GRB030501	03:10:02	9.95-26.03	$-1.84^{+0.24}_{-0.15}$	$-3.52^{+1.46}_{-1.43}$	unconst.
GRB030529	19:53:18	34.27-42.41	$-1.59^{+0.59}_{-0.41}$	$-3.34^{+1.43}_{-1.66}$	unconst.
GRB030529	19:53:18	42.41-54.81	-	-	-
GRB030529	19:53:18	54.81-68.57	-	-	-
GRB031203	22:01:27	-1.01-14.73	$-1.49^{+0.22}_{-0.22}$	$-3.27^{+1.54}_{-1.59}$	0.665 (l.l.)
GRB031203	22:01:27	218.53-218.56	$-1.36^{+1.24}_{-0.64}$	$-3.17^{+1.53}_{-1.61}$	unconst.
GRB040106	17:55:10	2.5-5.29	$-1.69^{+0.75}_{-0.31}$	$-3.37^{+1.47}_{-1.60}$	unconst.
GRB040106	17:55:10	42.3-52.18	$-1.34^{+0.28}_{-0.30}$	$-3.27^{+1.50}_{-1.61}$	0.652 (l.l.)
GRB040323	13:02:58	0.91-12.75	$-0.60^{+0.38}_{-0.39}$	$-3.53^{+1.44}_{-1.45}$	$0.241^{+0.142}_{-0.064}$
GRB040422	06:57:59	3.45-5.47	$-1.90^{+0.20}_{-0.10}$	$-3.47^{+1.46}_{-1.41}$	unconst.
GRB040422	06:57:59	5.47-6.56	$-1.90^{+0.15}_{-0.09}$	$-3.48^{+1.41}_{-1.47}$	unconst.
GRB040730	02:12:06	10.43-21.36	$-0.98^{+0.69}_{-0.53}$	$-3.27^{+1.48}_{-1.72}$	unconst.
GRB040812	06:01:52	39.57-39.67	-	-	-
GRB041218	15:45:44	2.22-6.43	$-1.29^{+0.41}_{-0.29}$	$-3.45^{+1.47}_{-1.54}$	0.181 (l.l.)
GRB041218	15:45:44	6.43-20.65	$-1.34^{+0.28}_{-0.53}$	$-3.81^{+1.38}_{-1.18}$	0.085 (l.l.)
GRB041218	15:45:44	34.3-34.33	$-0.71^{+3.10}_{-1.28}$	$-3.44^{+1.76}_{-1.40}$	unconst.
GRB041218	15:45:44	34.33-41.03	$-1.79^{+0.17}_{-0.17}$	$-3.33^{+1.43}_{-1.54}$	unconst.
GRB041219A	01:42:13	5.33-8.68	$0.11^{+0.28}_{-0.32}$	$-3.27^{+0.96}_{-1.57}$	$0.240^{+0.044}_{-0.032}$
GRB041219A	01:42:13	8.68-11.89	$-1.51^{+0.37}_{-0.23}$	$-3.40^{+1.61}_{-1.53}$	unconst.

Continued on Next Page

Table 1: Continued

Global			Band		
GRB-Name	**Ref. Time**	**Active Time [s]**	α	β	E_{peak} **[MeV]**
GRB041219A	01:42:13	11.89-21.18	$-1.59^{+0.35}_{-0.35}$	$-3.31^{+1.49}_{-1.62}$	unconst.
GRB041219A	01:42:13	218.93-239.37	$-0.86^{+0.84}_{-0.54}$	$-3.31^{+1.52}_{-1.67}$	unconst.
GRB041219A	01:42:13	239.37-265.77	$-1.44^{+0.21}_{-0.22}$	$-3.58^{+1.51}_{-1.41}$	$0.287^{+1.017}_{-0.170}$
GRB041219A	01:42:13	265.77-267.79	$-1.56^{+0.18}_{-0.16}$	$-3.26^{+1.57}_{-1.57}$	unconst.
GRB041219A	01:42:13	267.79-272.99	$-1.17^{+0.15}_{-0.17}$	$-3.47^{+1.22}_{-1.48}$	$0.260^{+0.092}_{-0.061}$
GRB041219A	01:42:13	272.99-275.91	-	-	-
GRB041219A	01:42:13	275.91-277.53	$-1.19^{+0.15}_{-0.15}$	$-3.44^{+1.17}_{-1.52}$	$0.322^{+0.127}_{-0.082}$
GRB041219A	01:42:13	277.53-283.01	-	-	-
GRB041219A	01:42:13	283.01-285.61	-	-	-
GRB041219A	01:42:13	285.61-286.7	-	-	-
GRB041219A	01:42:13	286.7-288.23	-	-	-
GRB041219A	01:42:13	288.23-293.17	-	-	-
GRB041219A	01:42:13	293.17-297.14	$-1.42^{+0.13}_{-0.13}$	$-3.60^{+1.28}_{-1.40}$	$0.308^{+0.153}_{-0.090}$
GRB041219A	01:42:13	297.14-304.81	-	-	-
GRB041219A	01:42:13	304.81-312.8	-	-	-
GRB041219A	01:42:13	312.8-317.41	$-1.63^{+0.19}_{-0.19}$	$-3.60^{+1.43}_{-1.39}$	0.133 (l.l.)
GRB041219A	01:42:13	317.41-325.82	$-1.69^{+0.23}_{-0.11}$	$-3.34^{+1.50}_{-1.51}$	0.142 (l.l.)
GRB041219A	01:42:13	325.82-333.96	$-1.72^{+0.12}_{-0.11}$	$-3.45^{+1.49}_{-1.54}$	unconst.
GRB041219A	01:42:13	333.96-360.46	$-1.94^{+0.23}_{-0.06}$	$-3.44^{+1.33}_{-1.48}$	unconst.
GRB041219A	01:42:13	360.46-364.16	$-1.95^{+0.09}_{-0.05}$	$-3.50^{+1.34}_{-1.46}$	unconst.
GRB041219A	01:42:13	364.16-370.04	$-1.68^{+0.20}_{-0.16}$	$-3.58^{+1.41}_{-1.42}$	0.134 (l.l.)
GRB041219A	01:42:13	370.04-381.41	-	-	-
GRB041219A	01:42:13	381.41-386.22	$-1.94^{+0.26}_{-0.06}$	$-3.56^{+1.31}_{-1.44}$	unconst.
GRB041219A	01:42:13	386.22-388.93	$-1.90^{+0.11}_{-0.10}$	$-3.33^{+1.11}_{-1.46}$	0.010 (l.l.)
GRB041219A	01:42:13	388.93-390.89	$-1.93^{+0.09}_{-0.07}$	$-3.45^{+1.48}_{-1.40}$	unconst.
GRB041219A	01:42:13	390.89-391.68	$-1.52^{+0.34}_{-0.41}$	$-3.75^{+1.40}_{-1.25}$	0.088 (l.l.)
GRB041219A	01:42:13	391.68-399.56	-	-	-
GRB041219A	01:42:13	399.56-407.54	$-1.55^{+0.14}_{-0.16}$	$-4.10^{+0.98}_{-0.90}$	$0.076^{+0.010}_{-0.010}$

Continued on Next Page

Table 1: Continued

Global			Band		
GRB-Name	**Ref. Time**	**Active Time [s]**	α	β	E_{peak} **[MeV]**
GRB041219A	01:42:13	407.54-408.79	$-1.88^{+0.11}_{-0.11}$	$-3.42^{+1.41}_{-1.45}$	unconst.
GRB041219A	01:42:13	408.79-412.52	$-1.92^{+0.08}_{-0.06}$	$-3.65^{+1.15}_{-1.21}$	$0.027^{+0.019}_{-0.017}$
GRB041219A	01:42:13	412.52-417.01	$-1.70^{+0.24}_{-0.19}$	$-4.12^{+1.13}_{-0.88}$	$0.045^{+0.013}_{-0.014}$
GRB041219A	01:42:13	417.01-420.23	$-1.98^{+0.20}_{-0.02}$	$-3.41^{+1.29}_{-1.45}$	unconst.
GRB041219A	01:42:13	420.23-426.25	-	-	-
GRB041219A	01:42:13	426.25-431.17	$-1.89^{+0.05}_{-0.11}$	$-3.54^{+1.09}_{-1.28}$	$0.015^{+2.193}_{-0.005}$
GRB041219A	01:42:13	431.17-441.15	$-1.72^{+0.21}_{-0.17}$	$-4.12^{+1.00}_{-0.87}$	$0.024^{+0.011}_{-0.011}$
GRB041219A	01:42:13	441.15-442.93	$-1.97^{+0.07}_{-0.03}$	$-3.42^{+1.32}_{-1.47}$	unconst.
GRB041219A	01:42:13	442.93-449.58	$-1.93^{+0.04}_{-0.03}$	$-3.77^{+1.28}_{-1.06}$	$0.015^{+0.012}_{-0.005}$
GRB041219A	01:42:13	449.58-469.74	$-1.78^{+0.09}_{-0.10}$	$-4.11^{+0.93}_{-0.86}$	$0.016^{+0.005}_{-0.005}$
GRB041219A	01:42:13	478.36-480.49	$-1.96^{+0.17}_{-0.04}$	$-3.36^{+1.31}_{-1.46}$	unconst.
GRB041219A	01:42:13	484.17-492.81	$-1.58^{+0.73}_{-0.42}$	$-3.33^{+0.96}_{-1.30}$	$0.037^{+0.013}_{-0.016}$
GRB050502A	02:13:55	8.51-21.14	$-1.12^{+0.51}_{-0.55}$	$-3.28^{+1.37}_{-1.65}$	0.097 (l.l.)
GRB050520	00:05:57	52.2-52.7	$-0.23^{+3.06}_{-1.17}$	$-3.24^{+1.62}_{-1.56}$	1.405 (l.l.)
GRB050525A	00:02:53	0.47-1.22	$-1.08^{+0.55}_{-0.47}$	$-4.03^{+1.22}_{-0.96}$	$0.108^{+0.036}_{-0.027}$
GRB050525A	00:02:53	1.22-1.94	$-0.68^{+0.37}_{-0.40}$	$-3.68^{+0.94}_{-1.20}$	$0.139^{+0.023}_{-0.021}$
GRB050525A	00:02:53	1.94-2.32	$-1.20^{+1.33}_{-0.80}$	$-3.55^{+1.25}_{-1.37}$	0.020 (l.l.)
GRB050525A	00:02:53	2.32-5.23	$-1.65^{+0.30}_{-0.30}$	$-4.08^{+1.16}_{-0.92}$	$0.051^{+0.032}_{-0.033}$
GRB050525A	00:02:53	5.23-7.76	$-1.11^{+0.33}_{-0.31}$	$-4.06^{+0.92}_{-0.92}$	$0.093^{+0.011}_{-0.011}$
GRB050525A	00:02:53	7.76-9.75	$-0.87^{+0.76}_{-0.81}$	$-4.00^{+1.07}_{-1.00}$	$0.038^{+0.013}_{-0.017}$
GRB051105B	11:05:41	-0.85-7.6	-	-	-
GRB060428C	02:30:35	0.27-5.86	$-1.82^{+0.21}_{-0.18}$	$-3.46^{+1.46}_{-1.47}$	unconst.
GRB060428C	02:30:35	5.86-7.47	$-1.81^{+0.21}_{-0.19}$	$-3.40^{+1.46}_{-1.48}$	unconst.
GRB060428C	02:30:35	7.47-10.62	$-0.14^{+0.37}_{-0.39}$	$-3.96^{+1.04}_{-1.00}$	$0.126^{+0.018}_{-0.015}$
GRB060901	18:43:55	-1.39-0.3	$-1.47^{+0.31}_{-0.30}$	$-3.27^{+1.49}_{-1.65}$	unconst.
GRB060901	18:43:55	0.3-4.16	$-0.79^{+0.64}_{-0.40}$	$-2.42^{+0.68}_{-2.23}$	$0.248^{+0.165}_{-0.122}$
GRB060901	18:43:55	4.16-8.05	$-1.49^{+0.56}_{-0.24}$	$-3.19^{+1.43}_{-1.69}$	unconst.
GRB061025	18:35:53	5.71-12.71	$-0.68^{+0.73}_{-0.69}$	$-3.39^{+1.15}_{-1.47}$	$0.153^{+0.161}_{-0.057}$

Continued on Next Page

Table 1: Continued

Global			Band		
GRB-Name	**Ref. Time**	**Active Time [s]**	α	β	E_{peak} **[MeV]**
GRB061122	07:56:50	-0.21-0.73	$-0.88^{+3.22}_{-0.98}$	$-3.28^{+1.56}_{-1.49}$	0.058 (l.l.)
GRB061122	07:56:50	0.73-1.96	$-1.84^{+0.10}_{-0.10}$	$-3.46^{+1.46}_{-1.46}$	0.419 (l.l.)
GRB061122	07:56:50	1.96-2.58	$-1.23^{+0.29}_{-0.30}$	$-3.52^{+1.35}_{-1.39}$	$0.240^{+0.259}_{-0.083}$
GRB061122	07:56:50	2.58-3.47	$-0.61^{+0.17}_{-0.16}$	$-4.18^{+1.04}_{-0.81}$	$0.222^{+0.025}_{-0.025}$
GRB061122	07:56:50	3.47-4.76	$-0.55^{+0.13}_{-0.13}$	$-3.70^{+0.83}_{-1.23}$	$0.193^{+0.015}_{-0.016}$
GRB061122	07:56:50	4.76-4.95	$-0.42^{+0.34}_{-0.36}$	$-4.09^{+0.94}_{-0.90}$	$0.151^{+0.024}_{-0.019}$
GRB061122	07:56:50	4.95-6.05	$-0.85^{+0.17}_{-0.17}$	$-4.19^{+0.87}_{-0.81}$	$0.121^{+0.011}_{-0.009}$
GRB061122	07:56:50	6.05-7.1	$-1.28^{+0.21}_{-0.25}$	$-3.76^{+1.19}_{-1.22}$	$0.153^{+0.052}_{-0.033}$
GRB061122	07:56:50	7.1-8.37	$-1.94^{+0.09}_{-0.06}$	$-3.40^{+1.37}_{-1.43}$	unconst.
GRB061122	07:56:50	8.37-12.45	$-1.96^{+0.09}_{-0.04}$	$-3.47^{+1.40}_{-1.39}$	unconst.
GRB070311	01:52:34	-2.86-36.01	$-1.36^{+0.20}_{-0.17}$	$-3.31^{+1.49}_{-1.65}$	0.356 (l.l.)
GRB070707	16:08:38	0.59-0.96	$-1.01^{+0.30}_{-0.29}$	$-3.41^{+1.51}_{-1.56}$	0.357 (l.l.)
GRB070925	15:52:32	11.86-14.48	$-1.48^{+0.31}_{-0.29}$	$-3.26^{+1.61}_{-1.54}$	0.600 (l.l.)
GRB070925	15:52:32	14.48-23.81	$-0.82^{+0.22}_{-0.21}$	$-3.20^{+1.05}_{-1.63}$	$0.190^{+0.045}_{-0.033}$
GRB071003	07:40:55	-1.61-0.08	-	-	-
GRB071003	07:40:55	0.08-2.5	$-0.75^{+0.30}_{-0.23}$	$-2.10^{+0.50}_{-2.38}$	$0.734^{+0.571}_{-0.371}$
GRB071003	07:40:55	2.5-4.06	$-1.30^{+0.42}_{-0.39}$	$-3.33^{+1.57}_{-1.62}$	unconst.
GRB071003	07:40:55	4.06-5.46	-	-	-
GRB071003	07:40:55	5.46-6.5	-	-	-
GRB071003	07:40:55	6.5-6.88	$-0.36^{+0.59}_{-0.63}$	$-3.30^{+1.45}_{-1.66}$	$0.797^{+1.925}_{-0.469}$
GRB071003	07:40:55	6.88-12.91	-	-	-
GRB071003	07:40:55	12.91-21.45	$-1.68^{+0.25}_{-0.22}$	$-3.36^{+1.44}_{-1.62}$	unconst.
GRB080723B	13:22:15	6.58-7.79	$-1.49^{+0.47}_{-0.21}$	$-3.32^{+1.52}_{-1.60}$	unconst.
GRB080723B	13:22:15	7.79-8.72	$-0.14^{+0.29}_{-0.33}$	$-3.92^{+0.96}_{-1.08}$	$0.190^{+0.032}_{-0.021}$
GRB080723B	13:22:15	9.04-9.29	$-0.98^{+0.33}_{-0.36}$	$-3.10^{+1.30}_{-1.68}$	$0.447^{+1.066}_{-0.209}$
GRB080723B	13:22:15	9.29-9.83	$-1.91^{+0.53}_{-0.09}$	$-3.49^{+1.46}_{-1.36}$	unconst.
GRB080723B	13:22:15	17.34-18.01	$-0.85^{+0.53}_{-0.75}$	$-4.01^{+1.41}_{-0.99}$	$0.191^{+0.374}_{-0.074}$
GRB080723B	13:22:15	18.01-18.31	$-0.41^{+0.31}_{-0.33}$	$-3.78^{+1.13}_{-1.18}$	$0.279^{+0.091}_{-0.057}$

Continued on Next Page

Table 1: Continued

Global			Band		
GRB-Name	**Ref. Time**	**Active Time [s]**	α	β	E_{peak} **[MeV]**
GRB080723B	13:22:15	18.31-18.96	$-1.03^{+0.34}_{-0.31}$	$-3.82^{+1.24}_{-1.18}$	$0.177^{+0.073}_{-0.048}$
GRB080723B	13:22:15	18.96-19.8	$-0.26^{+0.21}_{-0.22}$	$-3.19^{+0.75}_{-1.51}$	$0.220^{+0.029}_{-0.027}$
GRB080723B	13:22:15	19.8-20.5	$-0.69^{+0.26}_{-0.27}$	$-3.89^{+1.15}_{-1.10}$	$0.213^{+0.056}_{-0.039}$
GRB080723B	13:22:15	20.5-20.85	$-0.25^{+0.26}_{-0.27}$	$-3.87^{+0.96}_{-1.12}$	$0.218^{+0.036}_{-0.028}$
GRB080723B	13:22:15	20.85-21.67	$-0.60^{+0.25}_{-0.25}$	$-3.42^{+1.07}_{-1.38}$	$0.190^{+0.038}_{-0.031}$
GRB080723B	13:22:15	21.67-22.11	$-1.90^{+0.17}_{-0.10}$	$-3.35^{+1.38}_{-1.48}$	unconst.
GRB080723B	13:22:15	22.11-22.67	$-0.77^{+0.59}_{-0.60}$	$-3.60^{+1.20}_{-1.32}$	$0.140^{+0.069}_{-0.038}$
GRB080723B	13:22:15	22.67-24.38	$-1.81^{+0.19}_{-0.16}$	$-3.42^{+1.47}_{-1.46}$	unconst.
GRB080723B	13:22:15	24.38-26.73	$-1.86^{+2.80}_{-0.14}$	$-3.28^{+1.35}_{-1.56}$	unconst.
GRB080723B	13:22:15	26.73-27.0	$-1.41^{+0.27}_{-0.30}$	$-3.31^{+1.45}_{-1.68}$	0.711 (l.l.)
GRB080723B	13:22:15	27.0-27.39	$-0.44^{+0.25}_{-0.28}$	$-3.33^{+1.10}_{-1.55}$	$0.303^{+0.083}_{-0.060}$
GRB080723B	13:22:15	27.39-27.78	$-0.75^{+0.34}_{-0.40}$	$-3.60^{+1.27}_{-1.39}$	$0.288^{+0.209}_{-0.087}$
GRB080723B	13:22:15	27.78-28.3	$-1.18^{+0.70}_{-0.58}$	$-3.75^{+1.56}_{-1.24}$	0.118 (l.l.)
GRB080723B	13:22:15	28.3-28.85	$-0.53^{+0.27}_{-0.29}$	$-3.59^{+1.23}_{-1.41}$	$0.282^{+0.087}_{-0.060}$
GRB080723B	13:22:15	28.85-29.4	$-0.81^{+0.44}_{-0.49}$	$-3.76^{+1.34}_{-1.24}$	$0.200^{+0.180}_{-0.058}$
GRB080723B	13:22:15	29.4-30.61	$-1.88^{+0.47}_{-0.12}$	$-3.45^{+1.39}_{-1.46}$	unconst.
GRB080723B	13:22:15	30.61-31.09	$-1.45^{+0.51}_{-0.21}$	$-3.18^{+1.39}_{-1.72}$	0.158 (l.l.)
GRB080723B	13:22:15	31.09-32.37	$-1.80^{+0.23}_{-0.19}$	$-3.39^{+1.51}_{-1.43}$	unconst.
GRB080723B	13:22:15	46.63-48.42	$-0.66^{+0.33}_{-0.33}$	$-3.53^{+1.35}_{-1.46}$	$0.353^{+0.214}_{-0.119}$
GRB080723B	13:22:15	48.42-48.82	$-0.89^{+0.42}_{-0.33}$	$-2.93^{+1.31}_{-1.81}$	0.275 (l.l.)
GRB080723B	13:22:15	48.82-49.55	$-0.61^{+0.24}_{-0.23}$	$-2.81^{+0.97}_{-2.00}$	$0.504^{+0.223}_{-0.166}$
GRB080723B	13:22:15	49.55-49.98	$-1.37^{+0.24}_{-0.24}$	$-3.25^{+1.57}_{-1.53}$	0.437 (l.l.)
GRB080723B	13:22:15	49.98-50.33	$-0.53^{+0.32}_{-0.30}$	$-3.63^{+1.47}_{-1.35}$	$0.486^{+0.254}_{-0.168}$
GRB080723B	13:22:15	50.33-50.69	$-1.40^{+0.39}_{-0.26}$	$-3.27^{+1.43}_{-1.63}$	0.194 (l.l.)
GRB080723B	13:22:15	50.69-53.78	$-1.71^{+0.30}_{-0.15}$	$-3.46^{+1.51}_{-1.50}$	unconst.
GRB080723B	13:22:15	53.78-54.9	$-0.90^{+0.25}_{-0.23}$	$-2.53^{+0.75}_{-2.01}$	$0.299^{+0.133}_{-0.098}$
GRB080723B	13:22:15	54.9-58.31	$-1.07^{+0.16}_{-0.16}$	$-3.31^{+1.31}_{-1.59}$	$0.359^{+0.148}_{-0.107}$
GRB080723B	13:22:15	58.31-60.96	$-1.59^{+0.13}_{-0.13}$	$-3.31^{+1.61}_{-1.53}$	unconst.

Continued on Next Page

Table 1: Continued

Global			Band		
GRB-Name	**Ref. Time**	**Active Time [s]**	α	β	E_{peak} **[MeV]**
GRB080723B	13:22:15	60.96-61.2	$-0.98^{+0.37}_{-0.29}$	$-3.43^{+1.51}_{-1.55}$	0.332 (l.l.)
GRB080723B	13:22:15	61.2-61.37	$-0.60^{+0.27}_{-0.25}$	$-3.54^{+1.35}_{-1.46}$	$0.734^{+0.442}_{-0.256}$
GRB080723B	13:22:15	61.37-61.69	$-0.72^{+0.31}_{-0.30}$	$-3.71^{+1.36}_{-1.29}$	$0.458^{+0.263}_{-0.173}$
GRB080723B	13:22:15	61.69-61.96	$-0.56^{+0.27}_{-0.24}$	$-3.01^{+1.20}_{-1.71}$	$0.516^{+0.243}_{-0.164}$
GRB080723B	13:22:15	61.96-62.39	$-0.81^{+0.25}_{-0.25}$	$-3.48^{+1.43}_{-1.47}$	$0.563^{+0.378}_{-0.211}$
GRB080723B	13:22:15	62.39-63.14	$-0.59^{+0.16}_{-0.14}$	$-3.53^{+1.08}_{-1.44}$	$0.438^{+0.092}_{-0.068}$
GRB080723B	13:22:15	63.14-63.64	$-1.19^{+0.24}_{-0.28}$	$-3.29^{+1.31}_{-1.70}$	$0.481^{+1.524}_{-0.252}$
GRB080723B	13:22:15	63.64-64.69	$-1.08^{+0.28}_{-0.30}$	$-3.74^{+1.39}_{-1.26}$	$0.390^{+0.560}_{-0.180}$
GRB080723B	13:22:15	64.69-64.78	$-0.75^{+0.36}_{-0.41}$	$-3.56^{+1.43}_{-1.44}$	$0.558^{+0.954}_{-0.257}$
GRB080723B	13:22:15	64.78-65.31	$-0.78^{+0.25}_{-0.25}$	$-3.77^{+1.33}_{-1.23}$	$0.487^{+0.266}_{-0.156}$
GRB080723B	13:22:15	65.31-65.53	$-0.82^{+0.24}_{-0.24}$	$-3.86^{+1.28}_{-1.14}$	$0.475^{+0.216}_{-0.151}$
GRB080723B	13:22:15	65.53-65.84	$-1.60^{+0.19}_{-0.18}$	$-3.34^{+1.57}_{-1.52}$	unconst.
GRB080723B	13:22:15	65.84-68.72	$-1.45^{+0.18}_{-0.18}$	$-3.28^{+1.57}_{-1.57}$	0.905 (l.l.)
GRB080723B	13:22:15	68.72-82.21	$-1.60^{+0.24}_{-0.26}$	$-3.30^{+1.50}_{-1.57}$	unconst.
GRB080723B	13:22:15	82.21-83.5	$-1.22^{+0.50}_{-0.30}$	$-3.32^{+1.50}_{-1.62}$	0.207 (l.l.)
GRB080723B	13:22:15	83.5-92.17	$-1.63^{+0.17}_{-0.18}$	$-3.32^{+1.47}_{-1.65}$	0.405 (l.l.)
GRB081003B	20:48:08	2.02-15.47	-	-	-
GRB081016	06:51:31	1.48-2.05	$-1.49^{+0.76}_{-0.51}$	$-3.39^{+1.57}_{-1.56}$	unconst.
GRB081016	06:51:31	2.05-2.75	$-1.08^{+0.54}_{-0.57}$	$-3.38^{+1.32}_{-1.50}$	0.120 (l.l.)
GRB081016	06:51:31	4.56-4.97	$-0.83^{+0.43}_{-0.76}$	$-3.64^{+1.24}_{-1.33}$	$0.176^{+0.898}_{-0.061}$
GRB081016	06:51:31	24.71-26.43	$-1.80^{+0.38}_{-0.15}$	$-3.45^{+1.37}_{-1.53}$	unconst.
GRB081016	06:51:31	26.43-28.65	$-1.97^{+0.23}_{-0.03}$	$-3.54^{+1.49}_{-1.31}$	unconst.
GRB081226B	12:13:11	0.11-0.27	$-1.27^{+0.44}_{-0.41}$	$-3.27^{+1.58}_{-1.53}$	unconst.
GRB090107B	16:20:36	3.93-19.2	$-1.59^{+0.21}_{-0.21}$	$-3.29^{+1.57}_{-1.59}$	unconst.
GRB090625B	13:26:20	0.6-7.92	$-1.51^{+0.56}_{-0.19}$	$-3.34^{+1.45}_{-1.64}$	unconst.
GRB090817	00:51:23	2.39-5.85	$-0.63^{+0.37}_{-0.39}$	$-3.12^{+1.31}_{-1.68}$	$0.336^{+0.307}_{-0.119}$
GRB090817	00:51:23	5.85-14.04	$-1.89^{+0.18}_{-0.11}$	$-3.47^{+1.48}_{-1.41}$	unconst.
GRB100103A	17:42:30	8.43-13.46	$-1.03^{+0.35}_{-0.33}$	$-3.33^{+1.58}_{-1.58}$	0.703 (l.l.)

Continued on Next Page

Table 1: Continued

Global			Band		
GRB-Name	**Ref. Time**	**Active Time [s]**	α	β	E_{peak} **[MeV]**
GRB100103A	17:42:30	13.46-23.88	$-0.84^{+0.26}_{-0.25}$	$-3.66^{+1.32}_{-1.34}$	$0.240^{+0.094}_{-0.055}$
GRB100103A	17:42:30	23.88-38.63	$-1.81^{+0.18}_{-0.16}$	$-3.39^{+1.51}_{-1.47}$	unconst.
GRB101112A	22:10:20	11.98-13.96	$-1.10^{+0.34}_{-0.53}$	$-3.77^{+1.40}_{-1.23}$	$0.147^{+0.234}_{-0.053}$
GRB101112A	22:10:20	13.96-15.88	$-1.54^{+0.54}_{-0.45}$	$-3.24^{+1.39}_{-1.76}$	0.683 (l.l.)
GRB110206A	18:08:10	-0.26-3.8	$-1.67^{+0.27}_{-0.23}$	$-3.41^{+1.53}_{-1.49}$	unconst.
GRB110903A	02:38:30	64.15-68.63	-	-	-
GRB110903A	02:38:30	71.51-78.76	-	-	-
GRB110903A	02:38:30	82.29-85.83	$0.26^{+1.05}_{-1.07}$	$-3.61^{+1.39}_{-1.34}$	$0.181^{+0.135}_{-0.061}$
GRB110903A	02:38:30	258.78-273.42	-	-	-
GRB110903A	02:38:30	384.08-400.0	$-1.66^{+0.42}_{-0.34}$	$-3.32^{+1.48}_{-1.58}$	unconst.
GRB120512A	02:41:40	3.57-16.89	$-1.47^{+0.47}_{-0.38}$	$-3.37^{+1.52}_{-1.59}$	0.523 (l.l.)
GRB120711A	02:44:48	3.47-8.42	$-1.13^{+0.40}_{-0.30}$	$-3.39^{+1.45}_{-1.61}$	0.243 (l.l.)
GRB120711A	02:44:48	67.1-69.39	$-0.92^{+0.25}_{-0.25}$	$-3.18^{+1.43}_{-1.72}$	0.388 (l.l.)
GRB120711A	02:44:48	69.39-72.73	$-1.00^{+0.10}_{-0.10}$	$-3.24^{+1.63}_{-1.56}$	1.217 (l.l.)
GRB120711A	02:44:48	72.73-77.49	$-0.86^{+0.07}_{-0.07}$	$-3.67^{+1.40}_{-1.33}$	$1.228^{+0.254}_{-0.231}$
GRB120711A	02:44:48	77.49-81.43	$-0.94^{+0.11}_{-0.10}$	$-3.03^{+1.21}_{-1.78}$	$0.854^{+0.293}_{-0.247}$
GRB120711A	02:44:48	81.43-86.42	$-1.01^{+0.13}_{-0.12}$	$-3.75^{+1.41}_{-1.25}$	$0.749^{+0.328}_{-0.236}$
GRB120711A	02:44:48	86.42-88.16	$-0.77^{+0.23}_{-0.19}$	$-3.24^{+1.29}_{-1.74}$	$0.597^{+0.294}_{-0.217}$
GRB120711A	02:44:48	88.16-91.01	$-1.12^{+0.25}_{-0.24}$	$-3.00^{+1.33}_{-1.82}$	0.274 (l.l.)
GRB120711A	02:44:48	91.01-95.92	$-0.92^{+0.09}_{-0.08}$	$-3.14^{+1.36}_{-1.74}$	$0.966^{+0.278}_{-0.282}$
GRB120711A	02:44:48	95.92-98.96	$-0.93^{+0.10}_{-0.10}$	$-2.63^{+0.95}_{-2.07}$	$0.934^{+0.322}_{-0.291}$
GRB120711A	02:44:48	98.96-99.06	$-0.84^{+0.31}_{-0.25}$	$-3.37^{+1.52}_{-1.57}$	0.669 (l.l.)
GRB120711A	02:44:48	99.06-100.61	$-1.05^{+0.11}_{-0.09}$	$-3.31^{+1.55}_{-1.63}$	1.322 (l.l.)
GRB120711A	02:44:48	100.61-100.67	$-0.77^{+0.42}_{-0.33}$	$-3.13^{+1.52}_{-1.63}$	0.409 (l.l.)
GRB120711A	02:44:48	100.67-101.44	$-0.94^{+0.13}_{-0.13}$	$-3.30^{+1.52}_{-1.64}$	1.043 (l.l.)
GRB120711A	02:44:48	101.44-107.53	$-0.87^{+0.06}_{-0.06}$	$-3.68^{+1.35}_{-1.32}$	$1.349^{+0.269}_{-0.232}$
GRB120711A	02:44:48	107.53-107.93	$-0.55^{+0.21}_{-0.20}$	$-3.63^{+1.38}_{-1.37}$	$0.718^{+0.248}_{-0.189}$
GRB120711A	02:44:48	107.93-109.55	$-0.88^{+0.13}_{-0.13}$	$-3.44^{+1.44}_{-1.55}$	$1.011^{+0.445}_{-0.337}$

Continued on Next Page

Table 1: Continued

Global			Band		
GRB-Name	**Ref. Time**	**Active Time [s]**	α	β	E_{peak} **[MeV]**
GRB120711A	02:44:48	109.55-110.37	$-1.17^{+0.27}_{-0.22}$	$-3.14^{+1.47}_{-1.66}$	0.284 (l.l.)
GRB120711A	02:44:48	110.37-112.24	$-1.49^{+0.16}_{-0.16}$	$-3.36^{+1.62}_{-1.54}$	0.597 (l.l.)
GRB120711A	02:44:48	112.24-112.89	$-0.85^{+0.27}_{-0.28}$	$-3.19^{+1.38}_{-1.69}$	$0.883^{+1.579}_{-0.460}$
GRB120711A	02:44:48	112.89-116.03	$-1.65^{+0.17}_{-0.16}$	$-3.23^{+1.42}_{-1.69}$	unconst.
GRB120711A	02:44:48	116.03-126.73	$-1.58^{+0.24}_{-0.26}$	$-3.34^{+1.61}_{-1.52}$	unconst.
GRB121102A	02:27:02	1.98-11.73	$-1.90^{+0.18}_{-0.10}$	$-3.58^{+1.62}_{-1.29}$	unconst.
GRB121102A	02:27:02	11.73-11.74	-	-	-
GRB130513A	07:38:10	15.43-53.8	$-1.57^{+0.23}_{-0.24}$	$-3.27^{+1.50}_{-1.66}$	0.795 (l.l.)
GRB130514B	13:26:32	0.44-1.5	$-1.54^{+0.20}_{-0.17}$	$-3.34^{+1.60}_{-1.52}$	0.265 (l.l.)
GRB130514B	13:26:32	1.5-2.75	$-1.61^{+0.30}_{-0.23}$	$-3.42^{+1.55}_{-1.51}$	unconst.
GRB130514B	13:26:32	2.75-9.91	-	-	-
GRB131122A	21:25:01	10.6-17.22	$-1.06^{+1.92}_{-0.96}$	$-3.26^{+1.57}_{-1.58}$	0.539 (l.l.)
GRB131218A	21:05:32	0.77-5.53	$-1.39^{+0.64}_{-0.34}$	$-3.26^{+1.48}_{-1.61}$	unconst.
GRB131224A	16:54:37	14.23-14.4	$1.83^{+1.17}_{-2.62}$	$-3.26^{+1.30}_{-1.62}$	$0.145^{+0.418}_{-0.064}$
GRB140710B	21:37:30	3.7-28.55	$-1.88^{+0.17}_{-0.12}$	$-3.42^{+1.42}_{-1.47}$	unconst.
GRB140815A	21:55:05	0.62-2.49	$-1.73^{+0.56}_{-0.27}$	$-3.28^{+1.43}_{-1.63}$	unconst.
GRB140815A	21:55:05	103.41-103.43	$-0.24^{+1.97}_{-0.86}$	$-3.16^{+1.54}_{-1.63}$	unconst.
GRB141004A	23:20:54	0.36-1.13	$-1.80^{+0.20}_{-0.19}$	$-3.38^{+1.46}_{-1.48}$	unconst.
GRB151120	08:22:50	4.07-7.7	$0.14^{+0.31}_{-0.32}$	$-3.60^{+1.20}_{-1.33}$	$0.256^{+0.050}_{-0.037}$
GRB151120	08:22:50	7.7-18.24	$-1.07^{+0.25}_{-0.29}$	$-2.96^{+0.90}_{-1.78}$	$0.144^{+0.052}_{-0.033}$
GRB151120	08:22:50	18.24-25.21	$-1.96^{+0.10}_{-0.04}$	$-3.44^{+1.46}_{-1.36}$	unconst.
GRB160223B	09:58:58	2.63-16.86	$-1.17^{+0.29}_{-0.20}$	$-3.35^{+1.64}_{-1.53}$	0.331 (l.l.)
GRB160401A	20:20:30	1.8-38.1	$-1.90^{+0.13}_{-0.10}$	$-3.42^{+1.37}_{-1.52}$	unconst.
GRB160521	03:37:20	98.17-122.25	$-1.48^{+0.27}_{-0.25}$	$-3.35^{+1.51}_{-1.64}$	0.719 (l.l.)
GRB160629A	22:19:30	9.76-30.72	$-0.92^{+0.23}_{-0.25}$	$-3.38^{+1.32}_{-1.52}$	$0.287^{+0.148}_{-0.081}$
GRB161010A	13:36:25	4.73-8.09	$-1.70^{+0.46}_{-0.21}$	$-3.56^{+1.47}_{-1.41}$	0.111 (l.l.)
GRB161010A	13:36:25	8.09-9.27	$-1.28^{+0.34}_{-0.44}$	$-3.38^{+1.26}_{-1.56}$	$0.225^{+2.565}_{-0.110}$
GRB161010A	13:36:25	9.27-10.92	$-1.08^{+0.32}_{-0.25}$	$-2.37^{+0.55}_{-2.07}$	$0.258^{+0.130}_{-0.107}$

Continued on Next Page

Table 1: Continued

Global			Band		
GRB-Name	**Ref. Time**	**Active Time [s]**	α	β	E_{peak} **[MeV]**
GRB161010A	13:36:25	10.92-11.79	$-1.16^{+0.37}_{-0.35}$	$-3.43^{+1.35}_{-1.48}$	$0.300^{+0.411}_{-0.147}$
GRB161010A	13:36:25	11.79-13.46	$-1.23^{+0.36}_{-0.43}$	$-3.68^{+1.40}_{-1.32}$	$0.272^{+2.034}_{-0.124}$
GRB161010A	13:36:25	13.46-14.34	$-1.00^{+0.34}_{-0.28}$	$-3.57^{+1.31}_{-1.43}$	$0.353^{+0.246}_{-0.155}$
GRB161010A	13:36:25	14.34-16.94	$-1.82^{+0.10}_{-0.10}$	$-3.35^{+1.42}_{-1.54}$	unconst.
GRB161010A	13:36:25	16.94-25.92	$-1.88^{+0.15}_{-0.12}$	$-3.47^{+1.51}_{-1.40}$	unconst.
GRB161023A	22:38:40	14.4-19.16	$-1.48^{+0.47}_{-0.22}$	$-3.49^{+1.54}_{-1.51}$	0.151 (l.l.)
GRB161023A	22:38:40	19.16-29.94	$-1.37^{+0.15}_{-0.16}$	$-3.50^{+1.47}_{-1.49}$	$0.574^{+1.282}_{-0.353}$
GRB161023A	22:38:40	29.94-36.07	$-1.16^{+0.15}_{-0.13}$	$-3.08^{+1.25}_{-1.72}$	$0.501^{+0.279}_{-0.192}$
GRB161023A	22:38:40	36.07-38.22	$-1.11^{+0.35}_{-0.37}$	$-3.59^{+1.37}_{-1.39}$	$0.266^{+0.455}_{-0.113}$
GRB161023A	22:38:40	38.22-38.83	$-1.13^{+0.37}_{-0.38}$	$-3.24^{+1.29}_{-1.70}$	0.188 (l.l.)
GRB161023A	22:38:40	38.83-40.64	$-1.35^{+0.44}_{-0.32}$	$-3.31^{+1.36}_{-1.51}$	$0.200^{+0.277}_{-0.105}$
GRB161023A	22:38:40	40.64-42.95	$-1.88^{+0.11}_{-0.11}$	$-3.47^{+1.46}_{-1.43}$	unconst.
GRB161023A	22:38:40	42.95-50.67	$-1.61^{+0.23}_{-0.30}$	$-3.50^{+1.26}_{-1.44}$	0.092 (l.l.)
GRB161023A	22:38:40	50.67-66.85	$-1.69^{+0.19}_{-0.21}$	$-3.28^{+1.52}_{-1.56}$	unconst.
GRB180626	08:21:04	3.42-7.17	$-1.84^{+0.34}_{-0.16}$	$-3.41^{+1.44}_{-1.53}$	unconst.
GRB180626	08:21:04	7.17-13.41	-	-	-
GRB180626	08:21:04	13.41-29.05	-	-	-
GRB181127A	06:46:21	4.25-11.18	$-1.83^{+0.43}_{-0.17}$	$-3.25^{+1.34}_{-1.67}$	unconst.
GRB181201A	02:38:00	1.94-23.06	$-1.42^{+0.34}_{-0.16}$	$-2.89^{+1.27}_{-1.82}$	0.158 (l.l.)
GRB181201A	02:38:00	23.06-49.81	$-1.97^{+0.06}_{-0.03}$	$-3.44^{+1.45}_{-1.33}$	unconst.
GRB181201A	02:38:00	113.37-114.3	$-1.17^{+0.37}_{-0.39}$	$-3.69^{+1.40}_{-1.30}$	$0.319^{+1.052}_{-0.145}$
GRB181201A	02:38:00	114.3-115.38	$-1.14^{+0.21}_{-0.21}$	$-3.17^{+1.02}_{-1.60}$	$0.227^{+0.075}_{-0.054}$
GRB181201A	02:38:00	115.38-116.46	$-1.06^{+0.21}_{-0.18}$	$-2.61^{+0.60}_{-1.37}$	$0.235^{+0.061}_{-0.062}$
GRB181201A	02:38:00	116.46-117.99	$-0.95^{+0.24}_{-0.17}$	$-2.66^{+0.57}_{-1.63}$	$0.218^{+0.048}_{-0.054}$
GRB181201A	02:38:00	117.99-119.97	$-0.95^{+0.10}_{-0.09}$	$-3.08^{+0.49}_{-0.73}$	$0.189^{+0.016}_{-0.016}$
GRB181201A	02:38:00	119.97-121.17	$-0.88^{+0.17}_{-0.15}$	$-2.85^{+0.38}_{-0.54}$	$0.130^{+0.013}_{-0.012}$
GRB181201A	02:38:00	121.17-122.48	$-1.13^{+0.21}_{-0.23}$	$-2.48^{+0.29}_{-0.86}$	$0.128^{+0.033}_{-0.020}$
GRB181201A	02:38:00	122.48-125.16	$-1.18^{+0.21}_{-0.23}$	$-2.51^{+0.27}_{-0.76}$	$0.101^{+0.019}_{-0.013}$

Continued on Next Page

Table 1: Continued

Global			Band		
GRB-Name	**Ref. Time**	**Active Time [s]**	α	β	E_{peak} **[MeV]**
GRB181201A	02:38:00	125.16-126.17	$-1.37^{+0.39}_{-0.30}$	$-3.30^{+0.88}_{-1.46}$	$0.081^{+0.015}_{-0.014}$
GRB181201A	02:38:00	126.17-127.97	$-1.67^{+0.17}_{-0.16}$	$-3.19^{+0.83}_{-1.31}$	$0.076^{+0.015}_{-0.018}$
GRB181201A	02:38:00	127.97-131.08	$-1.52^{+0.19}_{-0.19}$	$-3.98^{+0.92}_{-1.00}$	$0.073^{+0.010}_{-0.011}$
GRB181201A	02:38:00	131.08-135.12	$-1.94^{+0.14}_{-0.06}$	$-3.43^{+1.20}_{-1.52}$	0.011 (l.l.)
GRB181201A	02:38:00	135.12-139.54	$-1.84^{+0.23}_{-0.16}$	$-3.45^{+1.21}_{-1.41}$	0.010 (l.l.)
GRB181201A	02:38:00	139.54-147.77	$-1.76^{+0.31}_{-0.19}$	$-3.26^{+0.99}_{-1.53}$	$0.033^{+0.021}_{-0.020}$
GRB181201A	02:38:00	147.77-162.07	$-1.97^{+0.08}_{-0.03}$	$-3.48^{+1.41}_{-1.40}$	unconst.
GRB190220B	20:14:30	56.25-95.83	$-1.66^{+0.22}_{-0.22}$	$-3.38^{+1.57}_{-1.52}$	unconst.
GRB190411A	09:45:48	-1.21-1.21	$-1.22^{+1.72}_{-0.68}$	$-3.21^{+1.54}_{-1.63}$	unconst.
GRB190411A	09:45:48	1.21-3.84	$-1.41^{+0.31}_{-0.21}$	$-3.32^{+1.56}_{-1.60}$	0.877 (l.l.)
GRB190411A	09:45:48	3.84-4.42	$-1.37^{+0.45}_{-0.34}$	$-3.26^{+1.57}_{-1.62}$	1.120 (l.l.)
GRB190411A	09:45:48	4.42-6.24	$-1.34^{+0.20}_{-0.16}$	$-3.30^{+1.63}_{-1.53}$	1.921 (l.l.)
GRB190411A	09:45:48	29.58-34.96	-	-	-
GRB190411A	09:45:48	159.7-173.44	$-1.55^{+0.40}_{-0.25}$	$-3.49^{+1.54}_{-1.43}$	0.499 (l.l.)
GRB190701B	10:05:00	-1.28-1.49	$-1.13^{+0.91}_{-0.48}$	$-3.38^{+1.66}_{-1.47}$	unconst.
GRB190701B	10:05:00	1.49-2.9	$-1.36^{+0.41}_{-0.22}$	$-3.23^{+1.49}_{-1.63}$	0.194 (l.l.)
GRB190701B	10:05:00	2.9-7.1	$-1.57^{+0.17}_{-0.16}$	$-3.30^{+1.60}_{-1.56}$	unconst.
GRB190701B	10:05:00	7.1-19.51	$-1.83^{+0.16}_{-0.15}$	$-3.40^{+1.39}_{-1.54}$	unconst.
GRB190719B	03:13:40	320.77-320.83	-	-	-
GRB190828D	18:48:30	3.54-3.69	$-0.78^{+1.04}_{-0.52}$	$-3.17^{+1.56}_{-1.65}$	0.282 (l.l.)
GRB190828D	18:48:30	3.69-5.34	$-0.79^{+0.30}_{-0.26}$	$-3.36^{+1.58}_{-1.55}$	0.855 (l.l.)
GRB190828D	18:48:30	5.34-8.87	$-0.94^{+0.51}_{-0.34}$	$-3.44^{+1.67}_{-1.49}$	0.372 (l.l.)
GRB190919B	23:46:40	18.16-20.47	$-1.83^{+1.28}_{-0.17}$	$-3.42^{+1.51}_{-1.48}$	unconst.
GRB200424A	12:07:10	0.8-0.9	$-0.91^{+1.06}_{-0.62}$	$-3.43^{+1.56}_{-1.53}$	0.165 (l.l.)
GRB200424A	12:07:10	1.52-1.99	$-0.61^{+0.41}_{-0.40}$	$-3.52^{+1.49}_{-1.46}$	$0.645^{+0.892}_{-0.311}$
GRB200424A	12:07:10	6.69-9.23	$-0.82^{+0.25}_{-0.26}$	$-3.23^{+1.40}_{-1.72}$	$0.989^{+1.689}_{-0.579}$
GRB200424A	12:07:10	9.23-9.82	$-0.34^{+0.31}_{-0.27}$	$-2.54^{+0.94}_{-2.04}$	$0.720^{+0.353}_{-0.277}$
GRB200424A	12:07:10	9.82-11.5	$-0.90^{+0.36}_{-0.30}$	$-3.27^{+1.53}_{-1.63}$	0.372 (l.l.)

Continued on Next Page

Table 1: Continued

Global			**Band**		
GRB-Name	**Ref. Time**	**Active Time [s]**	α	β	E_{peak} **[MeV]**
GRB200424A	12:07:10	14.45-14.79	$-1.05^{+0.62}_{-0.38}$	$-3.35^{+1.49}_{-1.59}$	0.227 (l.l.)
GRB200424A	12:07:10	14.79-19.73	$-1.54^{+0.35}_{-0.38}$	$-3.37^{+1.58}_{-1.55}$	unconst.
GRB200424A	12:07:10	19.73-21.94	$-1.27^{+0.18}_{-0.14}$	$-3.24^{+1.47}_{-1.68}$	0.488 (l.l.)
GRB200424A	12:07:10	21.94-24.05	$-1.73^{+0.25}_{-0.27}$	$-3.40^{+1.40}_{-1.60}$	unconst.
GRB200424A	12:07:10	24.05-24.82	$-1.10^{+0.45}_{-0.35}$	$-3.50^{+1.53}_{-1.50}$	0.238 (l.l.)
GRB200424A	12:07:10	27.75-34.35	$-1.35^{+0.20}_{-0.17}$	$-3.45^{+1.47}_{-1.53}$	0.290 (l.l.)
GRB200424A	12:07:10	34.35-48.97	$-1.46^{+0.20}_{-0.16}$	$-3.37^{+1.62}_{-1.51}$	unconst.
GRB200424A	12:07:10	48.97-76.0	$-1.49^{+0.26}_{-0.31}$	$-3.24^{+1.53}_{-1.60}$	0.811 (l.l.)
GRB200715A	23:51:40	20.87-49.92	$-1.14^{+0.41}_{-0.31}$	$-3.20^{+1.47}_{-1.66}$	0.158 (l.l.)
GRB200715A	23:51:40	143.72-152.96	$-1.28^{+0.26}_{-0.22}$	$-3.29^{+1.66}_{-1.49}$	0.490 (l.l.)
GRB200715A	23:51:40	152.96-155.19	$-1.31^{+0.39}_{-0.39}$	$-3.29^{+1.48}_{-1.68}$	0.707 (l.l.)
GRB201006A	01:17:51	0.79-2.52	$-1.58^{+0.49}_{-0.42}$	$-3.24^{+1.42}_{-1.68}$	unconst.
GRB210208A	13:32:23	2.14-4.34	$-1.28^{+0.28}_{-0.27}$	$-3.30^{+1.60}_{-1.55}$	0.438 (l.l.)
GRB210406A	17:11:22	6.34-9.4	$-1.09^{+0.77}_{-0.41}$	$-3.47^{+1.50}_{-1.52}$	0.174 (l.l.)
GRB210406A	17:11:22	9.4-19.82	$-0.24^{+0.32}_{-0.33}$	$-2.70^{+0.75}_{-1.67}$	$0.173^{+0.039}_{-0.032}$
GRB210406A	17:11:22	19.82-23.91	$-0.80^{+0.72}_{-0.59}$	$-3.66^{+1.53}_{-1.34}$	0.143 (l.l.)
GRB210406A	17:11:22	23.91-39.78	$-1.79^{+0.24}_{-0.21}$	$-3.41^{+1.50}_{-1.49}$	0.546 (l.l.)

Table 2: Parameter constrains for empirical cutoff power law model fits. Entries with no parameter values indicate that the fit has failed for this time bin and spectral model. Entries with 'u.l.' and 'l.l.' indicate upper and lower limits and 'unconst.' that the parameter is unconstrained.

Global			**CPL**	
GRB-Name	**Ref. Time**	**Active Time [s]**	α	E_{peak} **[MeV]**
GRB030227	08:42:02	2.88-8.24	$-2.03^{+0.30}_{-0.30}$	unconst.
GRB030501	03:10:02	9.95-26.03	$-1.85^{+0.27}_{-0.19}$	unconst.
GRB030529	19:53:18	34.27-42.41	$-1.77^{+0.80}_{-1.05}$	unconst.
GRB030529	19:53:18	42.41-54.81	-	-
GRB030529	19:53:18	54.81-68.57	-	-
GRB031203	22:01:27	-1.01-14.73	$-1.48^{+0.21}_{-0.23}$	0.633 (l.l.)
GRB031203	22:01:27	218.53-218.56	$-1.61^{+1.16}_{-1.38}$	unconst.
GRB040106	17:55:10	2.5-5.29	$-1.88^{+0.77}_{-0.93}$	unconst.
GRB040106	17:55:10	42.3-52.18	$-1.35^{+0.31}_{-0.29}$	0.908 (l.l.)
GRB040323	13:02:58	0.91-12.75	$-0.50^{+0.51}_{-0.55}$	$0.224^{+0.163}_{-0.071}$
GRB040422	06:57:59	3.45-5.47	$-2.25^{+0.42}_{-0.49}$	unconst.
GRB040422	06:57:59	5.47-6.56	$-1.97^{+0.21}_{-0.21}$	unconst.
GRB040730	02:12:06	10.43-21.36	$-1.00^{+0.53}_{-0.54}$	unconst.
GRB040812	06:01:52	39.57-39.67	-	-
GRB041218	15:45:44	2.22-6.43	$-1.25^{+0.40}_{-0.33}$	0.188 (l.l.)
GRB041218	15:45:44	6.43-20.65	$-1.42^{+0.32}_{-0.49}$	0.081 (l.l.)
GRB041218	15:45:44	34.3-34.33	$-0.74^{+3.51}_{-1.58}$	unconst.
GRB041218	15:45:44	34.33-41.03	$-1.79^{+0.22}_{-0.23}$	unconst.
GRB041219A	01:42:13	5.33-8.68	$0.08^{+0.32}_{-0.32}$	$0.248^{+0.045}_{-0.034}$
GRB041219A	01:42:13	8.68-11.89	$-1.19^{+0.68}_{-0.53}$	0.104 (l.l.)
GRB041219A	01:42:13	11.89-21.18	$-1.60^{+0.41}_{-0.40}$	unconst.
GRB041219A	01:42:13	218.93-239.37	$-0.85^{+1.02}_{-0.58}$	0.256 (l.l.)
GRB041219A	01:42:13	239.37-265.77	$-1.43^{+0.19}_{-0.21}$	$0.286^{+0.852}_{-0.132}$
GRB041219A	01:42:13	265.77-267.79	$-1.56^{+0.18}_{-0.18}$	unconst.
GRB041219A	01:42:13	267.79-272.99	$-1.17^{+0.17}_{-0.16}$	$0.260^{+0.092}_{-0.059}$
GRB041219A	01:42:13	272.99-275.91	-	-

Continued on Next Page

Table 2: Continued

Global			CPL	
GRB-Name	**Ref. Time**	**Active Time [s]**	α	E_{peak} **[MeV]**
GRB041219A	01:42:13	275.91-277.53	$-1.20^{+0.16}_{-0.15}$	$0.326^{+0.123}_{-0.088}$
GRB041219A	01:42:13	277.53-283.01	-	-
GRB041219A	01:42:13	283.01-285.61	-	-
GRB041219A	01:42:13	285.61-286.7	-	-
GRB041219A	01:42:13	286.7-288.23	-	-
GRB041219A	01:42:13	288.23-293.17	-	-
GRB041219A	01:42:13	293.17-297.14	$-1.42^{+0.13}_{-0.13}$	$0.311^{+0.140}_{-0.096}$
GRB041219A	01:42:13	297.14-304.81	-	-
GRB041219A	01:42:13	304.81-312.8	-	-
GRB041219A	01:42:13	312.8-317.41	$-1.62^{+0.19}_{-0.20}$	0.141 (l.l.)
GRB041219A	01:42:13	317.41-325.82	$-1.69^{+0.24}_{-0.10}$	0.157 (l.l.)
GRB041219A	01:42:13	325.82-333.96	$-1.72^{+0.13}_{-0.11}$	unconst.
GRB041219A	01:42:13	333.96-360.46	$-1.95^{+0.22}_{-0.11}$	unconst.
GRB041219A	01:42:13	360.46-364.16	$-2.07^{+0.17}_{-0.18}$	0.449 (l.l.)
GRB041219A	01:42:13	364.16-370.04	$-1.68^{+0.20}_{-0.17}$	0.134 (l.l.)
GRB041219A	01:42:13	370.04-381.41	-	-
GRB041219A	01:42:13	381.41-386.22	$-2.00^{+0.21}_{-0.11}$	unconst.
GRB041219A	01:42:13	386.22-388.93	$-2.18^{+0.14}_{-0.13}$	0.862 (l.l.)
GRB041219A	01:42:13	388.93-390.89	$-1.95^{+0.11}_{-0.12}$	unconst.
GRB041219A	01:42:13	390.89-391.68	$-1.67^{+0.35}_{-0.30}$	0.090 (l.l.)
GRB041219A	01:42:13	391.68-399.56	-	-
GRB041219A	01:42:13	399.56-407.54	$-2.07^{+0.06}_{-0.06}$	1.249 (l.l.)
GRB041219A	01:42:13	407.54-408.79	$-1.90^{+0.14}_{-0.14}$	unconst.
GRB041219A	01:42:13	408.79-412.52	$-2.24^{+0.10}_{-0.11}$	1.136 (l.l.)
GRB041219A	01:42:13	412.52-417.01	$-2.25^{+0.12}_{-0.13}$	1.064 (l.l.)
GRB041219A	01:42:13	417.01-420.23	$-2.61^{+0.26}_{-0.23}$	0.998 (l.l.)
GRB041219A	01:42:13	420.23-426.25	-	-
GRB041219A	01:42:13	426.25-431.17	$-2.46^{+0.17}_{-0.18}$	0.465 (l.l.)

Continued on Next Page

Table 2: Continued

Global			CPL	
GRB-Name	**Ref. Time**	**Active Time [s]**	α	E_{peak} **[MeV]**
GRB041219A	01:42:13	431.17-441.15	$-2.53^{+0.15}_{-0.18}$	1.099 (l.l.)
GRB041219A	01:42:13	441.15-442.93	$-2.29^{+0.20}_{-0.20}$	0.557 (l.l.)
GRB041219A	01:42:13	442.93-449.58	$-2.50^{+0.17}_{-0.17}$	1.020 (l.l.)
GRB041219A	01:42:13	449.58-469.74	$-2.61^{+0.16}_{-0.17}$	1.117 (l.l.)
GRB041219A	01:42:13	478.36-480.49	$-2.18^{+0.19}_{-0.19}$	0.680 (l.l.)
GRB041219A	01:42:13	484.17-492.81	$-2.36^{+0.16}_{-0.16}$	1.085 (l.l.)
GRB050502A	02:13:55	8.51-21.14	$-1.47^{+0.60}_{-0.22}$	0.139 (l.l.)
GRB050520	00:05:57	52.2-52.7	$-0.30^{+3.13}_{-1.42}$	1.437 (l.l.)
GRB050525A	00:02:53	0.47-1.22	$-1.08^{+0.58}_{-0.55}$	$0.109^{+0.037}_{-0.026}$
GRB050525A	00:02:53	1.22-1.94	$-0.73^{+0.40}_{-0.37}$	$0.142^{+0.024}_{-0.018}$
GRB050525A	00:02:53	1.94-2.32	$-2.19^{+0.26}_{-0.27}$	0.848 (l.l.)
GRB050525A	00:02:53	2.32-5.23	$-2.31^{+0.18}_{-0.21}$	1.107 (l.l.)
GRB050525A	00:02:53	5.23-7.76	$-1.14^{+0.30}_{-0.28}$	$0.094^{+0.012}_{-0.012}$
GRB050525A	00:02:53	7.76-9.75	$-2.65^{+0.31}_{-0.29}$	1.132 (l.l.)
GRB051105B	11:05:41	-0.85-7.6	-	-
GRB060428C	02:30:35	0.27-5.86	$-1.86^{+0.26}_{-0.29}$	unconst.
GRB060428C	02:30:35	5.86-7.47	$-1.85^{+0.27}_{-0.29}$	unconst.
GRB060428C	02:30:35	7.47-10.62	$-0.35^{+0.26}_{-0.31}$	$0.134^{+0.019}_{-0.015}$
GRB060901	18:43:55	-1.39-0.3	$-1.47^{+0.36}_{-0.29}$	0.468 (l.l.)
GRB060901	18:43:55	0.3-4.16	$-0.94^{+0.26}_{-0.27}$	$0.310^{+0.152}_{-0.090}$
GRB060901	18:43:55	4.16-8.05	$-1.49^{+0.48}_{-0.22}$	unconst.
GRB061025	18:35:53	5.71-12.71	$-0.99^{+0.75}_{-0.63}$	$0.196^{+0.383}_{-0.103}$
GRB061122	07:56:50	-0.21-0.73	$0.03^{+2.70}_{-1.77}$	0.083 (l.l.)
GRB061122	07:56:50	0.73-1.96	$-1.84^{+0.11}_{-0.11}$	0.593 (l.l.)
GRB061122	07:56:50	1.96-2.58	$-1.31^{+0.23}_{-0.31}$	$0.271^{+0.697}_{-0.104}$
GRB061122	07:56:50	2.58-3.47	$-0.63^{+0.15}_{-0.16}$	$0.225^{+0.026}_{-0.025}$
GRB061122	07:56:50	3.47-4.76	$-0.57^{+0.11}_{-0.11}$	$0.197^{+0.013}_{-0.012}$
GRB061122	07:56:50	4.76-4.95	$-0.44^{+0.34}_{-0.37}$	$0.153^{+0.030}_{-0.018}$

Continued on Next Page

Table 2: Continued

Global			CPL	
GRB-Name	**Ref. Time**	**Active Time [s]**	α	E_{peak} **[MeV]**
GRB061122	07:56:50	4.95-6.05	$-0.89^{+0.15}_{-0.18}$	$0.124^{+0.010}_{-0.009}$
GRB061122	07:56:50	6.05-7.1	$-1.29^{+0.20}_{-0.21}$	$0.157^{+0.047}_{-0.030}$
GRB061122	07:56:50	7.1-8.37	$-1.99^{+0.14}_{-0.14}$	unconst.
GRB061122	07:56:50	8.37-12.45	$-2.28^{+0.26}_{-0.26}$	0.727 (l.l.)
GRB070311	01:52:34	-2.86-36.01	$-1.36^{+0.22}_{-0.17}$	0.340 (l.l.)
GRB070707	16:08:38	0.59-0.96	$-1.03^{+0.30}_{-0.28}$	0.355 (l.l.)
GRB070925	15:52:32	11.86-14.48	$-1.48^{+0.32}_{-0.31}$	unconst.
GRB070925	15:52:32	14.48-23.81	$-0.88^{+0.19}_{-0.20}$	$0.200^{+0.047}_{-0.035}$
GRB071003	07:40:55	-1.61-0.08	-	-
GRB071003	07:40:55	0.08-2.5	$-0.84^{+0.16}_{-0.16}$	$0.972^{+0.513}_{-0.340}$
GRB071003	07:40:55	2.5-4.06	$-1.30^{+0.45}_{-0.42}$	unconst.
GRB071003	07:40:55	4.06-5.46	$-0.39^{+0.27}_{-0.30}$	$1.260^{+0.949}_{-0.480}$
GRB071003	07:40:55	5.46-6.5	-	-
GRB071003	07:40:55	6.5-6.88	$-0.40^{+0.53}_{-0.58}$	$0.844^{+2.019}_{-0.438}$
GRB071003	07:40:55	6.88-12.91	-	-
GRB071003	07:40:55	12.91-21.45	$-1.68^{+0.40}_{-0.26}$	unconst.
GRB080723B	13:22:15	6.58-7.79	$-1.50^{+0.50}_{-0.23}$	unconst.
GRB080723B	13:22:15	7.79-8.72	$-0.14^{+0.29}_{-0.31}$	$0.191^{+0.031}_{-0.022}$
GRB080723B	13:22:15	9.04-9.29	$-0.98^{+0.33}_{-0.37}$	$0.456^{+1.110}_{-0.207}$
GRB080723B	13:22:15	9.29-9.83	$-2.54^{+0.45}_{-0.45}$	0.949 (l.l.)
GRB080723B	13:22:15	17.34-18.01	$-0.85^{+0.63}_{-0.65}$	$0.191^{+0.235}_{-0.077}$
GRB080723B	13:22:15	18.01-18.31	$-0.34^{+0.34}_{-0.34}$	$0.271^{+0.084}_{-0.048}$
GRB080723B	13:22:15	18.31-18.96	$-1.06^{+0.30}_{-0.29}$	$0.182^{+0.069}_{-0.042}$
GRB080723B	13:22:15	18.96-19.8	$-0.32^{+0.18}_{-0.17}$	$0.232^{+0.025}_{-0.022}$
GRB080723B	13:22:15	19.8-20.5	$-0.68^{+0.25}_{-0.25}$	$0.212^{+0.051}_{-0.035}$
GRB080723B	13:22:15	20.5-20.85	$-0.24^{+0.26}_{-0.25}$	$0.218^{+0.033}_{-0.025}$
GRB080723B	13:22:15	20.85-21.67	$-0.68^{+0.23}_{-0.24}$	$0.203^{+0.043}_{-0.030}$
GRB080723B	13:22:15	21.67-22.11	$-2.04^{+0.28}_{-0.33}$	unconst.

Continued on Next Page

Table 2: Continued

Global			CPL	
GRB-Name	**Ref. Time**	**Active Time [s]**	α	E_{peak} **[MeV]**
GRB080723B	13:22:15	22.11-22.67	$-0.99^{+0.35}_{-0.38}$	$0.159^{+0.078}_{-0.036}$
GRB080723B	13:22:15	22.67-24.38	$-1.83^{+0.19}_{-0.17}$	unconst.
GRB080723B	13:22:15	24.38-26.73	$-2.09^{+0.46}_{-0.46}$	unconst.
GRB080723B	13:22:15	26.73-27.0	$-1.41^{+0.29}_{-0.29}$	0.726 (l.l.)
GRB080723B	13:22:15	27.0-27.39	$-0.44^{+0.27}_{-0.26}$	$0.308^{+0.084}_{-0.057}$
GRB080723B	13:22:15	27.39-27.78	$-0.82^{+0.33}_{-0.36}$	$0.313^{+0.222}_{-0.099}$
GRB080723B	13:22:15	27.78-28.3	$-1.26^{+0.54}_{-0.49}$	0.124 (l.l.)
GRB080723B	13:22:15	28.3-28.85	$-0.55^{+0.25}_{-0.27}$	$0.290^{+0.086}_{-0.060}$
GRB080723B	13:22:15	28.85-29.4	$-0.89^{+0.45}_{-0.52}$	$0.221^{+0.260}_{-0.068}$
GRB080723B	13:22:15	29.4-30.61	$-1.92^{+0.21}_{-0.19}$	unconst.
GRB080723B	13:22:15	30.61-31.09	$-1.48^{+0.28}_{-0.18}$	unconst.
GRB080723B	13:22:15	31.09-32.37	$-1.84^{+0.28}_{-0.29}$	unconst.
GRB080723B	13:22:15	46.63-48.42	$-0.71^{+0.34}_{-0.32}$	$0.377^{+0.241}_{-0.131}$
GRB080723B	13:22:15	48.42-48.82	$-0.94^{+0.34}_{-0.28}$	0.353 (l.l.)
GRB080723B	13:22:15	48.82-49.55	$-0.67^{+0.20}_{-0.18}$	$0.565^{+0.205}_{-0.156}$
GRB080723B	13:22:15	49.55-49.98	$-1.36^{+0.25}_{-0.25}$	0.463 (l.l.)
GRB080723B	13:22:15	49.98-50.33	$-0.55^{+0.26}_{-0.29}$	$0.502^{+0.218}_{-0.159}$
GRB080723B	13:22:15	50.33-50.69	$-1.32^{+0.44}_{-0.32}$	0.174 (l.l.)
GRB080723B	13:22:15	50.69-53.78	$-1.71^{+0.26}_{-0.17}$	unconst.
GRB080723B	13:22:15	53.78-54.9	$-0.94^{+0.22}_{-0.20}$	$0.327^{+0.140}_{-0.082}$
GRB080723B	13:22:15	54.9-58.31	$-1.08^{+0.15}_{-0.15}$	$0.377^{+0.143}_{-0.103}$
GRB080723B	13:22:15	58.31-60.96	$-1.59^{+0.12}_{-0.13}$	0.417 (l.l.)
GRB080723B	13:22:15	60.96-61.2	$-0.98^{+0.32}_{-0.29}$	0.390 (l.l.)
GRB080723B	13:22:15	61.2-61.37	$-0.59^{+0.26}_{-0.27}$	$0.733^{+0.448}_{-0.248}$
GRB080723B	13:22:15	61.37-61.69	$-0.72^{+0.28}_{-0.30}$	$0.459^{+0.278}_{-0.156}$
GRB080723B	13:22:15	61.69-61.96	$-0.59^{+0.26}_{-0.25}$	$0.548^{+0.261}_{-0.160}$
GRB080723B	13:22:15	61.96-62.39	$-0.80^{+0.24}_{-0.25}$	$0.561^{+0.391}_{-0.199}$
GRB080723B	13:22:15	62.39-63.14	$-0.61^{+0.14}_{-0.14}$	$0.451^{+0.084}_{-0.070}$

Continued on Next Page

Table 2: Continued

Global			CPL	
GRB-Name	**Ref. Time**	**Active Time [s]**	α	E_{peak} **[MeV]**
GRB080723B	13:22:15	63.14-63.64	$-1.20^{+0.26}_{-0.26}$	$0.496^{+1.473}_{-0.268}$
GRB080723B	13:22:15	63.64-64.69	$-1.07^{+0.28}_{-0.29}$	$0.382^{+0.475}_{-0.162}$
GRB080723B	13:22:15	64.69-64.78	$-0.69^{+0.38}_{-0.41}$	$0.524^{+0.673}_{-0.207}$
GRB080723B	13:22:15	64.78-65.31	$-0.78^{+0.24}_{-0.24}$	$0.493^{+0.250}_{-0.153}$
GRB080723B	13:22:15	65.31-65.53	$-0.81^{+0.24}_{-0.24}$	$0.472^{+0.224}_{-0.149}$
GRB080723B	13:22:15	65.53-65.84	$-1.60^{+0.20}_{-0.18}$	unconst.
GRB080723B	13:22:15	65.84-68.72	$-1.45^{+0.17}_{-0.19}$	0.761 (l.l.)
GRB080723B	13:22:15	68.72-82.21	$-1.60^{+0.25}_{-0.27}$	unconst.
GRB080723B	13:22:15	82.21-83.5	$-1.20^{+0.48}_{-0.33}$	0.188 (l.l.)
GRB080723B	13:22:15	83.5-92.17	$-1.62^{+0.17}_{-0.18}$	0.570 (l.l.)
GRB081003B	20:48:08	2.02-15.47	-	-
GRB081016	06:51:31	1.48-2.05	$-1.62^{+3.66}_{-1.03}$	unconst.
GRB081016	06:51:31	2.05-2.75	$-1.25^{+0.39}_{-0.39}$	0.143 (l.l.)
GRB081016	06:51:31	4.56-4.97	$-1.00^{+0.54}_{-0.66}$	0.103 (l.l.)
GRB081016	06:51:31	24.71-26.43	$-1.80^{+0.41}_{-0.15}$	unconst.
GRB081016	06:51:31	26.43-28.65	$-2.25^{+0.21}_{-0.21}$	0.846 (l.l.)
GRB081226B	12:13:11	0.11-0.27	$-1.28^{+0.40}_{-0.42}$	0.676 (l.l.)
GRB090107B	16:20:36	3.93-19.2	$-1.59^{+0.23}_{-0.22}$	unconst.
GRB090625B	13:26:20	0.6-7.92	$-1.52^{+0.39}_{-0.18}$	unconst.
GRB090817	00:51:23	2.39-5.85	$-0.63^{+0.38}_{-0.41}$	$0.335^{+0.357}_{-0.124}$
GRB090817	00:51:23	5.85-14.04	$-1.98^{+0.24}_{-0.27}$	unconst.
GRB100103A	17:42:30	8.43-13.46	$-1.02^{+0.35}_{-0.39}$	0.746 (l.l.)
GRB100103A	17:42:30	13.46-23.88	$-0.85^{+0.22}_{-0.24}$	$0.246^{+0.091}_{-0.054}$
GRB100103A	17:42:30	23.88-38.63	$-1.82^{+0.20}_{-0.19}$	unconst.
GRB101112A	22:10:20	11.98-13.96	$-1.07^{+0.35}_{-0.61}$	$0.151^{+0.368}_{-0.047}$
GRB101112A	22:10:20	13.96-15.88	$-1.80^{+0.80}_{-1.10}$	0.509 (l.l.)
GRB110206A	18:08:10	-0.26-3.8	$-1.67^{+0.32}_{-0.30}$	unconst.
GRB110903A	02:38:30	64.15-68.63	-	-

Continued on Next Page

Table 2: Continued

Global			CPL	
GRB-Name	**Ref. Time**	**Active Time [s]**	α	E_{peak} **[MeV]**
GRB110903A	02:38:30	71.51-78.76	-	-
GRB110903A	02:38:30	82.29-85.83	$0.42^{+1.57}_{-1.15}$	$0.176^{+0.121}_{-0.060}$
GRB110903A	02:38:30	258.78-273.42	-	-
GRB110903A	02:38:30	384.08-400.0	$-1.67^{+0.76}_{-0.52}$	unconst.
GRB120512A	02:41:40	3.57-16.89	$-1.48^{+0.48}_{-0.37}$	0.564 (l.l.)
GRB120711A	02:44:48	3.47-8.42	$-1.11^{+0.42}_{-0.32}$	0.244 (l.l.)
GRB120711A	02:44:48	67.1-69.39	$-0.93^{+0.26}_{-0.23}$	0.468 (l.l.)
GRB120711A	02:44:48	69.39-72.73	$-1.01^{+0.10}_{-0.10}$	1.281 (l.l.)
GRB120711A	02:44:48	72.73-77.49	$-0.86^{+0.07}_{-0.06}$	$1.231^{+0.262}_{-0.213}$
GRB120711A	02:44:48	77.49-81.43	$-0.95^{+0.10}_{-0.09}$	$0.893^{+0.262}_{-0.226}$
GRB120711A	02:44:48	81.43-86.42	$-1.00^{+0.13}_{-0.12}$	$0.752^{+0.315}_{-0.236}$
GRB120711A	02:44:48	86.42-88.16	$-0.79^{+0.20}_{-0.18}$	$0.637^{+0.294}_{-0.193}$
GRB120711A	02:44:48	88.16-91.01	$-1.16^{+0.22}_{-0.20}$	0.359 (l.l.)
GRB120711A	02:44:48	91.01-95.92	$-0.93^{+0.08}_{-0.08}$	$1.002^{+0.260}_{-0.219}$
GRB120711A	02:44:48	95.92-98.96	$-0.95^{+0.09}_{-0.09}$	$1.008^{+0.308}_{-0.241}$
GRB120711A	02:44:48	98.96-99.06	$-0.85^{+0.31}_{-0.26}$	0.710 (l.l.)
GRB120711A	02:44:48	99.06-100.61	$-1.05^{+0.10}_{-0.10}$	1.288 (l.l.)
GRB120711A	02:44:48	100.61-100.67	$-0.79^{+0.36}_{-0.30}$	0.587 (l.l.)
GRB120711A	02:44:48	100.67-101.44	$-0.93^{+0.13}_{-0.13}$	1.083 (l.l.)
GRB120711A	02:44:48	101.44-107.53	$-0.87^{+0.06}_{-0.06}$	$1.347^{+0.260}_{-0.241}$
GRB120711A	02:44:48	107.53-107.93	$-0.55^{+0.19}_{-0.21}$	$0.738^{+0.240}_{-0.199}$
GRB120711A	02:44:48	107.93-109.55	$-0.89^{+0.13}_{-0.13}$	$1.032^{+0.465}_{-0.324}$
GRB120711A	02:44:48	109.55-110.37	$-1.18^{+0.24}_{-0.20}$	0.359 (l.l.)
GRB120711A	02:44:48	110.37-112.24	$-1.50^{+0.15}_{-0.17}$	0.915 (l.l.)
GRB120711A	02:44:48	112.24-112.89	$-0.85^{+0.28}_{-0.30}$	$0.879^{+1.875}_{-0.445}$
GRB120711A	02:44:48	112.89-116.03	$-1.65^{+0.16}_{-0.16}$	unconst.
GRB120711A	02:44:48	116.03-126.73	$-1.58^{+0.22}_{-0.27}$	0.797 (l.l.)
GRB121102A	02:27:02	1.98-11.73	$-1.98^{+0.22}_{-0.25}$	0.456 (l.l.)

Continued on Next Page

Table 2: Continued

Global			CPL	
GRB-Name	**Ref. Time**	**Active Time [s]**	α	E_{peak} **[MeV]**
GRB121102A	02:27:02	11.73-11.74	-	-
GRB130513A	07:38:10	15.43-53.8	$-1.57^{+0.24}_{-0.25}$	0.801 (l.l.)
GRB130514B	13:26:32	0.44-1.5	$-1.54^{+0.22}_{-0.17}$	0.257 (l.l.)
GRB130514B	13:26:32	1.5-2.75	$-1.61^{+0.31}_{-0.26}$	unconst.
GRB130514B	13:26:32	2.75-9.91	$-1.84^{+0.30}_{-0.32}$	unconst.
GRB131122A	21:25:01	10.6-17.22	$-1.20^{+1.48}_{-1.78}$	0.568 (l.l.)
GRB131218A	21:05:32	0.77-5.53	$-1.12^{+0.99}_{-0.56}$	0.101 (l.l.)
GRB131224A	16:54:37	14.23-14.4	$1.67^{+1.33}_{-2.44}$	$0.155^{+0.324}_{-0.071}$
GRB140710B	21:37:30	3.7-28.55	$-1.96^{+0.24}_{-0.25}$	unconst.
GRB140815A	21:55:05	0.62-2.49	$-2.31^{+0.83}_{-0.69}$	0.497 (l.l.)
GRB140815A	21:55:05	103.41-103.43	$-0.36^{+1.37}_{-0.90}$	0.605 (l.l.)
GRB141004A	23:20:54	0.36-1.13	$-1.84^{+0.27}_{-0.25}$	unconst.
GRB151120	08:22:50	4.07-7.7	$0.12^{+0.32}_{-0.29}$	$0.262^{+0.049}_{-0.038}$
GRB151120	08:22:50	7.7-18.24	$-1.11^{+0.24}_{-0.27}$	$0.152^{+0.052}_{-0.032}$
GRB151120	08:22:50	18.24-25.21	$-2.13^{+0.21}_{-0.22}$	0.702 (l.l.)
GRB160223B	09:58:58	2.63-16.86	$-1.16^{+0.30}_{-0.23}$	0.304 (l.l.)
GRB160401A	20:20:30	1.8-38.1	$-1.95^{+0.18}_{-0.19}$	unconst.
GRB160521	03:37:20	98.17-122.25	$-1.47^{+0.25}_{-0.27}$	0.971 (l.l.)
GRB160629A	22:19:30	9.76-30.72	$-0.91^{+0.26}_{-0.26}$	$0.285^{+0.141}_{-0.082}$
GRB161010A	13:36:25	4.73-8.09	$-1.67^{+0.47}_{-0.24}$	0.111 (l.l.)
GRB161010A	13:36:25	8.09-9.27	$-1.36^{+0.31}_{-0.37}$	0.134 (l.l.)
GRB161010A	13:36:25	9.27-10.92	$-1.17^{+0.17}_{-0.16}$	$0.312^{+0.118}_{-0.080}$
GRB161010A	13:36:25	10.92-11.79	$-1.15^{+0.33}_{-0.32}$	$0.299^{+0.295}_{-0.127}$
GRB161010A	13:36:25	11.79-13.46	$-1.30^{+0.32}_{-0.37}$	0.160 (l.l.)
GRB161010A	13:36:25	13.46-14.34	$-0.99^{+0.29}_{-0.28}$	$0.357^{+0.251}_{-0.123}$
GRB161010A	13:36:25	14.34-16.94	$-1.82^{+0.11}_{-0.11}$	unconst.
GRB161010A	13:36:25	16.94-25.92	$-1.93^{+0.20}_{-0.22}$	unconst.
GRB161023A	22:38:40	14.4-19.16	$-1.46^{+0.42}_{-0.22}$	0.172 (l.l.)

Continued on Next Page

Table 2: Continued

Global			CPL	
GRB-Name	**Ref. Time**	**Active Time [s]**	α	E_{peak} **[MeV]**
GRB161023A	22:38:40	19.16-29.94	$-1.37^{+0.16}_{-0.16}$	$0.556^{+1.186}_{-0.293}$
GRB161023A	22:38:40	29.94-36.07	$-1.17^{+0.14}_{-0.12}$	$0.524^{+0.277}_{-0.168}$
GRB161023A	22:38:40	36.07-38.22	$-1.21^{+0.31}_{-0.33}$	$0.313^{+0.779}_{-0.142}$
GRB161023A	22:38:40	38.22-38.83	$-1.13^{+0.30}_{-0.38}$	$0.401^{+2.038}_{-0.191}$
GRB161023A	22:38:40	38.83-40.64	$-1.38^{+0.25}_{-0.26}$	$0.215^{+0.217}_{-0.077}$
GRB161023A	22:38:40	40.64-42.95	$-1.88^{+0.12}_{-0.12}$	unconst.
GRB161023A	22:38:40	42.95-50.67	$-1.48^{+0.23}_{-0.39}$	$0.132^{+1.859}_{-0.047}$
GRB161023A	22:38:40	50.67-66.85	$-1.70^{+0.19}_{-0.20}$	unconst.
GRB180626	08:21:04	3.42-7.17	-	-
GRB180626	08:21:04	7.17-13.41	-	-
GRB180626	08:21:04	13.41-29.05	-	-
GRB181127A	06:46:21	4.25-11.18	$-2.27^{+0.58}_{-0.72}$	0.565 (l.l.)
GRB181201A	02:38:00	1.94-23.06	$-1.41^{+0.33}_{-0.17}$	0.184 (l.l.)
GRB181201A	02:38:00	23.06-49.81	$-2.22^{+0.20}_{-0.20}$	unconst.
GRB181201A	02:38:00	113.37-114.3	$-1.17^{+0.36}_{-0.38}$	$0.321^{+0.773}_{-0.146}$
GRB181201A	02:38:00	114.3-115.38	$-1.17^{+0.18}_{-0.21}$	$0.239^{+0.084}_{-0.054}$
GRB181201A	02:38:00	115.38-116.46	$-1.11^{+0.16}_{-0.15}$	$0.257^{+0.063}_{-0.047}$
GRB181201A	02:38:00	116.46-117.99	$-1.05^{+0.11}_{-0.10}$	$0.250^{+0.033}_{-0.028}$
GRB181201A	02:38:00	117.99-119.97	-	-
GRB181201A	02:38:00	119.97-121.17	-	-
GRB181201A	02:38:00	121.17-122.48	$-1.34^{+0.14}_{-0.13}$	$0.163^{+0.029}_{-0.021}$
GRB181201A	02:38:00	122.48-125.16	$-1.38^{+0.13}_{-0.13}$	$0.120^{+0.013}_{-0.011}$
GRB181201A	02:38:00	125.16-126.17	$-1.72^{+0.15}_{-0.38}$	0.028 (l.l.)
GRB181201A	02:38:00	126.17-127.97	$-2.07^{+0.07}_{-0.07}$	0.925 (l.l.)
GRB181201A	02:38:00	127.97-131.08	$-2.11^{+0.07}_{-0.07}$	1.519 (l.l.)
GRB181201A	02:38:00	131.08-135.12	$-2.06^{+0.08}_{-0.08}$	0.762 (l.l.)
GRB181201A	02:38:00	135.12-139.54	$-2.11^{+0.12}_{-0.11}$	0.824 (l.l.)
GRB181201A	02:38:00	139.54-147.77	$-2.30^{+0.15}_{-0.15}$	0.801 (l.l.)

Continued on Next Page

Table 2: Continued

Global			CPL	
GRB-Name	**Ref. Time**	**Active Time [s]**	α	E_{peak} **[MeV]**
GRB181201A	02:38:00	147.77-162.07	$-2.37^{+0.28}_{-0.29}$	0.690 (l.l.)
GRB190220B	20:14:30	56.25-95.83	-	-
GRB190411A	09:45:48	-1.21-1.21	$-1.24^{+1.12}_{-0.66}$	0.430 (l.l.)
GRB190411A	09:45:48	1.21-3.84	$-1.43^{+0.35}_{-0.19}$	1.022 (l.l.)
GRB190411A	09:45:48	3.84-4.42	$-1.37^{+0.45}_{-0.32}$	1.075 (l.l.)
GRB190411A	09:45:48	4.42-6.24	$-1.34^{+0.19}_{-0.16}$	1.714 (l.l.)
GRB190411A	09:45:48	29.58-34.96	-	-
GRB190411A	09:45:48	159.7-173.44	$-1.56^{+0.39}_{-0.25}$	0.551 (l.l.)
GRB190701B	10:05:00	-1.28-1.49	$-1.17^{+0.59}_{-0.39}$	unconst.
GRB190701B	10:05:00	1.49-2.9	$-1.37^{+0.42}_{-0.22}$	unconst.
GRB190701B	10:05:00	2.9-7.1	$-1.57^{+0.17}_{-0.16}$	0.402 (l.l.)
GRB190701B	10:05:00	7.1-19.51	$-1.85^{+0.18}_{-0.19}$	unconst.
GRB190719B	03:13:40	320.77-320.83	-	-
GRB190828D	18:48:30	3.54-3.69	$-0.79^{+0.92}_{-0.54}$	0.348 (l.l.)
GRB190828D	18:48:30	3.69-5.34	$-0.77^{+0.34}_{-0.27}$	0.856 (l.l.)
GRB190828D	18:48:30	5.34-8.87	$-0.96^{+0.48}_{-0.36}$	0.383 (l.l.)
GRB190919B	23:46:40	18.16-20.47	$-2.24^{+0.62}_{-0.64}$	unconst.
GRB200424A	12:07:10	0.8-0.9	$-0.86^{+1.14}_{-0.65}$	0.186 (l.l.)
GRB200424A	12:07:10	1.52-1.99	$-0.56^{+0.43}_{-0.41}$	$0.602^{+0.694}_{-0.275}$
GRB200424A	12:07:10	6.69-9.23	$-0.83^{+0.24}_{-0.25}$	$1.027^{+1.585}_{-0.541}$
GRB200424A	12:07:10	9.23-9.82	$-0.42^{+0.23}_{-0.23}$	$0.855^{+0.355}_{-0.260}$
GRB200424A	12:07:10	9.82-11.5	$-0.91^{+0.37}_{-0.30}$	0.336 (l.l.)
GRB200424A	12:07:10	14.45-14.79	$-0.99^{+0.70}_{-0.43}$	0.235 (l.l.)
GRB200424A	12:07:10	14.79-19.73	$-1.55^{+0.38}_{-0.44}$	unconst.
GRB200424A	12:07:10	19.73-21.94	$-1.27^{+0.19}_{-0.15}$	0.485 (l.l.)
GRB200424A	12:07:10	21.94-24.05	$-1.75^{+0.29}_{-0.39}$	unconst.
GRB200424A	12:07:10	24.05-24.82	$-1.04^{+0.52}_{-0.40}$	0.247 (l.l.)
GRB200424A	12:07:10	27.75-34.35	$-1.33^{+0.19}_{-0.18}$	0.275 (l.l.)

Continued on Next Page

Table 2: Continued

Global			**CPL**	
GRB-Name	**Ref. Time**	**Active Time [s]**	α	E_{peak} **[MeV]**
GRB200424A	12:07:10	34.35-48.97	$-1.46^{+0.17}_{-0.14}$	0.318 (l.l.)
GRB200424A	12:07:10	48.97-76.0	$-1.49^{+0.31}_{-0.30}$	0.597 (l.l.)
GRB200715A	23:51:40	20.87-49.92	$-1.16^{+0.33}_{-0.28}$	0.193 (l.l.)
GRB200715A	23:51:40	143.72-152.96	$-1.28^{+0.26}_{-0.24}$	0.503 (l.l.)
GRB200715A	23:51:40	152.96-155.19	$-1.32^{+0.39}_{-0.42}$	0.820 (l.l.)
GRB201006A	01:17:51	0.79-2.52	$-1.65^{+0.67}_{-0.78}$	unconst.
GRB210208A	13:32:23	2.14-4.34	$-1.28^{+0.27}_{-0.28}$	unconst.
GRB210406A	17:11:22	6.34-9.4	$-0.97^{+0.75}_{-0.52}$	0.166 (l.l.)
GRB210406A	17:11:22	9.4-19.82	$-0.28^{+0.26}_{-0.29}$	$0.182^{+0.034}_{-0.025}$
GRB210406A	17:11:22	19.82-23.91	$-0.80^{+0.58}_{-0.59}$	$0.351^{+2.114}_{-0.198}$
GRB210406A	17:11:22	23.91-39.78	$-1.84^{+0.33}_{-0.34}$	unconst.

Table 3: Parameter constrains for synchrotron model fits. Entries with no parameter values indicate that the fit has failed for this time bin and spectral model. Entries with 'u.l.' and 'l.l.' indicate upper and lower limits and 'unconst.' that the parameter is unconstrained.

Global			**Synchrotron**	
GRB-Name	**Ref. Time**	**Active Time [s]**	**p**	$\mathcal{X}$
GRB030529	19:53:18	42.41-54.81	-	-
GRB041219A	01:42:13	5.33-8.68	4.440 (l.l.)	0.710 (l.l.)
GRB041219A	01:42:13	239.37-265.77	2.340 (l.l.)	−0.010 (u.l.)
GRB041219A	01:42:13	267.79-272.99	2.710 (l.l.)	$-0.35^{+0.54}_{-0.51}$
GRB041219A	01:42:13	272.99-275.91	2.930 (l.l.)	$-0.51^{+0.38}_{-0.40}$
GRB041219A	01:42:13	275.91-277.53	2.880 (l.l.)	$-0.42^{+0.42}_{-0.46}$
GRB041219A	01:42:13	277.53-283.01	-	-
GRB041219A	01:42:13	283.01-285.61	-	-
GRB041219A	01:42:13	285.61-286.7	-	-
GRB041219A	01:42:13	286.7-288.23	-	-
GRB041219A	01:42:13	288.23-293.17	-	-
GRB041219A	01:42:13	293.17-297.14	2.960 (l.l.)	−0.560 (u.l.)
GRB041219A	01:42:13	297.14-304.81	-	-
GRB041219A	01:42:13	304.81-312.8	-	-
GRB041219A	01:42:13	312.8-317.41	2.690 (l.l.)	−0.610 (u.l.)
GRB041219A	01:42:13	317.41-325.82	2.070 (l.l.)	−0.320 (u.l.)
GRB041219A	01:42:13	325.82-333.96	unconst.	1.610 (u.l.)
GRB041219A	01:42:13	333.96-360.46	2.930 (l.l.)	−0.430 (u.l.)
GRB041219A	01:42:13	360.46-364.16	5.720 (u.l.)	unconst.
GRB041219A	01:42:13	364.16-370.04	unconst.	−0.420 (u.l.)
GRB041219A	01:42:13	370.04-381.41	-	-
GRB041219A	01:42:13	381.41-386.22	2.310 (l.l.)	1.870 (u.l.)
GRB041219A	01:42:13	386.22-388.93	4.120 (l.l.)	−1.430 (l.l.)
GRB041219A	01:42:13	388.93-390.89	3.030 (u.l.)	unconst.
GRB041219A	01:42:13	390.89-391.68	2.730 (l.l.)	2.250 (u.l.)
GRB041219A	01:42:13	391.68-399.56	7.570 (u.l.)	1.780 (u.l.)
GRB041219A	01:42:13	399.56-407.54	4.640 (l.l.)	−0.440 (u.l.)

Continued on Next Page

Table 3: *Continued*

Global			Synchrotron	
GRB-Name	**Ref. Time**	**Active Time [s]**	**p**	$\mathcal{X}$
GRB041219A	01:42:13	407.54-408.79	unconst.	2.320 (u.l.)
GRB041219A	01:42:13	408.79-412.52	$2.55^{+0.90}_{-0.42}$	unconst.
GRB041219A	01:42:13	412.52-417.01	3.340 (l.l.)	0.930 (u.l.)
GRB041219A	01:42:13	426.25-431.17	$3.08^{+1.03}_{-0.56}$	unconst.
GRB041219A	01:42:13	441.15-442.93	$2.89^{+3.62}_{-0.77}$	unconst.
GRB041219A	01:42:13	442.93-449.58	$3.10^{+0.96}_{-0.50}$	unconst.
GRB041219A	01:42:13	449.58-469.74	$3.27^{+0.91}_{-0.41}$	unconst.
GRB041219A	01:42:13	484.17-492.81	2.290 (l.l.)	2.320 (u.l.)
GRB050525A	00:02:53	0.47-1.22	3.870 (l.l.)	−1.460 (l.l.)
GRB050525A	00:02:53	1.22-1.94	4.890 (l.l.)	0.420 (l.l.)
GRB050525A	00:02:53	5.23-7.76	4.570 (l.l.)	−0.220 (l.l.)
GRB060428C	02:30:35	7.47-10.62	5.260 (l.l.)	0.680 (l.l.)
GRB060901	18:43:55	0.3-4.16	2.730 (l.l.)	−0.240 (l.l.)
GRB061122	07:56:50	0.73-1.96	6.940 (u.l.)	unconst.
GRB061122	07:56:50	1.96-2.58	2.630 (l.l.)	0.570 (u.l.)
GRB061122	07:56:50	2.58-3.47	6.000 (l.l.)	0.880 (l.l.)
GRB061122	07:56:50	3.47-4.76	6.810 (l.l.)	1.070 (l.l.)
GRB061122	07:56:50	4.76-4.95	5.460 (l.l.)	0.660 (l.l.)
GRB061122	07:56:50	4.95-6.05	5.810 (l.l.)	0.590 (l.l.)
GRB061122	07:56:50	6.05-7.1	3.120 (l.l.)	−0.980 (l.l.)
GRB061122	07:56:50	7.1-8.37	2.400 (l.l.)	1.430 (u.l.)
GRB070707	16:08:38	0.59-0.96	2.400 (l.l.)	−0.880 (l.l.)
GRB070925	15:52:32	14.48-23.81	3.470 (l.l.)	0.390 (l.l.)
GRB071003	07:40:55	0.08-2.5	-	-
GRB071003	07:40:55	4.06-5.46	-	-
GRB071003	07:40:55	6.88-12.91	-	-
GRB080723B	13:22:15	7.79-8.72	4.990 (l.l.)	0.730 (l.l.)
GRB080723B	13:22:15	9.04-9.29	2.530 (l.l.)	−0.740 (l.l.)

Continued on Next Page

Table 3: *Continued*

Global			Synchrotron	
GRB-Name	**Ref. Time**	**Active Time [s]**	**p**	$\mathcal{X}$
GRB080723B	13:22:15	18.01-18.31	4.360 (l.l.)	0.560 (l.l.)
GRB080723B	13:22:15	18.31-18.96	3.320 (l.l.)	−0.190 (l.l.)
GRB080723B	13:22:15	18.96-19.8	5.790 (l.l.)	0.910 (l.l.)
GRB080723B	13:22:15	19.8-20.5	4.570 (l.l.)	0.540 (l.l.)
GRB080723B	13:22:15	20.5-20.85	5.430 (l.l.)	0.810 (l.l.)
GRB080723B	13:22:15	20.85-21.67	4.550 (l.l.)	0.580 (l.l.)
GRB080723B	13:22:15	22.11-22.67	4.100 (l.l.)	0.250 (l.l.)
GRB080723B	13:22:15	22.67-24.38	unconst.	1.580 (u.l.)
GRB080723B	13:22:15	27.0-27.39	3.970 (l.l.)	0.580 (l.l.)
GRB080723B	13:22:15	27.39-27.78	3.230 (l.l.)	−0.350 (l.l.)
GRB080723B	13:22:15	28.3-28.85	3.950 (l.l.)	0.570 (l.l.)
GRB080723B	13:22:15	28.85-29.4	3.670 (l.l.)	−0.080 (l.l.)
GRB080723B	13:22:15	30.61-31.09	2.880 (l.l.)	−1.600 (l.l.)
GRB080723B	13:22:15	46.63-48.42	3.620 (l.l.)	0.410 (l.l.)
GRB080723B	13:22:15	48.42-48.82	2.150 (l.l.)	−1.040 (l.l.)
GRB080723B	13:22:15	48.82-49.55	3.620 (l.l.)	0.560 (l.l.)
GRB080723B	13:22:15	49.98-50.33	3.810 (l.l.)	0.400 (l.l.)
GRB080723B	13:22:15	50.33-50.69	2.730 (l.l.)	2.480 (u.l.)
GRB080723B	13:22:15	50.69-53.78	2.260 (l.l.)	1.250 (u.l.)
GRB080723B	13:22:15	53.78-54.9	$4.49^{+3.46}_{-1.74}$	−0.070 (l.l.)
GRB080723B	13:22:15	54.9-58.31	2.690 (l.l.)	$-0.13^{+1.02}_{-0.52}$
GRB080723B	13:22:15	58.31-60.96	2.300 (l.l.)	−0.510 (u.l.)
GRB080723B	13:22:15	60.96-61.2	2.590 (l.l.)	−1.400 (l.l.)
GRB080723B	13:22:15	61.2-61.37	3.410 (l.l.)	0.260 (l.l.)
GRB080723B	13:22:15	61.37-61.69	3.840 (l.l.)	0.290 (l.l.)
GRB080723B	13:22:15	61.69-61.96	3.480 (l.l.)	0.490 (l.l.)
GRB080723B	13:22:15	61.96-62.39	3.570 (l.l.)	−0.050 (l.l.)
GRB080723B	13:22:15	62.39-63.14	4.940 (l.l.)	0.790 (l.l.)

Continued on Next Page

Table 3: *Continued*

Global			Synchrotron	
GRB-Name	**Ref. Time**	**Active Time [s]**	**p**	$\mathcal{X}$
GRB080723B	13:22:15	63.14-63.64	2.650 (l.l.)	0.960 (u.l.)
GRB080723B	13:22:15	63.64-64.69	3.050 (l.l.)	−1.050 (l.l.)
GRB080723B	13:22:15	64.69-64.78	3.540 (l.l.)	−0.330 (l.l.)
GRB080723B	13:22:15	64.78-65.31	4.040 (l.l.)	0.290 (l.l.)
GRB080723B	13:22:15	65.31-65.53	4.080 (l.l.)	0.380 (l.l.)
GRB080723B	13:22:15	65.53-65.84	2.060 (l.l.)	2.430 (u.l.)
GRB081003B	20:48:08	2.02-15.47	2.410 (l.l.)	2.170 (u.l.)
GRB081016	06:51:31	2.05-2.75	3.230 (l.l.)	−0.520 (l.l.)
GRB081016	06:51:31	4.56-4.97	2.860 (l.l.)	−0.830 (l.l.)
GRB081016	06:51:31	24.71-26.43	2.710 (l.l.)	2.130 (u.l.)
GRB090817	00:51:23	2.39-5.85	3.180 (l.l.)	−0.050 (l.l.)
GRB100103A	17:42:30	13.46-23.88	3.770 (l.l.)	0.150 (l.l.)
GRB101112A	22:10:20	11.98-13.96	3.570 (l.l.)	0.000 (l.l.)
GRB110903A	02:38:30	258.78-273.42	-	-
GRB120711A	02:44:48	67.1-69.39	2.710 (l.l.)	−1.290 (l.l.)
GRB120711A	02:44:48	69.39-72.73	unconst.	$-1.06^{+0.57}_{-0.40}$
GRB120711A	02:44:48	72.73-77.49	2.880 (l.l.)	$-0.05^{+2.07}_{-0.47}$
GRB120711A	02:44:48	77.49-81.43	2.740 (l.l.)	$-0.21^{+0.48}_{-0.41}$
GRB120711A	02:44:48	81.43-86.42	2.850 (l.l.)	$-0.19^{+2.08}_{-0.54}$
GRB120711A	02:44:48	86.42-88.16	3.210 (l.l.)	−0.040 (l.l.)
GRB120711A	02:44:48	88.16-91.01	2.480 (l.l.)	1.120 (u.l.)
GRB120711A	02:44:48	91.01-95.92	2.560 (l.l.)	$-0.21^{+1.38}_{-0.44}$
GRB120711A	02:44:48	95.92-98.96	2.690 (l.l.)	$-0.26^{+0.46}_{-0.42}$
GRB120711A	02:44:48	98.96-99.06	2.720 (l.l.)	−1.200 (l.l.)
GRB120711A	02:44:48	99.06-100.61	unconst.	$-1.09^{+0.57}_{-0.41}$
GRB120711A	02:44:48	100.61-100.67	2.430 (l.l.)	−1.170 (l.l.)
GRB120711A	02:44:48	100.67-101.44	2.070 (l.l.)	$-0.59^{+2.84}_{-0.83}$
GRB120711A	02:44:48	101.44-107.53	3.000 (l.l.)	$0.02^{+2.24}_{-0.49}$

Continued on Next Page

Table 3: *Continued*

Global			Synchrotron	
GRB-Name	**Ref. Time**	**Active Time [s]**	**p**	$\mathcal{X}$
GRB120711A	02:44:48	107.53-107.93	4.010 (l.l.)	0.680 (l.l.)
GRB120711A	02:44:48	107.93-109.55	3.010 (l.l.)	−0.420 (l.l.)
GRB120711A	02:44:48	109.55-110.37	2.320 (l.l.)	1.080 (u.l.)
GRB120711A	02:44:48	112.24-112.89	2.920 (l.l.)	−0.840 (l.l.)
GRB130514B	13:26:32	0.44-1.5	unconst.	0.890 (u.l.)
GRB151120	08:22:50	4.07-7.7	4.630 (l.l.)	0.660 (l.l.)
GRB151120	08:22:50	7.7-18.24	2.880 (l.l.)	−0.190 (l.l.)
GRB160629A	22:19:30	9.76-30.72	3.040 (l.l.)	−0.090 (l.l.)
GRB161010A	13:36:25	8.09-9.27	2.620 (l.l.)	2.330 (u.l.)
GRB161010A	13:36:25	9.27-10.92	2.310 (l.l.)	−0.580 (l.l.)
GRB161010A	13:36:25	10.92-11.79	2.860 (l.l.)	−0.370 (l.l.)
GRB161010A	13:36:25	11.79-13.46	2.920 (l.l.)	unconst.
GRB161010A	13:36:25	13.46-14.34	3.250 (l.l.)	−0.280 (l.l.)
GRB161010A	13:36:25	14.34-16.94	7.320 (u.l.)	−1.560 (l.l.)
GRB161023A	22:38:40	19.16-29.94	2.600 (l.l.)	−0.310 (u.l.)
GRB161023A	22:38:40	29.94-36.07	2.540 (l.l.)	$-0.45^{+0.37}_{-0.40}$
GRB161023A	22:38:40	36.07-38.22	2.910 (l.l.)	−1.130 (l.l.)
GRB161023A	22:38:40	38.22-38.83	2.840 (l.l.)	−0.630 (l.l.)
GRB161023A	22:38:40	38.83-40.64	2.440 (l.l.)	−1.510 (l.l.)
GRB161023A	22:38:40	40.64-42.95	5.970 (u.l.)	unconst.
GRB161023A	22:38:40	42.95-50.67	2.940 (l.l.)	0.300 (u.l.)
GRB180626	08:21:04	7.17-13.41	-	-
GRB181201A	02:38:00	1.94-23.06	2.230 (l.l.)	−0.970 (l.l.)
GRB181201A	02:38:00	113.37-114.3	2.710 (l.l.)	1.410 (u.l.)
GRB181201A	02:38:00	114.3-115.38	2.710 (l.l.)	−0.650 (l.l.)
GRB181201A	02:38:00	115.38-116.46	$3.82^{+3.72}_{-1.18}$	−0.400 (l.l.)
GRB181201A	02:38:00	116.46-117.99	3.170 (l.l.)	−0.200 (l.l.)
GRB181201A	02:38:00	117.99-119.97	$4.97^{+2.72}_{-1.02}$	0.000 (l.l.)

Continued on Next Page

Table 3: *Continued*

Global			**Synchrotron**	
GRB-Name	**Ref. Time**	**Active Time [s]**	**p**	$\mathcal{X}$
GRB181201A	02:38:00	119.97-121.17	$5.04^{+1.41}_{-1.07}$	0.490 (l.l.)
GRB181201A	02:38:00	121.17-122.48	$3.80^{+3.06}_{-1.02}$	−0.500 (l.l.)
GRB181201A	02:38:00	122.48-125.16	$3.88^{+1.21}_{-0.82}$	−0.210 (l.l.)
GRB181201A	02:38:00	125.16-126.17	3.290 (l.l.)	unconst.
GRB181201A	02:38:00	126.17-127.97	3.060 (l.l.)	2.310 (u.l.)
GRB181201A	02:38:00	127.97-131.08	4.440 (l.l.)	−0.270 (u.l.)
GRB181201A	02:38:00	131.08-135.12	2.460 (l.l.)	−0.170 (u.l.)
GRB181201A	02:38:00	135.12-139.54	unconst.	2.470 (u.l.)
GRB190411A	09:45:48	1.21-3.84	unconst.	1.850 (u.l.)
GRB190411A	09:45:48	3.84-4.42	unconst.	2.400 (u.l.)
GRB190411A	09:45:48	4.42-6.24	7.950 (u.l.)	1.730 (u.l.)
GRB190411A	09:45:48	159.7-173.44	unconst.	2.490 (u.l.)
GRB200424A	12:07:10	1.52-1.99	3.140 (l.l.)	0.220 (l.l.)
GRB200424A	12:07:10	6.69-9.23	2.870 (l.l.)	−0.790 (l.l.)
GRB200424A	12:07:10	9.23-9.82	3.130 (l.l.)	0.520 (l.l.)
GRB200424A	12:07:10	19.73-21.94	2.450 (l.l.)	−0.130 (u.l.)
GRB200424A	12:07:10	27.75-34.35	2.690 (l.l.)	−0.380 (u.l.)
GRB200715A	23:51:40	20.87-49.92	2.740 (l.l.)	−0.730 (l.l.)
GRB210406A	17:11:22	9.4-19.82	4.070 (l.l.)	0.630 (l.l.)

Table 4: GRBs with significant signal in the SPI detectors but not listed in the IBAS. Most likely all these GRBs were outside of the coded field of view.

GRB name	**Trigger Time**
GRB040421	02:30:17
GRB041212	18:34:17
GRB060213	13:11:09
GRB070418	17:16:22
GRB080303	21:34:48
GRB090902	11:05:08
GRB110318	12:44:02
GRB110918	21:27:02
GRB120911	06:26:14
GRB121209	16:30:25
GRB130505	08:22:28
GRB130527	14:21:30
GRB130606	11:55:33
GRB131014	05:09:00
GRB140219	19:46:02
GRB140320	20:21:38
GRB150210	22:26:24
GRB150214	01:37:18
GRB150314	04:54:52
GRB150403	21:54:26
GRB150704	02:14:12
GRB151229	03:01:20
GRB151229	21:24:16
GRB160131	08:20:31
GRB160509	08:58:46
GRB160623	04:59:37
GRB160625	22:43:24
GRB170510	05:12:25
GRB170522	23:22:04
GRB180113	10:02:05
GRB180218	15:14:05
GRB180720	14:21:44
GRB180914	18:23:02
GRB190114	20:57:03
GRB190530	10:19:08
GRB200422	07:22:17
GRB201009	03:08:15

Continued on Next Page

Table 4: *Continued*

GRB name	**Trigger Time**
GRB201216	23:07:31
GRB210619	23:59:25

Bibliography

Abbott, B et al. (Oct. 2017). "GW170817: Observation of Gravitational Waves from a Binary Neutron Star Inspiral". In: *Physical Review Letters* 119.16, p. 161101. ISSN: 0031-9007. DOI: 10.1103/PhysRevLett.119.161101. eprint: 1710.05832.

Abdo, A. A. et al. (2009a). "Fermi large area telescope observations of the cosmic-ray induced γ-ray emission of the Earth's atmosphere". In: *Physical Review D* 80.12, p. 122004. ISSN: 1550-7998. DOI: 10.1103/physrevd.80.122004. eprint: 0912.1868.

Abdo, A.A. et al. (2009b). "The on-orbit calibration of the Fermi Large Area Telescope". In: *Astroparticle Physics* 32.3-4, pp. 193–219. ISSN: 0927-6505. DOI: 10.1016/j.astropartphys.2009.08.002. eprint: 0904.2226.

Ackermann, M. et al. (2012). "Fermi detection of γ-ray emission from the M2 soft X-ray flare on 2010 June 12". In: *The Astrophysical Journal* 745.2, p. 144. ISSN: 0004-637X. DOI: 10.1088/0004-637x/745/2/144. eprint: 1111.7026.

Ajello, M et al. (2008). "Cosmic X-Ray Background and Earth Albedo Spectra with Swift BAT". In: *The Astrophysical Journal* 689.2, pp. 666–677. ISSN: 0004-637X. DOI: 10.1086/592595. eprint: 0808.3377.

Alexander, D. M. et al. (2003). "The Chandra Deep Field North Survey. XIV. X-Ray-detected Obscured AGNs and Starburst Galaxies in the Bright Submillimeter Source Population". In: *The Astronomical Journal* 125.2, pp. 383–397. ISSN: 0004-6256. DOI: 10.1086/346088. eprint: astro-ph/0211267.

Allen, James A. van and Louis A. Frank (1959). "Radiation Around the Earth to a Radial Distance of 107,400 km." In: *Nature* 183.4659, pp. 430–434. ISSN: 0028-0836. DOI: 10.1038/183430a0.

Ananna, Tonima Tasnim et al. (2020). "Accretion History of AGNs. II. Constraints on AGN Spectral Parameters Using the Cosmic X-Ray Background". In: *The Astrophysical Journal* 889.1, p. 17. ISSN: 0004-637X. DOI: 10.3847/1538-4357/ab5aef. eprint: 1911.10706.

Arnaud, K. A. (Jan. 1996). "XSPEC: The First Ten Years". In: *Astronomical Data Analysis Software and Systems V*. Ed. by George H. Jacoby and Jeannette Barnes. Vol. 101. Astronomical Society of the Pacific Conference Series, p. 17.

Atwood, W. B. et al. (2009). "The large area telescope on the Fermi gamma-ray space telescope mission". In: *The Astrophysical Journal* 697.2, pp. 1071–1102. ISSN: 0004-637X. DOI: 10.1088/0004-637x/697/2/1071. eprint: 0902.1089.

Axelsson, Magnus and Luis Borgonovo (Jan. 2015). "The width of gamma-ray burst spectra". In: *Monthly Notices of the Royal Astronomical Society* 447.4, pp. 3150–3154. ISSN: 0035-8711. DOI: 10.1093/mnras/stu2675.

Band, D et al. (Aug. 1993). "BATSE observations of gamma-ray burst spectra. I - Spectral diversity". In: *The Astrophysical Journal* 413, p. 281. ISSN: 0004-637X. DOI: 10.1086/172995.

Baring, Matthew G (1997). "Diffusive Shock Acceleration: the Fermi Mechanism". In: *Very High Energy Phenomena in the Universe; Moriond Workshop*. arXiv. DOI: 10.48550/arxiv.astro-ph/9711177.

Barthelmy, Scott D. et al. (Oct. 2005). "The Burst Alert Telescope (BAT) on the SWIFT Midex Mission". In: *Space Science Reviews* 120.3-4, pp. 143–164. ISSN: 0038-6308. DOI: 10.1007/s11214-005-5096-3. eprint: astro-ph/0507410.

Bayes, Thomas and Price (Dec. 1763). "LII. An essay towards solving a problem in the doctrine of chances. By the late Rev. Mr. Bayes, F. R. S. communicated by Mr. Price, in a letter to John Canton, A. M. F. R. S". In: *Philosophical Transactions of the Royal Society of London* 53.53, pp. 370–418. ISSN: 0261-0523. DOI: 10.1098/rstl.1763.0053.

Beckmann, V et al. (June 2004). "Time resolved spectroscopy of GRB030501 using INTEGRAL". In: *Nuclear Physics B - Proceedings Supplements* 132, pp. 301–304. ISSN: 0920-5632. DOI: 10.1016/j.nuclphysbps.2004.04.052. eprint: astro-ph/0307070.

Beloborodov, A. M. et al. (2011). "Is gamma-ray burst afterglow emission intrinsically anisotropic?" In: *Monthly Notices of the Royal Astronomical Society* 410.4, pp. 2422–2427. ISSN: 0035-8711. DOI: 10.1111/j.1365-2966.2010.17616.x. eprint: 1003.1265.

Beniamini, Paz, Rodolfo Barniol Duran, and Dimitrios Giannios (Feb. 2018). "Marginally fast cooling synchrotron models for prompt GRBs". In: *Monthly Notices of the Royal Astronomical Society* 476.2, pp. 1785–1795. ISSN: 0035-8711. DOI: 10.1093/mnras/sty340. eprint: 1801.04944.

Berlato, F., J. Greiner, and J. Michael Burgess (2019). "Improved Fermi-GBM GRB Localizations Using BALROG". In: *The Astrophysical Journal* 873.1, p. 60. ISSN: 0004-637X. DOI: 10.3847/1538-4357/ab0413. eprint: 1902.01082.

Betancourt, Michael (Jan. 2017). "A Conceptual Introduction to Hamiltonian Monte Carlo". In: *arXiv*. DOI: 10.48550/arXiv.1701.02434. eprint: 1701.02434.

Beuermann, K et al. (1999). "VLT observations of GRB 990510 and its environment". In: *Astronomy and Astrophysics* 352, pp. 26–30. DOI: 10.48550/arxiv.astro-ph/9909043. eprint: astro-ph/9909043.

Bildsten, Lars et al. (1997). "Observations of Accreting Pulsars". In: *The Astrophysical Journal Supplement Series* 113.2, pp. 367–408. ISSN: 0067-0049. DOI: 10.1086/313060. eprint: astro-ph/9707125.

Biltzinger, B. et al. (2020). "A physical background model for the Fermi Gamma-ray Burst Monitor". In: *Astronomy & Astrophysics* 640, A8. ISSN: 0004-6361. DOI: 10.1051/0004-6361/201937347. eprint: 2005.11219.

Biltzinger, Björn, J. Michael Burgess, and Jochen Greiner (submitted). "Time-Resolved Spectral Catalogue of INTEGRAL/SPI GRBs". In: *Astronomy and Astrophysics*.

Biltzinger, Björn, J Michael Burgess, and Thomas Siegert (Mar. 2022). "PySPI: A python analysis framework for INTEGRAL/SPI". In: *Journal of Open Source Software* 7.71, p. 4017. DOI: 10.21105/joss.04017.

Biltzinger, Björn et al. (2022). "Improving INTEGRAL/SPI data analysis of GRBs". In: *Astronomy & Astrophysics* 663, A102. ISSN: 0004-6361. DOI: 10.1051/0004-6361/202243189. eprint: 2201.10310.

Bissaldi, E and V Connaughton (Oct. 2009). *GCN Circular 10070*.

Bissaldi, E. et al. (2009). "Ground-based calibration and characterization of the Fermi gamma-ray burst monitor detectors". In: *Experimental Astronomy* 24.1-3, pp. 47–88. ISSN: 0922-6435. DOI: 10.1007/s10686-008-9135-4. eprint: 0812.2908.

Blandford, R D and C F McKee (Jan. 1976). "Fluid dynamics of relativistic blast waves". In: *Physics of Fluids* 19.8, p. 1130. ISSN: 0031-9171. DOI: 10.1063/1.861619.

Bouchet, L et al. (2008). "INTEGRAL SPI All-Sky View in Soft Gamma Rays: A Study of Point-Source and Galactic Diffuse Emission". In: *The Astrophysical Journal* 679.2, pp. 1315–1326. ISSN: 0004-637X. DOI: 10.1086/529489. eprint: 0801.2086.

Bouchet, Laurent et al. (2011). "Diffusse emisssion measurement with the Spectrometer on INTEGRAL as an indirect probe of comsic-ray electrons and positrons". In: *The Astrophysical Journal* 739.1, p. 29. ISSN: 0004-637X. DOI: 10.1088/0004-637x/739/1/29. eprint: 1107.0200.

Bošnjak, Ž. et al. (Jan. 2014). "The spectral catalogue of INTEGRAL gamma-ray bursts". In: *Astronomy & Astrophysics* 561, A25. ISSN: 0004-6361. DOI: 10.1051/0004-6361/201322256. eprint: 1309.3174.

Bromberg, Omer and Alexander Tchekhovskoy (Dec. 2015). "Relativistic MHD simulations of core-collapse GRB jets: 3D instabilities and magnetic dissipation". In: *Monthly Notices of the Royal Astronomical Society* 456.2, pp. 1739–1760. ISSN: 0035-8711. DOI: 10.1093/mnras/stv2591.

Bucciantini, N. et al. (Jan. 2012). "Short gamma-ray bursts with extended emission from magnetar birth: jet formation and collimation". In: *Monthly Notices of the Royal Astronomical Society* 419.2, pp. 1537–1545. ISSN: 0035-8711. DOI: 10.1111/j.1365-2966.2011.19810.x.

Buchner, J. et al. (Apr. 2014). "X-ray spectral modelling of the AGN obscuring region in the CDFS: Bayesian model selection and catalogue". In: *Astronomy & Astrophysics* 564, A125. ISSN: 0004-6361. DOI: 10.1051/0004-6361/201322971. eprint: 1402.0004.

Burgess, J M (Aug. 2019). "Is spectral width a reliable measure of GRB emission physics?" In: *Astronomy & Astrophysics* 629, A69. ISSN: 0004-6361. DOI: 10.1051/0004-6361/201935140. eprint: 1705.05718.

Burgess, J Michael (Oct. 2014). "On spectral evolution and temporal binning in gamma-ray bursts". In: *Monthly Notices of the Royal Astronomical Society* 445.3, pp. 2589–2598. ISSN: 0035-8711. DOI: 10.1093/mnras/stu1925. eprint: 1408.3973.

Burgess, J Michael et al. (May 2016). "An external shock origin of GRB 131028A". In: *The Astrophysical Journal* 822.2, p. 63. ISSN: 0004-637X. DOI: 10.3847/0004-637X/822/2/63. eprint: 1506.05131.

Burgess, J Michael et al. (2017). "Awakening the BALROG: BAyesian Location Reconstruction Of GRBs". In: *Monthly Notices of the Royal Astronomical Society* 476.2, pp. 1427–1444. ISSN: 0035-8711. DOI: 10.1093/mnras/stx2853.

Burgess, J. Michael et al. (Feb. 2020). "Gamma-ray bursts as cool synchrotron sources". In: *Nature Astronomy* 4.2, pp. 174–179. DOI: 10.1038/s41550-019-0911-z. eprint: 1810.06965.

Bégué, D. and J. Michael Burgess (Mar. 2016). "The anatomy of a long gamma-ray burst: A simple classsification scheme for the emission mechanism(s)". In: *The Astrophysical Journal* 820.1, p. 68. ISSN: 0004-637X. DOI: 10.3847/0004-637X/820/1/68. eprint: 1602.04600.

Cano, Zach (July 2013). "A new method for estimating the bolometric properties of Ibc supernovae". In: *Monthly Notices of the Royal Astronomical Society* 434.2, pp. 1098–1116. ISSN: 0035-8711. DOI: 10.1093/mnras/stt1048. eprint: 1306.1488.

Cappelluti, Nico et al. (2017). "The Chandra COSMOS legacy survey: Energy Spectrum of the Cosmic X-ray Background and constraints on undetected populations". In: *The Astrophysical Journal* 837.1, p. 19. DOI: 10.3847/1538-4357/aa5ea4. eprint: 1702.01660.

Carpenter, Bob et al. (2017). "Stan: A Probabilistic Programming Language." In: *Journal of statistical software* 76.1. ISSN: 1548-7660. DOI: 10.18637/jss.v076.i01.

Cash, W (Mar. 1979). "Parameter estimation in astronomy through application of the likelihood ratio". In: *The Astrophysical Journal* 228, p. 939. ISSN: 0004-637X. DOI: 10.1086/156922.

Cavallo, G and M J Rees (July 1978). "A qualitative study of cosmic fireballs and -ray bursts". In: *Monthly Notices of the Royal Astronomical Society* 183.3, pp. 359–365. ISSN: 0035-8711. DOI: 10.1093/mnras/183.3.359.

Chauvin, Maxime (2021). *Geant4$_{SPI}$*. URL: https://github.com/MCvin/Geant4_SPI.

Chiang, James and Charles D Dermer (Feb. 1999). "Synchrotron and Synchrotron Self-Compton Emission and the Blast-Wave Model of Gamma-Ray Bursts". In: *The Astrophysical Journal* 512.2, pp. 699–710. ISSN: 0004-637X. DOI: 10.1086/306789. eprint: astro-ph/9803339.

Churazov, E et al. (2007). "INTEGRAL observations of the cosmic X-ray background in the 5–100 keV range via occultation by the Earth". In: *Astronomy & Astrophysics* 467.2, pp. 529–540. ISSN: 0004-6361. DOI: 10.1051/0004-6361:20066230. eprint: astro-ph/0608250.

Comisso, Luca and Lorenzo Sironi (Nov. 2019). "The Interplay of Magnetically Dominated Turbulence and Magnetic Reconnection in Producing Nonthermal Particles". In: *The Astrophysical Journal* 886.2, p. 122. ISSN: 0004-637X. DOI: 10.3847/1538-4357/ab4c33. eprint: 1909.01420.

Courvoisier, T. J.-L. et al. (2003). "The INTEGRAL Science Data Centre (ISDC)". In: *Astronomy & Astrophysics* 411.1, pp. L53–L57. ISSN: 0004-6361. DOI: 10.1051/0004-6361:20031172. eprint: astro-ph/0308047.

Craig, I and J Brown (1986). *Inverse problems in astronomy*. Institute of Physics Publishing. URL: https://www.osti.gov/biblio/5734250.

Crampton, D et al. (1976). "Spectroscopic analysis of Scorpius X-1." In: *The Astrophysical Journal* 207, p. 907. ISSN: 0004-637X. DOI: 10.1086/154561.

Crider, A et al. (Dec. 1996). "Evolution of the Low-Energy Photon Spectra in Gamma-Ray Bursts". In: *arXiv* 479.1, pp. L39–L42. ISSN: 0004-637X. DOI: 10.1086/310574. eprint: astro-ph/9612118.

Daigne and Mochkovitch (1998). "Gamma-ray bursts from internal shocks in a relativistic wind: temporal and spectral properties". In: *Monthly Notices of the Royal Astronomical Society* 296.2, pp. 275–286. ISSN: 0035-8711. DOI: 10.1046/j.1365-8711.1998.01305.x. eprint: astro-ph/9801245.

Dainotti, Maria Giovanna, Giuseppe Sarracino, and Salvatore Capozziello (Aug. 2022). "Gamma-ray bursts, supernovae Ia, and baryon acoustic oscillations: A binned cosmological analysis". In: *Publications of the Astronomical Society of Japan* 74.5, pp. 1095–1113. ISSN: 0004-6264. DOI: 10.1093/pasj/psac057. eprint: 2206.07479.

DeLaunay, James and Aaron Tohuvavohu (2022). "Harvesting BAT-GUANO with NITRATES (Non-Imaging Transient Reconstruction and Temporal Search): Detecting and Localizing the Faintest Gamma-Ray Bursts with a Likelihood Framework". In: *The Astrophysical Journal* 941.2, p. 169. ISSN: 0004-637X. DOI: 10.3847/1538-4357/ac9d38. eprint: 2111.01769.

Diehl, Roland et al. (2018). "INTEGRAL/SPI γ-ray line spectroscopy". In: *Astronomy & Astrophysics* 611, A12. ISSN: 0004-6361. DOI: 10.1051/0004-6361/201731815. eprint: 1710.10139.

Drenkhahn, G (May 2002). "Acceleration of GRB outflows by Poynting flux dissipation". In: *Astronomy & Astrophysics* 387.2, pp. 714–724. ISSN: 0004-6361. DOI: 10.1051/0004-6361:20020390. eprint: astro-ph/0112509.

Drenkhahn, G. and H. C. Spruit (2002). "Efficient acceleration and radiation in Poynting flux powered GRB outflows". In: *Astronomy & Astrophysics* 391.3, pp. 1141–1153. ISSN: 0004-6361. DOI: 10.1051/0004-6361:20020839. eprint: astro-ph/0202387.

Eichler, David et al. (July 1989). "Nucleosynthesis, neutrino bursts and γ-rays from coalescing neutron stars". In: *Nature* 340.6229, pp. 126–128. ISSN: 0028-0836. DOI: 10.1038/340126a0.

Enikeeva, Farida and Zaid Harchaoui (2019). "High-dimensional change-point detection under sparse alternatives". In: *The Annals of Statistics* 47.4, pp. 2051–2079. ISSN: 0090-5364. DOI: 10.1214/18-aos1740.

Evans, P A et al. (2014). "GRB 130925A: an ultralong gamma ray burst with a dust-echo afterglow, and implications for the origin of the ultralong GRBs". In: *Monthly Notices of the Royal Astronomical Society* 444.1, pp. 250–267. ISSN: 0035-8711. DOI: 10.1093/mnras/stu1459. eprint: 1403.4079.

Feroz, F and M P Hobson (Jan. 2008). "Multimodal nested sampling: an efficient and robust alternative to Markov Chain Monte Carlo methods for astronomical data analyses: Multimodal nested sampling". In: *Monthly Notices of the Royal Astronomical Society*

384.2, pp. 449–463. ISSN: 0035-8711. DOI: 10.1111/j.1365-2966.2007.12353.x. eprint: 0704.3704.

Feroz, F, M P Hobson, and M Bridges (Oct. 2009). "MultiNest: an efficient and robust Bayesian inference tool for cosmology and particle physics". In: *Monthly Notices of the Royal Astronomical Society* 398.4, pp. 1601–1614. ISSN: 0035-8711. DOI: 10.1111/j.1365-2966.2009.14548.x. eprint: 0809.3437.

Feroz, Farhan et al. (2019). "Importance Nested Sampling and the MultiNest Algorithm". In: *The Open Journal of Astrophysics* 2.1. DOI: 10.21105/astro.1306.2144. eprint: 1306.2144.

Filliatre, P. et al. (Aug. 2005). "Out of the darkness: the infrared afterglow of the INTEGRAL burst GRB 040422 observed with the VLT". In: *Astronomy & Astrophysics* 438.3, pp. 793–801. ISSN: 0004-6361. DOI: 10.1051/0004-6361:20042609. eprint: astro-ph/0503688.

Filliatre, P. et al. (Mar. 2006). "The weak INTEGRAL bursts GRB 040223 and GRB 040624: an emerging population of dark afterglows". In: *Astronomy & Astrophysics* 448.3, pp. 971–982. ISSN: 0004-6361. DOI: 10.1051/0004-6361:20054072.

Fitzpatrick, Gerard et al. (2012). "Background estimation in a wide-field background-limited instrument such as Fermi GBM". In: *Space Telescopes and Instrumentation 2012: Ultraviolet to Gamma Ray*, 84433B–84433B–9. ISSN: 0277-786X. DOI: 10.1117/12.928036. eprint: 1210.5369.

Foley, S et al. (2008). "Global characteristics of GRBs observed with INTEGRAL and the inferred large population of low-luminosity GRBs". In: *arXiv*. DOI: 10.1051/0004-6361:20078399. eprint: 0803.1821.

Freeman, Peter, Stephen Doe, and Aneta Siemiginowska (2001). "Sherpa: a mission-independent data analysis application". In: *Astronomical Data Analysis*, pp. 76–87. ISSN: 0277-786X. DOI: 10.1117/12.447161. eprint: astro-ph/0108426.

Fryzlewicz, Piotr (2014). "Wild binary segmentation for multiple change-point detection". In: *The Annals of Statistics* 42.6, pp. 2243–2281. ISSN: 0090-5364. DOI: 10.1214/14-aos1245. eprint: 1411.0858.

Ganushkina, N. Yu et al. (2011). "Locations of boundaries of outer and inner radiation belts as observed by Cluster and Double Star". In: *Journal of Geophysical Research: Space Physics* 116.A9, n/a–n/a. ISSN: 0148-0227. DOI: 10.1029/2010ja016376.

Gelman, A. et al. (2014). *Bayesian Data Analysis (3rd ed.)* Chapman and Hall/CRC, p. 675. DOI: https://doi.org/10.1201/b16018.

Geyer, Charles J (Nov. 1992). "Practical Markov Chain Monte Carlo". In: *Statistical Science* 7.4. ISSN: 0883-4237. DOI: 10.1214/ss/1177011137.

Giacconi, Riccardo et al. (2002). "Chandra Deep Field South: The 1 Ms Catalog". In: *The Astrophysical Journal Supplement Series* 139.2, pp. 369–410. ISSN: 0067-0049. DOI: 10.1086/338927. eprint: astro-ph/0110452.

Giannios, D and H C Spruit (Jan. 2005). "Spectra of Poynting-flux powered GRB outflows". In: *Astronomy & Astrophysics* 430.1, pp. 1–7. ISSN: 0004-6361. DOI: 10.1051/0004-6361:20047033. eprint: astro-ph/0401109.

Goldstein, A. et al. (Oct. 2017). "An Ordinary Short Gamma-Ray Burst with Extraordinary Implications: Fermi-GBM Detection of GRB 170817A". In: *The Astrophysical Journal Letters* 848.2, p. L14. ISSN: 2041-8205. DOI: 10.3847/2041-8213/aa8f41. eprint: 1710.05446.

Goldwurm, A. et al. (2003). "The INTEGRAL/IBIS scientific data analysis". In: *Astronomy & Astrophysics* 411.1, pp. L223–L229. ISSN: 0004-6361. DOI: 10.1051/0004-6361:20031395. eprint: astro-ph/0311172.

Golenetskii, S et al. (Oct. 2009). *GCN Circular 10083*.

Grebenev, S. A. and I. V. Chelovekov (Dec. 2007). "Cosmic GRB 060428C detected in the field of view of the IBIS and SPI telescopes onboard the INTEGRAL observatory and its early afterglow". In: *Astronomy Letters* 33.12, pp. 789–796. ISSN: 1063-7737. DOI: 10.1134/S1063773707120018.

Greiner, J. et al. (Apr. 2009). "The redshift and afterglow of the extremely energetic gamma-ray burst GRB 080916C". In: *Astronomy & Astrophysics* 498.1, pp. 89–94. ISSN: 0004-6361. DOI: 10.1051/0004-6361/200811571. eprint: 0902.0761.

Greiner, J. et al. (2014). "GROND coverage of the main peak of gamma-ray burst 130925A". In: *Astronomy & Astrophysics* 568, A75. ISSN: 0004-6361. DOI: 10.1051/0004-6361/201424250. eprint: 1407.4210.

Gruber, D. et al. (2011). "Fermi/GBM observations of the ultra-long GRB 091024". In: *Astronomy & Astrophysics* 528, A15. ISSN: 0004-6361. DOI: 10.1051/0004-6361/201015891. eprint: 1101.1099.

Gruber, D E et al. (1999). "The Spectrum of Diffuse Cosmic Hard X-Rays Measured with HEAO 1". In: *The Astrophysical Journal* 520.1, pp. 124–129. ISSN: 0004-637X. DOI: 10.1086/307450. eprint: astro-ph/9903492.

Grundy, Thomas, Rebecca Killick, and Gueorgui Mihaylov (2020). "High-dimensional change-point detection via a geometrically inspired mapping". In: *Statistics and Computing* 30.4, pp. 1155–1166. ISSN: 0960-3174. DOI: 10.1007/s11222-020-09940-y. eprint: 2001.05241.

Hannah, I. G. et al. (2007). "First Limits on the 3-200 keV X-Ray Spectrum of the Quiet Sun Using RHESSI". In: *The Astrophysical Journal Letters* 659.1, pp. L77–L80. ISSN: 0004-637X. DOI: 10.1086/516750. eprint: astro-ph/0702726.

Hasinger, G (2004). "The X-ray background and AGNs". In: *Nuclear Physics B - Proceedings Supplements* 132, pp. 86–96. ISSN: 0920-5632. DOI: 10.1016/j.nuclphysbps.2004.04.127. eprint: astro-ph/0310804.

Hastings, W K (Apr. 1970). "Monte Carlo sampling methods using Markov chains and their applications". In: *Biometrika* 57.1, pp. 97–109. ISSN: 0006-3444. DOI: 10.1093/biomet/57.1.97.

Hester, J Jeff (2008). "The Crab Nebula: An Astrophysical Chimera". In: *Annual Review of Astronomy and Astrophysics* 46.1, pp. 127–155. ISSN: 0066-4146. DOI: 10.1146/annurev.astro.45.051806.110608.

Hickox, Ryan C. and Maxim Markevitch (2006). "Absolute Measurement of the Unresolved Cosmic X-Ray Background in the 0.5-8 keV Band with Chandra". In: *The Astrophysical*

Journal 645.1, pp. 95–114. ISSN: 0004-637X. DOI: 10.1086/504070. eprint: astro-ph/0512542.

Hjorth, Jens et al. (2003). "A very energetic supernova associated with the γ-ray burst of 29 March 2003". In: *Nature* 423.6942, pp. 847–850. ISSN: 0028-0836. DOI: 10.1038/nature01750. eprint: astro-ph/0306347.

Hoffman, Matthew D and Andrew Gelman (2014). "The No-U-Turn Sampler: Adaptively Setting Path Lengths in Hamiltonian Monte Carlo". In: *Journal of Machine Learning Research* 15.47, pp. 1593–1623. DOI: 10.48550/arxiv.1111.4246. eprint: 1111.4246.

Horváth, Lajos and Marie Hušková (2012). "Change-point detection in panel data: Change-point detection in panel data". In: *Journal of Time Series Analysis* 33.4, pp. 631–648. ISSN: 0143-9782. DOI: 10.1111/j.1467-9892.2012.00796.x.

Hubbell, J H, H A Gimm, and I Overbo (1980). "Pair, Triplet, and Total Atomic Cross Sections (and Mass Attenuation Coefficients) for 1 MeV-100 GeV Photons in Elements Z =1 to 100". In: *Journal of Physical and Chemical Reference Data* 9.4, pp. 1023–1148. ISSN: 0047-2689. DOI: 10.1063/1.555629.

IceCube Collaboration, The et al. (2018). "Multimessenger observations of a flaring blazar coincident with high-energy neutrino IceCube-170922A". In: *Science* 361.6398. ISSN: 0036-8075. DOI: 10.1126/science.aat1378. eprint: 1807.08816.

Isi, Maximiliano, Will M. Farr, and Katerina Chatziioannou (July 2022). "Comparing Bayes factors and hierarchical inference for testing general relativity with gravitational waves". In: *Physical Review D* 106.2, p. 024048. ISSN: 2470-0010. DOI: 10.1103/PhysRevD.106.024048. eprint: 2204.10742.

Jackson, B et al. (2005). "An algorithm for optimal partitioning of data on an interval". In: *IEEE Signal Processing Letters* 12.2, pp. 105–108. ISSN: 1070-9908. DOI: 10.1109/lsp.2001.838216. eprint: math/0309285.

Jenke, P. A. et al. (2016). "Fermi observations of v404 Cyg during its 2015 outburst". In: *The Astrophysical Journal* 826.1, p. 37. ISSN: 0004-637X. DOI: 10.3847/0004-637x/826/1/37. eprint: 1601.00911.

Jourdain, Elisabeth (July 2009). "5 years of survey on the Crab Nebula with SPI/INTEGRAL". In: *Proceedings of 7th INTEGRAL Workshop — PoS(Integral08)*, p. 143. DOI: 10.22323/1.067.0143.

Kass, Robert E and Adrian E Raftery (June 1995). "Bayes Factors". In: *Journal of the American Statistical Association* 90.430, pp. 773–795. ISSN: 0162-1459. DOI: 10.1080/01621459.1995.10476572.

Kienlin, A. von et al. (Nov. 2003a). "INTEGRAL results on GRB 030320: A long gamma-ray burst detected at the edge of the field of view". In: *Astronomy & Astrophysics* 411.1, pp. L321–L325. ISSN: 0004-6361. DOI: 10.1051/0004-6361:20031232.

Kienlin, A. von et al. (Nov. 2003b). "INTEGRAL Spectrometer SPI's GRB detection capabilities". In: *Astronomy & Astrophysics* 411.1, pp. L299–L305. ISSN: 0004-6361. DOI: 10.1051/0004-6361:20031231. eprint: astro-ph/0308346.

Kienlin, A. von et al. (Apr. 2020). "The Fourth Fermi-GBM Gamma-Ray Burst Catalog: A Decade of Data". In: *The Astrophysical Journal* 893.1, p. 46. ISSN: 0004-637X. DOI: 10.3847/1538-4357/ab7a18. eprint: 2002.11460.

Kinzer, R L et al. (1997). "Diffuse Cosmic Gamma Radiation Measured by HEAO 1". In: *The Astrophysical Journal* 475.1, pp. 361–372. ISSN: 0004-637X. DOI: 10.1086/303507.

Kippen, R. M. et al. (2007). "Instrument Response Modeling and Simulation for the GLAST Burst Monitor". In: *AIP Conference Proceedings* 921.1, pp. 590–591. ISSN: 0094-243X. DOI: 10.1063/1.2757466.

Klebesadel, Ray W, Ian B Strong, and Roy A Olson (June 1973). "Observations of Gamma-Ray Bursts of Cosmic Origin". In: *The Astrophysical Journal* 182, p. L85. ISSN: 0004-637X. DOI: 10.1086/181225.

Knodlseder, J et al. (Mar. 1999). "Image Reconstruction of COMPTEL 1.8 MeV 26Al Line Data". In: *arXiv*. DOI: 10.48550/arXiv.astro-ph/9903172. eprint: astro-ph/9903172.

Kobayashi, Shiho, Tsvi Piran, and Re'em Sari (Nov. 1997). "Can Internal Shocks Produce the Variability in Gamma-Ray Bursts?" In: *The Astrophysical Journal* 490.1, pp. 92–98. ISSN: 0004-637X. DOI: 10.1086/512791. eprint: astro-ph/9705013.

— (Mar. 1999). "Hydrodynamics of a Relativistic Fireball: The Complete Evolution". In: *The Astrophysical Journal* 513.2, pp. 669–678. ISSN: 0004-637X. DOI: 10.1086/306868. eprint: astro-ph/9803217.

Kobayashi, Shiho and Re'em Sari (Apr. 2001). "Ultraefficient Internal Shocks". In: *The Astrophysical Journal* 551.2, pp. 934–939. ISSN: 0004-637X. DOI: 10.1086/320249.

Koshut, Thomas M et al. (1996). "Systematic Effects on Duration Measurements of Gamma-Ray Bursts". In: *The Astrophysical Journal* 463, p. 570. ISSN: 0004-637X. DOI: 10.1086/177272.

Kouveliotou, Chryssa et al. (1993). "Identification of two classes of gamma-ray bursts". In: *The Astrophysical Journal* 413, p. L101. ISSN: 0004-637X. DOI: 10.1086/186969.

Kreykenbohm, I. et al. (2008). "High variability in Vela X-1: giant flares and off states". In: *Astronomy & Astrophysics* 492.2, pp. 511–525. ISSN: 0004-6361. DOI: 10.1051/0004-6361:200809956. eprint: 0810.2981.

Krimm, H. A. et al. (2013). "The Swift/BAT hard X-ray transient monitor". In: *The Astrophysical Journal Supplement Series* 209.1, p. 14. ISSN: 0067-0049. DOI: 10.1088/0067-0049/209/1/14. eprint: 1309.0755.

Krivonos, R. et al. (2007). "Hard X-ray emission from the Galactic ridge". In: *Astronomy & Astrophysics* 463.3, pp. 957–967. ISSN: 0004-6361. DOI: 10.1051/0004-6361:20065626. eprint: astro-ph/0605420.

Kulkarni, S. R. et al. (Apr. 1999). "The afterglow, redshift and extreme energetics of the γ-ray burst of 23 January 1999". In: *Nature* 398.6726, pp. 389–394. ISSN: 0028-0836. DOI: 10.1038/18821.

Kunzweiler, F et al. (2022). "Automatic detection of long-duration transients in Fermi - GBM data". In: *Astronomy & Astrophysics* 665, A112. ISSN: 0004-6361. DOI: 10.1051/0004-6361/202243287. eprint: 2205.13649.

Lee, Hyun Kyu, R.A.M.J. Wijers, and G.E. Brown (2000). "The Blandford–Znajek process as a central engine for a gamma-ray burst". In: *Physics Reports* 325.3, pp. 83–114. ISSN: 0370-1573. DOI: 10.1016/s0370-1573(99)00084-8. eprint: astro-ph/9906213.

Leung, Shing-Chi and Thomas Siegert (June 2022). "Gamma-ray light curves and spectra of classical novae". In: *Monthly Notices of the Royal Astronomical Society* 516.1, pp. 1008–1021. ISSN: 0035-8711. DOI: 10.1093/mnras/stac1672. eprint: 2112.06893.

Levan, A. J. et al. (2014). "A new population of ultra-long duration gamma-ray bursts". In: *The Astrophysical Journal* 781.1, p. 13. ISSN: 0004-637X. DOI: 10.1088/0004-637x/781/1/13. eprint: 1302.2352.

Levan, Andrew et al. (Dec. 2016). "Gamma-Ray Burst Progenitors". In: *Space Science Reviews* 202.1-4, pp. 33–78. ISSN: 0038-6308. DOI: 10.1007/s11214-016-0312-x. eprint: 1611.03091.

Li, T P and Y Q Ma (Sept. 1983). "Analysis methods for results in gamma-ray astronomy". In: *The Astrophysical Journal* 272, p. 317. ISSN: 0004-637X. DOI: 10.1086/161295.

Lien, Amy et al. (Sept. 2016). "The third Swift Burst Alert Telescioe gamma-ray burst catalog". In: *The Astrophysical Journal* 829.1, p. 7. ISSN: 0004-637X. DOI: 10.3847/0004-637X/829/1/7. eprint: 1606.01956.

Loredo, Thomas J and Ira M Wasserman (Jan. 1995). "Inferring the spatial and energy distribution of gamma-ray burst sources. 1: Methodology". In: *The Astrophysical Journal Supplement Series* 96, p. 261. ISSN: 0067-0049. DOI: 10.1086/192119.

Luca, A. De and S. Molendi (2004). "The 2–8 keV cosmic X-ray background spectrum as observed with XMM-Newton ***". In: *Astronomy & Astrophysics* 419.3, pp. 837–848. ISSN: 0004-6361. DOI: 10.1051/0004-6361:20034421. eprint: astro-ph/0311538.

Lund, N et al. (Nov. 2003). "JEM–X: The X-ray monitor aboard INTEGRAL". In: *Astronomy & Astrophysics* 411.1, pp. L231–L238. ISSN: 0004-6361. DOI: 10.1051/0004-6361:20031358.

MacFadyen, A I, S E Woosley, and A Heger (Mar. 2001). "Supernovae, Jets, and Collapsars". In: *The Astrophysical Journal* 550.1, pp. 410–425. ISSN: 0004-637X. DOI: 10.1086/319698. eprint: astro-ph/9910034.

Madsen, Kristin K. et al. (2017). "Measurement of the Absolute Crab Flux with NuSTAR". In: *The Astrophysical Journal* 841.1, p. 56. ISSN: 0004-637X. DOI: 10.3847/1538-4357/aa6970. eprint: 1703.10685.

Magdziarz, Paweł and Andrzej A Zdziarski (1995). "Angle-dependent Compton reflection of X-rays and gamma-rays". In: *Monthly Notices of the Royal Astronomical Society* 273.3, pp. 837–848. ISSN: 0035-8711. DOI: 10.1093/mnras/273.3.837.

MAGIC Collaboration, The et al. (2019). "Teraelectronvolt emission from the γ-ray burst GRB 190114C". In: *Nature* 575.7783, pp. 455–458. ISSN: 0028-0836. DOI: 10.1038/s41586-019-1750-x. eprint: 2006.07249.

Malaguti, G et al. (Nov. 2003). "GRB 021125: The first GRB imaged by INTEGRAL". In: *Astronomy & Astrophysics* 411.1, pp. L307–L310. ISSN: 0004-6361. DOI: 10.1051/0004-6361:20031155.

Martin-Carrillo, A. et al. (July 2014). "GRB 120711A: an intense INTEGRAL burst with long-lasting soft γ-ray emission and a powerful optical flash". In: *Astronomy & Astrophysics* 567, A84. ISSN: 0004-6361. DOI: 10.1051/0004-6361/201220872. eprint: 1405.7396.

Mas-Hesse, J. M. et al. (Nov. 2003). "OMC: An Optical Monitoring Camera for INTEGRAL". In: *Astronomy & Astrophysics* 411.1, pp. L261–L268. ISSN: 0004-6361. DOI: 10.1051/0004-6361:20031418.

Mazzali, Paolo A. et al. (2003). "The Type Ic Hypernova SN 2003dh/GRB 030329". In: *The Astrophysical Journal Letters* 599.2, pp. L95–L98. ISSN: 0004-637X. DOI: 10.1086/381259. eprint: astro-ph/0309555.

McBreen, S. et al. (Aug. 2006). "Observations of the intense and ultra-long burst GRB 041219a with the Germanium spectrometer on INTEGRAL". In: *Astronomy & Astrophysics* 455.2, pp. 433–440. ISSN: 0004-6361. DOI: 10.1051/0004-6361:20065203.

McGlynn, S. et al. (Aug. 2008). "GRB 070707: the first short gamma-ray burst observed by INTEGRAL". In: *Astronomy & Astrophysics* 486.2, pp. 405–410. ISSN: 0004-6361. DOI: 10.1051/0004-6361:20079295. eprint: 0805.2880.

McGlynn, S. et al. (May 2009). "High energy emission and polarisation limits for the INTEGRAL burst GRB 061122". In: *Astronomy & Astrophysics* 499.2, pp. 465–472. ISSN: 0004-6361. DOI: 10.1051/0004-6361/200810920. eprint: 0903.5218.

McIlwain, Carl E (1966). "Radiation Trapped in the Earth's Magnetic Field". In: *Astrophysics and Space Science Library*, pp. 45–61. ISSN: 0067-0057. DOI: 10.1007/978-94-010-3553-8_4.

Meegan, C A et al. (Jan. 1992). "Spatial distribution of γ-ray bursts observed by BATSE". In: *Nature* 355.6356, pp. 143–145. ISSN: 0028-0836. DOI: 10.1038/355143a0.

Meegan, Charles et al. (2009). "The Fermi gamma-ray burst monitor". In: *The Astrophysical Journal* 702.1, pp. 791–804. ISSN: 0004-637X. DOI: 10.1088/0004-637x/702/1/791. eprint: 0908.0450.

Mereghetti, S. et al. (Nov. 2003a). "GRB 021219: The first Gamma-Ray Burst localized in real time with IBAS". In: *Astronomy & Astrophysics* 411.1, pp. L311–L314. ISSN: 0004-6361. DOI: 10.1051/0004-6361:20031303. eprint: astro-ph/0308457.

Mereghetti, S et al. (May 2003b). "INTEGRAL and XMM-Newton Observations of the Weak Gamma-Ray Burst GRB 030227". In: *The Astrophysical Journal* 590.2, pp. L73–L77. ISSN: 0004-637X. DOI: 10.1086/376853.

Mereghetti, S. et al. (Nov. 2003c). "The INTEGRAL Burst Alert System". In: *Astronomy & Astrophysics* 411.1, pp. L291–L297. ISSN: 0004-6361. DOI: 10.1051/0004-6361:20031289. eprint: astro-ph/0308173.

Meszaros, P, P Laguna, and M J Rees (1993). "Gasdynamics of relativistically expanding gamma-ray burst sources - Kinematics, energetics, magnetic fields, and efficiency". In: *The Astrophysical Journal* 415, p. 181. ISSN: 0004-637X. DOI: 10.1086/173154. eprint: astro-ph/9301007.

Meszaros, P and M J Rees (1993). "Relativistic fireballs and their impact on external matter - Models for cosmological gamma-ray bursts". In: *The Astrophysical Journal* 405, p. 278. ISSN: 0004-637X. DOI: 10.1086/172360.

Metropolis, Nicholas et al. (June 1953). "Equation of State Calculations by Fast Computing Machines". In: *The Journal of Chemical Physics* 21.6, pp. 1087–1092. ISSN: 0021-9606. DOI: 10.1063/1.1699114.

Metzger, B. D., E. Quataert, and T. A. Thompson (Apr. 2008). "Short-duration gamma-ray bursts with extended emission from protomagnetar spin-down". In: *Monthly Notices of the Royal Astronomical Society* 385.3, pp. 1455–1460. ISSN: 0035-8711. DOI: 10.1111/j.1365-2966.2008.12923.x. eprint: 0712.1233.

Metzger, B. D. et al. (May 2011). "The protomagnetar model for gamma-ray bursts". In: *Monthly Notices of the Royal Astronomical Society* 413.3, pp. 2031–2056. ISSN: 0035-8711. DOI: 10.1111/j.1365-2966.2011.18280.x.

Milton, Philip et al. (2019). "Spatial analysis made easy with linear regression and kernels." In: *Epidemics* 29, p. 100362. ISSN: 1755-4365. DOI: 10.1016/j.epidem.2019.100362.

Moran, L et al. (Mar. 2005). "INTEGRAL and XMM-Newton observations of GRB040106". In: *Astronomy & Astrophysics* 432.2, pp. 467–473. ISSN: 0004-6361. DOI: 10.1051/0004-6361:20041267.

Morey, Richard D., Jan-Willem Romeijn, and Jeffrey N. Rouder (June 2016). "The philosophy of Bayes factors and the quantification of statistical evidence". In: *Journal of Mathematical Psychology* 72, pp. 6–18. ISSN: 0022-2496. DOI: 10.1016/j.jmp.2015.11.001.

Mozzoni, D T, M Mandea, and J Cain (2007). "Magnetic perturbations seen by CHAMP and evaluated using the TIE-GCM". In: *Annales Geophysicae* 25.7, pp. 1543–1554. DOI: 10.5194/angeo-25-1543-2007.

Mukherjee, Pia, David Parkinson, and Andrew R. Liddle (2006). "A Nested Sampling Algorithm for Cosmological Model Selection". In: *The Astrophysical Journal Letters* 638.2, pp. L51–L54. ISSN: 0004-637X. DOI: 10.1086/501068. eprint: astro-ph/0508461.

Murakami, T. et al. (Sept. 1988). "Evidence for cyclotron absorption from spectral features in gamma-ray bursts seen with Ginga". In: *Nature* 335.6187, pp. 234–235. ISSN: 0028-0836. DOI: 10.1038/335234a0.

Mészáros, P. and M. J. Rees (1997). "Optical and Long-Wavelength Afterglow from Gamma-Ray Bursts". In: *The Astrophysical Journal* 476.1, pp. 232–237. ISSN: 0004-637X. DOI: 10.1086/303625. eprint: astro-ph/9606043.

Möller, Julius (2023). "New Background Treatment for Constant Sources in INTEGRAL/SPI (working title)". MA thesis. Technische Universität München.

Nandra, K. and K. A. Pounds (1994). "Ginga observations of the X-ray spectra of Seyfert galaxies". In: *Monthly Notices of the Royal Astronomical Society* 268.2, pp. 405–429. ISSN: 0035-8711. DOI: 10.1093/mnras/268.2.405.

Ng, Kenny C. Y. et al. (2015). "Improved limits on sterile neutrino dark matter using full-sky Fermi Gamma-ray Burst Monitor data". In: *Physical Review D* 92.4, p. 043503. ISSN: 1550-7998. DOI: 10.1103/physrevd.92.043503. eprint: 1504.04027.

Oganesyan, G. et al. (Aug. 2019). "Prompt optical emission as a signature of synchrotron radiation in gamma-ray bursts". In: *Astronomy & Astrophysics* 628, A59. ISSN: 0004-6361. DOI: 10.1051/0004-6361/201935766. eprint: 1904.11086.

Pacini, F. (1968). "Rotating Neutron Stars, Pulsars and Supernova Remnants". In: *Nature* 219.5150, pp. 145–146. ISSN: 0028-0836. DOI: 10.1038/219145a0.

Paczynski, Bohdan (1991). "Cosmological gamma-ray bursts." In: *Acta Astronomica* 41, pp. 257–267. DOI: test. URL: https://ui.adsabs.harvard.edu/abs/1991AcA...41..257P/abstract.

Paczyński, Bohdan (Feb. 1998a). "Are Gamma-Ray Bursts in Star-Forming Regions?" In: *The Astrophysical Journal Letters* 494.1, pp. L45–L48. ISSN: 0004-637X. DOI: 10.1086/311148. eprint: astro-ph/9710086.

— (1998b). "Gamma-ray bursts as hypernovae". In: *Fourth Huntsville gamma-ray burst symposium* 428.1, pp. 783–787. ISSN: 0094-243X. DOI: 10.1063/1.55404. eprint: astro-ph/9706232.

Perkins, Jeremy S et al. (2020). "BurstCube: a CubeSat for gravitational wave counterparts". In: *Space Telescopes and Instrumentation 2020: Ultraviolet to Gamma Ray* 11444, p. 172. ISSN: 0277-786X. DOI: 10.1117/12.2562796.

Pesce-Rollins, Melissa (2009). "Extending the Galactic Cosmic Ray electron + positron spectrum measured by the Fermi LAT". In: *arXiv* 1, pp. 1–10. DOI: 10.48550/arxiv.0912.3611. eprint: 0912.3611.

Petry, Dirk (2005). "The Earth's Gamma-ray Albedo as observed by EGRET". In: *AIP Conference Proceedings* 745.1, pp. 709–714. ISSN: 0094-243X. DOI: 10.1063/1.1878488. eprint: astro-ph/0410487.

Pe'er, Asaf, Peter Mészáros, and Martin J. Rees (May 2006). "The observable effect of a photospheric component on GRB's prompt emission spectrum: peak energy clustering and flat spectra above the thermal peak". In: *AIP Conference Proceedings* 836.1, pp. 181–184. ISSN: 0094-243X. DOI: 10.1063/1.2207885.

Piran, T, A Shemi, and R Narayan (Aug. 1993). "Hydrodynamics of relativistic fireballs". In: *Monthly Notices of the Royal Astronomical Society* 263.4, pp. 861–867. ISSN: 0035-8711. DOI: 10.1093/mnras/263.4.861. eprint: astro-ph/9301004.

Piran, Tsvi (Jan. 2005). "The physics of gamma-ray bursts". In: *Reviews of Modern Physics* 76.4, pp. 1143–1210. ISSN: 0034-6861. DOI: 10.1103/RevModPhys.76.1143. eprint: astro-ph/0405503.

Pleintinger, Moritz M. M. et al. (2019). "Comparing simulated 26Al maps to gamma-ray measurements". In: *Astronomy & Astrophysics* 632, A73. ISSN: 0004-6361. DOI: 10.1051/0004-6361/201935911. eprint: 1910.06112.

Popham, Robert, S E Woosley, and Chris Fryer (June 1999). "Hyperaccreting Black Holes and Gamma-Ray Bursts". In: *The Astrophysical Journal* 518.1, pp. 356–374. ISSN: 0004-637X. DOI: 10.1086/307259.

Preece, R. D. et al. (Oct. 1998). "The Synchrotron Shock Model Confronts a "Line of Death" in the BATSE Gamma-Ray Burst Data". In: *The Astrophysical Journal Letters* 506.1, pp. L23–L26. ISSN: 0004-637X. DOI: 10.1086/311644. eprint: astro-ph/9808184.

Rees, M J and P Meszaros (1994). "Unsteady outflow models for cosmological gamma-ray bursts". In: *The Astrophysical Journal* 430, p. L93. ISSN: 0004-637X. DOI: 10.1086/187446. eprint: astro-ph/9404038.

Revnivtsev, M. et al. (Dec. 2003). "The spectrum of the cosmic X-ray background observed by RTXE/PCA". In: *Astronomy & Astrophysics* 411.3, pp. 329–334. ISSN: 0004-6361. DOI: 10.1051/0004-6361:20031386. eprint: astro-ph/0306569.

Ricci, C. et al. (2017). "BAT AGN Spectroscopic Survey. V. X-Ray Properties of the Swift/BAT 70-month AGN Catalog". In: *The Astrophysical Journal Supplement Series* 233.2, p. 17. ISSN: 0067-0049. DOI: 10.3847/1538-4365/aa96ad. eprint: 1709.03989.

Riess, Adam G et al. (Jan. 2018). "Type Ia Supernova Distances at Redshift >1.5 from the Hubble Space Telescope Multi-cycle Treasury Programs: The Early Expansion Rate". In: *The Astrophysical Journal* 853.2, p. 126. ISSN: 0004-637X. DOI: 10.3847/1538-4357/aaa5a9. eprint: 1710.00844.

Roberts, Gareth O. and Jeffrey S. Rosenthal (2004). "General state space Markov chains and MCMC algorithms". In: *Probability Surveys* 1.none, pp. 20–71. ISSN: 1549-5787. DOI: 10.1214/154957804100000024. eprint: math/0404033.

Rolke, Wolfgang A., Angel M. López, and Jan Conrad (2005). "Limits and confidence intervals in the presence of nuisance parameters". In: *Nuclear Instruments and Methods in Physics Research Section A: Accelerators, Spectrometers, Detectors and Associated Equipment* 551.2-3, pp. 493–503. ISSN: 0168-9002. DOI: 10.1016/j.nima.2005.05.068. eprint: physics/0403059.

Roques, J. P. et al. (Nov. 2003). "SPI/INTEGRAL in-flight performance". In: *Astronomy & Astrophysics* 411.1, pp. L91–L100. ISSN: 0004-6361. DOI: 10.1051/0004-6361:20031501. eprint: astro-ph/0310793.

Roques, Jean-Pierre and Elisabeth Jourdain (2019). "On the High-energy Emissions of Compact Objects Observed with INTEGRAL SPI: Event Selection Impact on Source Spectra and Scientific Results for the Bright Sources Crab Nebula, GS 2023+338 and MAXI J1820+070". In: *The Astrophysical Journal* 870.2, p. 92. ISSN: 0004-637X. DOI: 10.3847/1538-4357/aaf1c9. eprint: 1811.06391.

Ruderman, M. (1975). "Theories of γ-ray bursts". In: *Annals of the New York Academy of Sciences* 262.1, pp. 164–180. ISSN: 0077-8923. DOI: 10.1111/j.1749-6632.1975.tb31430.x.

Rybicki, George B. and Alan P. Lightman (1985). *Radiative Processes in Astrophysics*. John Wiley & Sons, Ltd. ISBN: 9783527618170. DOI: 10.1002/9783527618170.ch6.

Ryde, Felix et al. (2011). "Observational evidence of dissipative photospheres in gamma-ray bursts". In: *Monthly Notices of the Royal Astronomical Society* 415.4, pp. 3693–3705. ISSN: 0035-8711. DOI: 10.1111/j.1365-2966.2011.18985.x. eprint: 1103.0708.

Sakamoto, T., S. Barthelmy, and Baumgartner W. (Oct. 2009). *GCN Circular 10072*.

Salvaterra, Ruben (Sept. 2015). "High redshift Gamma-Ray Bursts". In: *Journal of High Energy Astrophysics* 7, pp. 35–43. ISSN: 2214-4048. DOI: 10.1016/j.jheap.2015.03.001.

Sari, Re'em (Nov. 1997). "Hydrodynamics of Gamma-Ray Burst Afterglow". In: *The Astrophysical Journal Letters* 489.1, pp. L37–L40. ISSN: 0004-637X. DOI: 10.1086/310957.

Sari, Re'em, Ramesh Narayan, and Tsvi Piran (Dec. 1996). "Cooling Timescales and Temporal Structure of Gamma-Ray Bursts". In: *The Astrophysical Journal* 473.1, pp. 204–218. ISSN: 0004-637X. DOI: 10.1086/178136.

Sari, Re'em, Tsvi Piran, and Ramesh Narayan (Apr. 1998). "Spectra and Light Curves of Gamma-Ray Burst Afterglows". In: *The Astrophysical Journal Letters* 497.1, pp. L17–L20. ISSN: 0004-637X. DOI: 10.1086/311269. eprint: astro-ph/9712005.

Savchenko, V. et al. (Oct. 2017). "INTEGRAL Detection of the First Prompt Gamma-Ray Signal Coincident with the Gravitational-wave Event GW170817". In: *The Astrophysical Journal Letters* 848.2, p. L15. ISSN: 2041-8205. DOI: 10.3847/2041-8213/aa8f94. eprint: 1710.05449.

Scargle, Jeffrey D (1998). "Studies in Astronomical Time Series Analysis. V. Bayesian Blocks, a New Method to Analyze Structure in Photon Counting Data". In: *The Astrophysical Journal* 504.1, pp. 405–418. ISSN: 0004-637X. DOI: 10.1086/306064. eprint: astro-ph/9711233.

Scargle, Jeffrey D. et al. (2013). "Studies in astronomical time series analysis. VI. Bayesian Block representations". In: *The Astrophysical Journal* 764.2, p. 167. ISSN: 0004-637X. DOI: 10.1088/0004-637x/764/2/167. eprint: 1207.5578.

Schaefer, R. K. et al. (2016). "Observation and modeling of the South Atlantic Anomaly in low Earth orbit using photometric instrument data". In: *Space Weather* 14.5, pp. 330–342. ISSN: 1542-7390. DOI: 10.1002/2016sw001371.

Shea, M.A., D.F. Smart, and L.C. Gentile (1987). "Estimating cosmic ray vertical cutoff rigidities as a function of the McIlwain L-parameter for different epochs of the geomagnetic field". In: *Physics of the Earth and Planetary Interiors* 48.3-4, pp. 200–205. ISSN: 0031-9201. DOI: 10.1016/0031-9201(87)90145-2.

Shemi, Amotz and Tsvi Piran (Dec. 1990). "The appearance of cosmic fireballs". In: *The Astrophysical Journal* 365, p. L55. ISSN: 0004-637X. DOI: 10.1086/185887.

Siegert, Thomas et al. (July 2015). "Revisiting INTEGRAL/SPI observations of 44Ti from Cassiopeia A". In: *Astronomy & Astrophysics* 579, A124. ISSN: 0004-6361. DOI: 10.1051/0004-6361/201525877. eprint: 1505.05999.

Siegert, Thomas et al. (2016). "Gamma-ray spectroscopy of positron annihilation in the Milky Way". In: *Astronomy & Astrophysics* 586, A84. ISSN: 0004-6361. DOI: 10.1051/0004-6361/201527510. eprint: 1512.00325.

Siegert, Thomas et al. (June 2019). "Background modelling for γ-ray spectroscopy with INTEGRAL/SPI". In: *Astronomy & Astrophysics* 626, A73. ISSN: 0004-6361. DOI: 10.1051/0004-6361/201834920. eprint: 1903.01096.

Silva, M R da and E M Rocco (2017). "Analysis of the passage of a spacecraft between the Van Allen belts considering a low and high solar activity". In: *Journal of Physics: Conference Series* 911.1, p. 012005. ISSN: 1742-6596. DOI: 10.1088/1742-6596/911/1/012005.

Skilling, John (Nov. 2004). "Nested Sampling". In: *AIP Conference Proceedings* 735.1, pp. 395–405. ISSN: 0094-243X. DOI: 10.1063/1.1835238.

— (2006). "Nested sampling for general Bayesian computation". In: *Bayesian Analysis* 1.4, pp. 833–859. ISSN: 1936-0975. DOI: 10.1214/06-ba127.

Skinner, G. and P. Connell (Nov. 2003). "The Spiros imaging software for the Integral SPI spectrometer". In: *Astronomy & Astrophysics* 411.1, pp. L123–L126. ISSN: 0004-6361. DOI: 10.1051/0004-6361:20031260. eprint: astro-ph/0308444.

Stan, Development Team (2022). *Stan Modeling Language Users Guide and Reference Manual, 2.30*. URL: https://mc-stan.org.

Stanek, K. Z. et al. (2003). "Spectroscopic Discovery of the Supernova 2003dh Associated with GRB 030329". In: *The Astrophysical Journal Letters* 591.1, pp. L17–L20. ISSN: 0004-637X. DOI: 10.1086/376976. eprint: astro-ph/0304173.

Stefanini, Matteo (2021). "Implementation of the Galactic Center as a Background Source of Gamma-Radiation for Fermi/GBM". Bsc Thesis. Technische Universität München.

Sturner, S. J. et al. (Nov. 2003). "Monte Carlo simulations and generation of the SPI response". In: *Astronomy & Astrophysics* 411.1, pp. L81–L84. ISSN: 0004-6361. DOI: 10.1051/0004-6361:20031171.

Szécsi, D. et al. (2013). "Direction dependent background fitting for the Fermi GBM data". In: *Astronomy & Astrophysics* 557, A8. ISSN: 0004-6361. DOI: 10.1051/0004-6361/201321068. eprint: 1306.3812.

Thompson, D. J., G. A. Simpson, and M. E. Özel (1981). "SAS 2 observations of the Earth albedo gamma radiation above 35 MeV". In: *Journal of Geophysical Research: Space Physics* 86.A3, pp. 1265–1270. ISSN: 0148-0227. DOI: 10.1029/ja086ia03p01265.

Treister, E., C. Megan Urry, and Shanil Virani (May 2009). "The space density af Compton-thick active galactic nucleus and the X-ray background". In: *The Astrophysical Journal* 696.1, pp. 110–120. ISSN: 0004-637X. DOI: 10.1088/0004-637X/696/1/110.

Türler, M. et al. (2010). "INTEGRAL hard X-ray spectra of the cosmic X-ray background and Galactic ridge emission". In: *Astronomy & Astrophysics* 512, A49. ISSN: 0004-6361. DOI: 10.1051/0004-6361/200913072. eprint: 1001.2110.

Ueda, Yoshihiro et al. (2014). "Toward the standard population synthesis model of the x-ray background: Evolution of X-ray luminosity and absorption functions of active galactic nuclei including Compton-thick populations". In: *The Astrophysical Journal* 786.2, p. 104. ISSN: 0004-637X. DOI: 10.1088/0004-637x/786/2/104. eprint: 1402.1836.

Vedrenne, G. et al. (Nov. 2003). "SPI: The spectrometer aboard INTEGRAL". In: *Astronomy & Astrophysics* 411.1, pp. L63–L70. ISSN: 0004-6361. DOI: 10.1051/0004-6361:20031482.

Vianello, Giacomo (2018). "The Significance of an Excess in a Counting Experiment: Assessing the Impact of Systematic Uncertainties and the Case with a Gaussian Background". In: *The Astrophysical Journal Supplement Series* 236.1, p. 17. ISSN: 0067-0049. DOI: 10.3847/1538-4365/aab780. eprint: 1712.00118.

Vianello, Giacomo et al. (2017). "The Multi-Mission Maximum Likelihood framework (3ML)". In: *Proceedings of 7th International Fermi Symposium — PoS(IFS2017)* 1, p. 130. DOI: 10.22323/1.312.0130.

Vietri, Mario (1997). "The Afterglow of Gamma-Ray Bursts: The Cases of GRB 970228 and GRB 970508". In: *The Astrophysical Journal Letters* 488.2, pp. L105–L108. ISSN: 0004-637X. DOI: 10.1086/310931. eprint: astro-ph/9706060.

— (2008). *Foundations of High-Energy Astrophysics*. The university of Chicago Press, All.

Vietri, Mario and Luigi Stella (1998). "A Gamma-Ray Burst Model with Small Baryon Contamination". In: *The Astrophysical Journal* 507.1, pp. L45–L48. ISSN: 0004-637X. DOI: 10.1086/311674. eprint: astro-ph/9808355.

Watanabe, K. et al. (May 1997). "The Cosmic γ-ray Background from supernovae". In: *Proceedings of the Fourth Compton Symposium*. Ed. by Charles D. Dermer, Mark S. Strickman, and James D. Kurfess. Vol. 410. American Institute of Physics Conference Series, pp. 1223–1227. DOI: 10.1063/1.53933.

Wheeler, J. Craig et al. (July 2000). "Asymmetric Supernovae, Pulsars, Magnetars, and Gamma-Ray Bursts". In: *The Astrophysical Journal* 537.2, pp. 810–823. ISSN: 0004-637X. DOI: 10.1086/309055. eprint: astro-ph/9909293.

Wilms, J, A Allen, and R McCray (2000). "On the Absorption of X-Rays in the Interstellar Medium". In: *The Astrophysical Journal* 542.2, pp. 914–924. ISSN: 0004-637X. DOI: 10.1086/317016. eprint: astro-ph/0008425.

Winkler, C. et al. (Nov. 2003). "The INTEGRAL mission". In: *Astronomy & Astrophysics* 411.1, pp. L1–L6. ISSN: 0004-6361. DOI: 10.1051/0004-6361:20031288.

Worsley, M. A. et al. (2005). "Resolving the X-ray Background". In: *AIP Conference Proceedings* 801.1, pp. 51–56. ISSN: 0094-243X. DOI: 10.1063/1.2141832.

Xu, Siyao, Yuan-Pei Yang, and Bing Zhang (Jan. 2018). "On the Synchrotron Spectrum of GRB Prompt Emission". In: *The Astrophysical Journal* 853.1, p. 43. ISSN: 0004-637X. DOI: 10.3847/1538-4357/aaa0ca.

Yu, Hoi-Fung et al. (Nov. 2015). "The sharpness of gamma-ray burst prompt emission spectra". In: *Astronomy & Astrophysics* 583, A129. ISSN: 0004-6361. DOI: 10.1051/0004-6361/201527015. eprint: 1507.05589.

Yu, Hoi-Fung et al. (2016). "The Fermi GBM gamma-ray burst time-resolved spectral catalog: brightest bursts in the first four years". In: *Astronomy & Astrophysics* 588, A135. ISSN: 0004-6361. DOI: 10.1051/0004-6361/201527509. eprint: 1601.05206.

Zhang, Nancy R et al. (2010). "Detecting simultaneous changepoints in multiple sequences." In: *Biometrika* 97.3, pp. 631–645. ISSN: 0006-3444. DOI: 10.1093/biomet/asq025.